HIERARCHICAL MATERIALS FOR ADVANCED ENERGY STORAGE

EDITED BY: Guanglin Xia, Tengfei Zhou and Xuebin Yu
PUBLISHED IN: Frontiers in Chemistry

frontiers Research Topics

frontiers

ISSN 1664-8714
ISBN 978-2-88966-185-5
DOI 10.3389/978-2-88966-185-5

About Frontiers

Frontiers is more than just an open-access publisher of scholarly articles: it is a pioneering approach to the world of academia, radically improving the way scholarly research is managed. The grand vision of Frontiers is a world where all people have an equal opportunity to seek, share and generate knowledge. Frontiers provides immediate and permanent online open access to all its publications, but this alone is not enough to realize our grand goals.

Frontiers Journal Series

The Frontiers Journal Series is a multi-tier and interdisciplinary set of open-access, online journals, promising a paradigm shift from the current review, selection and dissemination processes in academic publishing. All Frontiers journals are driven by researchers for researchers; therefore, they constitute a service to the scholarly community. At the same time, the Frontiers Journal Series operates on a revolutionary invention, the tiered publishing system, initially addressing specific communities of scholars, and gradually climbing up to broader public understanding, thus serving the interests of the lay society, too.

Dedication to Quality

Each Frontiers article is a landmark of the highest quality, thanks to genuinely collaborative interactions between authors and review editors, who include some of the world's best academicians. Research must be certified by peers before entering a stream of knowledge that may eventually reach the public - and shape society; therefore, Frontiers only applies the most rigorous and unbiased reviews.
Frontiers revolutionizes research publishing by freely delivering the most outstanding research, evaluated with no bias from both the academic and social point of view. By applying the most advanced information technologies, Frontiers is catapulting scholarly publishing into a new generation.

What are Frontiers Research Topics?

Frontiers Research Topics are very popular trademarks of the Frontiers Journals Series: they are collections of at least ten articles, all centered on a particular subject. With their unique mix of varied contributions from Original Research to Review Articles, Frontiers Research Topics unify the most influential researchers, the latest key findings and historical advances in a hot research area! Find out more on how to host your own Frontiers Research Topic or contribute to one as an author by contacting the Frontiers Editorial Office: researchtopics@frontiersin.org

HIERARCHICAL MATERIALS FOR ADVANCED ENERGY STORAGE

Topic Editors:
Guanglin Xia, Fudan University, China
Tengfei Zhou, University of Wollongong, Australia
Xuebin Yu, Fudan University, Chin

Citation: Xia, G., Zhou, T., Yu, X., eds. (2020). Hierarchical Materials for Advanced Energy Storage. Lausanne: Frontiers Media SA. doi: 10.3389/978-2-88966-185-5

Table of Contents

frontiers in Chemistry

EDITORIAL
published: 12 November 2020
doi: 10.3389/fchem.2020.601947

Editorial: Hierarchical Materials for Advanced Energy Storage

Guanglin Xia[1]*, *Tengfei Zhou*[2]* and *Xuebin Yu*[1]*

[1] Department of Materials Science, Fudan University, Shanghai, China, [2] Institute for Superconducting & Electronic Materials, University of Wollongong, Wollongong, NSW, Australia

Keywords: hierarchical structure, hydrogen storage, electrochemical energy storage, interface, metal hydrides

Editorial on the Research Topic

Hierarchical Materials for Advanced Energy Storage

It is urgent to search clean and renewable energy sources for maintaining the economic growth of modern society. In order to realize the versatile, clean, and efficient use of renewable energy, developing efficient energy storage materials and devices is of critical importance. To date, hydrogen storage and electrochemical energy storage are two main types of energy storage systems. Building hierarchical structures has been widely demonstrated to be an effective in advancing various energy storage materials owing to the unique physical and chemical properties induced by tuning their particle sizes, phases, and pores. Hierarchical structures offer several key advantages for advancing hydrogen storage materials and electrochemical energy storage materials, including: (i) the increased surface/contact area per unit mass, which could realize the fast diffusion and adsorption of active species; (ii) the tuned interface structures, which could promote the chemical reaction at the interface toward advanced energy storage performance; (iii) the accommodation of the mechanical strain, which could alleviate the structural damage upon the energy storage process and hence result in superior cycling stability. In this special issue, all the published papers could promote our understanding of the mechanism behind the improvement of energy storage materials via building hierarchical structures.

In this topic, Kim et al. reported the synthesis of binder-free cathode based on Fe foam modified with FeS_2 for application in thermal batteries. The work of Zhang et al. demonstrated that, when applied in supercapacitors, three-dimensional core-branch α-Fe_2O_3@NiO/Carbon cloth exhibits high areal capacitance and stable cycling performance due to the reduction of contact resistance and the free-standing structure of the flexible electrode. The flexible and boron-Doped carbon nanotube film built by Wang et al. presents good rate capability and excellent cycling performance when used as a flexible anode in Li ion batteries. Xia et al. demonstrated the potential application of hierarchical structured electrocatalysts for overall water splitting. Moreover, Liu et al. presented a brief review about the progress of electrocatalytic hydrogen production induced by hierarchical porous molybdenum carbide-based nanomaterials and Guan et al. reviewed the progress of advanced supercapacitor materials using two-dimensional transition metal oxide and hydroxide-based hierarchical architectures.

In the field of hydrogen storage, Ali et al. revealed that the catalytic role of K_2NbF_7 on the dehydrogenation performance of $LiAlH_4$ could be mainly attributed to in-formed NbF_4, LiF, and K or K-containing phases during heating for hydrogen storage while Li et al. investigated the influence of various Al sources on the dehydrogenation behavior of $LiBH_4$. According to the work of Chen et al., when adopting nanoporous Ni-based alloy as templates, the hydrogen storage performance of LiBH4 could be significantly improved owing to the reduction of particle size. In addition, Sun et al., reviewed the recent progress on improving the hydrogen storage performance of MgH_2 using transition metals and carbon materials.

OPEN ACCESS

Edited by:
Jie He,
University of Connecticut, United States

Reviewed by:
Sen Zhang,
University of Virginia, United States

Correspondence:
Guanglin Xia
xiaguanglin@fudan.edu.cn
Tengfei Zhou
tengfeiz@uow.edu.au
Xuebin Yu
yuxuebin@fudan.edu.cn

Specialty section:
This article was submitted to Nanoscience, a section of the journal Frontiers in Chemistry

Received: *02 September 2020*
Accepted: *26 October 2020*
Published: *12 November 2020*

Citation:
Xia G, Zhou T and Yu X (2020) Editorial: Hierarchical Materials for Advanced Energy Storage. Front. Chem. 8:601947. doi: 10.3389/fchem.2020.601947

Finally, as the Guest Editors of this topic issue, we would like to express our gratitude to all the authors for their valuable contributions and all the referees for their hard work and kind help. We hope that this special issue could boost the readers' research interest in building hierarchical structures toward advanced energy storage performance.

AUTHOR CONTRIBUTIONS

All authors listed have made a substantial, direct and intellectual contribution to the work, and approved it for publication.

FUNDING

This work was partially supported by the National Key R&D Program of China (No. 2018YFB1502101), National Science Fund for Distinguished Young Scholars (51625102), the National Natural Science Foundation of China (51971065 and 51901045), the Innovation Program of Shanghai Municipal Education Commission (2019-01-07-00-07-E00028), and the Programs for Professor of Special Appointment (Eastern Scholar) at Shanghai Institutions of Higher Learning.

Conflict of Interest: The authors declare that the research was conducted in the absence of any commercial or financial relationships that could be construed as a potential conflict of interest.

frontiers in Chemistry

ORIGINAL RESEARCH
published: 29 November 2019
doi: 10.3389/fchem.2019.00832

A Flexible and Boron-Doped Carbon Nanotube Film for High-Performance Li Storage

Lei Wang[1], *Wenlei Guo*[1], *Pengyi Lu*[1], *Tao Zhang*[1], *Feng Hou*[1]* *and Ji Liang*[1,2]*

[1] *Key Laboratory of Advanced Ceramics and Machining Technology of the Ministry of Education, School of Materials Science and Engineering, Tianjin University, Tianjin, China,* [2] *Institute for Superconducting & Electronic Materials, Australian Institute of Innovative Materials, Innovation, University of Wollongong, North Wollongong, NSW, Australia*

Boron-doped carbon nanotubes are a promising candidate for Li storage due to the unique electronic structure and high crystallinity brought by the boron dopants. However, the relatively low Li storage capacity has limited its application in the electrochemical energy storage field, which is mainly caused by the predominantly intact graphitic structure on their surface with limited access points for Li ion entering. Herein, we report a novel B-doped CNTs (py-B-CNTs) film, in which the CNTs possess intrinsically rough surface but flat internal graphitic structure. When used as a flexible anode material for LIBs, this py-B-CNTs film delivers significantly enhanced capacity than the conventional B-doped CNTs or the pristine CNTs films, with good rate capability and excellent cycling performance as well. Moreover, this flexible film also possesses excellent mechanical flexibility, making it capable of being used in a prototype flexible LIB with stable power output upon various bending states.

Keywords: boron-doped, carbon nanotube, flexible, film, lithium storage

OPEN ACCESS

Edited by:
Guanglin Xia,
Fudan University, China

Reviewed by:
Xuezhang Xiao,
Zhejiang University, China
Chaofeng Zhang,
Anhui University, China

***Correspondence:**
Feng Hou
houf@tju.edu.cn
Ji Liang
liangj@uow.edu.au

Specialty section:
This article was submitted to Electrochemistry, a section of the journal Frontiers in Chemistry

Received: *29 October 2019*
Accepted: *15 November 2019*
Published: *29 November 2019*

Citation:
Wang L, Guo W, Lu P, Zhang T, Hou F and Liang J (2019) A Flexible and Boron-Doped Carbon Nanotube Film for High-Performance Li Storage. Front. Chem. 7:832. doi: 10.3389/fchem.2019.00832

INTRODUCTION

The demand for high-performance energy storage devices is continuously increasing as a result of the rapid development of portable electronic devices and electric vehicles. Lithium-ion battery (LIB) has been continuously attracting attention in research during the past 30 years and widely applied in a range of applications (Li et al., 2018). However, graphite, the most widely applied commercial anode material for LIBs, is impeding the further improvement of the energy density and power density of LIBs, due to its limited Li storage capacity and hardness of varied structural design (Fang et al., 2017; Liu et al., 2018). Nanostructured carbon materials with highly conductive network provide adequate paths for electron transport; while their abundant pore structures can effectively facilitate the Li ion diffusion and accommodate the volume change of electrodes during an electrochemical process, which is highly beneficial for anode applications for LIBs (Roy and Srivastava, 2015; Tang et al., 2015). Among them, carbon nanotubes (CNTs) are especially promising, because of their superior electrical conductivity, large specific surface area to uniformly load the active substances, and more importantly, the outstanding flexibility for the application for flexible LIBs (Dai, 2002; Kim et al., 2006; Sheem et al., 2006).

Generally, to further enhance the intrinsic Li storage capacity of CNTs, surface modification (Hata et al., 2004; Kang et al., 2012; Lee and Park, 2015), chemical doping (Way and Dahn, 1994; Chen et al., 2013; Sharifi et al., 2015; Zhu et al., 2016), and integration of high capacity active materials (Chen et al., 2008, 2016) are the three major approaches. Among them, doping

of heteroatoms [e.g., boron (Stephan et al., 1994; Hsu et al., 2000; Maultzsch et al., 2002; Fujisawa et al., 2018), nitrogen (Maldonado et al., 2006; Bulusheva et al., 2011; Wang L. et al., 2016; Lu et al., 2017), phosphorus (Campos-Delgado et al., 2010; Zhang et al., 2013; Wu et al., 2017) or others] has been widely adopted. On the one hand, the presence of these heteroatoms can introduce more defects, serving as active sites for Li storage with a high capacity. For instance, doping CNTs with nitrogen has been reported to double the Li storage capacity compared with the pristine CNTs (494 vs. 260 mAh g^{-1}) (Li et al., 2012). Similar performance enhancement can be achieved by phosphorus or sulfur doping as well (Campos-Delgado et al., 2010; Zhang et al., 2013; Wang C. et al., 2016). On the other hand, heteroatom doping can also provide additional charge carriers that can substantially improve the electronic conductivity of CNTs to achieve a better rate performance for battery applications (Way and Dahn, 1994; Pan et al., 2016).

Among all the doping elements, boron has been considered a quite promising candidate, from several aspects. Firstly, the sizes of boron and carbon atom are similar, which means a minimized lattice distortion to the graphitic structure after doping. This is essential for maintaining the structural stability of the resulted materials during repeated charge-discharge in LIBs (Way and Dahn, 1994; Redlich et al., 1996; Zhang et al., 2016; Geng et al., 2019). Secondly, due to the smaller electronegativity of boron, it will turn the surrounding carbon atom into a negatively-charged center, which attracts more Li ion adsorption (Way and Dahn, 1994). For instance, the boron-doped graphite, which was prepared by annealing pitch coke and boron oxide at 2,800°C, showed a high discharge capacity of 315 mAh g^{-1} at a rate of 1.56 mA cm^{-2} (Tanaka et al., 2001). Thirdly, boron atoms replace the carbon atoms in an sp^2-type hybrid manner, which supplies more holes to the valence band of carbon, leading to better electronic conductivity of the obtained B-doped carbon materials (Lin et al., 2011; Yeh et al., 2014). Due to this, the boron-doped carbon particles also exhibited better rate capability than the undoped one (Chae et al., 2014). All these unique features of boron doping demonstrate the great potential of boron-doped carbon for Li storage.

Nevertheless, the reports on B-doped CNTs for LIBs are fairly rare, compared with doping them with other elements. One major limitation of the B-doped CNTs is the relatively low capacity, especially at high rates, which is mainly caused by the nearly "intact" graphitic structure with limited access for Li ions to enter the interlayer space as mentioned above. One commonly adopted strategy to tackle with this issue is to create extra surface openings on B-doped carbons, either by mechanical (e.g., shatter or grind) or chemical (e.g., oxidation) methods (Tsang et al., 1994; Eom et al., 2004). Unfortunately, this will inevitably cripple the original framework of B-doped CNTs and compromise their electrochemical performance, especially the cycling stability. In contrast, directly constructing B-doped CNTs with an intrinsically rough surface could be a more attractive method that can not only provide more entrance for Li ions but also maintain the desirable graphitic structure of B-doped CNTs for better electrochemical performance. This is, however, not yet achieved according to the reports by far.

Based on these considerations, we herein report a flexible B-doped CNTs film, which was prepared by a modified floating catalyst chemical vapor deposition (FCCVD) method. By introducing pyridine into the FCCVD method, the morphology of the obtained B-doped CNTs has been successfully altered from a flat surface to a highly rough one, while the inherent graphitic structure remains. As a result, such modified B-doped CNTs (py-B-CNTs) shows much enhanced Li storage performance in comparison with the unmodified B-doped CNTs (B-CNTs), in terms of much-improved capacity, rate capability, and cycling stability. Meanwhile, the as-prepared material also possesses excellent mechanical stability, making it capable of being used in a prototype flexible LIB, which can function well under different bending states. As a result, this flexible and free-standing B-doped CNTs film with excellent Li storage capability has a very good potential to be applied in the next-generation flexible LIBs as well as other battery systems.

EXPERIMENTAL SECTION

Synthesis of py-B-CNTs Film

The py-B-CNTs film was synthesized by a pyridine-modified FCCVD method. Ethanol was chosen as carbon precursor dissolved with ferrocene and thiophene at a mass ratio of 95:1.5:1 (Guo et al., 2019). Then, boric acid (i.e., the boron precursor) and pyridine (i.e., the structure-modifying agent) were added into the precursor solution at proportions of 2 and 4 wt.%, respectively, and ultrasonically agitated for 20 min until fully dissolved. Subsequently, the precursor was treated through an ultrasonic nebulization device and injected into a vertical furnace (1150°C) from the top of the furnace tube. Traveling downwards with the H_2 carrier gas, the precursor was converted into py-B-CNTs at the hot zone of the furnace and assembled into a film, which was collected continuously at the bottom of the furnace tube. For comparison, non-doped and B-doped CNTs film (denoted CNTs and B-CNTs, respectively) were prepared by unmodified FCCVD method, and non-doped CNTs film (py-CNTs) was prepared through the pyridine-modified FCCVD method as well, without adding boric acid in the precursor.

Sample Characterization

The tensile strength and resilience of the prepared films were measured by fiber tensile tester (XQ-1C, Shanghai New Fiber Instrument Co., Ltd.) and electronic tensile testing machine (UTM2203, SUNS), respectively. The morphology and microstructure of the films were analyzed by scanning electron microscopy (SEM, S-4800, Hitachi) and transmission electron microscopy (TEM, JEM-2100, JEOL). The chemical state of the materials was studied by X-ray photoelectron spectroscopy (XPS, ESCALAB 250Xi, Thermo Scientific). The infrared spectrum (IR spectrum) was obtained on an infrared spectrometer (Nicolet iS5, ThermoFisher Scientific). The Raman spectra were collected on a Raman spectrometer (LabRAM HR 800, Renishaw) using 532 nm laser. X-ray diffraction (XRD) patterns of NB-CNT films were recorded by a RIGAKU D/Max 2500 Vdiffractometer with Cu Kα radiation source at room temperature. Nitrogen adsorption

and desorption isotherms were obtained by at 77 K (ASAP 2020, Micromeritics).

Electrochemical Measurements

All the samples were cut into an electrode disc (12 mm diameter) by a wafer cutting machine (MSK-T10, HF-Kejing) and used without adding any binders or conductive agents. Coin-type CR2032 cells were assembled in an argon-filled glove box [SUPER (1220/750), Mikrouna, $[O_2] < 0.1$ ppm, $[H_2O] < 0.1$ ppm], using Li foil as the counter electrode. 1 M $LiPF_6$ in ethylene carbonate (EC), diethyl carbonate (DEC) and dimethyl carbonate (DMC) (volume ratio of 1:1:1) solution was used as the electrolyte and a porous film (Celgard, 2400, Celgard) was used as the separator. Galvanostatic charge-discharge measurement was performed on a battery tester (CT-3008W-5V1mA-S4, Neware) over a voltage range of 0.01–3.0 V vs. Li/Li^+. Cyclic voltammogram (CV) and electrochemical impedance spectroscopy (EIS) tests were carried out on an electrochemical workstation (CHI 660D, CH Instruments). CV was performed over a potential range of 0.01–3.0 V at a scan rate of 0.5 mV s^{-1}. EIS was measured in the frequency range of 0.01–10^5 Hz with a disturbance amplitude of 5 mV. All the experiments were performed at room temperature.

RESULTS AND DISCUSSION

The fabrication process of the py-B-CNTs film is illustrated in **Figure 1A**. The precursor solution, consisting of ethanol, thiophene, ferrocene, boric acid, and pyridine, was gasified through an ultrasonic nebulization device and injected into the vertical furnace tube with an H_2 atmosphere. The resultant py-B-CNTs film traveled down with the gas flow and was collected at the bottom of the furnace tube. The as-prepared film is light-weight and self-standing, which can withstand various extreme deformation without any structural failures, including being stretched, folded multiple times, and twisted as shown in **Figures 1B–E**. In particular, the py-B-CNTs film possesses exceptional toughness and stretchability with nearly 50% strain before final fracture (**Figure 1F** and **Figure S1**) and high recovery rate of 50% after 10% stretching (**Figure S2**), which are obviously superior to CNTs film and highly advantageous for flexible LIB applications.

The morphology and microstructure of the materials were firstly characterized by SEM and TEM, as shown in **Figure 2**. On the pristine CNTs film, except for a few clusters, which are typically composed of amorphous carbon (Song et al., 2019) and short crinkly tubes (circled in **Figure 2A**), the majority of the material are intertwined bunches of long and smooth CNTs (inset of **Figure 2A**). Under TEM, these long tubes are found to be few-walled CNTs with diameters of 6–8 nm (**Figure S3**) and the crinkly tubes are multi-walled with a diameter of ∼20 nm as well as an average interlayer distance of 0.34 nm, typical of the graphitic structure (**Figures 2B,C** and **Figure S4**). In contrast, the involvement of pyridine in the precursor significantly altered the morphology of the obtained CNTs (i.e., py-CNTs). On the one hand, the tangled nanotubes in the pristine CNTs film were scattered into numerous short and curved tubes (**Figure 2D**), which may be attributed to the reduced interaction forces between short tubes owing to the crinkly surfaces and distorted graphitic structures on their wall as shown in **Figures 2E,F** and **Figure S5** (Nitze et al., 2009). According to previous studies, the appearance of high surface roughness and distorted structures is owing to the distortion to the graphitic structures (e.g., five-member rings in the graphitic framework) introduced by the nitrogen-containing species during the formation of CNTs (Nitze et al., 2009; Yeh et al., 2014). On the other hand, the amount of amorphous carbon around CNTs increased as well. In the case of introducing boron, on the contrary, the obtained B-CNTs film showed another unique morphology, where well-oriented CNTs and rod-like tubes structure were observed (**Figure 2G**), with an increased diameter up to 30–40 nm in comparison with the pristine CNTs. The graphitic structure of the B-CNTs is, however, seemingly intact with parallel and straight graphitic layers (interlayer distance of 0.35 nm) on its wall (**Figures 2H–I**), which may be owing to the catalytic graphitization effect of boron on CNTs (Antunes et al., 2006). Specifically, the flat graphitic layers appeared slightly tilted relative to the lumen, thus resulted in a few openings along CNTs and provided extra entrances for Li ions to insert. Moreover, the amorphous carbon wrapped outside nanotubes as observed in both CNTs and py-CNTs almost disappeared, possibly due to the cleaning effect of the water released from the decomposition of boric acid at high temperature (Hata et al., 2004; Cui et al., 2011). However, a few clusters with short tubes were still observable as circled in **Figure 2G** and **Figure S6**, probably indicating that boron did not dope in these areas.

In contrast, by modifying the fabrication process using pyridine (i.e., py-B-CNTs), the good alignment of CNTs, which is similar to the B-CNTs, still predominantly remains, with uniformly-distributed crooked tubes surrounding CNTs (**Figure 2J**). In this case, the py-B-CNTs show a rough surface as in the case of py-CNTs, with the graphitic structure remaining similar to B-CNTs (**Figures 2K–L** and **Figure S7**). This clearly demonstrates that the introduction of pyridine in the synthesis of B-CNTs effectively changed the surface morphology of CNTs into a rough one without significantly compromising the graphitic structure of the material. This unique nanostructure of py-B-CNTs with the more exposed surface could provide more access sites for Li ions to enter the tilted graphitic layers of the CNTs to be stored and the intact graphite framework is able to provide enhanced cycling stability in comparison with other defect-rich carbons (Hu et al., 2013; Li et al., 2014; Lin et al., 2014).

XRD and Raman spectroscopy were then carried out to better study the structure of the material (**Figures 3A,B**). The typical peaks at around 26°, corresponding to the (002) diffraction, indicate the predominant graphitic structure in CNTs and the latter one at 44° can be attributed to the (101) planes of CNTs. Compared with pristine CNTs, the (002) peak of B-CNTs is narrower and sharper, due to the catalytic graphitization effect of boron, well consistent with the HRTEM observations. Moreover, the slight shift of ∼0.9° of (002) peak toward a lower 2θ degree in B-CNTs and py-B-CNTs are observed, indicating a relatively larger interlayer distance than CNTs. By contrast, the broad (002) peak of py-CNTs confirmed the numerous defects created by pyridine additive. At the meantime, the py-B-CNTs also showed

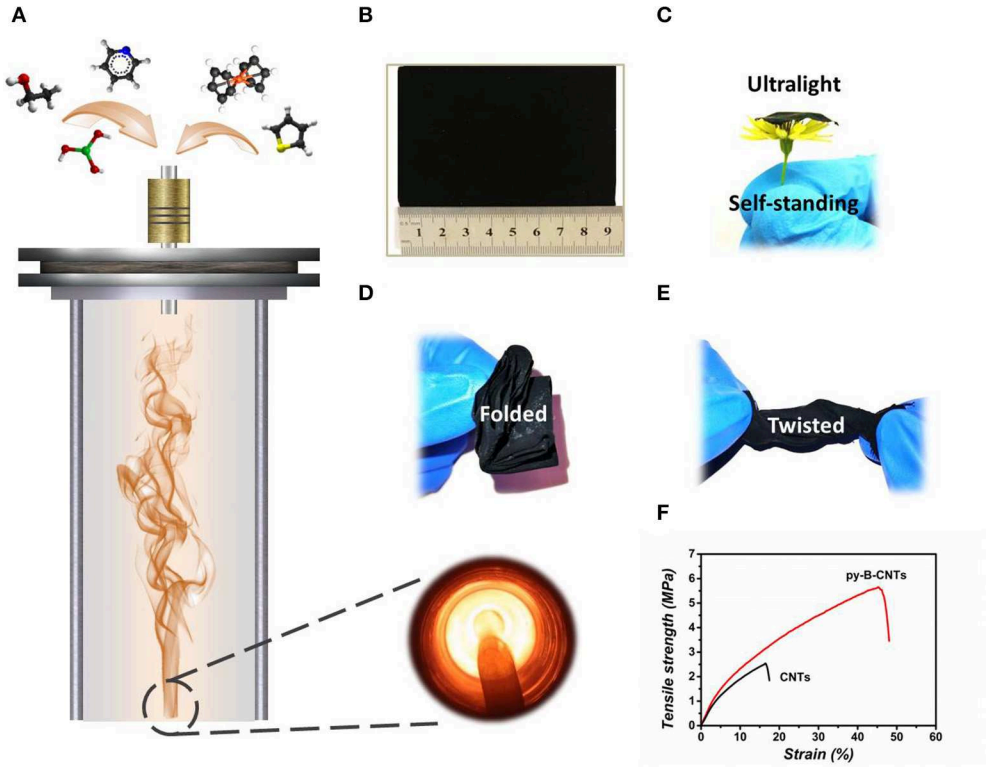

FIGURE 1 | Illustration of the fabrication and flexibility of the py-B-CNTs film. **(A)** Schematic illustration of the synthesis of the py-B-CNTs film from a vertical furnace and corresponding photograph taken from the bottom of the furnace tube; **(B)** optical image of a piece of py-B-CNTs film of ~9 × 7 cm; **(C)** optical image of the ultralight and self-standing film; **(D,E)** optical images of the film under various deformations; and **(F)** tensile strength curves of py-B-CNTs and pristine CNTs films.

a slight shift to lower 2θ degrees but a narrower (002) peak in comparison with that of py-CNTs, due to the B doping and pyridine addition, comprehensively.

More structural information of the materials was obtained from Raman spectra (**Figure 3B**). The D band at 1,346 cm^{-1} is associated with defects and distortions in the graphitic framework; while the G band at 1,579 cm^{-1} corresponds to the graphitic layers and stretching vibration of carbon atoms (Yang et al., 2017). A slight shift to the higher wavenumber of the G-band for B-CNTs, py-CNTs, and py-B-CNTs is observed in comparison with pristine CNTs, which might be due to the modification in the electronic structure of CNTs (Handuja et al., 2009; Koós et al., 2010). On the other hand, the up-shift of D-band indicates the appearance of new types of disorders or chemical bonds (i.e., B-C or B-O bonds) in B-CNTs, py-CNTs, and py-B-CNTs compared with those of pristine CNTs (Bulusheva et al., 2011), while the shoulder at 1616 cm^{-1} (i.e., D' band) for py-CNTs should be ascribed to the slightly damaged graphite structure (Antunes et al., 2006). In addition, the intensity ratios of the D and G bands (I_D/I_G) of py-B-CNTs, B-CNTs, CNTs, and py-CNTs were calculated to be 0.43, 0.89, 0.95, and 1.12, respectively. The relatively lower I_D/I_G ratio of B-CNTs can be attributed to the removal of amorphous carbon and catalytic graphitization effect of B on CNTs, while the higher I_D/I_G of py-CNTs is mainly owing to the defects created by pyridine and increased amorphous carbon compared with pristine CNTs. Remarkably, py-B-CNTs showed the smallest I_D/I_G, possibly owing to the loosening of the tangled tubes as in B-CNTs and the more thorough catalytic graphitization from boron.

To further investigate the pore structure of the materials, nitrogen adsorption and desorption isotherms were obtained (**Figure 3C** and **Figure S8**). The specific surface area of py-B-CNTs was calculated to be 229.8 $m^2\ g^{-1}$, and a combined type III and type IV isotherm with hysteresis loop at medium to high pressure regions was obtained. This indicates the existence of small amounts of mesopores or macropores in py-B-CNTs, which may originate from the arrangement of the intertwined nanotubes (Ding et al., 2017). The pore size distribution in the inset of **Figure 3C** further showed that these small mesopores are mainly 1.6–2.4 nm, which may originate from the interspaces between tangled nanotubes and long CNTs in py-B-CNTs. Similar results can also be observed in py-CNTs, B-CNTs, and pristine CNTs, as shown in **Figure S8**. The corresponding specific surface areas were calculated to be 198.8, 137.1, and 127.2 $m^2\ g^{-1}$, respectively. Based on this, the high surface area of py-B-CNTs is mainly owing to the rough surface as well as scattered clusters induced by pyridine and the removal of amorphous carbon during the fabrication. The large surface area of py-B-CNTs would provide abundant access sites for Li ions during the charge/discharge process in LIBs.

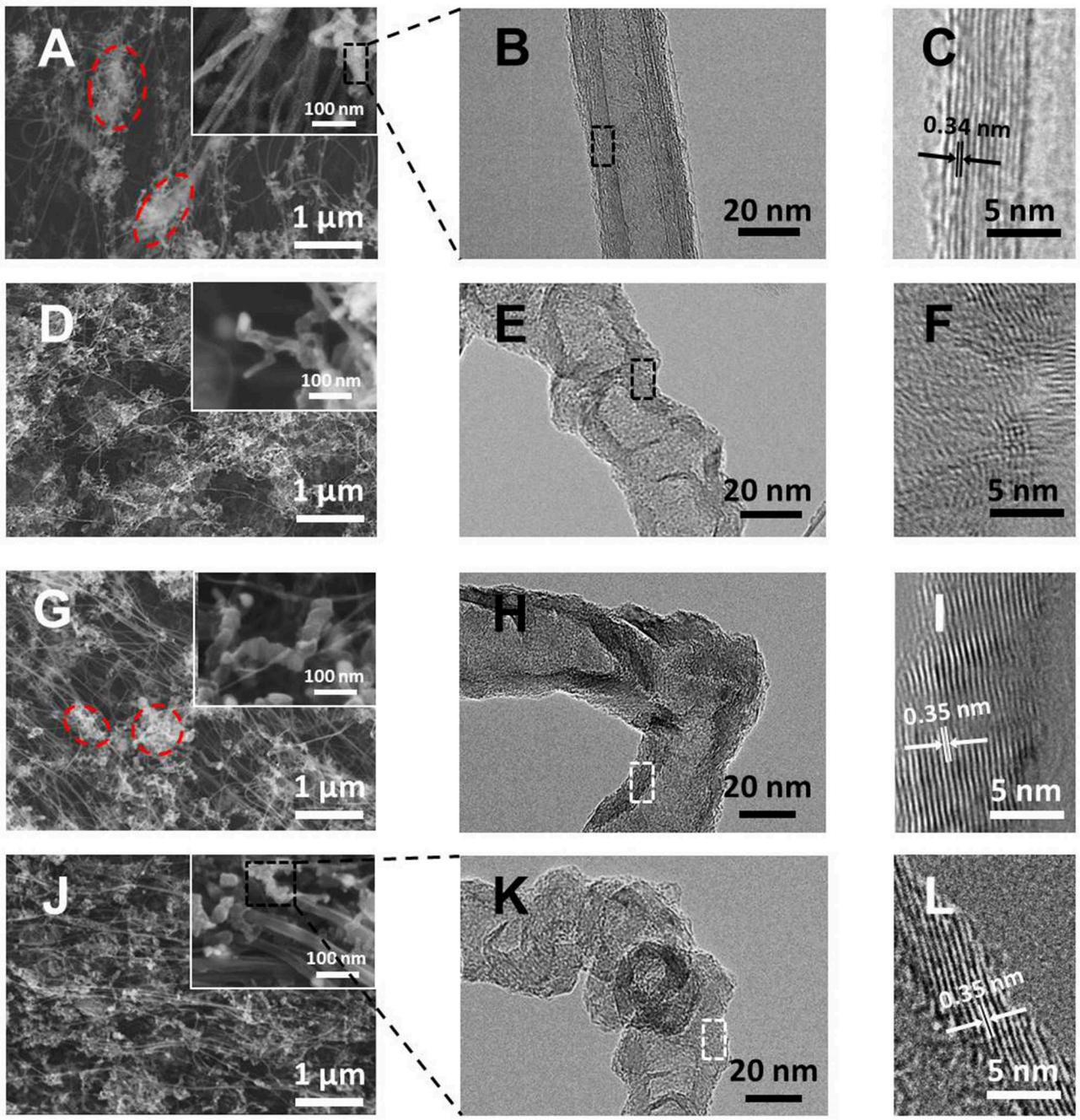

FIGURE 2 | (A,D,G,J) SEM images of CNTs, py-CNTs, B-CNTs, and py-B-CNTs films at different magnifications; **(B,E,H,K)** TEM images; and **(C,F,I,L)** high-resolution TEM images of CNTs, py-CNTs, B-CNTs, and py-B-CNTs films, respectively.

The materials' chemical composition was then studied by energy dispersive spectroscopy (**Figure 3D** and **Table S1**), and it was measured that content of B, C, O, Fe was 11.47, 85.28, 2.91, and 0.34 at.%, respectively, for py-B-CNTs film and no nitrogen was detected. For other materials, py-CNTs possessed higher O content of 5.66 at.% than B-CNTs (0.90 at.%) and CNTs (1.16 at.%), attributed to the easier oxygen adsorption on the defect sites (Yang et al., 2011; Song et al., 2019). The elemental mapping of the materials (**Figure 3D** and **Figures S9**, **S10**) reveals the uniform distribution of carbon, boron, and oxygen over the whole material. The absence of nitrogen indicates that pyridine only participated in the CNTs formation process and changed the morphology of CNTs, but did not cause N-doping in the CNTs, which is also in agreement with the EDS results and

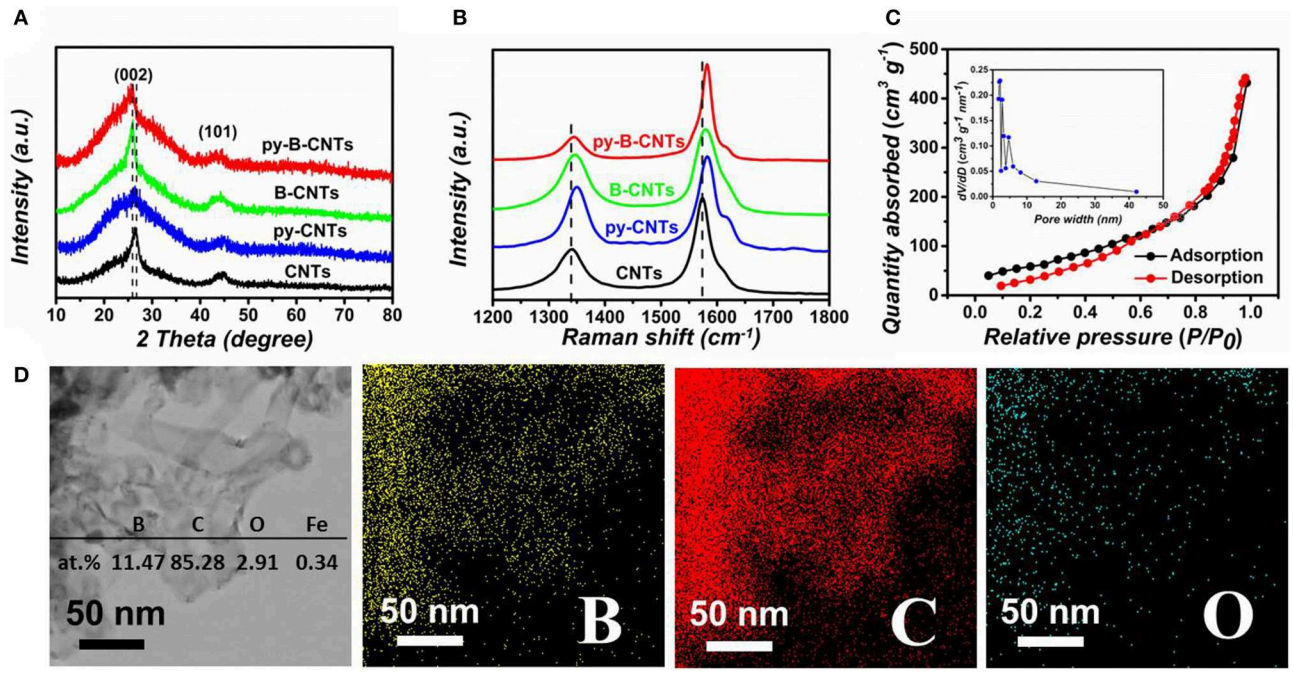

FIGURE 3 | (A) XRD patterns and **(B)** Raman spectra of the samples; **(C)** nitrogen adsorption/desorption isotherms with the pore-size distribution (inset) of py-B-CNTs film; **(D)** the EDS elemental analysis of py-B-CNTs and corresponding elemental mapping of the region.

has been observed in our previous studies (Song et al., 2019). The chemical states of the elements in py-B-CNTs and other materials were further characterized by XPS survey spectrums (**Figures S11**–**S14**). Especially, in the high-resolution spectrums, the total amount of oxygen-containing functional groups (C-OH, C=O, COOH) on py-B-CNTs is obvious higher than on B-CNTs, demonstrating the active sites effectively introduced by pyridine, which is advantageous for Li storage. Similar results can be observed for py-CNTs and CNTs in high-resolution XPS (**Figures S13**, **S14**).

To characterize the electrochemical performances of py-B-CNTs film and the analog materials, they were assembled in a coin cell using a Li foil as the counter electrode. CV loops of py-B-CNTs and CNTs film of the first three scanning cycles are presented in **Figure 4A** and **Figure S15**. For both materials, in the first discharge process of the materials, a strong peak appeared at 0.7 V, which disappeared in the subsequent cycles. This is caused by the decomposition of the electrolyte to form the solid electrolyte interface (SEI) that prevents further contact between electrodes and electrolyte, causing an irreversible capacity. On the other hand, the peak at around 0.2 V is related to the Li ion intercalation process into the graphitic structure of the materials (Chae et al., 2014). Compared with the pristine CNTs, two extra peaks at 0.8 and 1.5 V are observed for py-B-CNTs. The former one, which was also observed in py-CNTs and B-CNTs (**Figure S16**), might be attributed to the defects created by pyridine additive during the fabrication of CNTs to serve as Li storage sites (Pan et al., 2016), or the existence of new type of chemical bond (e.g., B-O bond) (Chae et al., 2014). As for the other peak at 1.5 V, which was also seen in B-CNTs (**Figure S16**), it should be attributed to the formation of $Li_x(B_zC_{1-z})_6$ species, allowing more Li ions to be stored (Way and Dahn, 1994; Chae et al., 2014). As previously discussed, boron acts as an electron acceptor in the carbon lattice and Li will donate its 2s electrons when intercalated into the carbon host (Redlich et al., 1996). Therefore, the introduction of boron strengthens the chemical bond between the intercalated Li ion and the B-doped carbon host, compared to the pure carbon host (Way and Dahn, 1994). In the subsequent cycles, the curves were almost overlapped, demonstrating the good electrochemical stability of py-B-CNTs film anodes.

The GCD profiles of py-B-CNTs film anode in the first, second, and tenth cycles at the current density of 100 mA g^{-1} are shown in **Figure 4B**. In the first discharge process, the potential plateau at ~0.8 V is ascribed to the formation of the SEI, which is consistent with the CV results. The initial discharge and charge capacities are 1182 and 377 mAh g^{-1}, corresponding to an initial Coulombic efficiency of 32%. The large irreversible capacity is also reflected on py-CNTs, B-CNTs, and CNTs anodes (initial Coulombic efficiency of 35, 39, and 43%, respectively) as shown in **Figure S17**, which mainly result from the decomposition of the electrolyte during the formation of SEI on the large surface of the CNTs films (Zhang et al., 2016; Lu et al., 2017). In the following cycles, the Coulombic efficiency increased to 83% in the second cycle and over 97% in the tenth cycle, indicating the high reversibility of py-B-CNTs film electrode.

In order to further measure the cycling performance of py-B-CNTs and CNTs films, the anodes were tested at 100 mA g^{-1}

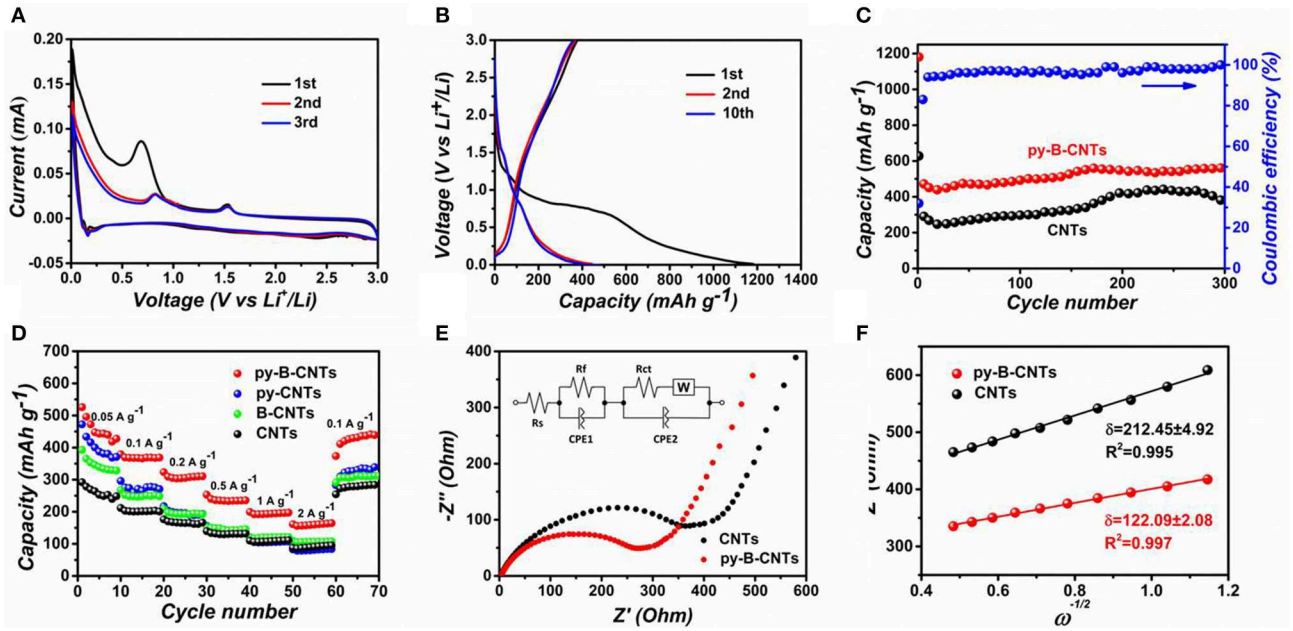

FIGURE 4 | (A) CV loops of the py-B-CNTs film obtained at 0.1 mV s^{-1}; **(B)** galvanostatic charge-discharge (GCD) profiles of py-B-CNTs film; **(C)** cycling performances of the py-B-CNTs and pristine CNTs films for 300 cycles at 100 mA g^{-1}; **(D)** rate capability of the materials at various rates of 0.05-2 A g^{-1}; **(E)** electrochemical impedance spectra of py-B-CNTs and pristine CNTs films and the equivalent circuit to fit the EIS; **(F)** the fitted curve of impedance (Z′) vs. the reciprocal square root of the angular frequency (ω) for py-B-CNTs film.

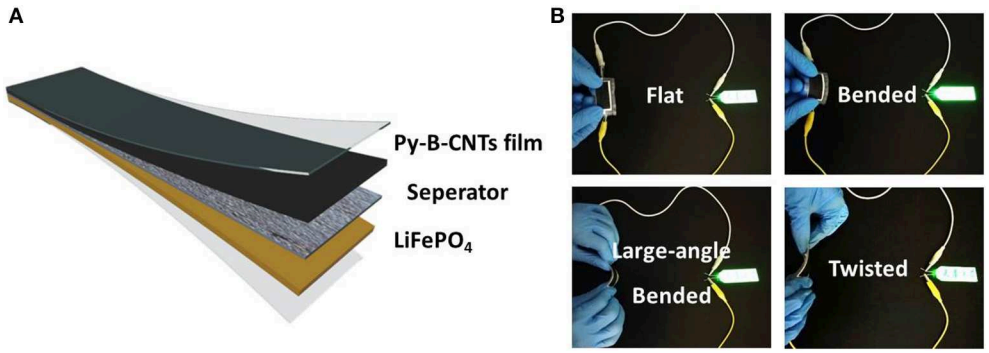

FIGURE 5 | (A) Schematic illustration of the flexible LIB with py-B-CNTs film and commercial $LiFePO_4$ as electrodes; **(B)** photographs of the flexible LIB powering a light-emitting diode board under various bending conditions.

for 300 cycles. As shown in **Figure 4C**, the py-B-CNTs film delivered a high reversible capacity of 548 mAh g^{-1} after 300 cycles, which is significantly higher than that of CNTs, and the columbic efficiency was always over 97%. The excellent cycling performance of py-B-CNTs film mainly benefitted from the high conductivity and stably doped B atoms in the py-B-CNTs. It is noticeable that the capacities of both electrodes slightly increased along with the number of cycles, which could be attributed to two main reasons. On the one hand, the nature of porous films results in the gradual infiltration of electrolyte for active materials. On the other hand, the interlayer spacing of CNTs becomes more expanded with the continuous insertion-extraction of Li ions, which is advantageous to the further Li ion transport between electrodes and the electrolyte and has been also observed in other previous reports (Li et al., 2012; Wang L. et al., 2016; Lu et al., 2017). Besides, a downward trend of the CNTs anode appeared after 250 cycles due to the irreversible lithiation-delithiation process caused by the channel-block phenomenon (Pan et al., 2016), which does not exist for py-B-CNTs anode because of the more abundant entrance sites on the py-B-CNTs, as previously discussed (Wang L. et al., 2016).

The rate capacities of the materials were evaluated at various current densities and compared in **Figure 4D**. Among these materials, the py-B-CNTs film delivered specific capacities of 474, 378, 312, 235, 198, and 167 mAh g^{-1} at current densities from 0.05 to 2 A g^{-1}, which were much higher than those of py-CNTs,

B-CNTs, and CNTs films. The relatively lower capacities of B-CNTs than py-B-CNTs might be owing to that the graphitic layers was not active for Li ions adsorption while introducing extra defects at the openings could ameliorate this. Moreover, it is noted that py-B-CNTs also showed higher capacity retention than py-CNTs at high current densities (56% for py-B-CNTs and 39% for py-CNTs from 0.2 to 2 A g^{-1}), which is due to the improved electrical conductivity by boron doping. Similar results can also be found in the B-CNTs and CNTs samples. Moreover, all the electrodes showed good recovery capability when the rate was switched back to 0.1 A g^{-1}, benefiting from the stability of prepared films.

To further confirm the advantages in the kinetics of the electrochemical process of the py-B-CNTs film, EIS measurement was carried out on the py-B-CNTs and CNTs (**Figure 4E**). It is observed that the Nyquist plots of both materials consist of a depressed semicircle in the high-frequency region and a linear Warburg part in the low frequency region, attributed to charge-transfer resistance and Li-ion diffusion in CNTs network structure, respectively (Sang et al., 2018). Specifically, an equivalent circuit was fitted as shown in the inset of **Figure 4E**. R_s denotes the ohmic resistance of electrolyte, while R_f and R_{ct} correspond to SEI film resistance and charge-transfer resistance. CPE1 and CPE2 represent SEI film capacitance and double layer capacitance, while W is the finite length Warburg impedance related to the solid-state diffusion in the electrodes. The fitted R_{ct} value of py-B-CNTs is 264 Ω, lower than CNTs (373 Ω), indicating a lower charge-transfer resistance in the py-B-CNTs film anode, benefiting from the uniform and well-oriented microstructure of py-B-CNTs film. Besides, the corresponding charge-transfer resistance of B-CNTs and py-CNTs films can also be fitted as 109 and 664 Ω, respectively (**Figure S18**). Moreover, the influence factors for Li-ion diffusion efficiency (D_{Li}) was calculated by Equation 1, in which R is the gas constant, T is the absolute temperature, A is the surface area of the electrode, n is the number of electrons per molecule during oxidization, F is the Faraday constant, C is the concentration of the Li ion, and δ is the Warburg factor (Jin et al., 2017):

$$D_{Li} = \frac{R^2T^2}{2A^2n^4F^4C^2\delta^2} \quad (1)$$

Among these, δ can be obtained according to the slope of the fitting curve referring to the real impedance (Z′) and angular frequency (ω) as shown in **Figure 4F**. Obviously, the smaller δ value for py-B-CNTs film anode reflects faster Li-ion diffusion process compared with CNTs film anode.

To further demonstrate the feasibility of py-B-CNTs film for flexible electronic devices, flexible LIBs was assembled with commercial $LiFePO_4$ cathode as illustrated in **Figure 5A**. As shown in **Figure 5B**, after being charged to 3.5 V, the flexible LIB could stably work to power a light-emitting diode (LED) board, regardless of a series of large-angle bending and twisting, demonstrating the superior conductivity and mechanical stability by boron doping, effectively promising its applications in flexible electronics.

Based on the measurements and analysis above, the unique microstructure and excellent electrochemical performance of py-B-CNTs film can be attributed to several reasons. Firstly, the doping of boron in the carbon framework supplied more holes to the valence band and led to the better electronic conductivity of CNTs. Secondly, the catalytic graphitization of B guaranteed the cycling stability of CNTs during rapid intercalation/deintercalation of Li ion process. Moreover, the surface modification created by pyridine provides more access sites for Li ions to enter the graphitic layers along the CNTs. These factors should comprehensively endow the py-B-CNTs film anodes with outstanding rate capability and cycling stability, as well as excellent toughness for flexible LIBs application.

CONCLUSIONS

In summary, a highly flexible and free-standing py-B-CNTs film was facilely prepared via one-step FCCVD method. The introduction of B endowed CNTs with large surface area as well as high graphitization degree and the involvement of pyridine in the growth of CNTs created abundant active sites for Li storage. The unique structure of py-B-CNTs film is conducive to the high specific capacity with excellent cycle performance of 548 mAh g^{-1} after 300 cycles at 0.1 A g^{-1}. Moreover, the py-B-CNTs film could endure nearly 50% strain without any fractures, which guaranteed its desirable application in full flexible LIBs.

DATA AVAILABILITY STATEMENT

All datasets generated for this study are included in the article/**Supplementary Material**.

AUTHOR CONTRIBUTIONS

LW designed this project and was in charge of the analysis of data and drafting of the work. WG, PL, and TZ prepared samples and performed tensile test. All the authors contributed to the manuscript preparation.

FUNDING

This work was supported by the National Natural Science Foundation of China (Nos. 51072130 and 51502045), and the Australian Research Council (ARC) through Discovery Early Career Researcher Award (DECRA, No. DE170100871) program.

SUPPLEMENTARY MATERIAL

The Supplementary Material for this article can be found online at: https://www.frontiersin.org/articles/10.3389/fchem.2019.00832/full#supplementary-material

REFERENCES

Antunes, E. F., Lobo, A. O., Corat, E. J., Trava-Airoldi, V. J., Martin, A. A., and Verissimo, C. (2006). Comparative study of first- and second-order raman spectra of MWCNT at visible and infrared laser excitation. *Carbon N. Y.* 44, 2202–2211. doi: 10.1016/j.carbon.2006.03.003

Bulusheva, L. G., Okotrub, A. V., Kurenya, A. G., Zhang, H., Zhang, H., Chen, X., et al. (2011). Electrochemical properties of nitrogen-doped carbon nanotube anode in Li-ion batteries. *Carbon N. Y.* 49, 4013–4023. doi: 10.1016/j.carbon.2011.05.043

Campos-Delgado, J., Maciel, I. O., Cullen, D. A., Smith, D. J., Jorio, A., Pimenta, M. A., et al. (2010). Chemical vapor deposition synthesis of n-, p-, and si-doped single-walled carbon nanotubes. *ACS Nano* 4, 1696–1702. doi: 10.1021/nn901599g

Chae, Y. J., Kim, S. O., and Lee, J. K. (2014). Employment of boron-doped carbon materials for the anode materials of lithium ion batteries. *J. Alloy. Compd.* 582, 420–427. doi: 10.1016/j.jallcom.2013.07.059

Chen, G., Wang, Z., and Xia, D. (2008). One-pot synthesis of carbon nanotube@SnO_2-Au coaxial nanocable for lithium-ion batteries with high rate capability. *Chem. Mater.* 20, 6951–6956. doi: 10.1021/cm801853c

Chen, Y., Li, X., Park, K., Song, J., Hong, J., Zhou, L., et al. (2013). Hollow carbon-nanotube/carbon-nanofiber hybrid anodes for li-ion batteries. *J. Am. Chem. Soc.* 135, 16280–16283. doi: 10.1021/ja408421n

Chen, Y. M., Yu, X. Y., Li, Z., Paik, U., and Lou, X. W. (2016). Hierarchical MoS_2 tubular structures internally wired by carbon nanotubes as a highly stable anode material for lithium-ion batteries. *Sci. Adv.* 2:e1600021. doi: 10.1126/sciadv.1600021

Cui, C. J., Qian, W. Z., and Wei, F. (2011). Water-assisted growth of carbon nanotubes over Co/Mo/Al_2O_3 catalyst. *Acta Phys. Chim. Sin.* 27, 2462–2468. doi: 10.3866/Pku.Whxb20111007

Dai, H. J. (2002). Carbon nanotubes: opportunities and challenges. *Surf. Sci.* 500, 218–241. doi: 10.1016/S0039-6028(01)01558-8

Ding, K., Gao, B., Fu, J. J., An, W. L., Song, H., Li, X. X., et al. (2017). Intertwined nitrogen-doped carbon nanotubes for high-rate and long-life sodium-ion battery anodes. *ChemElectroChem* 4, 2542–2546. doi: 10.1002/celc.201700590

Eom, J. Y., Kwon, H. S., Liu, J., and Zhou, O. (2004). Lithium insertion into purified and etched multi-walled carbon nanotubes synthesized on supported catalysts by thermal CVD. *Carbon N. Y.* 42, 2589–2596. doi: 10.1016/j.carbon.2004.05.039

Fang, R. P., Li, G. X., Zhao, S. Y., Yin, L. C., Du, K., Hou, P. X., et al. (2017). Single-wall carbon nanotube network enabled ultrahigh sulfur-content electrodes for high-performance lithium-sulfur batteries. *Nano Energy* 42, 205–214. doi: 10.1016/j.nanoen.2017.10.053

Fujisawa, K., Hayashi, T., Endo, M., Terrones, M., Kim, J. H., and Kim, Y. A. (2018). Effect of boron doping on the electrical conductivity of metallicity-separated single walled carbon nanotubes. *Nanoscale* 10, 12723–12733. doi: 10.1039/C8NR02323A

Geng, Q. H., Huang, G. X., Liu, Y. B., Li, Y. Y., Liu, L. H., Yang, X. H., et al. (2019). Facile synthesis of B/N co-doped 2D porous carbon nanosheets derived from ammonium humate for supercapacitor electrodes. *Electrochim. Acta* 298, 1–13. doi: 10.1016/j.electacta.2018.12.038

Guo, W. L., Yan, X., Hou, F., Wen, L., Dai, Y. J., Yang, D. M., et al. (2019). Flexible and free-standing SiO_x/CNT composite films for high capacity and durable lithium ion batteries. *Carbon N. Y.* 152, 888–897. doi: 10.1016/j.carbon.2019.06.088

Handuja, S., Srivastava, P., and Vankar, V. D. (2009). Structural modification in carbon nanotubes by boron incorporation. *Nanoscale Res. Lett.* 4, 789–793. doi: 10.1007/s11671-009-9315-9

Hata, K., Futaba, D. N., Mizuno, K., Namai, T., Yumura, M., and Iijima, S. (2004). Water-assisted highly efficient synthesis of impurity-free single-walled carbon nanotubes. *Science* 306, 1362–1364. doi: 10.1126/science.1104962

Hsu, W. K., Firth, S., Redlich, P., Terrones, M., Terrones, H., Zhu, Y. Q., et al. (2000). Boron-doping effects in carbon nanotubes. *J. Mater. Chem.* 10, 1425–1429. doi: 10.1039/b000720j

Hu, Y. H., Li, X. F., Wang, J. J., Li, R. Y., and Sun, X. L. (2013). Free-standing graphene-carbon nanotube hybrid papers used as current collector and binder free anodes for lithium ion batteries. *J. Power Sources* 237, 41–46. doi: 10.1016/j.jpowsour.2013.02.065

Jin, T., Liu, Y. C., Li, Y., Cao, K. Z., Wang, X. J., and Jiao, L. F. (2017). Electrospun $NaVPO_4F$/C nanofibers as self-standing cathode material for ultralong cycle life Na-ion batteries. *Adv. Energy Mater.* 7:1700087 doi: 10.1002/aenm.201700087

Kang, C., Lahiri, I., Baskaran, R., Kim, W.-G., Sun, Y.-K., and Choi, W. (2012). 3-dimensional carbon nanotube for li-ion battery anode. *J. Power Sources* 219, 364–370. doi: 10.1016/j.jpowsour.2012.07.050

Kim, T., Mo, Y. H., Nahm, K. S., and Oh, S. M. (2006). Carbon nanotubes (CNTs) as a buffer layer in silicon/CNTs composite electrodes for lithium secondary batteries. *J. Power Sources* 162, 1275–1281. doi: 10.1016/j.jpowsour.2006.07.062

Koós, A. A., Dillon, F., Obraztsova, E. A., Crossley, A., and Grobert, N. (2010). Comparison of structural changes in nitrogen and boron-doped multi-walled carbon nanotubes. *Carbon N. Y.* 48, 3033–3041. doi: 10.1016/j.carbon.2010.04.026

Lee, C. K., and Park, Y. J. (2015). Polyimide-wrapped carbon nanotube electrodes for long cycle li-air batteries. *Chem. Commun.* 51, 1210–1213. doi: 10.1039/C4CC08542F

Li, M., Lu, J., Chen, Z., and Amine, K. (2018). 30 years of lithium-ion batteries. *Adv. Mater.* 30:1800561. doi: 10.1002/adma.201800561

Li, M. Y., Wu, Y., Zhao, F., Wei, Y., Wang, J. P., Jiang, K. L., et al. (2014). Cycle and rate performance of chemically modified super-aligned carbon nanotube electrodes for lithium ion batteries. *Carbon N. Y.* 69, 444–451. doi: 10.1016/j.carbon.2013.12.047

Li, X. F., Liu, J., Zhang, Y., Li, Y. L., Liu, H., Meng, X. B., et al. (2012). High concentration nitrogen doped carbon nanotube anodes with superior Li^+ storage performance for lithium rechargeable battery application. *J. Power Sources* 197, 238–245. doi: 10.1016/j.jpowsour.2011.09.024

Lin, H. J., Weng, W., Ren, J., Qiu, L. B., Zhang, Z. T., Chen, P. N., et al. (2014). Twisted aligned carbon nanotube/silicon composite fiber anode for flexible wire-shaped lithium-ion battery. *Adv. Mater.* 26, 1217–1222. doi: 10.1002/adma.201304319

Lin, T., Huang, F., Liang, J., and Wang, Y. (2011). A facile preparation route for boron-doped graphene, and its CdTe solar cell application. *Energy Environ. Sci.* 4, 862–865. doi: 10.1039/C0EE00512F

Liu, T., Zhang, M., Wang, Y. L., Wang, Q. Y., Lv, C., Liu, K. X., et al. (2018). Engineering the surface/interface of horizontally oriented carbon nanotube macrofilm for foldable lithium-ion battery withstanding variable weather. *Adv. Energy Mater.* 8:1802349. doi: 10.1002/aenm.201802349

Lu, H., Chen, R., Hu, Y., Wang, X., Wang, Y., Ma, L., et al. (2017). Bottom-up synthesis of nitrogen-doped porous carbon scaffolds for lithium and sodium storage. *Nanoscale* 9, 1972–1977. doi: 10.1039/C6NR08296C

Maldonado, S., Morin, S., and Stevenson, K. J. (2006). Structure, composition, and chemical reactivity of carbon nanotubes by selective nitrogen doping. *Carbon N. Y.* 44, 1429–1437. doi: 10.1016/j.carbon.2005.11.027

Maultzsch, J., Reich, S., Thomsen, C., Webster, S., Czerw, R., Carroll, D. L., et al. (2002). Raman characterization of boron-doped multiwalled carbon nanotubes. *Appl. Phys. Lett.* 81, 2647–2649. doi: 10.1063/1.1512330

Nitze, F., Andersson, B. M., and Wagberg, T. (2009). Ammonia assisted growth of multiwalled carbon nanotubes. *Phys. Status Solidi B* 246, 2440–2443. doi: 10.1002/pssb.200982260

Pan, Z., Ren, J., Guan, G., Fang, X., Wang, B., Doo, S.-G., et al. (2016). Synthesizing nitrogen-doped core-sheath carbon nanotube films for flexible lithium ion batteries. *Adv. Energy Mater.* 6:1600271. doi: 10.1002/aenm.201600271

Redlich, P., Loeffler, J., Ajayan, P. M., Bill, J., Aldinge, F., and Riihle, M. (1996). BCN nanotubes and boron doping of carbon nanotubes. *Chem. Phys. Lett.* 260, 465–470. doi: 10.1016/0009-2614(96)00817-2

Roy, P., and Srivastava, S. K. (2015). Nanostructured anode materials for lithium ion batteries. *J. Mater. Chem. A* 3, 2454–2484. doi: 10.1039/C4TA04980B

Sang, Z. Y., Zhao, Z. H., Su, D., Miao, P. S., Zhang, F. R., Ji, H. M., et al. (2018). SiOC nanolayer wrapped 3D interconnected graphene sponge as a high-performance anode for lithium ion batteries. *J. Mater. Chem. A* 6, 9064–9073. doi: 10.1039/C8TA01570H

Sharifi, T., Valvo, M., Gracia-Espino, E., Sandstrom, R., Edstrom, K., and Wagberg, T. (2015). Hierarchical self-assembled structures based on nitrogen-doped carbon nanotubes as advanced negative electrodes for Li-ion batteries and 3D microbatteries. *J. Power Sources* 279, 581–592. doi: 10.1016/j.jpowsour.2015.01.036

Sheem, K., Lee, Y. H., and Lim, H. S. (2006). High-density positive electrodes containing carbon nanotubes for use in Li-ion cells. *J. Power Sources* 158, 1425–1430. doi: 10.1016/j.jpowsour.2005.10.077

Song, D., Guo, W. L., Zhang, T., Lu, P. Y., Guo, A. R., Hou, F., et al. (2019). A freestanding CNTs film fabricated by pyrrole-modified CVD for capacitive deionization. *Surf. Innov*. 7, 10–17. doi: 10.1680/jsuin.18.00036

Stephan, O., Ajayan, P. M., Colliex, C., Redlich, P., Lambert, J. M., Bernier, P., et al. (1994). Doping graphitic and carbon nanotube structures with boron and nitrogen. *Science* 266, 1683–1685. doi: 10.1126/science.266.5191.1683

Tanaka, U., Sogabe, T., Sakagoshi, H., Ito, M., and Tojo, T. (2001). Anode property of boron doped graphite materials for rechargeable lithium ion batteries. *Carbon N. Y.* 39, 931–936. doi: 10.1016/S0008-6223(00)00211-6

Tang, Y., Zhang, Y., Li, W., Ma, B., and Chen, X. (2015). Rational material design for ultrafast rechargeable lithium-ion batteries. *Chem. Soc. Rev.* 44, 5926–5940. doi: 10.1039/C4CS00442F

Tsang, S. C., Chen, Y. K., Harris, P. J. F., and Green, M. L. H. (1994). A simple chemical method of opening and filling carbon nanotubes. *Nature* 372, 159–162. doi: 10.1038/372159a0

Wang, C., Zhang, F., Wang, X., Huang, G., Yuan, D., Yin, D., et al. (2016). Preparation of a graphitic N-doped multi-walled carbon nanotube composite for lithium–sulfur batteries with long-life and high specific capacity. *RSC Adv.* 6, 76568–76574. doi: 10.1039/C6RA11898D

Wang, L., Yang, C. L., Dou, S., Wang, S. Y., Zhang, J. T., Gao, X., et al. (2016). Nitrogen-doped hierarchically porous carbon networks: synthesis and applications in lithium-ion battery, sodium-ion battery and zinc-air battery. *Electrochim. Acta* 219, 592–603. doi: 10.1016/j.electacta.2016.10.050

Way, B. M., and Dahn, J. R. (1994). The effect of boron substitution in carbon on the intercalation of lithium in $Li_x(B_zC_{1-z})_6$. *J. Electrochem. Soc.* 141, 907–912. doi: 10.1149/1.2054856

Wu, C., Kopold, P., van Aken, P. A., Maier, J., and Yu, Y. (2017). High performance graphene/Ni_2P hybrid anodes for lithium and sodium storage through 3D yolk-shell-like nanostructural design. *Adv. Mater.* 29:1604015. doi: 10.1002/adma.201604015

Yang, J. Q., Zhou, X. L., Wu, D. H., Zhao, X. D., and Zhou, Z. (2017). S-doped N-rich carbon nanosheets with expanded interlayer distance as anode materials for sodium-ion batteries. *Adv. Mater.* 29:1604108. doi: 10.1002/adma.201604108

Yang, S. Y., Chang, K. H., Tien, H. W., Lee, Y. F., Li, S. M., Wang, Y. S., et al. (2011). Design and tailoring of a hierarchical graphene-carbon nanotube architecture for supercapacitors. *J. Mater. Chem.* 21, 2374–2380. doi: 10.1039/C0JM 03199B

Yeh, M. H., Lin, L. Y., Li, T. J., Leu, Y. A., Chen, G. L., Tien, T. C., et al. (2014). Synthesis of boron-doped multi-walled carbon nanotubes by an ammonia-assisted substitution reaction for applying in supercapacitors. *Energy Procedia* 61, 1764–1767. doi: 10.1016/j.egypro.2014.12.207

Zhang, C., Mahmood, N., Yin, H., Liu, F., and Hou, Y. (2013). Synthesis of phosphorus-doped graphene and its multifunctional applications for oxygen reduction reaction and lithium ion batteries. *Adv. Mater.* 25, 4932–4937. doi: 10.1002/adma.201301870

Zhang, L., Xia, G. L., Guo, Z. P., Li, X. G., Sun, D. L., and Yu, X. B. (2016). Boron and nitrogen co-doped porous carbon nanotubes webs as a high-performance anode material for lithium ion batteries. *Int. J. Hydrogen Energ.* 41, 14252–14260. doi: 10.1016/j.ijhydene.2016.06.016

Zhu, S., Li, J. J., Li, Q. F., He, C. N., Liu, E. Z., He, F., et al. (2016). Space-confined synthesis of three-dimensional boron/nitrogen-doped carbon nanotubes/carbon nanosheets line-in-wall hybrids and their electrochemical energy storage applications. *Electrochim. Acta* 212, 621–629. doi: 10.1016/j.electacta.2016.07.065

Conflict of Interest: The authors declare that the research was conducted in the absence of any commercial or financial relationships that could be construed as a potential conflict of interest.

frontiers in Chemistry

ORIGINAL RESEARCH
published: 08 January 2020
doi: 10.3389/fchem.2019.00887

Three-Dimensional Core-Branch α-Fe_2O_3@NiO/Carbon Cloth Heterostructured Electrodes for Flexible Supercapacitors

Miao Zhang[1,2]*, *Xifei Li*[1], *Xiaohua Wang*[2], *Dejun Li*[1] and *Naiqin Zhao*[2]*

[1] Tianjin International Joint Research Centre of Surface Technology for Energy Storage Materials, School of Physics and Materials Science, Tianjin Normal University, Tianjin, China, [2] School of Materials Science and Engineering and Tianjin Key Laboratory of Composite and Functional Materials, Tianjin University, Tianjin, China

A convenient and scalable hydrothermal method was developed for the fabrication of the core-branch Fe_2O_3@NiO nanorods arrays directly grown on flexible carbon cloth (denoted as Fe_2O_3@NiO/CC). Such a unique architecture was applied as an electrode of the supercapacitors. As a result, the Fe_2O_3@NiO/CC exhibited a high areal capacitance ~800 mF cm^{-2} at 10 mA cm^{-2}, which was about 10 times increase with respect to Fe_2O_3 nanorods array grown on carbon cloth (Fe_2O_3/CC). The Fe_2O_3@NiO/CC also had the long life cycle (96.8 % capacitance retention after 16,000 cycles) and remarkable rate capability (44.0 % capacitance loss at a very large current density of 100 mA cm^{-2}). The superior performance of the Fe_2O_3@NiO/CC should be ascribed to the reduction of the contact resistance and the free-standing structure of the flexible electrode. This study provides a novel strategy to construct high-performance flexible electrode materials with unique core-branch structure by incorporating two different pseudocapacitive materials.

Keywords: flexible supercapacitors, nanorods arrays, core-branch, carbon cloth, electrochemical performance

OPEN ACCESS

Edited by:
Tengfei Zhou,
University of Wollongong, Australia

Reviewed by:
Chengchao Liu,
South-Central University for Nationalities, China
Hui Xia,
Nanjing University of Science and Technology, China
Xiaomei Zheng,
China Jiliang University, China

***Correspondence:**
Miao Zhang
miaozhang@tju.edu.cn
Naiqin Zhao
nqzhao@tju.edu.cn

Specialty section:
This article was submitted to Electrochemistry, a section of the journal Frontiers in Chemistry

Received: *07 October 2019*
Accepted: *09 December 2019*
Published: *08 January 2020*

Citation:
Zhang M, Li X, Wang X, Li D and Zhao N (2020) Three-Dimensional Core-Branch α-Fe_2O_3@NiO/Carbon Cloth Heterostructured Electrodes for Flexible Supercapacitors. Front. Chem. 7:887. doi: 10.3389/fchem.2019.00887

INTRODUCTION

With the growing needs of power and energy for the portable devices, electric vehicles and portable electronics, more and more attention has been focused on the advanced energy storage devices (Xia et al., 2018; Li J. M. et al., 2019). Among them, supercapacitors, also called as electrochemical capacitors (ECs), have been regarded as a new type of alternative energy resources, combining the advantages of the lithium ion batteries and the traditional capacitors (Ke and Wang, 2016; Xu et al., 2016). Supercapacitors have become the candidates for the high-performance power devices, because of the fast charging and discharging, high power density, long cycle life and the superior electrochemical stability (Yang W. et al., 2018). The property of the supercapacitors strongly depends on the characteristics of the electrode materials. At present, the main electrode materials of the supercapacitors are carbon materials, metal oxides/hydroxides, and conducting polymers (Geng et al., 2018). Carbon materials store energy via the electric double layer capacitance, whose capacitance is relatively low. On the other hand, the metal oxides/hydroxides and the conducting polymers store energy via the fast faradic pseudocapacitance, which achieve relatively high capacitance and high energy density (Liu et al., 2016; Savjani et al., 2016; Zhu et al., 2017). Therefore, the pseudocapacitive materials have been attracted more attention in the application in supercapacitors.

Hematite (α-Fe_2O_3) is one of the most promising candidates due to its high theoretical specific capacitance, suitable working window, low cost, abundance, and environmental benignity (Quan et al., 2016). However, the practical implementation of Fe_2O_3 is prevented by the poor electrical conductivity ($\sim 10^{-14}$ S cm^{-1}) (Lee et al., 2012). To improve the electrochemical performance of the Fe_2O_3, many works have been done to achieve different nanostructured Fe_2O_3, such as nanoparticals, nanorods, nanowires, and nanoflowers (Reddy et al., 2010; Binitha et al., 2013; Zheng et al., 2016). The strategy can improve the available surface area and shorten the transmission paths of ions and electrons. Other researchers alternatively incorporate Fe_2O_3 with highly conductive carbon materials (mesoporous carbons, carbon nanotubes, carbon fibers, carbon sheets, etc.) or conducting polymers to improve the electrical conductivity (Hu et al., 2015; Raut and Sankapal, 2016). Most above materials are powder-like in macrostate, which have to be applied in supercapacitors by traditional assembly processes. However, the traditional assembly processes require polymer binder and additive, which increase the contact resistance and reduce the rate capability because of the electrochemical inactivity and insulativity (Yang W. et al., 2013; Zhang et al., 2017).

The binder-free material with the free-standing structure which can effectively simplify the preparation process of the electrodes and improve the electrochemical property of the supercapacitors (Li M. et al., 2015). Directly anchored on the current collector, the active materials can achieve outstanding performance, including remarkable rate capability and long life cycle stability, owing to the great electrode-electrolyte contact, the short ion/electron transport paths and the low contact resistance. More than that, a relatively low weight fraction of faradaic pseudocapacitive material is considered to achieve better rate performance and longer life cycles at the sacrifice of energy density in most cases (Fischer et al., 2007). Therefore, many efforts have been made for pseudocapacitive materials such as mixed oxides and binary metal oxide/hydroxides to increase the energy density (Li H. et al., 2015; Tian et al., 2017). The core-shell nanostructure is usually fabricated to incorporation two different metal oxides. But the homogeneous shell prohibits the ion penetration into the core region, leading to the core cannot realize electroactivity and reducing the speed of electron transfer. Due to the lack of well-defined microstructures and the poor contact between the mixed oxides, electrochemical performance is always not satisfactory. The big challenge is how to set up an integrated structure, in which both of metal oxides are excellent pseudocapacitive materials (Fe_2O_3, NiO, Co_3O_4, and MnO_2), and the structural features and electrochemical property of each component are fully used, as well as the fast ion/ electron transmission path can be achieved (Kim et al., 2017).

Herein, we synthesize a simple and scalable approach by building a hybrid metal oxides core/branch nanorods arrays for supercapacitors. The NiO possessing relatively low electrical resistance and high theoretical specific capacitance is decided as branch. The core-branch Fe_2O_3@NiO nanorods arrays are directly grown on flexible carbon cloth (denoted as Fe_2O_3@NiO/CC) as high-performance flexible binder-free ECs. Avoiding the use of polymer binder and conductive additives, the carbon cloth acts as current collector providing more active sites and reducing the resistance. The Fe_2O_3 and NiO are excellent pseudocapacitive metal oxides with earth-abundant, easily available, very cheap, and environment friendly. The core-branch structure can contribute to the energy storage. Different from core-shell structure, the core-branch is more beneficial to the ion penetration into the core region and realizes each constituent effectively utilized. Moreover, the unique core-branch structure can provide a large reaction interface, improve the charge transportation and obtain the high electrical conductivity of the electrodes, and supply more

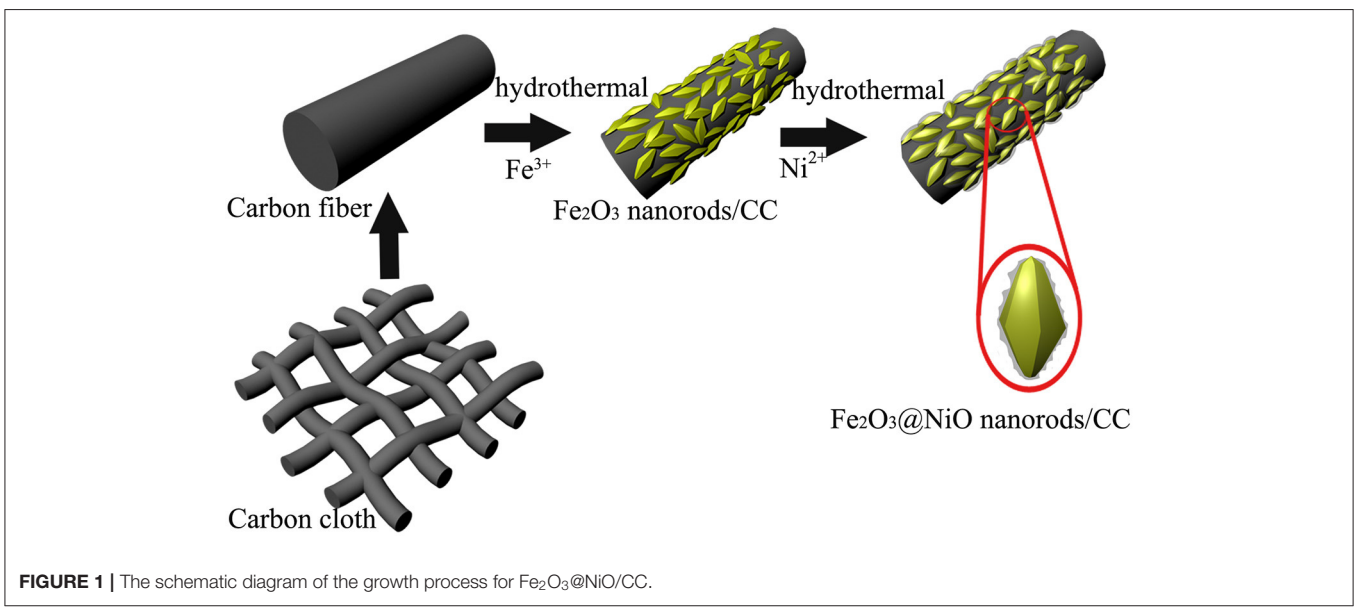

FIGURE 1 | The schematic diagram of the growth process for Fe_2O_3@NiO/CC.

channels to increase the diffusion path of the electrolyte ions. The growth mechanism of this structure has been further analyzed according to the experiment. The electrochemical performance of Fe_2O_3@NiO/CC as the electrode materials in ECs has been investigated as well. This research provides a promising measure to design and prepare the hybrid metal oxides anodes with the improved electrochemical performance, which is hopeful for the application in energy storage/conversion devices.

EXPERIMENT SECTION

Materials

Carbon cloth was purchased from Alfa Aesar China (Tianjin) Co. Ltd., $FeCl_3$, Na_2SO_4, HNO_3, $Ni(NO_3)_2{\cdot}6H_2O$ and urea were purchased from Tianjin Chemical Reagent Company (Tianjin, China). Reagents were of analytical grade and used without further purification process.

Synthesis

Typically, carbon cloth was ultrasonically cleaned in 32% HNO_3, ethanol and deionized water in sequence and dried under the atmospheric condition. $FeCl_3$ (0.32 g), Na_2SO_4 (0.28 g) were dissolved into deionized water (40 mL) by vigorous stirring about 30 min to form a homogeneous solution, and then transferred to 50 ml Teflon-lined autoclave. A piece of carbon cloth (3 * 5 cm) was immersed into the prepared solution, then sealed and maintained at 120°C for 8 h. After the hydrothermal reaction, the carbon cloth was taken out and washed by deionized water and ethanol and then dried in air. Then, the production was soaked into 30 ml of aqueous solution containing 3.57 g $Ni(NO_3)_2{\cdot}6H_2O$ and 0.45 g urea, which was stirred for 30 min, and transferred to 50 mL Teflon-lined autoclave. After heating 90°C for different time, simple was taken out and washed with deionized water and ethanol and then dried in air. Finally, the three-dimensional (3D) core-branch Fe_2O_3@NiO/CC was obtained through annealing in air 400°C for 1 h.

Structural Characterization

The morphologies and characteristics of the products were characterized by the field emission scanning electron microscope (SEM, HITACHI S4800) and the high-resolution transmission electron microscope (TEM, JEOLJEM-2100f). The crystal structures of the samples were investigated by X-ray diffraction (XRD, Bruker D8 Advanced). The Brunauer–Emmett–Teller (BET) surface area and the pore size distribution were measured by the nitrogen adsorption isotherms with the autosorbiQ instrument (Quantachrome, U.S.).

Electrochemical Test

All electrochemical measurements were carried out with a CHI660D electrochemical workstation in a conventional three-electrode mode in 3 M KOH aqueous solution as the electrolyte. The Fe_2O_3@NiO/CC, platinum, and Hg/HgO electrode were used as the working electrode, counter and reference electrode, respectively. The loading amount of Fe_2O_3@NiO for electrochemical testing is about 10.0 wt%. Cyclic voltammetry (CV) was investigated at various scan rates of 5, 10, 50, 100, 200 mV s^{-1}, galvanostatic charge/discharge (GCD) measurements was employed at the current density of 5, 10, 20, 50, 100 mA cm^{-2}, and electrochemical impedance spectroscopy (EIS) was conducted under a frequency from 10^5 to 0.01 Hz. The areal specific capacitance measured by chronopotentiometry was calculated according to the equation as follows:

$$C_a = I^* \Delta t / (s^* \Delta V)$$

Where I is the constant discharging current, Δt is the discharging time, ΔV is the voltage change excluding IR drop at a constant discharge current and s is the effective electrode area.

The structure and the electrochemical performances of carbon cloth and the single Fe_2O_3 nanorods grow on carbon cloth (denoted as Fe_2O_3/CC) also were tested.

RESULTS AND DISCUSSION

Carbon cloth with 3D textile structure and the diameter of 8-10 μm (**Figure S1**) serves as a scaffold for the composite architecture. With good flexibility and conductivity, carbon cloth directly acts as the current collector for the deposition of active material. As illustrated in **Figure 1**, 3D core-branch Fe_2O_3@NiO nanorods are synthesized on the carbon cloth through a process with simple two steps. Firstly, the Fe_2O_3 nanorods arrays are grown from carbon cloth substrate via the simple hydrothermal process, possessing many functional groups and improving their

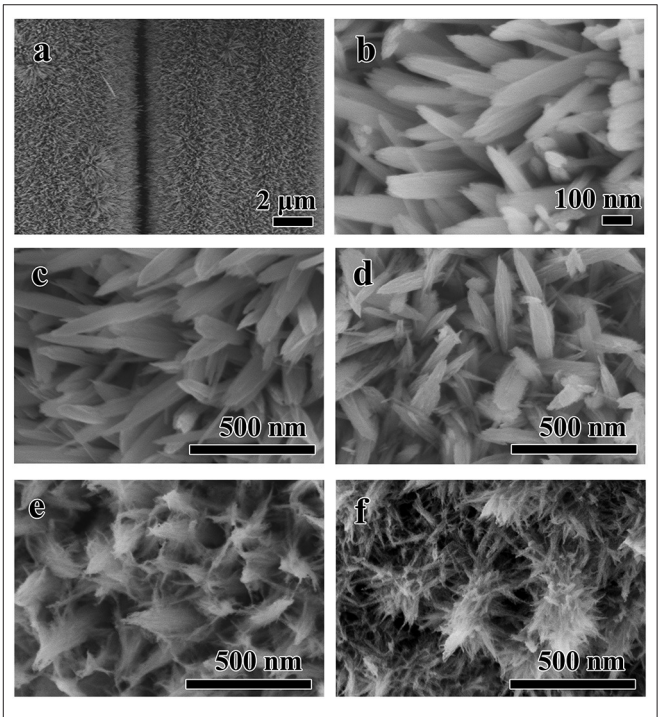

FIGURE 2 | The typical SEM images of **(a,b)** the Fe_2O_3 nanorods/CC obtained after the first hydrothermal process and the Fe_2O_3@NiO/CC with different hydrothermal time during the second hydrothermal process **(c)** 3 h, **(d)** 6 h, **(e)** 9 h, **(f)** 18 h.

electrochemical activity. Secondly, the obtained porous nanorods are impregnated in the aqueous solution of Ni^{2+} and followed by the post-annealing in air, leading to the branch-like layer of NiO on the surface of the Fe_2O_3 nanorods. The bending state of the Fe_2O_3@NiO/CC has been shown in **Figure S2**, which proves the flexibility of Fe_2O_3@NiO/CC is excellent.

As shown in **Figures 2a,b**, the Fe_2O_3 nanorods with the diameter and length about 60∼80 and 400∼600 nm are grown homogeneously on the surface of the carbon cloth after first hydrothermal process. And then, the obtained nanorods work as the substrate for the subsequent growth of branch-like NiO through hydrothermal method. **Figures 2c–f** displays the typical SEM images of the samples during different hydrothermal time, which demonstrate the important roles of the reaction time in the hydrothermal reaction. Gradually, crystal growth of the NiO nanobranches based on the nucleation takes place along the easiest direction of the crystallization. Compared with the precursor, there is no obvious change after 3 h (**Figure 2c**), but the nanorods turn to be rough on the surface at 6 h (**Figure 2d**). When the reaction time is extended to 9 h, the NiO nanobranches grow along vertical direction without collapsing and cracking (**Figure 2e**). Dense NiO nanobranches are twined around every Fe_2O_3 nanorods uniformly with the forming of stable protective shell after 18 h hydrothermal time as displayed in **Figure 2f**.

In order to further explore the structure, the core-branch structure of the Fe_2O_3@NiO on carbon cloth was further confirmed by TEM, as shown in **Figure 3**. **Figure 3a** reveals the formed NiO nuclei attaches to the surface of the Fe_2O_3 nanorods. Due to the hydrothermal time only 3 h, NiO nanobranches are unhomogeneous with the height about 10 nm. **Figure 3b** is the

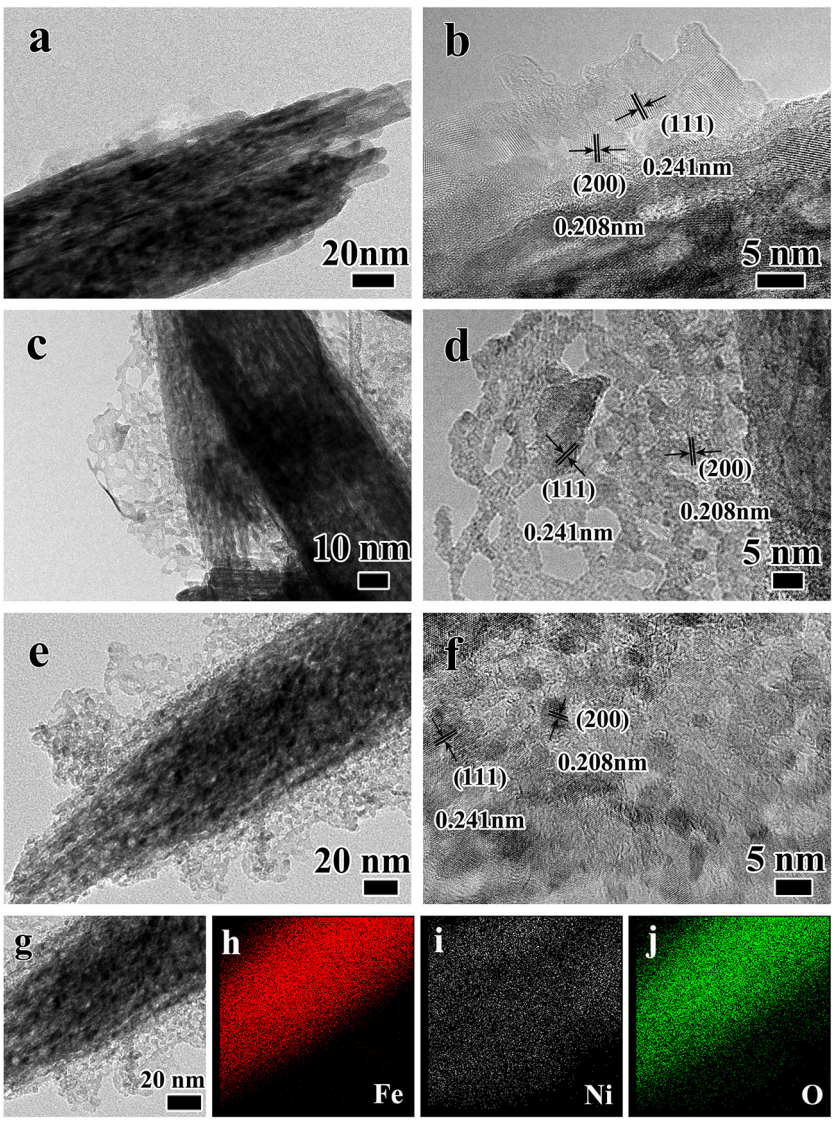

FIGURE 3 | The TEM images of Fe_2O_3@NiO/CC at different hydrothermal time **(a,b)** 3 h, **(c,d)** 6 h, **(e,f)** 9 h, **(g)** the selected region TEM images of Fe_2O_3@NiO and the mapping analysis of Fe_2O_3@NiO, in which **(h)** the red one is Fe, **(i)** the white one is Ni and **(j)** the green one is O.

high-reslution image of the nanobranch structure, which showed the distances of crystal planes were 0.208 nm and 0.241 nm respectively, corresponding to the (200) and (111) crystal planes of NiO. Sequentially, crystal growth of the NiO nanobranches based on the nucleation takes place along the easiest direction of the crystallization with the height increasing to 50 nm in **Figure 3c**. The porous structure of the nanobranch NiO is because of the dehydration and contraction during the annealing process (**Figure 3d**). The height of the nanobranches increases with an increase in the time of hydrothermal process. After 9 h reaction time, there are dense branches attach to the surface of Fe_2O_3 nanorods with the excellent crystallinity (**Figures 3e,f**). In order to further analyze of the core-branch structure, the Energy-dispersive X-ray spectrometry (EDS) mapping analysis was used, the result was shown in **Figures 3g–i**. A single heterostructure unambiguously confirms the Fe_2O_3 core/NiO branch hybrid structure. Specifically, the Fe and O elements are mainly located at the nanorods region and the Ni is a fairly homogeneous and unapparent distribution due to the ultrathin nanostructure.

According to the experiment, during the hydrothermal process, the NiO nucleated and grew gradually along the direction perpendicular to the Fe_2O_3 nanorods with the extension of time, eventually forming the dendritic structure and loading on the surface of Fe_2O_3 uniformly. Generally, the crystal growth of NiO can be divided into two steps: initial nucleation and crystal growth (Zhang et al., 2010). At the initial stage with the high temperature and pressure, the urea hydrolyzed and NiO formed on the surface of Fe_2O_3 gradually. With the extension of reaction time, the NiO microcrystalline core continued to grow selectively along the direction of <100>. With the length increased, the small nanobranch structure formed and then the dendritic structure obtained.

To further understand the materials, the XRD was applied to analyze the elemental relative composition of the samples (**Figure 4A**). As the comparison, the XRD pattern of the carbon cloth is shown by the black line. Apart from the strong diffraction peak of carbon cloth, other diffraction peaks in the XRD pattern of α-Fe_2O_3 nanorods (red line) can be corresponded with the standard phase of hematite (JCPDS No. 33-0664). XRD pattern of Fe_2O_3@NiO/CC (blue line) reveals some new diffraction peaks at 37.25°, 43.28°, 62.87°, and 75.41° appear corresponding to (111), (100), (220), and (311) planes of NiO (JCPDS No. 47-1049), respectively. On the other hand, the Raman spectra had been conducted to characterize the structure and chemical composition of the materials (**Figure 4B**). The Raman peaks at 1,325 and 1,580 cm^{-1} are corresponded with the D band and G band of carbon materials (Zhang et al., 2017), which is contributed from the carbon cloth. The Raman peaks at about 229, 292, 403, and 1,300 cm^{-1} belong to the typical Fe_2O_3, which can be clearly observed, showing the homogeneous distribution of the Fe_2O_3 nanorods (Dong et al., 2015; Lu et al., 2015). Moreover, the Raman peaks at 381, 545, and 766 cm^{-1}

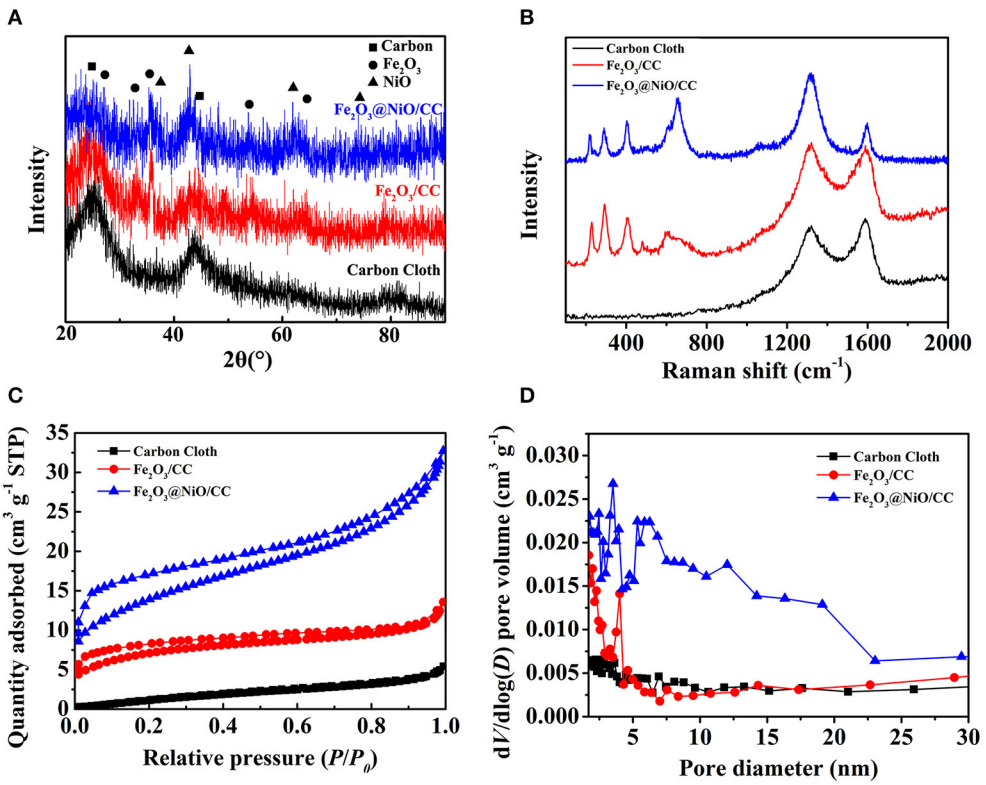

FIGURE 4 | (A) The XRD patterns, **(B)** the Raman spectrum, **(C)** the N_2 adsorption-desorption and **(D)** the pore size distributions by BJH method of carbon cloth, Fe_2O_3/CC and Fe_2O_3@NiO/CC.

are contributed by the NiO in Fe_2O_3@NiO/CC. The uniform distribution of Fe_2O_3@NiO on carbon cloth is important for the electrochemical property of the electrode. Furthermore, the specific surface area and the pore size distribution of the core-branch structure are also significant to promote the high-performance supercapacitors. The N_2 adsorption isotherm is conducted in **Figure 4C** showing the typical II isotherm. The BET surface area of Fe_2O_3@NiO/CC and carbon cloth of is 23 and 6.71 m^2g^{-1}, indicating the increase of porous structures in the composite. It indicates that the specific surface area dramatically influenced by the content of Fe_2O_3@NiO. The Barrett-Joyner-Halenda (BJH) pore size distributions of the samples are as shown in **Figure 4D**. Most of the pores are distributed in the mesoporous range, the nanoporous range at 3, 4, and 5 nm, as well as the mesoporous range between 10 and 20 nm. The multistage pore structure may be favorable for the access of the electrolyte through the pore channels to increase effective contact area.

To examine the electrochemical properties of the different electrodes, the CV, GCD and EIS were conducted in 3 M KOH aqueous solution electrolyte by the three-electrode test. **Figures 5A,B** shows the CV and GCD curves of pure carbon cloth, respectively. The slight redox peaks of the CV curves are probably caused by the oxygen functional groups which brought by the HNO_3 clean process. The GCD curves also in accord with the CV curves. By the calculation, the specific capacitances are 30.7, 26.3, and 24.8 mF cm^{-2} at the current densities of 10, 20, and 50 mA cm^{-2}, respectively. The electrochemical properties of the Fe_2O_3/CC electrode is also explored by the test. In **Figure 5C**, with the scan rate increasing, the shapes of the CV curves are similar, indicating the structure stability of the Fe_2O_3/CC. Because of the small load of Fe_2O_3 and the fast charge-discharge process, the redox peak cannot be found obviously. Typical GCD curves of the Fe_2O_3/CC at the current densities from 10 to 50 mA cm^{-2} are shown in **Figure 5D**. The curves are approximately symmetrical and linear, meaning the electrodes have outstanding electrochemical reversibility. By the calculation, the specific capacitances are respectively 422.2, 402.7, and 378.3 mF cm^{-2} at 10, 20, and 50 mA cm^{-2}. Compared with the Fe_2O_3/CC electrode, the pure carbon cloth exhibits rather small capacitance, indicating the carbon cloth makes little contribute to the total capacitance of the Fe_2O_3/CC electrode. Besides, there are no obvious anodic/cathodic peaks appearing, which might be ascribed to that the porous Fe_2O_3 nanorodes are charged and discharged with a rapid Faradic reaction at a pseudo-constant rate (Chen et al., 2014).

The electrochemical studies for the Fe_2O_3@NiO/CC obtained by different hydrothermal time were also done by the three-electrode cell in 3 M KOH electrolyte. The CV curves of Fe_2O_3@NiO/CC are close to rectangular shape at the scan rate 50 mV s^{-1}, which is an important characteristic in the supercapacitor showing the excellent electrical conductivity

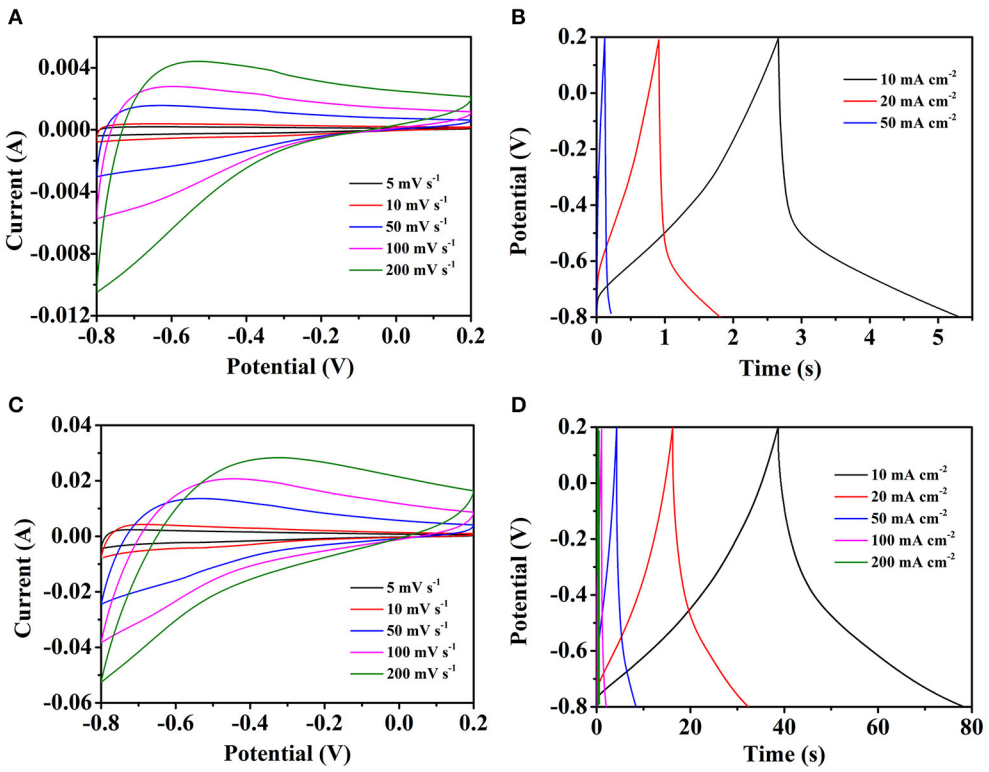

FIGURE 5 | Representative CV curves of **(A)** carbon cloth and **(C)** Fe_2O_3/CC at different scan rate. The GCD curves of **(B)** carbon cloth and **(D)** Fe_2O_3/CC at different current densities.

(**Figure 6A**). With the extended hydrothermal time, the core-branch Fe_2O_3@NiO on carbon cloth displays a pair of redox peaks. Compared with CV curves of Fe_2O_3/CC electrodes at the scan rate 50 mV s^{-1}, the results indicates that the NiO realizes the electrochemical activity. Researches show that the anodic peak is caused by the oxidation of NiO to NiOOH, while the corresponding reverse process leads to generate of the cathodic peak, as shown in the following equation (Kong et al., 2011):

$$NiO + OH^- \leftrightarrow NiOOH + e^-$$

Because of the coefficient by carbon cloth and Fe_2O_3, the cathodic peak is not obvious.

Figure 6B illustrates the GCD curves of Fe_2O_3@NiO/CC between −0.8 and 0.2 V at the current density of 10 mA cm^{-2}. The curves exhibits a predominantly symmetric nature and low IR drop, revealing the Fe_2O_3@NiO/CC nanostructures are good electrochemical capacitive characteristic with reversible redox reactions and small electrochemical impedance. The area specific capacitances of Fe_2O_3@NiO/CC derived from the discharge curves are 682.43, 816.13, 756.98, and 696.67 mF cm^{-2} for different hydrothermal time of 3, 6, 9, and 18 h, respectively. It is found that the area specific capacitances were enhanced with the extending the hydrothermal time from 3 to 6 h. However, further prolonging the time to 9 or 18 h, the capacitance decreased. In order to understand the inferior performance, the EIS study of Fe_2O_3@NiO/CC with different hydrothermal time is carried out (**Figure 6C**). The real axis intercept represents the equivalent series resistance (Meher and Rao, 2011; Meher et al., 2011). It is noteworthy that the equivalent series resistance of the Fe_2O_3@NiO/CC for 6 h is the minimum, which could be mainly attributed to the little synthetic quantity of NiO in 3 h and the increase in the thickness of the NiO layer from 6 to 18 h that hinders the diffusion and migration process of ions. Thus, the optimal experiment parameter can be determined to the hydrothermal time 6 h.

To further explore electrochemical performance of the Fe_2O_3@NiO/CC with the optimum capacity, the CV and GCD tests of Fe_2O_3@NiO/CC obtained for 6 h hydrothermal process were performed (**Figures 7A,B**). As shown in **Figure 7A**, a series of CV curves of the optimal experiment parameter are collected at the scan rates from 5 to 200 mV s^{-1}. With the scan rates increased, the shapes of the CV curves remain great and have little change, indicating a good kinetic reversibility of the Fe_2O_3@NiO/CC. The GCD curves for the optimal experiment parameter are nearly symmetric at 2–100 mA cm^{-2} (**Figure 7B**). The curves can be observed that the charge curves are symmetrical with their corresponding discharge curves, revealing that the electrode presents a great reversibility with a rapid response and small equivalent series resistance (Chen et al., 2013). Attributing to the high conductivity of carbon cloth and the porous feature of Fe_2O_3@NiO, the migration or

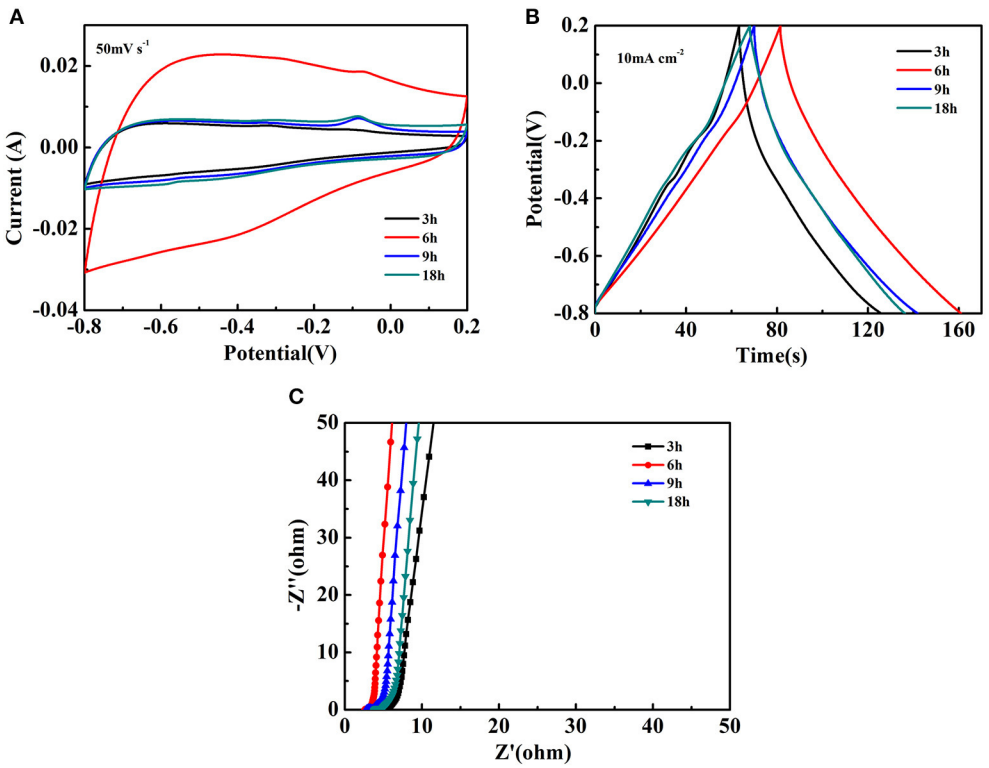

FIGURE 6 | The electrochemical performance of Fe_2O_3@NiO/CC at different hydrothermal time: **(A)** the CV curves at the scan rate of 50 mV s^{-1}, **(B)** the GCD curves at the current density of 10 mA cm^{-2}, **(C)** the Nyquist plots.

diffusion of electron/ion can occur sufficiently during the rapid charge/discharge process (Fan et al., 2011). The areal capacitance are calculated by the charge-discharge curves (**Figure 7B**). The areal capacitance of Fe_2O_3@NiO are 849.54, 816.13, 768.29, 691.77, 542.33, and 490.12 mF cm^{-2} at current density of 5, 10, 20, 50, 100, and 200 mA cm^{-2}, respectively. With the current density increasing, the areal capacitance is decreased. At high scan rates, the low areal capacitance is because the electrolyte ion movement and diffusion have be limited by the time constraint and only the outer active surface can be utilized for charge storage. On the other hand, the active surface area no matter outer or inner can be used for charge storage which thus leads to higher specific capacitance at lower scan rates (Wang et al., 2011). Those results directly reveal the advantage of Fe_2O_3@NiO for capacitance as electrode of supercapacitor.

In order to evaluate the contribution of NiO and Fe_2O_3 to the capacitance of the heterostructures, comparing the CV curves of Fe_2O_3@NiO/CC, Fe_2O_3/CC and pure carbon cloth (**Figures 5A,C**, **7A**), the contribution of NiO and Fe_2O_3 to the capacitance of the heterostructures has been evaluated. The results indicate that the combination of NiO and Fe_2O_3 to a heterostructures can substantially enhance the electrochemical properties. Carbon cloth serves as current collector and substrate for deposition Fe_2O_3 nanorod, avoiding the addition of polymer binders/conducting additives and maintaining the robust mechanical stability. With the facile hydrothermal method, the Fe_2O_3 nanorods are directly grown on carbon cloth to ensure well mechanical adhesion, reducing the contact resistance between the active material and the current collector. Coating with branch-like NiO, the Fe_2O_3 nanorod material enhances its electrical conductivity, leading to a relatively small charge-transfer reaction resistance. It is beneficial for the rate capability of supercapacitors. Besides, the ultrathin NiO are incompletely wrapped on the surface of Fe_2O_3, which not only benefit for achieving fully electrochemical activity but also guarantee the core active material completely available to the ion in the electrolyte. The NiO also prevent the Fe_2O_3 nanorods from collapsing over long-time cycles in the electrolyte to improve the cycling stability. The excellent electrochemical performance of the supercapacitor device is owing to the good synergistic effect of branch-like NiO and Fe_2O_3 nanorods. Moreover, the porous feature of Fe_2O_3@NiO is beneficial for the electrons and ion transport more efficiently during the process of charge-discharge. It causes the specific capacitance have a large improvement. Those highlights have demonstrated the way to fabricate hybrid pseudocapacitive materials in exploiting the energy storage devices with outstanding electrochemical property.

In order to explore the internal resistance and the performance of electrode materials, EIS experiments were conducted (**Figure 7C**). In the **Figure 7C**, the diameter of the semicircle for the Fe_2O_3@NiO/CC electrode in the high frequency region is significantly smaller than that of Fe_2O_3/CC

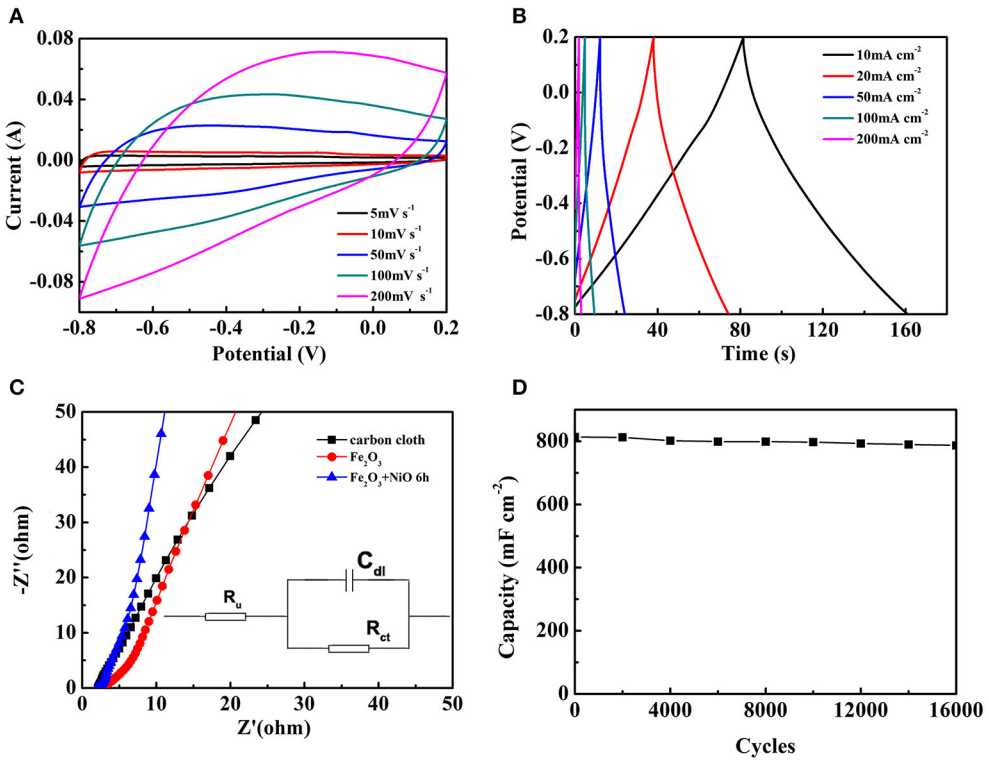

FIGURE 7 | The electrochemical performance of Fe_2O_3@NiO/CC whose hydrothermal time is 6 h: **(A)** the CV curves at different scan rate, **(B)** the GCD curves at different current density. **(C)** The Nyquist plots of carbon cloth, Fe_2O_3/CC and Fe_2O_3@NiO/CC. **(D)** The long-term cycling performance of Fe_2O_3@NiO/CC.

and pure carbon cloth, which illustrates the superior rate performance of the Fe_2O_3@NiO/CC electrode as well as implies that the Fe_2O_3@NiO/CC can reduce the contact and charge-transfer resistances in the electrode. The slope at low frequency part of Fe_2O_3@NiO/CC is also higher than that of Fe_2O_3/CC, demonstrating superior ion diffusion ability. To properly describe the action of an alternating potential input on supercapacitors, one can in principle consider at least two coupled interface processes influencing the impedance of the system: the electron transfer process across the electrolyte/electrode interface and the double-layer effect (Meher and Rao, 2011; Meher et al., 2011). The equivalent circuit typically has been schematized in the insert of **Figure 7C**, constituted by a solution resistance (R_u), a charge transfer resistance (R_{ct}) and a double-layer capacitance (C_{dl}). R_u represents the uncompensated resistance of the electrolyte and other possible ohmic resistances, whereas R_{ct} represents the ohmic drop that can be associated to the electron transfer process. The double-layer defect, which roughly consists of charge separation in the electrode/electrolyte interphase as a result of charge migration, can be assimilated to a capacitor of capacitance C_{dl}. The EIS further confirms the favorable performance of the Fe_2O_3@NiO/CC.

Cycling life test over 16,000 cycles for Fe_2O_3@NiO/CC was carried out at 20 mA cm^{-2} (**Figure 7D**). After 16,000 cycles of charge and discharge, Fe_2O_3@NiO/CC with 96.8 % capacitance retention shows better durability than the Fe_2O_3/CC (88.6 %). The morphology and structure change of Fe_2O_3@NiO/CC electrode after charge/discharge cycles were explored by SEM. **Figure S3** demonstrates the Fe_2O_3@NiO/CC electrode after cycling for 16,000 cycles (as shown in **Figure 7D**). The structure is very similar to the morphology of pristine product (see **Figures 2e,f**). The stable cycling performance could be attributed to branch-like NiO which is covered on the surface of Fe_2O_3 and prevent the core part from collapsing during the reaction in long time (Guan et al., 2012). Besides, the synergistic effect between NiO and Fe_2O_3 could also make a contribution on the excellent cycling performance (Liu et al., 2011). The enhanced capacitance, rate capability and long cycling performance benefit from the improvement electrical conductivity after coating branch-like NiO. The high specific capacity and superior long-life cycle performance are much larger than those in previous works on Fe_2O_3/CC-based composites or nanostructured Fe_2O_3 (Jiao et al., 2014; Hu et al., 2015; Lu et al., 2015; Raut and Sankapal, 2016; Zheng et al., 2016; Zhang et al., 2017; Yang F. et al., 2018; Li F. et al., 2019).

CONCLUSIONS

A novel and cost-efficient strategy has been developed to design a core-branch Fe_2O_3@NiO electrode active material on carbon cloth for flexible supercapacitor application. The Fe_2O_3@NiO nanorods directly grown on the carbon cloth can shorten the transfer paths of ions/electrons effectively, which reduces the contact resistance and avoid the use of polymer binders and conducting additives. The designed electrode exhibits a remarkably enhanced reversible capacity and cycling stability in comparison with Fe_2O_3 electrode, which should be ascribed to the fact that the ultrathin branch-like NiO incomplete coating on the surface of Fe_2O_3 nanorods. This study provides a novel strategy to construct high-performance flexible electrode materials with unique core-branch structure by incorporating two different pseudocapacitive materials.

DATA AVAILABILITY STATEMENT

All datasets generated for this study are included in the article/**Supplementary Material**.

AUTHOR CONTRIBUTIONS

MZ and NZ contributed conception and design of the study. MZ organized the database. MZ and XW performed the statistical analysis. MZ wrote the first draft of the manuscript. XL and DL wrote sections of the manuscript. All authors contributed to manuscript revision, read, and approved the submitted version.

FUNDING

This work was supported by the National Natural Science Foundation of China (Nos. 51272173 and 51572194), Tianjin Science and Technology Major Project (No. 16ZXCLGX00110) and Doctor Foundation (043135202-XB1709) of Tianjin Normal University.

SUPPLEMENTARY MATERIAL

The Supplementary Material for this article can be found online at: https://www.frontiersin.org/articles/10.3389/fchem.2019.00887/full#supplementary-material

REFERENCES

Binitha, G., Soumya, M. S., Madhavan, A. A., Praveen, P., Balakrishnan, A., Subramanian, K. R. V., et al. (2013). Electrospun α-Fe_2O_3 nanostructures for supercapacitor applications. *J. Mater. Chem. A* 1, 11698–11704. doi: 10.1039/c3ta12352a

Chen, L. F., Huang, Z. H., Liang, H. W., Guan, Q. F., and Yu, S. H. (2013). Bacterial-cellulose-derived carbon nanofiber@MnO_2 and nitrogen-doped carbon nanofiber electrode materials: an asymmetric supercapacitor with high energy and power density. *Adv. Mater.* 25, 4746–4752. doi: 10.1002/adma.201204949

Chen, L. F., Yu, Z.-Y., Ma, X., Li, Z.-Y., and Yu, S.-H. (2014). *In situ* hydrothermal growth of ferric oxides on carbon cloth for low-cost and scalable high-energy-density supercapacitors. *Nano Energy* 9, 345–354. doi: 10.1016/j.nanoen.2014.07.021

Dong, H., Xu, Y., Ji, M., Zhang, H., Zhao, Z., and Zhao, C. (2015). High performance of mesoporous γ-Fe_2O_3 nanoparticle/Ketjen black composite

as anode material for lithium ion batteries. *Electrochim. Acta* 151, 118–125. doi: 10.1016/j.electacta.2014.10.022

Fan, Z., Yan, J., Wei, F., Zhi, L., Ning, G., and Li, T. (2011). Asymmetric supercapacitors based on graphene/MnO_2 and activated carbon nanofiber electrodes with high power and energy density. *Adv. Func. Mater*. 21, 2366–2375. doi: 10.1002/adfm.201100058

Fischer, A. E., Pettigrew, K. A., Rolison, D. R., Stroud, R. M., and Long, J. W. (2007). Incorporation of homogeneous, nanoscale MnO_2 within ultra-porous carbon structures via self-limiting electroless deposition: implications for electrochemical capacitors. *Nano Lett*. 7, 281–286. doi: 10.1021/nl062263i

Geng, P., Zheng, S., Tang, H., Zhu, R., Zhang, L., Cao, S., et al. (2018). Transition metal sulfides based on graphene for electrochemical energy storage. *Adv. Energ. Mater*. 8:1703259. doi: 10.1002/aenm.201703259

Guan, C., Xia, X., Meng, N., Zeng, Z., Cao, X., Soci, C., et al. (2012). Hollow core-shell nanostructure supercapacitor electrodes: gap matters. *Energ. Environ. Sci.* 5, 9085–9090. doi: 10.1039/c2ee22815g

Hu, J., Noked, M., Gillette, E., Han, F., Gui, Z., and Wang, C., et al. (2015). Dual-template synthesis of ordered mesoporous carbon/Fe_2O_3 nanowires: high porosity and structural stability for supercapacitors. *J. Mater. Chem. A* 3, 21501–21510. doi: 10.1039/C5TA06372H

Jiao, Y., Liu, Y., Yin, B., Zhang, S., Qu, F., and Wu, X. (2014). Hybrid α-Fe_2O_3@NiO heterostructures for flexible and high performance supercapacitor electrodes and visible light driven photocatalysts. *Nano Energy* 10, 90–98. doi: 10.1016/j.nanoen.2014.09.002

Ke, Q., and Wang, J. (2016). Graphene-based materials for supercapacitor electrodes- a review. *J. Mater*. 2, 37–54. doi: 10.1016/j.jmat.2016.01.001

Kim, D. K., Hwang, M., Ko, D., Kang, J., Seong, K.-D., and Piao, Y. (2017). Electrochemical performance of 3D porous Ni-Co oxide with electrochemically exfoliated graphene for asymmetric supercapacitor applications. *Electrochim. Acta* 246, 680–688. doi: 10.1016/j.electacta.2017.06.099

Kong, D. S., Wang, J.-M., Shao, H.-B., Zhang, J.-Q., and Cao, C.-N. (2011). Electrochemical fabrication of a porous nanostructured nickel hydroxide film electrode with superior pseudocapacitive performance. *J. Alloy. Compd*. 509, 5611–5616. doi: 10.1016/j.jallcom.2011.02.086

Lee, H. Y., Deng, S., Fan, H. M., Mhaisalkar, S., Tan, H. R., Tok, E. S., et al. (2012). αAlpha-Fe_2O_3 nanotubes-reduced graphene oxide composites as synergistic electrochemical capacitor materials. *Nanoscale* 4, 2958–2961. doi: 10.1039/c2nr11902a

Li, F., Liu, Y., Wang, G.-G., Zhang, H., Zhang, B., Li, G.-Z., et al. (2019). Few-layered $Ti_3C_2T_x$ MXene coupled with Fe_2O_3 nanorod arrays grown on carbon cloth as anodes for flexible asymmetric supercapacitors. *J. Mater. Chem. A*. 7, 22631–22641. doi: 10.1039/C9TA08144E

Li, H., Yuqian, G., Wang, C., and Yang, G. (2015). A simple electrochemical route to access amorphous mixed-metal hydroxides for supercapacitor electrode materials. *Adv. Energ. Mater*. 5:1401767. doi: 10.1002/aenm.201401767

Li, J. M., Kurra, N., Seredych, M., Meng, X., Wang, H., and Gogotsi, Y. (2019). Bipolar carbide-carbon high voltage aqueous lithium-ion capacitors. *Nano Energy* 56, 151–159. doi: 10.1016/j.nanoen.2018.11.042

Li, M., Tang, TZ., Leng, M., and Xue, J. (2015). Flexible solid-state supercapacitor based on graphene-based hybrid films. *Adv. Func. Mater*. 24, 7495–7502. doi: 10.1002/adfm.201402442

Liu, J., Jiang, J., Cheng, C., Li, H., Zhang, J., Gong, H., et al. (2011). Co_3O_4 nanowire@MnO_2 ultrathin nanosheet Core-shell arrays: a new class of high-performance pseudocapacitive materials. *Adv. Mater*. 23, 2076–2081. doi: 10.1002/adma.201100058

Liu, X. Y., Gao, Y. Q., and Yang, G. W. (2016). Flexible, transparent and super-long life supercapacitor based on ultrafine Co3O4 nanocrystals electrodes. *Nanoscale* 8, 4227–4235. doi: 10.1039/C5NR09145D

Lu, X. F., Chen, X.-Y., Zhou, W., Tong, Y.-X., and Li, G. R. (2015). α-Fe_2O_3@PANI core–shell nanowire arrays as negative electrodes for asymmetric supercapacitors. *ACS Appl. Mater. Inter*. 7, 14843–14850. doi: 10.1021/acsami.5b03126

Meher, S. K., Justin, P., and Gangavarapu, R. R. (2011). Microwave-mediated synthesis for improved morphology and pseudocapacitance performance of nickel oxide. *ACS Appl. Mater. Inter*. 3, 2063–2073. doi: 10.1021/am200294k

Meher, S. K., and Rao, G. (2011). Ultralayered Co_3O_4 for high-performance supercapacitor applications. *J. Phys. Chem. C* 115, 15646–15654. doi: 10.1021/jp201200e

Quan, H., Cheng, B., Xiao, Y., and Lei, S. (2016). One-pot synthesis of α-Fe_2O_3, nanoplates-reduced graphene oxide composites for supercapacitor application. *Chem. Eng. J*. 286, 165–173. doi: 10.1016/j.cej.2015.10.068

Raut, S. S., and Sankapal, B. R. (2016). Comparative studies on MWCNTs, Fe_2O_3 and Fe_2O_3/MWCNTs thin films towards supercapacitor application. *New J. Chem*. 40, 2619–2627. doi: 10.1039/C5NJ03628C

Reddy, M. V., Yu, T., Sow, C. H., Shen, Z. X., Lim, C. T., Rao, G. V. S., et al. (2010). αAlpha-Fe2O3 nanoflakes as an anode material for li-ion batteries. *Adv. Func. Mater*. 17, 2792–2799. doi: 10.1002/adfm.200601186

Savjani, G. W., Lewis, E. A., Bissett, M. A., Brent, J., Dryfe, R. A.W., Haigh, S. J., et al. (2016). Synthesis of lateral size-controlled monolayer 1H-MoS_2@oleylamine as supercapacitor electrodes. *Chem. Mater*. 28, 657–664. doi: 10.1021/acs.chemmater.5b04476

Tian, X. D., Xiao, L., Tao, Y., Yan, S., Zhan-Jun, L., Quan-Gui, G., et al. (2017). Recent advances on synthesis and supercapacitor application of binary metal oxide. *J. Inorg. Mater*. 32, 459–468. doi: 10.15541/jim20160452

Wang, D. W., Wang, Q., and Wang, T. (2011). Controlled synthesis of mesoporous hematite nanostructures and their application as electrochemical capacitor electrodes. *Nanotechnology* 22:135604. doi: 10.1088/0957-4484/22/13/135604

Xia, X., Deng, S., Xie, D., Wang, Y., Feng, S., and Wu, J.-B. (2018). Boosting sodium ion storage by anchoring MoO2 on vertical graphene arrays. *J. Mater. Chem. A* 6, 15546–15552. doi: 10.1039/C8TA06232C

Xu, Y., Tao, Y., Zheng, X., Ma, H., Luo, J., Kang, F., et al. (2016). Supercapacitors: a metal-free supercapacitor electrode material with a record high volumetric capacitance over 800 F cm^{-3}. *Adv. Mater*. 27, 7898–7898. doi: 10.1002/adma.201570328

Yang, F., Xu, K., and Hu, J. (2018). Construction of Co3O4@Fe2O3 core-shell nanowire arrays electrode for supercapacitors. *J. Alloy. Compd*. 729, 1172–1176. doi: 10.1016/j.jallcom.2017.09.259

Yang, W., Gao, Z., Wang, J., Wang, B., and Liu, L. (2013). Hydrothermal synthesis of reduced graphene sheets/Fe_2O_3 nanorods composites and their enhanced electrochemical performance for supercapacitors. *Solid State Sci.* 20, 46–53. doi: 10.1016/j.solidstatesciences.2013.03.011

Yang, W., Yang, W., Kong, L., Song, A., Qin, X., and Shao, G. (2018). Phosphorus-doped 3D hierarchical porous carbon for high-performance supercapacitors: a balanced strategy for pore structure and chemical composition. *Carbon* 127, 557–567. doi: 10.1016/j.carbon.2017.11.050

Zhang, M., Zhang, M., Sha, J., Miao, X., Liu, E., Shi, C., et al. (2017). Three-dimensional graphene anchored Fe_2O_3@C core-shell nanoparticles as supercapacitor electrodes. *J. Alloy. Compd,*. 696, 956–963. doi: 10.1016/j.jallcom.2016.12.058

Zhang, X., Shi, W., Zhu, W., Ma, J., and Mhaisalkar, S. G. (2010). Synthesis of porous NiO nanocrystals with controllable surface area and their application as supercapacitor electrodes. *Nano Res.* 3, 643–652. doi: 10.1007/s12274-010-0024-6

Zheng, X., Yan, X., Sun, Y., Yu, Y., Zhang, G., Shen, Y., et al. (2016). Temperature-dependent electrochemical capacitive performance of the α-Fe_2O_3 hollow nanoshuttles as supercapacitor electrodes. *J. Colloid Interf. Sci.* 466, 291–296. doi: 10.1016/j.jcis.2015.12.024

Zhu, D., Wang, Y., Lu, W., Zhang, H., Song, Z., Luo, D., et al. (2017). Novel synthesis of hierarchical porous carbons from interpenetrating polymer networks for high performance supercapacitor electrodes. *Carbon* 111, 667–674. doi: 10.1016/j.carbon.2016.10.016

Conflict of Interest: The authors declare that the research was conducted in the absence of any commercial or financial relationships that could be construed as a potential conflict of interest.

frontiers in Chemistry

ORIGINAL RESEARCH
published: 10 January 2020
doi: 10.3389/fchem.2019.00904

Binder-Free Cathode for Thermal Batteries Fabricated Using FeS_2 Treated Metal Foam

In Yea Kim[1], Sung Pil Woo[2], Jaehwan Ko[1], Seung-Ho Kang[3], Young Soo Yoon[1], Hae-Won Cheong[3] and Jae-Hong Lim[1]**

[1] Department of Materials Science and Engineering, Gachon University, Seongnam, South Korea, [2] Department of Materials Science and Engineering, Yonsei University, Seoul, South Korea, [3] Agency for Defense Development, Daejeon, South Korea

In this study, we fabricated a cathode with lower amounts of additive materials and higher amounts of active materials than those of a conventional cathode. A thermal battery was fabricated using FeS_2 treated foam as the cathode frame, and its feasibility was verified. X-ray diffraction, transmission electron microscopy, and scanning electron microscopy were used to analyze the effects of thermal sulfidation temperature (400 and 500°C) on the structure and surface morphology of the FeS_2 foam. The optimal temperature for the fabrication of the FeS_x treated foam was determined to be 500°C. The FeS_2 treated foam reduced the interfacial resistance and improved the mechanical strength of the cathode. The discharge capacity of the thermal battery using the FeS_2 treated foam was about 1.3 times higher than that of a thermal battery using pure Fe metal foam.

Keywords: thermal battery, FeS_2 foam, metal foam, thermal sulfidation, cathode frame

OPEN ACCESS

Edited by:
Nosang Vincent Myung, University of California, Riverside, United States

Reviewed by:
Pankaj Madhukar Koinkar, Tokushima University, Japan
Xianhong Rui, Guangdong University of Technology, China

****Correspondence:***
Hae-Won Cheong
hwcheong@add.re.kr
Jae-Hong Lim
limjh@gachon.ac.kr

Specialty section:
This article was submitted to Electrochemistry, a section of the journal Frontiers in Chemistry

Received: *03 September 2019*
Accepted: *13 December 2019*
Published: *10 January 2020*

Citation:
Kim IY, Woo SP, Ko J, Kang S-H, Yoon YS, Cheong H-W and Lim J-H (2020) Binder-Free Cathode for Thermal Batteries Fabricated Using FeS_2 Treated Metal Foam. Front. Chem. 7:904. doi: 10.3389/fchem.2019.00904

INTRODUCTION

Thermal batteries are potential power sources for nuclear weapons and warhead missiles and are used in aerospace applications owing to their excellent mechanical properties, reliability, and low self-discharge characteristics (Guidotti and Masset, 2006; Kang et al., 2016; Jin et al., 2018). Cathodes of commercial thermal batteries are fabricated using transition metals such as FeS_2, CoS_2, and NiS_2; their anodes are fabricated with Li-alloys (Li-Si and Li-Al); and a eutectic mixture of LiCl-KCl, which exists in the molten state at the operating temperature of thermal batteries (~500°C), is used as the electrolyte (Guidotti and Masset, 2008; Masset and Guidotti, 2008a; Giagloglou et al., 2016). Although the electrochemical properties of CoS_2 and NiS_2 are similar to those of FeS_2, sulfur exhibits a high loss rate when it encounters electrolytic salts (Preto et al., 1983). In addition, synthesis of CoS_2 is expensive, thereby limiting its usage in large-scale applications (Jin et al., 2017).

Generally, cathodes of thermal batteries are in the form of cold-pressed pellets. To manufacture a pellet-type cathode, the cathode active material is mixed with various additives such as salts, electrolyte, and a binder (Au, 2003; Singh et al., 2004; Masset et al., 2005; Yang et al., 2014). Such cathodes are called catholytes (cathode + electrolyte) because they contain a large amount of electrolyte to transfer ions to the cathode during the operation of thermal batteries (Au, 2003; Guidotti and Preston, 2007; Masset and Guidotti, 2008a; Yang et al., 2014). Moreover, binder materials such as MgO and SiO_2 are added to the cathode to ensure the molten salt is maintained at the high operating temperatures of thermal batteries (Kim et al., 2017; Cha et al., 2018; Wu et al., 2018). However, these additives increase the internal resistance of the electrodes, and their addition reduces the amount of cathode active material, thus deteriorating the discharge characteristics of

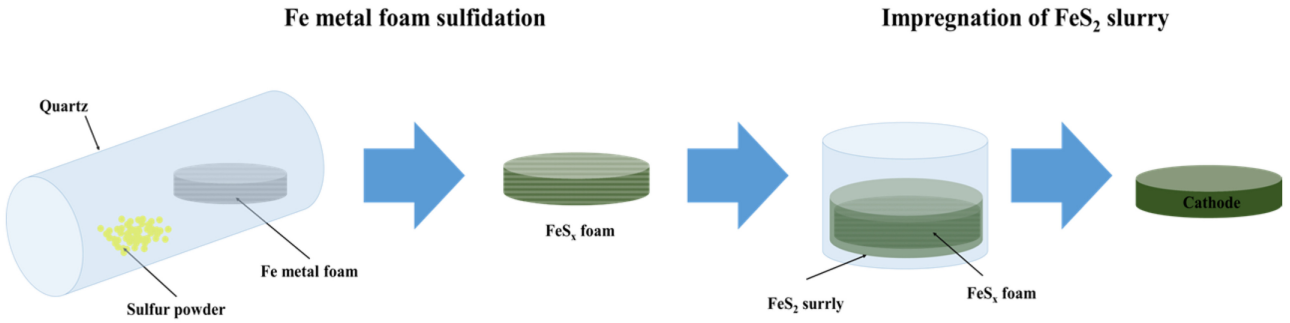

FIGURE 1 | Schematic representation of the synthesis process of the cathode using FeS_x foam for thermal batteries.

the cathode (Masset and Guidotti, 2007; Ko et al., 2017). In addition, it is difficult to manufacture large-sized cathodes with sufficient mechanical strength through a cold-press method (Guidotti et al., 2000, 2002; Leviatan, 2011).

Various methods to manufacture reliable cathodes with sufficient mechanical strength have been studied. The most notable methods are tape casting and thermal spraying. Via tape casting, a cathode can directly be fabricated onto the current collector or on a graphite paper substrate from slurry by blending the active cathode material and some polymeric binders, thus fabricating thin cathodes; the size of the cathodes can be easily scaled up. However, the process of manufacturing the slurry is complicated, and the method increases the internal resistance of the batteries because of the presence of various polymer binders (Masset et al., 2005; Cha et al., 2018). Thermal spraying is a coating process in which the FeS_2 active material is sprayed through a heated feedstock onto the surface of a prepared current collector. In this method, the surface of the current collector is coated by spraying raw materials. Electrode formation by thermal spraying is simpler than that by tape casting. However, decomposition of FeS_2 may lead to the deposition of FeS or S_2 in the heated feedstock, causing a spike during thermal battery discharge (Guidotti and Preston, 2007). In addition, the thermal spray method requires expensive equipment. However, electrodes fabricated by the two methods mentioned are very thin to allow loading of large active materials. A small amount of active material in the positive electrode degrades the discharge characteristics of thermal batteries. Therefore, a simple, inexpensive method for fabricating cathodes containing the necessary active materials with lesser additives needs to be developed.

Thermal battery cathodes have been fabricated using metal foam as an electrode support and conductor (Ji et al., 2012; Sun et al., 2019). Metal foams of various sizes and thicknesses with high porosity (>90%) can be added to various active materials to improve mechanical strength. However, metal foams increase the contact resistance with the active material because of low structural similarity with the cathode active material. Furthermore, they reduce the capacity of the batteries because the metal does not participate in the electrochemical reaction during thermal battery operation. To improve these characteristics, the metal foam needs to be treated with a material with structural characteristics similar to those of the active material of the cathode. Fe metal foam is a promising option because it can react with S_2 powders to form FeS_2, a thermal battery cathode material, via simple thermal sulfidation, as shown in **Figure 1** (Ferrer and Sánchez, 1991; Liu et al., 2016). The purpose of this study is to synthesize a cathode frame whose structural characteristics are the most similar to those of cathode materials (FeS_2) of thermal batteries. In addition, the thermal battery discharge characteristics were evaluated. The discharge performance of a thermal cathode with FeS_2 foam and that with Fe foam in a single cell configuration were compared to evaluate the efficiency of the sulfidation reaction. The discharge capacity of the unit cell with the synthesized FeS_2 foam electrode was 538.3 A s/g at the cut-off value of 1.3 V and that for the single cell with Fe metal foam was 404.04 A s/g. These results indicate that the use of FeS_2 foam is an effective method to fabricate thermal battery cathodes.

EXPERIMENTAL

Thermal sulfidation of FeS_2 foam was carried out in a sealed quartz tube to prevent oxidation and incorporate the evaporated sulfur. Fe foam (porosity: 95%, pore size: ~450 μm, Alantum Corporation, Seongnam, South Korea) and sulfur powder (purity: 99%, Sigma Aldrich, St. Louis, Missouri, USA) were used as starting materials to fabricate the FeS_2 foam. The Fe foam was cut into a circle of diameter 56.2 mm, which was the size of the cathode. The Fe foam and sulfur powder (twice the amount of Fe in terms of molar ratio) were placed in the quartz tube, which was purged with Ar gas and subsequently sealed. The precursors placed in the quartz tube were then sulfidized at 400 and 500°C (HT-400 and HT-500) for 3 h. The heating rate was maintained at 2°C/min. After thermal sulfidation, the quartz tube was slowly cooled to room temperature. All the experiments were performed in a glove box to prevent contact with oxygen and moisture.

FeS_2 slurry was impregnated into FeS_2 foam to fabricate the thermal battery cathodes. The FeS_2 slurry was prepared as

Abbreviations: SEM, scanning electron microscopy; EDX, energy dispersive X-ray spectroscopy; XRD, X-ray diffraction.

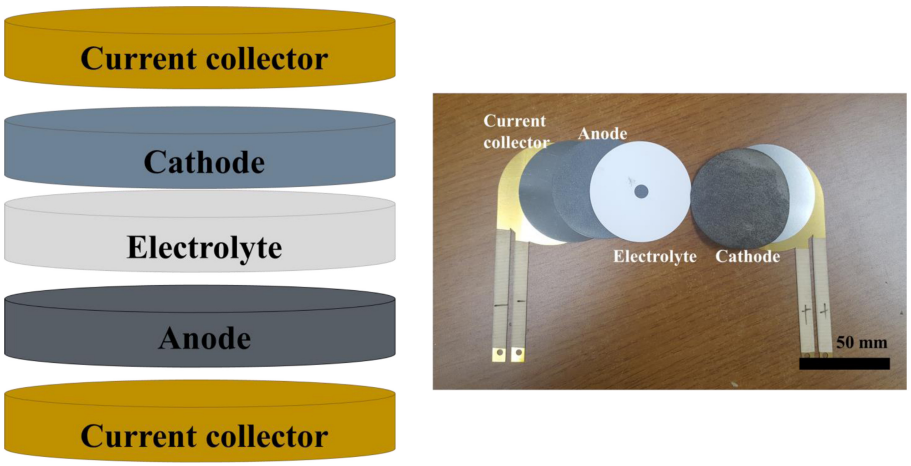

FIGURE 2 | Structure and images of a single cell for a thermal battery.

follows. FeS_2 powder (mean size: 98 μm, purity: 99% LinYi, China) was dispersed in acetone by ball milling using a BYK-111 (Altana) dispersant for 24 h. The initial particle size of the FeS_2 powder was about 98 μm; however, the particle size reduced to about 20 μm after ball milling for 24 h. The size reduction of the particles by ball milling has been confirmed in previous studies (Ko et al., 2017). The FeS_2 slurry was placed in a glass petri dish along with Fe and FeS_2 foam, and the resulting mixtures were left under ambient conditions for several minutes. The mixtures were subsequently dried at 70°C for 24 h to completely remove acetone. A schematic representation of the entire process of cathode fabrication via FeS_2 impregnation on Fe foam and the FeS_2 foam prepared by thermal sulfidation is shown in **Figure 1**.

The crystalline phases of FeS_2 foams, which were synthesized at different sulfidation temperatures, were analyzed by X-ray diffraction (XRD, PANalytical X'Pert PRO) with Cu Kα radiation. The surface morphological properties and element ratios of the samples were examined using a field-emission scanning electron microscope (Hitachi S-4200) with an energy dispersive X-ray spectrometer (EDX). The resistances of the FeS_2 foams were measured at room temperature by electrochemical impedance spectroscopy (EIS, IM6Ex) over a frequency range of 100 mHz−2 MHz with an amplitude voltage of 10 mV.

The cathodes fabricated using the pure Fe and FeS_2 foams were used to evaluate the discharge characteristics of thermal battery single cells. **Figure 2** shows the general procedure of assembly of the single cell used to confirm the discharge characteristics of the cathode using HT-500 foam.

To verify the characteristics of the cathode, a commercial pellet-type electrode was used as the separator and anode. The discharge test of the single cell was performed under conditions similar to the operating conditions of thermal batteries and by using Daque 9,000 at 500°C with a load of 250 kg_f while applying a consecutive pulse current (10 A, 4.5 s → 0 A, 0.5 s). The discharge test was terminated when the voltage dropped below 1.3 V.

RESULTS AND DISCUSSION

FeS_2 Foam Fabrication According to Sulfidation Temperature

FeS_2 foam was fabricated via thermal sulfidation at 400 and 500°C on Fe foams. The surface morphologies of the Fe and FeS_2 foams synthesized at different sulfidation temperatures were examined by SEM. **Figure 3A** shows that the Fe foam had a three-dimensional structure with interconnecting holes (200–450 μm) made up of arch ribs. The arch ribs of the Fe foam had smooth and uniform wrinkles on the highly porous surface. **Figures 3B,C** shows that HT-400 and HT-500 foams were prepared at different thermal sulfidation temperatures. SEM images of the foams treated by thermal sulfidization revealed that sulfur was deposited entirely on the surface of the arch ribs. Both HT-400 and HT-500 foams had porous structures with no wrinkles on their surfaces (**Figures 3B,C**) unlike the Fe foam. As the thermal sulfidation temperature increased, the amount of sulfur deposited on the surface of the arch ribs increased along with an increase in the surface grain size. However, the synthesized HT-400 and HT-500 foams increased in terms of grain size with increasing sulfidation temperature but did not exhibit pores and cracks (**Figure S1**). These results show an improvement in surface conditions over those obtained by Rahman and Wen (2016). In addition, the synthesized HT-400 and HT-500 foams are expected to exhibit stable mechanical strength because they have 3D architectures. Moreover, EDS mapping clearly showed the uniform distribution of S and Fe on the surface of the foams (**Figures 3D,E**). HT-500 foam consisted of 32.79% of Fe and 67.21% of S with an Fe/S ratio of 2.04, which is very close to the atomic ratio in the formula FeS_2 (**Table 1**). However, HT-400 foam consisted of 38.29% of Fe and 61.17% of S with an Fe/S ratio of 1.60. In other words, the sulfur content of the HT-400 foam was lesser than that of FeS_2 (the material of thermal battery cathodes).

Figure 4 shows the XRD peaks of HT-400 and HT-500 foams. Both samples showed peaks corresponding to the (111), (200), (210), (211), (220), (311), (222), (023), and (321) planes

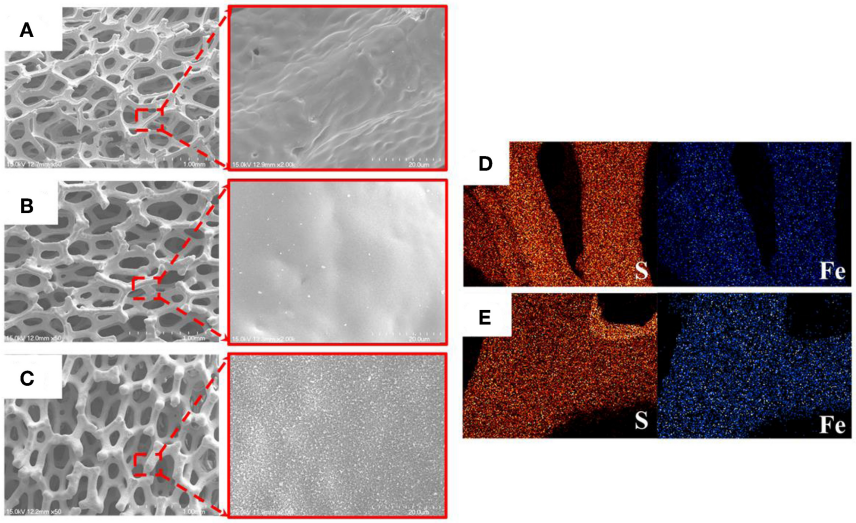

FIGURE 3 | SEM images of **(A)** Fe, **(B)** HT-400, and **(C)** HT-500 foams. EDX images of **(D)** HT-400 and **(E)** HT-500 foams.

TABLE 1 | Quantification results of EDX at different annealing temperatures.

Heat treatment temp. (°C)	Concentration (at %)	
	Fe	S
400	38.29	61.17
500	32.79	67.21

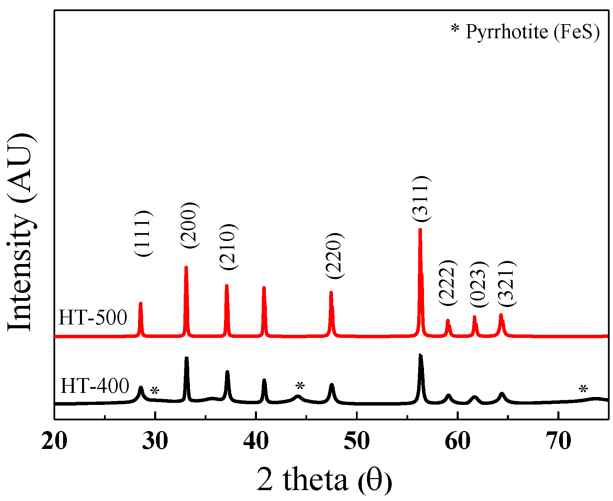

FIGURE 4 | XRD patterns of HT-400 and HT-500 foams.

(JCPDS card no. 42-1340). This exhibits a cubic pyrite (FeS_2) structure with the space group of *Pa3* (Cabán-Acevedo et al., 2013; Lucas et al., 2013; Miao et al., 2017). However, XRD peaks for FeS of HT-400 foam and the high Fe content by EDS analysis (in **Table 1**) indicate the coexistence of FeS and FeS_2. Pyrrhotite (FeS) causes thermal battery degradation owing to self-discharge by pyrolysis and impurity formation during the operation of thermal batteries (Schoeffert, 2005; Masset and Guidotti, 2008b). In contrast, the HT-500 foam confirmed good crystallinity with high intensity and sharp XRD peaks. To further analyze the crystallinity and phase purity of HT-400 and HT-500 foams, HRTEM and SAED analyses were carried out on them (**Figure S2**). The HT-400 foam showed lattice spacings of 3.126 and 2.050 Å corresponding to the pyrite (111) and pyrrhotite (208) planes, respectively (**Figure S1b**). However, the HT-500 foam showed a lattice spacing of 3.126 Å corresponding to the (111) plane (**Figure S1c**).Thus, the structure of HT-500 foam was similar to that of the cathode material, and HT-500 foam did not contain any FeS; it was expected that there would be no incidental reaction related to FeS during thermal battery discharge.

Figure 5 shows the Nyquist plots of the HT-400 and HT-500 foams obtained from their EIS results (to evaluate their electrochemical properties). From the EIS results, the total ohmic resistance associated with the series resistance of HT-400 and HT-500 foams was determined. The high-frequency intercept at the real axis (Z) corresponds to the total ohmic resistance (R_s) (Cooper and Smith, 2006; Gomez et al., 2011). In addition, a Warburg tail was not observed at low frequencies, indicating that only electrical conduction occurred (without ion conduction) at these frequencies (Sinclair, 1995). The electrical resistances of the HT-400 and HT-500 foams at room temperature were found to be 1.55×10^4 and 9.37×10^3 Ω, respectively. The diameter of the Nyquist curve semicircle of the HT-400 foam was larger than that of the HT-500 foam, indicating that the electrical resistance of the HT-400 foam was higher than that of the HT-500 foam.

These results suggest that the HT-400 foam was synthesized with a mixed phase rather than a single phase, thereby resulting in an increase in the total resistance (Thomas et al., 1998). The structure of HT-500 foam was similar to that of FeS_2, and HT-500 foam exhibited more stable electrochemical properties than HT-400 foam. Therefore, HT-400 foam is not discussed in detail in the rest of the study.

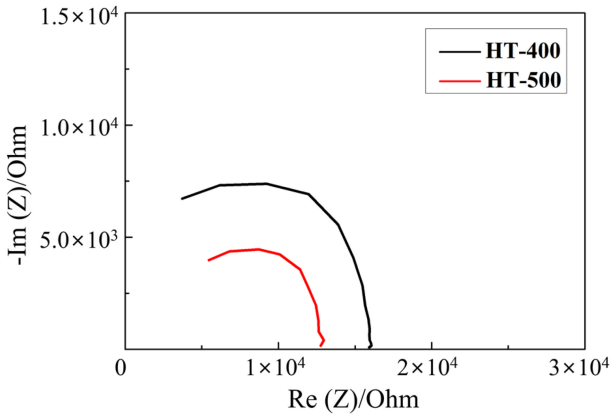

FIGURE 5 | Nyquist plots of HT-400 and HT-500 foams.

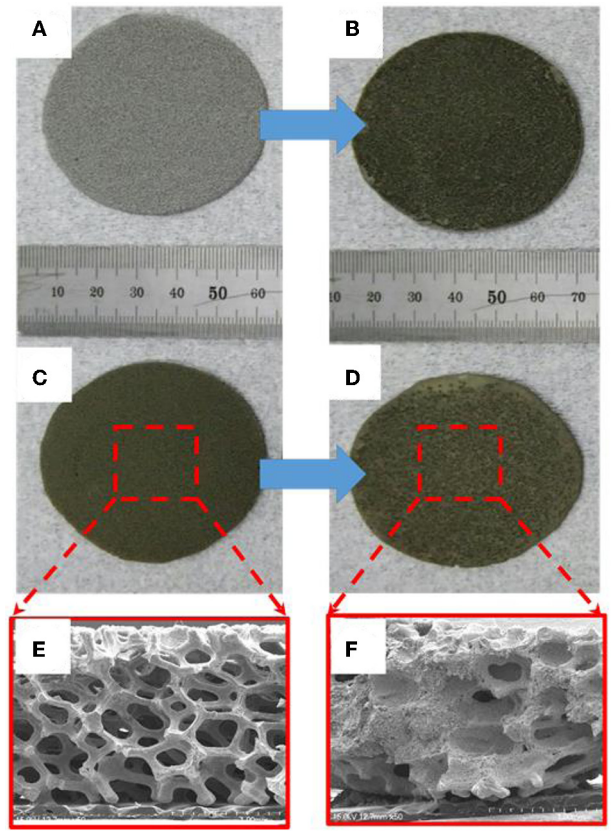

FIGURE 6 | Image of pure Fe foam **(A)** before and **(B)** after impregnation with FeS_2 slurry. HT-500 foam **(C)** before and **(D)** after impregnation with FeS_2 slurry. Cross-section of the SEM image of HT-500 **(E)** before and **(F)** after impregnation with FeS_2 slurry.

Single Cell Assembly Using Synthesized FeS_2 Foam

Cathodes for thermal batteries were fabricated using HT-500 and Fe foams to confirm the effect of thermal sulfidation. Both the cells were 16-mm thick and had a diameter of 56.2 mm. **Figures 6A,B** show images of the Fe foam before and after immersion in FeS_2 slurry, respectively. The color of the Fe foam changed after immersion in the FeS_2 slurry, indicating that the Fe foam was well-impregnated with the slurry. **Figures 6C,D** show images of the HT-500 foam before and after FeS_2 slurry impregnation, respectively. The color of the FeS_2 slurry impregnated HT-500 foam was similar to that of the FeS_2 slurry impregnated Fe foam. **Figures 6E,F** show cross-sectional SEM images of the HT-500 foam before and after FeS_2 slurry impregnation, respectively. The figures show that before impregnation, the HT-500 foam comprised void spaces. Such a frame structure can prevent separation of the cathode powder at the operating temperature of thermal batteries and can contain a large amount of active material. After impregnation, a large amount of fine FeS_2 particles filled the voids and increased the density of the HT-500 foam.

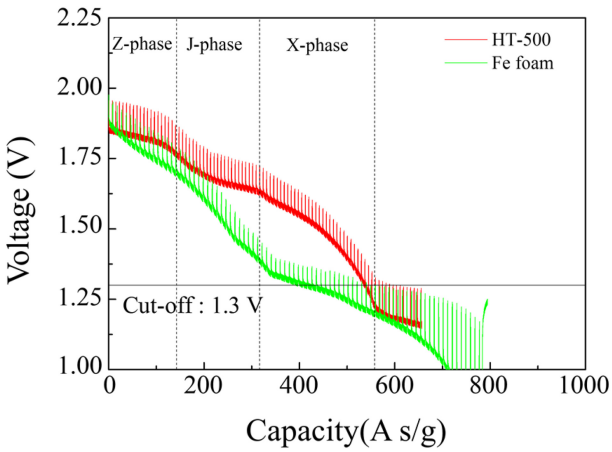

FIGURE 7 | Discharge graphs of cathodes using Fe and HT-500 foams.

TABLE 2 | Discharge performances of cathodes using Fe foam and HT-500.

Type	Thickness (mm)	Foam weight (g)	Total electrode weight (g)	Discharge capacity (A s/g)
Using Fe foam	1.6	1.209	4.739	404.04
Using HT-500	1.6	2.183	6.118	538.38

Evaluation of Discharge Characteristics of the Assembled Single Cells

Figure 7 shows the discharge performance of the HT-500 and Fe foam cathodes and the assembled cells. The fabricated cells were discharged into the pulse mode at the thermal battery operating temperature. The inversion voltage plateaus of the thermal battery using FeS_2 had three parts: the Z-phase reacts with FeS_2 and Li to form $Li_2Fe_2S_4$, the J-phase generates $Li_3Fe_2S_4$, and the X-phase was the final reaction step to produce elemental lithium sulfur and iron (Choi et al., 2014). The X-phase occurs at 1.3 V (Ulissi et al., 2018).

In this study, we confirmed the capacity of the single thermal cell by setting the cut-off value to 1.3 V, which is the voltage at which the main reaction of the thermal battery cathode

is completed, to confirm the final reaction of FeS_2. **Table 2** lists the thicknesses, foam weights, total electrode weights, and discharge capacities of the cathode using Fe and HT-500 foams. To determine the effect of Fe and HT-500 foams, the thermal battery capacity was calculated by considering the total cathode weight. The discharge capacity of the Fe foam cathode at the cut-off value of 1.3 V was found to be 404.04 A s/g. In contrast, the cell using the HT-500 foam cathode showed a discharge capacity of 538.38 A s/g. The reason for the higher discharge capacity of the HT-500 foam was the chemical reaction that occurs during discharging.

Based on the discharge evaluation shown in **Figure 8**, the total polarization of the single battery with a cathode frame was calculated using the formula reported by Fujiwara et al. (2011). The total polarization was calculated using the following equation:

$$Rt = \frac{V_{OC} - V_{CC}}{I} \quad (1)$$

where Rt: total polarization, Ω; V_{oc}: open circuit voltage, V; V_{cc}: close circuit voltage, V; and I: discharge current, A.

During discharge, the total polarization of the Fe foam cell is higher than that of the HT-500 cell. Furthermore, a strong internal resistance was observed during the reaction between 100 and 150 s. These results are consistent with the results in **Figure 7** which shows a region where the performance of the Fe foam cell rapidly decreased. These results indicate that the internal resistance increases as an intermediate product (in the X-phase and J-phase) during the thermal battery discharge is rapidly generated because of the reaction between the Fe foam and the melted electrolyte (Kam and Johnson, 1980). In addition, the total polarization appears to be lower after 150 s, which is due to the electrons generated upon the reaction of Fe and LiS_2, a byproduct of the thermal battery reaction (Peled and Lavi, 1998; Strauss and Peled, 2000; Masset and Guidotti, 2008a). Because this occurs when the thermal battery reaction is completed, the discharge capacity is less affected (**Figure S3**). These results have an impact on the discharge characteristics of the battery, causing a reduction in its capacity when compared with batteries using the HT-500 foam. **Table 3** shows a comparison of the discharge characteristics of the sample fabricated in this study to those fabricated through other methods. The thermal battery discharge profile depends on the pulse current. Generally, as the discharge current increases, the operation time and capacity of the battery reduce (Wesolowski and Papenguth, 2010; Ceriotti et al., 2011). These cells can be fabricated with diameters larger than those fabricated by other methods.

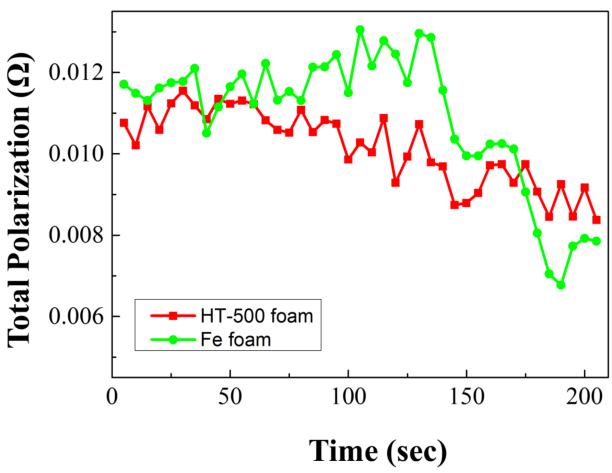

FIGURE 8 | Total polarization graphs of cathodes using Fe and HT-500 foams.

Furthermore, we compared the discharge performances of the cold-press electrode and the electrode using HT-500 (**Figure S4**). Typically, the thickness of the cathode electrode manufactured by the cold-press method is 0.5 mm, and that of the HT-500 cathode was also 0.5 mm. The former showed a capacity of 996.0 A s/g and the latter showed a capacity of 1251.2 A s/g. The capacity of the cathode using HT-500 foam was 1.2 times that of the cold-press electrode. The discharge characteristics of the single cell using the HT-500 foam show that the cell can be utilized to manufacture a thermal battery electrode.

CONCLUSIONS

HT-500 foam was synthesized through a sulfidation process for use as a thermal cathode frame. The HT-500 foam reduced the contact resistance between the active material and the Fe foam because of the formation of FeS_2 crystals, which was dependent on the thermal sulfidation temperature. The foam was used as a frame for thermal battery cathodes, and the discharge capacity of the cathode was measured. The discharge characteristics of

TABLE 3 | Characteristics of the cathodes based on production method.

Sample	Electrode manufacturing method	Theoretical capacity (A s/g) (Guidotti and Masset, 2006)	Capacity (A s/g)	Additive	Cut-off voltage (V)	Pulse load (A)	Battery size (mm)
This study	Using foam	1,206	538.38 (at 500°C)	No	1.3	10	Diameter: 56.2 Thickness: 1.6
1	Plasma spray	1,206	1,967 (at 550°C) (Ulissi et al., 2018)	No	1.0	2	Diameter: 31.8 Thickness: 0.13
2	Tape casting	1,206	597 (at 550°C) (Kim et al., 2017)	Polymeric binder	1.5	2.2	Diameter: 30 Thickness: 0.134
3	Cold pressing	1,206	647.4 (at 550°C) (Kim et al., 2017)	LiF-LiBr-LiCl, MgO	1.5	2.2	Diameter: 30 Thickness: -

the HT-500 and Fe foam cathodes were compared. The discharge capacity of a single cell with the HT-500 foam was 538.38 A s/g, which is 1.3 times higher than that of the single cell using the Fe foam. These results indicate that the discharge characteristics and mechanical strength of thermal battery cathodes can be improved by decreasing their interfacial resistance by coating active materials on their surfaces. Thus, HT-500 foam is a promising cathode frame for high-performance thermal batteries.

DATA AVAILABILITY STATEMENT

All datasets generated for this study are included in the article/**Supplementary Material**.

AUTHOR CONTRIBUTIONS

The concept for this study was designed by YY, H-WC, and J-HL. IK designed the experiment. IK and SW performed experiments on material selection and sulfidation temperature conditions. JK performed discharge evaluation. YY and J-HL performed raw material selection and helped in morphology analysis. H-WC and S-HK coordinates the interpretation of the electrochemical assessment. All authors helped write the manuscript.

FUNDING

This work was supported by Defense Acquisition Program Administration and Agency for Defense Development under the contract (UD190006GD). This work was also supported by the Gachon University research fund of 2019 (GCU-2019-0297).

SUPPLEMENTARY MATERIAL

The Supplementary Material for this article can be found online at: https://www.frontiersin.org/articles/10.3389/fchem.2019.00904/full#supplementary-material

REFERENCES

Au, M. (2003). Nanostructured thermal batteries with high power density. *J. Power Sources* 115, 360–366. doi: 10.1016/S0378-7753(02)00627-4

Cabán-Acevedo, M., Liang, D., Chew, K. S., DeGrave, J. P., Kaiser, N. S., and Jin, S. (2013). Synthesis, characterization, and variable range hopping transport of pyrite (FeS_2) nanorods, nanobelts, and nanoplates. *ACS Nano* 7, 1731–1739. doi: 10.1021/nn305833u

Ceriotti, M., Corrà, M., Orazio, L. D., Doriguzzi, R., Facchin, D., Gună, S. T., et al. (2011). "Is there light at the ends of the tunnel? Wireless sensor networks for adaptive lighting in road tunnels," in *Proceedings of the 10th ACM/IEEE International Conference on Information Processing in Sensor Networks* (Chicago, IL), 12–14.

Cha, Y. L., Park, I. H., Moon, K. H., Kim, D. H., Jung, S. I., and Yoon, Y. S. (2018). Simultaneous control of phase transformation and crystal of amorphous TiO_2 coating on MWCNT surface. *J. Korean Ceram. Soc.* 55, 618–624. doi: 10.4191/kcers.2018.55.6.09

Choi, Y., Cho, S., and Lee, Y. S. (2014). Effect of the addition of carbon black and carbon nanotube to FeS_2 cathode on the electrochemical performance of thermal battery. *J. Ind. Eng. Chem.* 20, 3584–3589. doi: 10.1016/j.jiec.2013.12.052

Cooper, K. R., and Smith, M. (2006). Electrical test methods for on-line fuel cell ohmic resistance measurement. *J. Power Sources* 160, 1088–1095. doi: 10.1016/j.jpowsour.2006.02.086

Ferrer, I. J., and Sánchez, C. (1991). Characterization of FeS_2 thin films prepared by thermal sulfidation of flash evaporated iron. *J. Appl. Phys.* 70, 2641–2647. doi: 10.1063/1.349377

Fujiwara, S., Inaba, M., and Tasaka, A. (2011). New molten salt systems for high temperature molten salt batteries: ternary and quaternary molten salt systems based on LiF–LiCl, LiF–LiBr, and LiCl–LiBr. *J. Power Sources* 196, 4012–4018. doi: 10.1016/j.jpowsour.2010.12.009

Giagloglou, K., Payne, J. L., Crouch, C., Gover, R. K. B., Connor, P. A., and Irvine, J. T. S. (2016). Zirconium trisulfide as a promising cathode material for Li primary thermal batteries. *J. Electrochem. Soc.* 163, A3126–A3130. doi: 10.1149/2.1351614jes

Gomez, J., Nelson, R., Kalu, E. E., Weatherspoon, M. H., and Zheng, J. P. (2011). Equivalent circuit model parameters of a high-power Li-ion battery: thermal and state of charge effects. *J. Power Sources* 196, 4826–4831. doi: 10.1016/j.jpowsour.2010.12.107

Guidotti, R., and Preston, S. (2007). "Electrode fabrication processes for thermal batteries," in *5th International Energy Conversion Engineering Conference and Exhibit* (St. Louis, MO), 25–27.

Guidotti, R. A., and Masset, P. (2006). Thermally activated ("thermal") battery technology Part I: an overview. *J. Power Sources* 161, 1443–1449. doi: 10.1016/j.jpowsour.2006.06.013

Guidotti, R. A., and Masset, P. J. (2008). Thermally activated ("thermal") battery technology Part IV: anode materials. *J. Power Sources* 183, 388–398. doi: 10.1016/j.jpowsour.2008.04.090

Guidotti, R. A., Reinhardt, F. W., Dai, J., Roth, J., and Reisner, D. E. (2002). Characterization of plasma-sprayed pyrite/electrolyte composite cathodes for thermal batteries. *J. New Mat. Electrochem. Syst.* 5, 273–279. Available online at: https://www.researchgate.net/profile/Ronald_Guidotti/publication/267725303_Characterization_of_Plasma-Sprayed_PyriteElectrolyte_Composite_Cathodes_for_Thermal_Batteries/links/547784960cf2a961e483ac59.pdf

Guidotti, R. A., Reinhardt, F. W., Jinxiang, D., Xiao, T. D., and Reisner, D. (2000). "Thermal-sprayed, thin-film pyrite cathodes for thermal batteries-discharge-rate and temperature studies in single cells," in *35th Intersociety Energy Conversion Engineering Conference and Exhibit* (Las Vegas, NV), 24–28.

Ji, H., Zhang, L., Pettes, M. T., Li, H., Chen, S., Shi, L., et al. (2012). Ultrathin graphite foam: a three-dimensional conductive network for battery electrodes. *Nano. Lett.* 12, 2446–2451. doi: 10.1021/nl300528p

Jin, C., Fu, L., Zhu, J., Yang, W., Li, D., and Zhou, L. (2018). A hierarchical carbon modified nano-NiS_2 cathode with high thermal stability for a high energy thermal battery. *J. Mater. Chem. A.* 6, 7123–7132. doi: 10.1039/C8TA00346G

Jin, C., Zhou, L., Fu, L., Zhu, J., Li, D., and Yang, W. (2017). The acceleration intermediate phase (NiS and Ni_3S_2) evolution by nanocrystallization in Li/NiS2 thermal batteries with high specific capacity. *J. Power Sources* 352, 83–89. doi: 10.1016/j.jpowsour.2017.03.119

Kam, K. W., and Johnson, K. E. (1980). Cycle voltammetry of Li_2S, FeS and FeS_2 in LiC1-KCl eutectic melt. *J. Electroanal. Chem.* 115, 53–64. doi: 10.1016/S0022-0728(80)80495-5

Kang, S. H., Lee, J. U., Hur, T., Cheong, H. W., and Yi, J. (2016). Heat treatment effect on microstrain and electrochemical performance of nano-sized FeS_2 cathode for thermal batteries. *Int. J. Electrochem. Sci.* 6, 4371–4379. doi: 10.20964/2016.06.41

Kim, I. Y., Shin, S. Y., Ko, J. H., Lee, K. S., Woo, S. P., Kim, D. K., et al. (2017). Functional Li-M (Ti, Al, Co, Ni, Mn, Fe)-O energy materials. *J. Korean Ceram. Soc.* 54, 9–22. doi: 10.4191/kcers.2017.54.1.11

Ko, J., Kim, I. Y., Jung, H. M., Cheong, H., and Yoon, Y. S. (2017). Thin cathode for thermal batteries using a tape-casting process. *Ceram. Int.* 43, 5789–5793. doi: 10.1016/j.ceramint.2017.01.126

Leviatan, T. (2011). "Development of thin layer electrochemical components for advanced thermal batteries," in *9th Annual International Energy Conversion Engineering Conference (IECEC)* (San Diego, CA).

Liu, X., Ho, J. Y. L., Wong, M., Kwok, H. S., and Liu, Z. (2016). Synthesis, characterization and fabrication of ultrathin iron pyrite (FeS_2) thin films and field-effect transistors. *RSC Adv*. 6, 8290–8296. doi: 10.1039/C5RA23344E

Lucas, J. M., Tuan, C.-C., Lounis, S. D., Britt, D. K., Qiao, R., Yang, W., et al. (2013). Ligand-controlled colloidal synthesis and electronic structure characterization of cubic iron pyrite (FeS_2) nanocrystals. *Chem. Mat*. 25, 1615–1620. doi: 10.1021/cm304152b

Masset, P., and Guidotti, R. A. (2007). Thermal activated (thermal) battery technology Part II. molten salt electrolytes. *J. Power Sources* 164, 397–414. doi: 10.1016/j.jpowsour.2006.10.080

Masset, P., Schoeffert, S., Poinso, J.-Y., and Poignet, J.-C. (2005). LiF-LiCl-LiI vs. LiF-LiBr-KBr as molten salt electrolyte in thermal batteries. *J. Electrochem. Soc*. 152, A405–A410. doi: 10.1149/1.1850861

Masset, P. J., and Guidotti, R. A. (2008a). Thermal activated ("thermal") battery technology Part IIIa: FeS_2 cathode material. *J. Power Sources* 177, 595–609. doi: 10.1016/j.jpowsour.2007.11.017

Masset, P. J., and Guidotti, R. A. (2008b). Thermal activated ("thermal") battery technology Part IIIb: sulfur and oxide based cathode materials. *J. Power Sources* 178, 456–466. doi: 10.1016/j.jpowsour.2007.11.073

Miao, R., Dutta, B., Sahoo, S., He, J., Zhong, W., Cetegen, S. A., et al. (2017). Mesoporous iron sulfide for highly efficient electrocatalytic hydrogen evolution. *J. Am. Chem. Soc*. 139, 13604–13607. doi: 10.1021/jacs.7b07044

Peled, E., and Lavi, Y. (1998). Li/CPE/FeS_2 rechargeable battery. *Electrochim. Acta* 43, 1593–1599 doi: 10.1016/S0013-4686(97)10059-7

Preto, S. K., Tomczuk, Z., von Winbush, S., and Roche, M. F. (1983). Reactions of FeS_2, CoS_2, and NiS_2 electrodes in molten LiCI-KCI electrolytes. *Electrochem. Soc*. 130, 264–273. doi: 10.1149/1.2119692

Rahman, M. A., and Wen, C. (2016). A study of the capacity fade of porous NiO/Ni foam as negative electrode for lithium-ion batteries. *Ionics* 22, 173–184. doi: 10.1007/s11581-015-1542-8

Schoeffert, S. (2005). Thermal batteries modeling, self-discharge and self-heating. *J. Power Sources* 142, 361–369. doi: 10.1016/j.jpowsour.2004.09.038

Sinclair, D. C. (1995). Characterization of electro-materials using ac impedance spectroscopy. *Cerámicay Vidrio* 32, 55–65.

Singh, P., Guidotti, R. A., and Reisner, D. (2004). AC impedance measurements of molten salt thermal batteries. *J. Power Sources* 138:323–326. doi: 10.1016/j.jpowsour.2004.06.038

Strauss, E., and Peled, E. (2000). Study of phase changes during 500 full cycles of Li/composite polymer electrolyte/FeS_2 battery. *Electrochim. Acta* 45, 1519–1525 doi: 10.1016/S0013-4686(99)00368-0

Sun, C., Li, Y., Jin, J., Yang, J., and Wen, Z. (2019). ZnO nanoarray-modified nickel foam as a lithiophilic skeleton to regulate lithium deposition for lithium-metal batteries. *J. Mater. Chem. A* 7, 7752–7759. doi: 10.1039/C9TA00862D

Thomas, B., Cibik, T., Höpfner, C., Diesner, K., Ehlers, G., Fiechter, S., et al. (1998). Formation of secondary iron-sulphur phases during the growth of polycrystalline iron pyrite (FeS_2) thin films by MOCVD. *J. Mater. Sci. Mater. Electron*. 9, 61–64. doi: 10.1023/A:1008888801424

Ulissi, U., Ito, S., Hosseini, S. M., Varzi, A., Aihara, Y., and Passerini S. (2018). High capacity all-solid-state lithium batteries enabled by pyrite-sulfur composites. *Adv. Energy Mater*. 8:1801462. doi: 10.1002/aenm.201801462

Wesolowski, D. E., and Papenguth, H. W. (2010). "Study of cell performance in long-life thermal battery design space," in *44th Power Sources Conference* (Las Vegas, NV), 14–17.

Wu, Z., Sun, L., and Wang, J. (2018). Progresses on the optimal processing and properties of highly porous rare earth silicate thermal insulators. *J. Korean Ceram. Soc*. 55, 527–555. doi: 10.4191/kcers.2018.55.6.12

Yang, Z., Liu, X., Feng, X., Cui, Y., and Yang, X. (2014). Hydrothermal synthesized micro/nano-sized pyrite usedas cathode material to improve the electrochemical performance of thermal battery. *J. Appl. Electrochem*. 44, 1075–1080. doi: 10.1007/s10800-014-0724-9

Conflict of Interest: The authors declare that the research was conducted in the absence of any commercial or financial relationships that could be construed as a potential conflict of interest.

frontiers in Chemistry

ORIGINAL RESEARCH
published: 15 April 2020
doi: 10.3389/fchem.2020.00283

Enhanced Low-Temperature Hydrogen Storage in Nanoporous Ni-Based Alloy Supported $LiBH_4$

Xi Chen, Zhao Li, Yue Zhang, Dongming Liu, Chunyang Wang, Yongtao Li, Tingzhi Si and Qingan Zhang*

School of Materials Science and Engineering, Anhui University of Technology, Maanshan, China

To reveal the synergistic effect of nanoconfinement and metallic catalysis on the hydrogen storage properties of $LiBH_4$, the nanoporous Ni-based alloy (np-Ni) was prepared herein by dealloying of the $Mn_{70}Ni_{30}$ alloy in $(NH_4)_2SO_4$ solution, and then $LiBH_4$ was loaded into np-Ni to construct the $LiBH_4$/np-Ni hydrogen storage system using wet impregnation. It was found that dehydrogenation of the $LiBH_4$/np-Ni (1:5) system starts at around 70°C and ends before 400°C, with ~11.9 wt.% of hydrogen desorbed. The apparent dehydrogenation activation energy for the $LiBH_4$/np-Ni (1:5) system was remarkable decreased to about 11.4 kJ/mol. After rehydrogenation at 450°C under 8 MPa hydrogen pressure, ~8.2 wt.% of hydrogen can be released from about 60°C upon second dehydrogenation. These obtained results would provide an efficient strategy for improving the hydrogen storage properties of other metal borohydrides.

Keywords: hydrogen storage, lithium borohydride, nanoporous metal, nanoconfinement, catalysis

OPEN ACCESS

Edited by:
Guanglin Xia,
Fudan University, China

Reviewed by:
Teng He,
Chinese Academy of Sciences, China
Hailiang Chu,
Guilin University of Electronic Technology, China

****Correspondence:***
Dongming Liu
ldm_ahut@163.com

Specialty section:
This article was submitted to Nanoscience, a section of the journal Frontiers in Chemistry

Received: *14 February 2020*
Accepted: *23 March 2020*
Published: *15 April 2020*

Citation:
Chen X, Li Z, Zhang Y, Liu D, Wang C, Li Y, Si T and Zhang Q (2020) Enhanced Low-Temperature Hydrogen Storage in Nanoporous Ni-Based Alloy Supported $LiBH_4$. Front. Chem. 8:283. doi: 10.3389/fchem.2020.00283

INTRODUCTION

Nowadays, the issue of energy shortage has been called into public focus. Hydrogen is considered to be the most ideal secondary source because of its high calorific value, low environmental impact and abundant resources (Abe et al., 2019). To meet the need of storing hydrogen with high efficiency and safety, it is necessary to develop hydrogen storage materials with high mass and volume hydrogen density (Yang et al., 2010; Li H. W. et al., 2011; Abdalla et al., 2018). $LiBH_4$ has attracted much more attention due to its extremely high theoretical hydrogen storage capacity of 18.5 wt.%. However, the elevated dehydrogenation temperature, complicated dehydrogenation behavior and poor reversibility limit its practical applications (Züttel et al., 2003; Orimo et al., 2005; Mauron et al., 2008; Li C. et al., 2011). In order to overcome these deficiencies, the strategies of constructing reactive hydride system (Liu D. M. et al., 2013; Liu et al., 2015, 2016; Ding et al., 2019), cation/anion substitution (Yin et al., 2008; Fang et al., 2011), adding catalyst (Zhang et al., 2017; Cai et al., 2018) and nanoconfinement (Guo et al., 2017; Xu et al., 2017; Meng et al., 2018) were developed in the last decade.

Nanoconfinement of $LiBH_4$ in nanoporous material can maintain the particle within a nanoscale structure, which is exceedingly beneficial to enlarge the reaction interface and shorten the element diffusion distance, thus significantly enhancing the de-/rehydrogenation properties (Ngene et al., 2010b; Shao et al., 2015; Meng et al., 2018; Gasnier et al., 2019). For example, Zhang et al. found that $LiBH_4$ nanoparticles supported by disordered mesoporous carbon (CMK-3) showed a single dehydrogenation peak at about 332°C and a large dehydrogenation amount of 14 wt.% below 600°C (Zhang et al., 2007). Fang et al. embedded $LiBH_4$ into active carbon (AC) by chemical impregnation.

Due to the enhancement of both the thermodynamic and kinetic properties, the $LiBH_4$/AC system began to release hydrogen at 220°C, which is 150°C lower than bulk $LiBH_4$ without nanostructure modulation (Fang et al., 2008b). Other nanoporous material scaffolds, such as carbon aerogel (Zhao et al., 2014; Surrey et al., 2016), ordered mesoporous carbon (Cai et al., 2016), metallic organic framework (MOFs) (Sun et al., 2011) and mesoporous silicon dioxide (SBA-15) (Ngene et al., 2010a), were also used as the confinement carriers to support $LiBH_4$.

However, the above reported nanoconfinement carriers are composed of non-metallic material that can only provide a single nanoconfinement role for $LiBH_4$ in general. Taking into account that transition metal elements (e.g., Ni and Co) can serve as the active catalyst in improving the hydrogen storage properties of complex hydrides owing to their high electronegativity0 (Ngene et al., 2011; Liu et al., 2018; Zhang et al., 2018), a synergistic effect of nanoconfinement and catalysis would be achieved by confining $LiBH_4$ in nanoporous transition metal. Based on this consideration, nanoporous Ni-based alloy was prepared by dealloying of the $Mn_{70}Ni_{30}$ alloy and then used as the carrier to support $LiBH_4$ in this work, and a significantly improved low-temperature hydrogen storage in $LiBH_4$ was successfully obtained.

EXPERIMENTAL SECTION

Sample Preparation

Commercial $LiBH_4$ powder (95%, Alfa Aesar), Mn bulk (99.5%, Alfa Aesar), Ni sheet (99.5%, Alfa Aesar) and tetrahydrofuran (THF) (99.8%, anhydrous, Alfa Aesar) were used in experiments. The $Mn_{70}Ni_{30}$ alloy was prepared by induction melting of appropriate amounts of Mn and Ni metals. For compensating the loss of Mn during melting, the extra 3 wt.% of Mn was added on the basis of stoichiometric amount. The as-cast $Mn_{70}Ni_{30}$ alloy was mechanically crushed into powders of 200 mesh, and the nanoporous Ni-based alloy (denoted as np-Ni) was prepared by dealloying of the $Mn_{70}Ni_{30}$ alloy powders in 1 mol/L $(NH_4)_2SO_4$ solution at 50°C for 2 h. The $LiBH_4$/np-Ni (1:5) system was prepared by loading $LiBH_4$ into np-Ni using wet impregnation method. Firstly, $LiBH_4$ was dissolved in anhydrous THF. Then, np-Ni was put in the $LiBH_4$ solution according to the $LiBH_4$/np-Ni weight ratio of 1:5. Finally, the mixture was evacuated for 24 h to remove THF solvent.

Sample Characterization

De-/rehydrogenation properties were examined based on the volumetric method by using a carefully calibrated Sieverts-type apparatus. Thermal dehydrogenation was performed by heating the sample from ambient temperature to 500°C at a rate of 2°C/min. Isothermal dehydogenation was performed by quickly heating and then keeping the sample at a given temperature. The hydrogen back pressure for the above temperature ramp and isothermal dehydrogenation examinations was below 0.1 MPa. Isothermal rehydrogenation was carried out at 450°C under 8 MPa hydrogen pressure. The weight of np-Ni was not taken into account in calculating the hydrogen de-/absorption amounts.

X-ray diffraction (XRD) measurement was performed by a Rigaku D/Max 2500VL/PC diffractometer at 50 kV and 200 mA with Cu Kα radiation. A special Ar-filled holder was applied to seal the XRD sample to avoid contact with air in the course of measurement. To quantitatively investigate the phase structure change of the $Mn_{70}Ni_{30}$ alloy before and after dealloying, the XRD profiles were analyzed with the Rietveld refinement program RIETAN-2000 (Izumi and Ikeda, 2000). Scanning electron microscopy (SEM) was carried out using a Nova NanoSEM 430 microscope equipped with an energy dispersive X-ray spectrometer (EDS). Transmission electron microscopy (TEM) observation was performed on a JEM-2100F instrument. Pore size distribution, pore volume and specific surface area were determined by a Micromeritics ASAP 2020 fully-automatic analyzer based on the Brunauer–Emmett–Teller (BET) and Barrett–Joyner–Halenda (BJH) methods (Lowell et al., 2004). Fourier transform infrared (FTIR) spectrum was collected using a Nicolet 6700 FTIR spectrometer.

RESULTS AND DISCUSSION

Structural Analysis of $LiBH_4$/np-Ni System

Figure 1 gives the observed XRD patterns and the Rietveld analysis results of $Mn_{70}Ni_{30}$ alloy before and after dealloying, and the phase abundances and structural parameters refined by

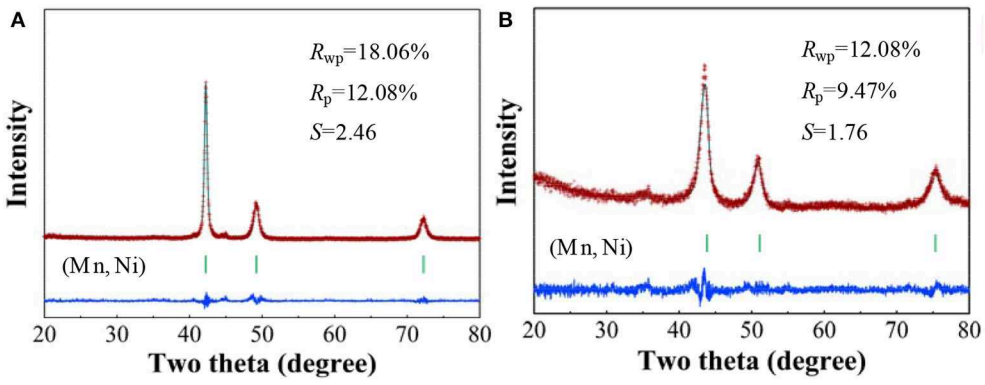

FIGURE 1 | Rietveld refinements of the observed XRD patterns for $Mn_{70}Ni_{30}$ alloy **(A)** before and **(B)** after dealloying.

the Rietveld analysis are listed in **Table 1**. It can be seen that the $Mn_{70}Ni_{30}$ alloy before and after dealloying are both composed of a single phase of (Mn, Ni) solid solution with a Cu-type structure. However, the XRD peaks of np-Ni are relatively broadened and move toward higher angle as compared with the $Mn_{70}Ni_{30}$ alloy. The results indicate that the grain size and cell parameters of the sample were both decreased with the extraction of Mn atom from (Mn, Ni) solid solution upon dealloying due to that Mn has a larger atomic radius relative to Ni.

TABLE 1 | Phase components and structural parameters of $Mn_{70}Ni_{30}$ alloy and np-Ni.

Sample	Phase	Space group	Lattice parameters (Å)			Abundance (%)
			a	*b*	*c*	
$Mn_{70}Ni_{30}$ alloy	(Mn, Ni)	*Fm-3m*	3.6907(2)	3.6907(2)	3.6907(2)	100
np-Ni	(Mn, Ni)	*Fm-3m*	3.5601(1)	3.5601(1)	3.5601(1)	100

Figure 2 presents the SEM images and corresponding EDS spectra of $Mn_{70}Ni_{30}$ alloy and np-Ni. As seen from **Figure 2A**, the $Mn_{70}Ni_{30}$ alloy has a smooth surface with a particle size of about ~70 μm. The EDS result (see **Figure 2C**) indicates that it consists of 70.22 at.% Mn and 29.78 at.% Ni, agreeing well with its nominal element composition. For np-Ni, as given in **Figure 2D**, the element content of Mn is decreased to 21.09 at.%. It is reasonably considered that the massive lixiviation of Mn atom can bring large lattice distortion and physical shrinkage stress, thus leading to the formation of a nanoporous structure as shown in **Figure 2B**.

Figure 3A demonstrates the N_2 adsorption/desorption isotherms for np-Ni and the $LiBH_4$/np-Ni (1:5) system. It can be seen that np-Ni has a typical IV-type adsorption isotherm with an obvious hysteresis loop. Those are the characteristics of mesoporous material. In comparison, the hysteresis loop has almost disappeared for the $LiBH_4$/np-Ni (1:5) system. The pore size distributions of np-Ni and the $LiBH_4$/np-Ni (1:5) system are compared in **Figure 3B**, which indicates that the peak in pore size distribution of np-Ni moves to a lower position with

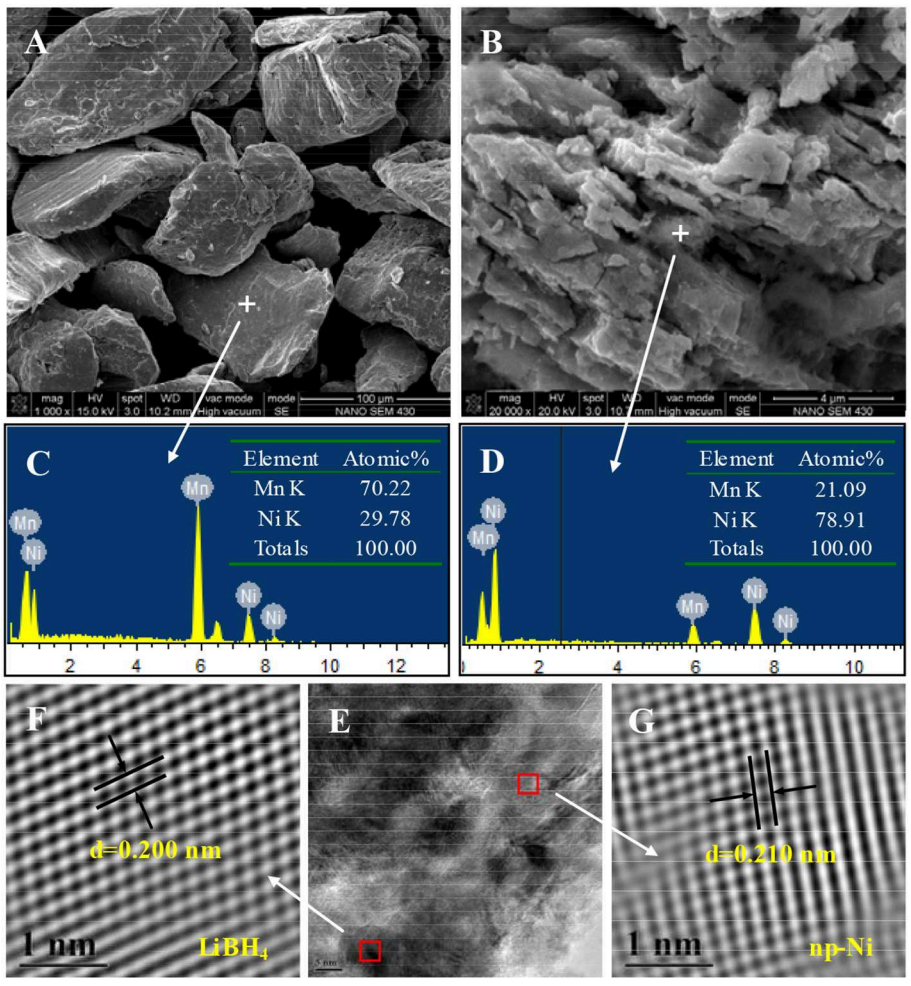

FIGURE 2 | SEM images and EDS spectra of **(A,C)** $Mn_{70}Ni_{30}$ alloy and **(B,D)** np-Ni; **(E)** TEM micrograph of the $LiBH_4$/np-Ni (1:5) system and **(F,G)** atomic lattice images of the square regions in **(E)**.

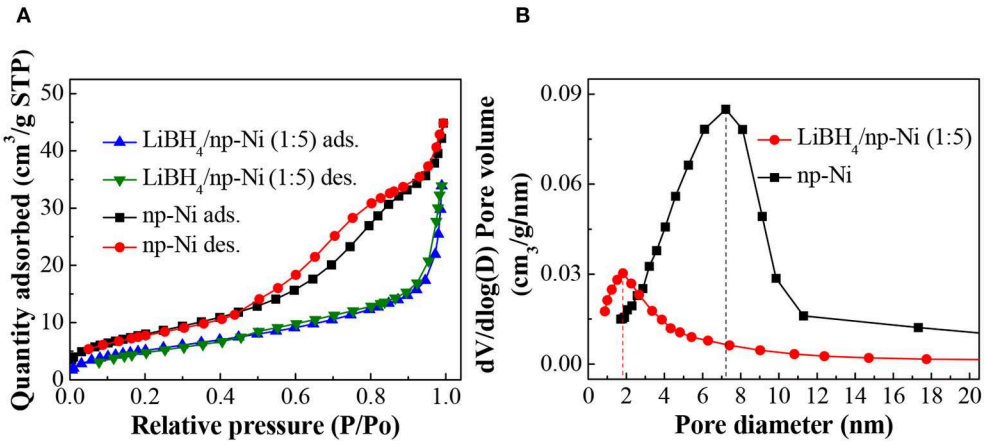

FIGURE 3 | (A) N_2 adsorption/desorption isotherms and **(B)** pore size distributions of np-Ni and the $LiBH_4$/np-Ni (1:5) system.

TABLE 2 | Pore parameters and specific surface area of np-Ni and the $LiBH_4$/np-Ni (1:5) system.

Sample	Pore size (nm)	Pore volume (cm^3/g)	Specific surface area (m^2/g)
np-Ni	7.21	0.0586	155
$LiBH_4$/np-Ni	1.80	0.0339	17

an intensive decline in intensity after supporting $LiBH_4$. **Table 2** gives the pore parameters and specific surface area of np-Ni and the $LiBH_4$/np-Ni (1:5) system. It is observed that np-Ni has the pore diameter, pore volume and specific surface area of 7.21 nm, 0.0586 cm^3/g and 155 m^2/g, respectively. However, those values reduce to 1.80 nm, 0.0339 cm^3/g and 17 m^2/g, respectively, for the $LiBH_4$/np-Ni (1:5) system. These results imply that $LiBH_4$ was loaded on the surface and impregnated into the pores of np-Ni. **Figure 2E** gives the TEM micrograph of the $LiBH_4$/np-Ni (1:5) system, and **Figures 2F,G** present the atomic lattice images of the square regions in **Figure 2E** obtained by inverse fast Fourier transform (IFFT). The fringe spacings of 0.200 nm in **Figure 2F** and 0.210 nm in **Figure 2G** correspond to (121) plane of $LiBH_4$ and (111) plane of Ni, respectively. The TEM results reveal that $LiBH_4$ and np-Ni indeed co-existed in the sample.

Thermal Dehydrogenation Characteristics of $LiBH_4$/np-Ni System

Figure 4 shows the temperature-programmed dehydrogenation curves of the $LiBH_4$/np-Ni (1:5) system and pristine $LiBH_4$. It can be seen that hydrogen release from the $LiBH_4$/np-Ni (1:5) system initiates at about 70°C and ends before 400°C, with ∼11.9 wt.% of hydrogen desorbed. In contrast, the starting dehydrogenation temperature is as high as 330°C for pristine $LiBH_4$, and only 3.5 wt.% of hydrogen can be released when heating to 500°C. Evidently, the thermal dehydrogenation stability of $LiBH_4$ was notably reduced by np-Ni. In addition, **Table 3** compares the dehydrogenation temperature of $LiBH_4$ supported on different

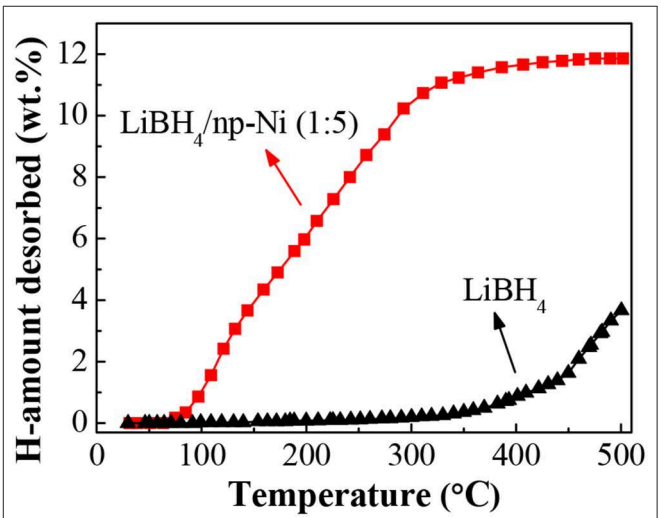

FIGURE 4 | Hydrogen desorption curves of the $LiBH_4$/np-Ni (1:5) system and pristine $LiBH_4$.

carriers. It is observed that the present $LiBH_4$/np-Ni (1:5) system has lower starting and ending dehydrogenation temperatures as compared with the reported $LiBH_4$-based supporting systems. In other words, np-Ni can provide a stronger destabilization effect on $LiBH_4$ relative to other carriers due to its synergistic effect of nanoconfinement and metallic catalysis. On the one hand, nanoconfinement of $LiBH_4$ in np-Ni can decrease the particle size to nanoscale level, which is very helpful to facilitate the dehydrogenation by enlarging the reaction interface and shortening the element diffusion distance. On the other hand, Ni itself can act as the dehydrogenation catalyst for $LiBH_4$ by enhancing charge donation ability of Li atom to BH_4 unit and thus weakening the B–H bond due to its high electronegativity.

To further monitor the dehydrogenation process, **Figure 5** gives the FTIR spectra of $LiBH_4$/np-Ni (1:5) systems after dehydrogenation at different temperatures. As can be seen

TABLE 3 | Hydrogen desorption temperature of $LiBH_4$ with different carriers.

Carriers	Starting temperature (°C)	Ending temperature (°C)	References
$ZnO/ZnCo_2O_4$	169	<500	Xu et al., 2017
CMK-3	220	<600	Zhang et al., 2007
Carbon aerogels@CoNiB	192	600	Zhao et al., 2014
SBA-15	150	>500	Ngene et al., 2010a
Single-walled carbon nanotubes	270	550	Fang et al., 2008a
Carbon nanotubes	250	<600	Yu et al., 2007
Nanoporous carbon	220	420	Liu et al., 2010
Nanoscale SiO_2	200	500	Chen et al., 2010
np-Ni	70	400	This work

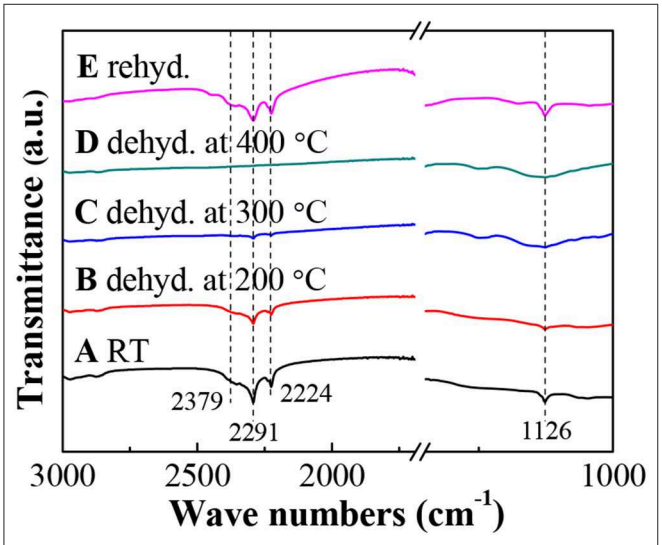

FIGURE 5 | FTIR spectra of the $LiBH_4$/np-Ni (1:5) system dehydrogenated at different temperatures and rehydrogenated.

in **Figure 5**A, the obvious characteristic bands for B–H bond vibrations located at 2,379, 2,291, 2,224 and 1,126 cm^{-1} (Zhang et al., 2011) confirm the existence of $LiBH_4$. With increasing the dehydrogenation temperature, the band intensity of B–H bond vibrations decreases gradually, indicating a continuous consumption of $LiBH_4$. Moreover, almost no FTIR bands can be observed in **Figure 5**D, which means that $LiBH_4$ was almost completely decomposed at 400°C. This result is in good agreement with the dehydrogenation phenomenon shown in **Figure 4**.

Dehydrogenation Kinetics of $LiBH_4$/np-Ni Systetm

Figure 6A presents the isothermal dehydrogenation curves of the $LiBH_4$/np-Ni (1:5) system at the temperatures of 250, 300, and 350°C, respectively. It is observed that the dehydrogenation rate increases as the temperature rises. For example, the amounts of hydrogen desorbed within 5 min are 7.3, 9.4, and 10.4 wt.% at 250, 300, and 350°C, respectively. In order to further reveal the dehydrogenation mechanism, the experimental dehydrogenation data were fitted by the kinetic modeling of $g(\alpha) = \int d\alpha/f(\alpha) = kt$, where α is the reacted fraction at time t, $g(\alpha)$ and $f(\alpha)$ are the functions representing different reaction mechanisms, and k is the rate constant (Li Y. et al., 2011; Liu D. M. et al., 2013). As the result, the function of -ln(1-α) gives the best linearity (see **Figure 6B**) over a broader α range for each measurement with the correlation coefficient of R^2 >0.99. This result indicates that dehydrogenation of the $LiBH_4$/np-Ni (1:5) system follows the first-order mechanism in the investigated temperature range.

According to the slope of the fitted straight line in **Figure 6B**, the k value at different temperatures can be obtained. Then the apparent activation energy for hydrogen desorption (E_a) can be determined based on the Arrhenius equation of $k = k_0 \cdot \exp[-E_a/(RT)]$, where k_0 is the pre-exponential factor, R is the gas constant, and T is the temperature. **Figure 6C** gives the Arrhenius plot for the $LiBH_4$/np-Ni (1:5) system. From the slope ($-E_a/R$) of the fitted straight line, E_a was calculated to be 11.4 kJ/mol. As reported in the literatures that E_a for $LiBH_4$ supported on CMK-3 and carbon aerogels@CoNiB are 40 and 46.39 kJ/mol, respectively (Zhang et al., 2007; Zhao et al., 2014). The lower E_a value for the present $LiBH_4$/np-Ni (1:5) system is originating from the synergistic effect of nanoconfinement and metallic catalysis of np-Ni, and can be regarded as one of the most important reasons for the enhanced dehydrogenation properties shown in **Figures 4**, **6A**. Moreover, the preparation process of np-Ni carrier for $LiBH_4$ by dealloying method is far more convenient than that of CMK-3 based on template method.

Rehydrogenation Characteristics of $LiBH_4$/np-Ni System

The dehydrogenated residue of the $LiBH_4$/np-Ni (1:5) system was subjected to rehydrogenation, and **Figure 7** demonstrates the isothermal rehydrogenation curve. It is observed that the $LiBH_4$/np-Ni (1:5) system can readily reabsorb 8.3 wt.% of hydrogen at 450°C under 8 MPa hydrogen pressure. The FTIR spectrum for the rehydrogenated product shown in **Figure 5**E suggests that $LiBH_4$ was regenerated. The inset of **Figure 7** gives the second hydrogen desorption curve of the $LiBH_4$/np-Ni (1:5) system. It can be seen that ∼8.2 wt.% of hydrogen can be released during the second dehydrogenation process. Note that the starting dehydrogenation temperature keeps in a low value of about 60°C. The result indicates undoubtedly that the synergistic effect of nanoconfinement and metallic catalysis of np-Ni maintains well upon repeated dehydrogenation/hydrogenation.

CONCLUSIONS

In order to improve the hydrogen storage properties of $LiBH_4$, the nanoporous Ni-based alloy was prepared by dealloying of the precursor $Mn_{70}Ni_{30}$ alloy and then used as the carrier to support $LiBH_4$ by wet impregnation method. It was found that the constructed $LiBH_4$/np-Ni (1:5) system can release ∼11.9

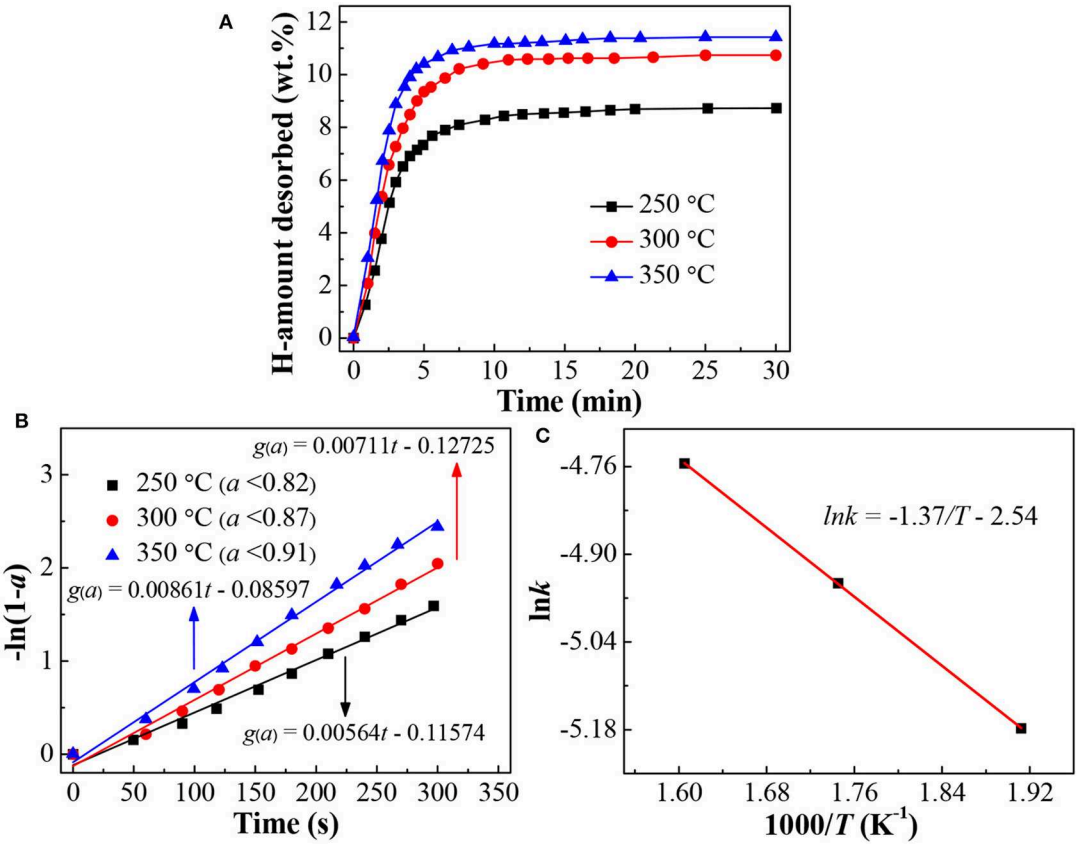

FIGURE 6 | (A) Isothermal dehydrogenation curves, **(B)** Plots of -ln(1-*a*) vs. *t* at different temperatures, and **(C)** Arrhenius plot for the dehydrogenation of the $LiBH_4$/np-Ni (1:5) system.

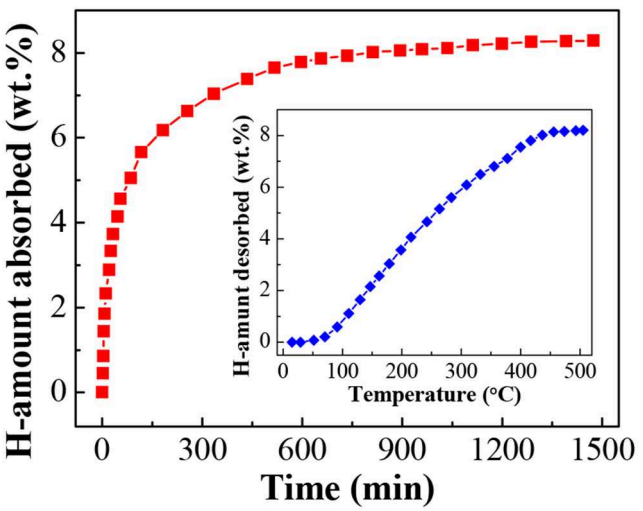

FIGURE 7 | Isothermal rehydrogenation curve of the $LiBH_4$/np-Ni (1:5) system. Inset shows the second hydrogen desorption curve.

wt.% of hydrogen with the starting and ending dehydrogenation temperatures as low as about 70 and 400°C, respectively. Due to the synergistic effect of nanoconfinement and metallic catalysis of nanoporous Ni-based alloy, the apparent dehydrogenation activation energy of $LiBH_4$ was remarkable decreased to about 11.4 kJ/mol. The dehydrogenated residue can readily absorb hydrogen to regenerate $LiBH_4$ at 450°C under 8 MPa hydrogen pressure. Moreover, the starting dehydrogenation temperature keeps in a low value of about 60°C during the second dehydrogenation process.

DATA AVAILABILITY STATEMENT

All datasets generated for this study are included in the article.

AUTHOR CONTRIBUTIONS

XC and DL contributed conception and design of the study. XC and YZ were in charge of the analysis of data. ZL and CW prepared samples and performed characterization. All authors contributed to manuscript revision, read, and approved the submitted version.

FUNDING

This work was supported by the National Natural Science Foundation of China (Nos. U1503192 and 51371008).

REFERENCES

Abdalla, A. M., Hossain, S., Nisfindy, O. B., Azad, A. T., Dawood, M., and Azad,. A. K. (2018). Hydrogen production, storage, transportation and key challenges with applications: a review. *Energ. Convers. Manage.* 165, 602–627. doi: 10.1016/j.enconman.2018.03.088

Abe, J. O., Popoola, A. P. I., Ajenifuja, E., and Popoola, O. M. (2019). Hydrogen energy, economy and storage: review and recommendation. *Inter. J. Hydr. Energy* 44, 15072–15086. doi: 10.1016/j.ijhydene.2019.04.068

Cai, R., Sun, L. X., Xu, F., Zou, Y. J., and Chu, H. L. (2016). $LiBH_4$ confined in nitrogen-doped ordered mesoporous carbons for hydrogen storage. *Mater. Sci. Forum* 852, 858–863. doi: 10.4028/www.scientific.net/MSF.852.858

Cai, W., Hou, J., Tao, P., and Yang, Y. (2018). An insight into the dehydrogenation behaviour of $LiBH_4$ exhibiting remarkable kinetics enhanced by nanostructured h-BN. *J. Alloy Compd.* 750, 443–450. doi: 10.1016/j.jallcom.2018.04.022

Chen, X. Y., Guo, Y. H., Gao, L., and Yu, X. B. (2010). Improved dehydrogenation of $LiBH_4$ supported on nanoscale SiO_2 via liquid phase method. *J. Mater. Res.* 25, 2415–2421. doi: 10.1557/JMR.2010.0301

Ding, Z., Wu, P., and Shaw, L. (2019). Solid-state hydrogen desorption of $2MgH_2 + LiBH_4$ nano-mixture: a kinetics mechanism study. *J. Alloy Compd.* 806, 350–360. doi: 10.1016/j.jallcom.2019.07.218

Fang, Z. Z., Kang, X. D., Wang, P., and Cheng, H. M. (2008a). Improved reversible dehydrogenation of lithium borohydride by milling with as-prepared single-walled carbon nanotubes. *J. Phys. Chem. C* 112, 17023–17029. doi: 10.1021/jp803916k

Fang, Z. Z., Kang, X. D., Yang, Z. X., Walker, G. S., and Wang, P. (2011). Combined effects of functional cation and anion on the reversible dehydrogenation of $LiBH_4$. *J. Phys. Chem. C* 115, 11839–11845. doi: 10.1021/jp200137n

Fang, Z. Z., Wang, P., Rufford, T. E., Kang, X. D., Lu, G. Q., and Cheng, H. M. (2008b). Kinetic- and thermodynamic-based improvements of lithium borohydride incorporated into activated carbon. *Acta Mater.* 56, 6257–6263. doi: 10.1016/j.actamat.2008.08.033

Gasnier, A., Luguet, M., Pereira, A. G., Troiani, H., Zampieri, G., and Gennari, F. C. (2019). Entanglement of N-doped graphene in resorcinol-formaldehyde: Effect over nanoconfined $LiBH_4$ for hydrogen storage. *Carbon* 147, 284–294. doi: 10.1016/j.carbon.2019.02.090

Guo, L., Li, Y., Ma, Y., Liu, Y., Peng, D., Zhang, L., et al. (2017). Enhanced hydrogen storage capacity and reversibility of $LiBH_4$ encapsulated in carbon nanocages. *Inter. J. Hydr. Energy* 42, 2215–2222. doi: 10.1016/j.ijhydene.2016.11.184

Izumi, F., and Ikeda, T. (2000). A rietveld-analysis programm RIETAN-98 and its applications to zeolites. *Mater. Sci. Forum* 321–324, 198–205. doi: 10.4028/www.scientific.net/MSF.321-324.198

Li, C., Peng, P., Zhou, D. W., and Wan, L. (2011). Research progress in $LiBH_4$ for hydrogen storage: a review. *Inter. J. Hydrogen Energy* 36, 14512–14526. doi: 10.1016/j.ijhydene.2011.08.030

Li, H. W., Yan, Y. G., Orimo, S., Züttel, A., and Jensen, C. M. (2011). Recent progress in metal borohydrides for hydrogen storage. *Energies* 4, 185–214. doi: 10.3390/en4010185

Li, Y., Zhou, G., Fang, F., Yu, X., Zhang, Q., Ouyang, L., et al. (2011). De-/re-hydrogenation features of $NaAlH_4$ confined exclusively in nanopores. *Acta Mater.* 59, 1829–1838. doi: 10.1016/j.actamat.2010.11.049

Liu, D. M., Huang, W. J., Si, T. Z., and Zhang, Q. A. (2013). Hydrogen storage properties of $LiBH_4$ destabilized by SrH_2. *J. Alloy Compd.* 551, 8–11. doi: 10.1016/j.jallcom.2012.09.138

Liu, D. M., Tan, Q. J., Gao, C., Sun, T., and Li, Y. T. (2015). Reversible hydrogen storage properties of $LiBH_4$ combined with hydrogenated $Mg_{11}CeNi$ alloy. *Inter. J. Hydr. Energy* 40, 6600–6605. doi: 10.1016/j.ijhydene.2015.03.130

Liu, H., Wang, X., Zhou, H., Gao, S., Ge, H., Li, S., et al. (2016). Improved hydrogen desorption properties of $LiBH_4$ by AlH_3 addition. *Inter. J. Hydrogen Energy* 41, 22118–22127. doi: 10.1016/j.ijhydene.2016.09.177

Liu, X. F., Peaslee, D., Jost, C. Z., and Majzoub, E. H. (2010). Controlling the decomposition pathway of $LiBH_4$ via confinement in highly ordered nanoporous carbon. *J. Phys. Chem. C* 114, 14036–14041. doi: 10.1021/jp1055045

Liu, Y., Heere, M., Vasquez, L. C., Paterakis, C., Sørby, M. H., Hauback, B. C., et al. (2018). Dehydrogenation and rehydrogenation of a $0.62LiBH_4$-$0.38NaBH_4$ mixture with nano-sized Ni. *Inter. J. Hydrogen Energy* 43, 16782–16792. doi: 10.1016/j.ijhydene.2018.04.211

Lowell, S., Shields, J. E., Thomas, M. A., and Thommes, M. (2004). *Characterization of Porous Solids and Powders: Surface Area, Pore Size and Density*. Dordrecht: Springer.

Mauron, P., Buchter, F., Friedrichs, O., Remhof, A., Bielmann, M., Zwicky, C. N., et al. (2008). Stability and reversibility of $LiBH_4$. *J. Phys. Chem. B* 112, 906–910. doi: 10.1021/jp077572r

Meng, X., Wan, C., Wang, Y., and Ju, X. (2018). Porous Ni@C derived from bimetallic metal-organic frameworks and its application for improving $LiBH_4$ dehydrogenation. *J. Alloy Compd.* 735, 1637–1647. doi: 10.1016/j.jallcom.2017.11.191

Ngene, P., Adelhelm, P., Beale, A. M., de Jong, K. P., and de Jong, P. E. (2010a). $LiBH_4$/SBA-15 nanocomposites prepared by melt infiltration under hydrogen pressure: synthesis and hydrogen sorption properties. *J. Phys. Chem. C* 114, 6163–6168. doi: 10.1021/jp9065949

Ngene, P., van Zwienen, M. R., and de Jongh, P. E. (2010b). Reversibility of the hydrogen desorption from $LiBH_4$: a synergetic effect of nanoconfinement and Ni addition. *Chem. Commun.* 46, 8201–8203. doi: 10.1039/c0cc03218b

Ngene, P., Verkuijlen, M. H., Zheng, Q., Kragten, J., Bentum, P. J. M., Bitter, J. H., et al. (2011). The role of Ni in increasing the reversibility of the hydrogen release from nanoconfined $LiBH_4$. *Faraday Discuss.* 151, 47–58. doi: 10.1039/C0FD00028K

Orimo, S., Nakamori, Y., Kitahara, G., Miwa, K., Ohba, N., Towata, S., et al. (2005). Dehydriding and rehydriding reactions of $LiBH_4$. *J. Alloy Compd.* 404, 427–430. doi: 10.1016/j.jallcom.2004.10.091

Shao, J., Xiao, X., Fan, X., Huang, X., Zhai, B., Li, S., et al. (2015). Enhanced hydrogen storage capacity and reversibility of $LiBH_4$ nanoconfined in the densified zeolite-templated carbon with high mechanical stability. *Nano Energy* 15, 244–255. doi: 10.1016/j.nanoen.2015.04.023

Sun, W. W., Li, S. F., Mao, J. F., Guo, Z. P., Liu, H. K., Dou, S. X., et al. (2011). Nanoconfinement of lithium borohydride in Cu-MOFs towards low temperature dehydrogenation. *Dalton Trans.* 40, 5673–5676. doi: 10.1039/c0dt01727b

Surrey, A., Minella, C. B., Fechler, N., Antonietti, M., Grafe, H. J., Schultz, L., et al. (2016). Improved hydrogen storage properties of $LiBH_4$ via nanoconfinement in micro-and mesoporous aerogel-like carbon. *Inter. J. Hydr. Energy* 41, 5540–5548. doi: 10.1016/j.ijhydene.2016.01.163

Xu, X. H., Zang, L., Zhao, Y. R., Zhao, Y., Wang, Y. J., and Jiao, L. F. (2017). Hydrogen storage behavior of $LiBH_4$ improved by the confinement of hierarchical porous $ZnO/ZnCo_2O_4$ nanoparticles. *J. Power Sources* 359, 134–141. doi: 10.1016/j.jpowsour.2017.05.047

Yang, J., Sudik, A., Wolverton, C., and Siegel, D. J. (2010). High capacity hydrogen storage materials: attributes for automotive applications and techniques for materials discovery. *Chem. Soc. Rev.* 39, 656–675. doi: 10.1039/b802882f

Yin, L., Wang, P., Fang, Z., and Cheng, H. (2008). Thermodynamically tuning $LiBH_4$ by fluorine anion doping for hydrogen storage: a density functional study. *Chem. Phys. Lett.* 450, 318–321. doi: 10.1016/j.cplett.2007.11.060

Yu, X. B., Wu, Z., Chen, Q. R., Li, Z. L., Weng, B. C., and Huang, T. S. (2007). Improved hydrogen storage properties of $LiBH_4$ destabilized by carbon. *Appl. Phys. Lett.* 90:034106. doi: 10.1063/1.2432240

Zhang, B. J., Liu, B. H., and Li, Z. P. (2011). Destabilization of $LiBH_4$ by $(Ce, La)(Cl, F)_3$ for hydrogen storage. *J. Alloy Compd.* 509, 751–757. doi: 10.1016/j.jallcom.2010.09.066

Zhang, L., Zheng, J., Xiao, X., Wang, X., Huang, X., Liu, M., et al. (2017). A new strategy to remarkably improve the low-temperature reversible hydrogen desorption performances of $LiBH_4$ by compositing with fluorographene. *Inter. J. Hydr. Energy* 42, 20046–20055. doi: 10.1016/j.ijhydene.2017.05.060

Zhang, Y., Liu, Y., Yang, Y., Li, Y., Hu, J., Gao, M., et al. (2018). Superior catalytic activity of in situ reduced metallic Co for hydrogen storage in a $Co(OH)_2$-containing $LiBH_4/2LiNH_2$ composite. *Mater. Res. Bull.* 97, 544–552. doi: 10.1016/j.materresbull.2017.09.037

Zhang, Y., Zhang, W. S., Wang, A. Q., Sun, L. X., Fan, M. Q., Chu, H. L., et al. (2007). $LiBH_4$ nanoparticles supported by disordered mesoporous carbon: Hydrogen storage performances and destabilization mechanisms. *Inter. J. Hydr. Energy* 32, 3976–3980. doi: 10.1016/j.ijhydene.2007.04.010

Zhao, Y. P., Jiao, L. F., Liu, Y. C., Guo, L. J., Li, L., Liu, H. Q., et al. (2014). A synergistic effect between nanoconfinement of carbon aerogels and catalysis of CoNiB nanoparticles on dehydrogenation of $LiBH_4$. *Inter. J. Hydr. Energy* 39, 917–926. doi: 10.1016/j.ijhydene.2013.10.137

Züttel, A., Rentsch, S., Fischer, P., Wenger, P., Sudan, P., Mauron, P.h., et al. (2003). Hydrogen storage properties of $LiBH_4$. *J. Alloy Compd.* 356, 515–520. doi: 10.1016/s0925-8388(02)01253-7

Conflict of Interest: The authors declare that the research was conducted in the absence of any commercial or financial relationships that could be construed as a potential conflict of interest.

frontiers in Chemistry

ORIGINAL RESEARCH
published: 15 April 2020
doi: 10.3389/fchem.2020.00227

Dehydrogenation Performances of Different Al Source Composite Systems of $2LiBH_4 + M$ (M = Al, $LiAlH_4$, Li_3AlH_6)

Yun Li[1,2], *Shaolong Wu*[1]*, *Dongdong Zhu*[3]*, *Jun He*[4], *Xuezhang Xiao*[2] *and Lixin Chen*[2]

[1] School of Mechanical and Electrical Engineering, Quzhou College of Technology, Quzhou, China, [2] Key Laboratory of Advanced Materials and Applications for Batteries of Zhejiang Province, Zhejiang University, Hangzhou, China, [3] School of Mechanical Engineering, Quzhou University, Quzhou, China, [4] Quzhou Special Equipment Inspection Center, Quzhou, China

OPEN ACCESS

Edited by:
Guanglin Xia,
Fudan University, China

Reviewed by:
Jian Zhang,
Changsha University of Science and Technology, China
Hujun Cao,
Chinese Academy of Sciences, China

***Correspondence:**
Shaolong Wu
shanxiliyun2006@163.com
Dongdong Zhu
zhudd8@163.com

Specialty section:
This article was submitted to Inorganic Chemistry, a section of the journal Frontiers in Chemistry

Received: 19 February 2020
Accepted: 10 March 2020
Published: 15 April 2020

Citation:
Li Y, Wu S, Zhu D, He J, Xiao X and Chen L (2020) Dehydrogenation Performances of Different Al Source Composite Systems of $2LiBH_4 + M$ ($M = Al, LiAlH_4, Li_3AlH_6$). Front. Chem. 8:227. doi: 10.3389/fchem.2020.00227

Hydrogen has become a promising energy source due to its efficient and renewable properties. Although promising, hydrogen energy has not been in widespread use due to the lack of high-performance materials for hydrogen storage. Previous studies have shown that the addition of Al-based compounds to $LiBH_4$ can create composites that have good properties for hydrogen storage. In this work, the dehydrogenation performances of different composite systems of $2LiBH_4$+ M (M = Al, $LiAlH_4$, Li_3AlH_6) were investigated. The results show that, under a ball to powder ratio of 25:1 and a rotation speed of 300 rpm, the optimum ball milling time is 50 h for synthesizing Li_3AlH_6 from LiH and $LiAlH_4$. The three studied systems destabilized $LiBH_4$ at relatively low temperatures, and the $2LiBH_4$-Li_3AlH_6 composite demonstrated excellent behavior. Based on the differential scanning calorimetry results, pure $LiBH_4$ released hydrogen at 469°C. The dehydrogenation temperature of $LiBH_4$ is 416°C for $2LiBH_4$-Li_3AlH_6 versus 435°C for $2LiBH_4$-$LiAlH_4$ and 445°C for $2LiBH_4$-Al. The $2LiBH_4$-Li_3AlH_6, $2LiBH_4$-$LiAlH_4$, and $2LiBH_4$-Al samples released 9.1, 8, and 5.7 wt.% of H_2, respectively. Additionally, the $2LiBH_4$-Li_3AlH_6 composite released the 9.1 wt.% H_2 within 150 min. An increase in the kinetics was achieved. From the results, it was concluded that $2LiBH_4$-Li_3AlH_6 exhibits the best dehydrogenation performance. Therefore, the $2LiBH_4$-Li_3AlH_6 composite is considered a promising hydrogen storage material.

Keywords: hydrogen storage materials, $LiBH_4$, composite system, $2LiBH_4$-Li_3AlH_6, dehydrogenation performance

INTRODUCTION

Hydrogen energy has become an ideal new energy resource due to its clean, efficient, and renewable properties (Schlapbach and Zuttel, 2001). Although the use of hydrogen energy is promising, widespread use has been hindered by issues in the advancement of high-performance materials for hydrogen storage (Liu et al., 2010). The complex hydride (Ley et al., 2014) $LiBH_4$, which has

a hydrogen capacity storage of 18.5 wt.%, has drawn extensive attention. $LiBH_4$ decomposes into an intermediate compound $Li_2B_{12}H_{12}$, which generates B and releases H_2 as described in Equation (1) (Orimo et al., 2006).

$$LiBH_4 \rightarrow 1/12Li_2B_{12}H_{12} + 5/6LiH + 13/12H_2 \rightarrow LiH + B + 3/2H_2 \quad (1)$$

However, many factors impede the commercial application of pure $LiBH_4$, such as high dehydrogenation temperature, slow dehydrogenation rate, and poor cycle reversibility (Lodziana and Vegge, 2004). To solve these issues, researchers have concentrated on modifying $LiBH_4$ (Vajo and Olson, 2007) through anion/cation substitution (Fang et al., 2011; Lombardo et al., 2019), catalytic modification (Kou et al., 2012; Huang et al., 2016; Zhai et al., 2016), the combined effect of composites (Vajo et al., 2010; Kou et al., 2012), and the application of the confinement effect of nano-materials (Vajo, 2011; Zhang et al., 2017).

Al and Al-based composites with $LiBH_4$ are of interest. Founded on first-principles calculation, Siegel et al. (2007) predicted that $LiBH_4$ would react with Al to generate AlB_2, LiH, and H_2 at 280°C under a hydrogen pressure of 1 bar. For the $LiAlH_4$-$LiBH_4$ system, Mao et al. (2009) found that the addition of TiF_3 decreased the onset temperatures of H_2 release by 64 and 150°C compared with the undoped system. The decomposition enthalpy values of $LiBH_4$ also reduced to 60.4 kJ/mol. He et al. (2019) studied the dehydrogenation performance of $LiBH_4$/$LiAlH_4$ composite, found that 8.7 wt.% of hydrogen was released at 500°C, and defined a "Li-Al-B-H" compound. Soru et al. (2014) focused on the phase structural transformation of the $LiAlH_4$ + $LiBH_4$ system, which can produce 6.8 wt.% of hydrogen. According to a study by Carrillo-Bucio et al. (2017), a surface-oxidized $2LiBH_4$ + Al composite did not release hydrogen until heated to 400°C under a 3 bar initial backpressure. With the catalytic effect of TiF_3, the mixture obtained 9.3 wt.% of hydrogen release as compared to the 5.8 wt.% of the undoped mixture. In research by Zhang et al. (2018), a combined mixture of MgH_2, $LiBH_4$, and $LiAlH_4$ showed superior performance, starting to release hydrogen at 280°C and maintaining reversibility. In our previous studies (Li et al., 2012), the dehydrogenation temperatures of $2LiBH_4$ + Li_3AlH_6 doped with titanium were decreased by 80 and 50°C, respectively, vs. the undoped system. From the previous studies, it can be summarized that Al can enhance the hydrogen storage performance of $LiBH_4$ to some extent. However, the dehydrogenation behaviors of different Al source composite systems have not been systematically studied. In this work, three Al-based $LiBH_4$ composite systems, $2LiBH_4$-Al, $2LiBH_4$-$LiAlH_4$, and $2LiBH_4$-Li_3AlH_6 were prepared, and the hydrogen storage performance was investigated.

MATERIALS AND METHODS

Table 1 shows the raw materials used in this study. All powders were carefully stored in a glove box (MIKROUNA), in which noble gas was loaded and the oxygen content and water vapor content were kept below 1 ppm. A planetary mill (QM-3SP2) was utilized to prepare the composites.

TABLE 1 | Raw materials used in the study.

Materials	$LiBH_4$	Al	$LiAlH_4$	LiH
Purity (%)	≥95	≥99	≥95	≥98
State	Powder	Powder	Powder	Powder
Supplier	Acros	Sinopharm	Sigma-Aldrich	Sigma-Aldrich

The dehydrogenation properties of the materials were tested with a Sievert-type device. The changes in temperature and pressure over time were recorded. The ideal gas state equation was utilized to calculate the dehydrogenation capacity. Thermal analysis was performed using differential scanning calorimetry (DSC, Netzsch 449C Jupiter) combined with thermogravimetric analysis (TG, QMS 403C). To protect the samples from oxidation, high purity argon gas was added at a flow rate of 50 mL/min. An empty aluminum crucible was used as a reference during analysis. The phase compositions of the samples were determined by X-ray powder diffraction (X'Pert-PRO, PANalytical); its scanning range (2θ) was 15°-80°. A specific sealed device was used to protect samples from being oxidized or damped during analysis. Fourier transform infrared spectroscopy (FTIR, Tensor 27) was employed to detect some amorphous substances with a scanning rate of 30 cm^{-1}/min and a resolution ratio of 0.5 cm^{-1}.

RESULTS AND DISCUSSION

Preparation of Li_3AlH_6 Powder

In this work, Li_3AlH_6 powder was synthesized *in-situ* by ball milling LiH and $LiAlH_4$. Approximately 15 g mixed powder of LiH and $LiAlH_4$ was milled each time with a molar ratio of 2:1, a ball to powder ratio of 25:1, and a milling speed of 300 rpm. To suppress temperature rise in the ball milling, every 30 min was set as an operation cycle, which contained a stop time of 6 min, periodically. After ball milling for 20 h, XRD patterns were obtained and examined to characterize the mixed powder. **Figure 1** shows the XRD results of pure LiH powder, $LiAlH_4$ powder, and the LiH and $LiAlH_4$ powder after ball milling for 20 h. No impurity phases were observed in any of the samples, which indicates that the samples were highly pure and did not oxidize. As shown in **Figure 1C**, a few Li_3AlH_6 diffraction peaks are present, while the rest are of $LiAlH_4$ and LiH. This shows that the synthesis reaction was not completed. Due to long milling time, LiH peaks were much lower than before. The LiH content was lower, and an amorphous structure was formed.

Further ball milling was carried out since the synthesis reaction to Li_3AlH_6 was not completed. The milling samples were taken for XRD analysis after every 10 h. **Figure 2** shows the XRD results of the milled powders after 20, 30, 40, and 50 h. Strong double peaks at 22° and 23° are detected, which are the characteristic peaks of Li_3AlH_6. After ball milling for 30 h, most of the diffraction peaks are Li_3AlH_6; however, some $LiAlH_4$ and

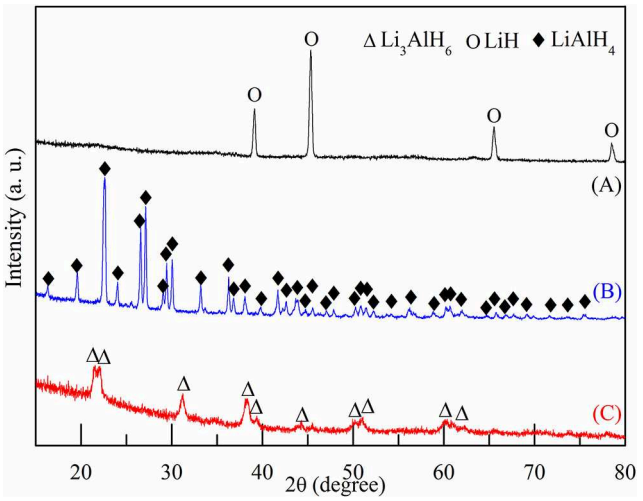

FIGURE 1 | XRD patterns of **(A)** pure LiH, **(B)** pure $LiAlH_4$, and **(C)** mixed powder of LiH and $LiAlH_4$ after ball milling for 20 h.

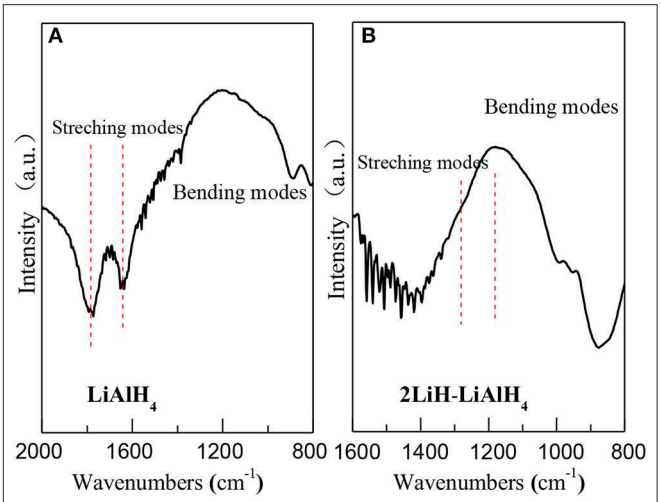

FIGURE 3 | FT-IR spectrums of **(A)** pure $LiAlH_4$ and **(B)** 2LiH-$LiAlH_4$ mixed powder after 50-h ball milling.

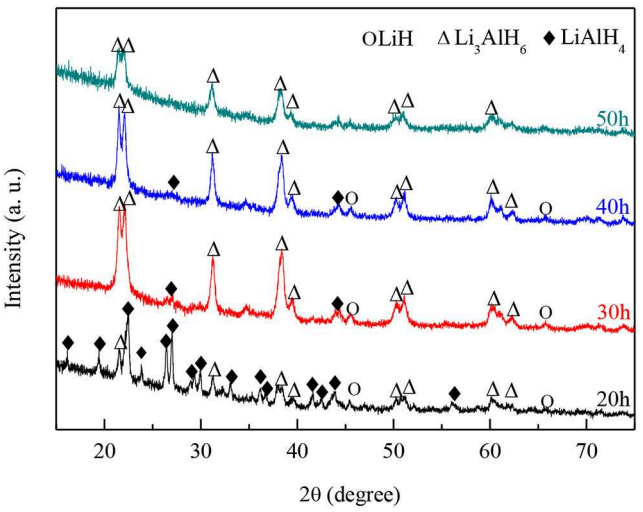

FIGURE 2 | XRD patterns of mixed powder of LiH and $LiAlH_4$ after ball-milling for different numbers of hours.

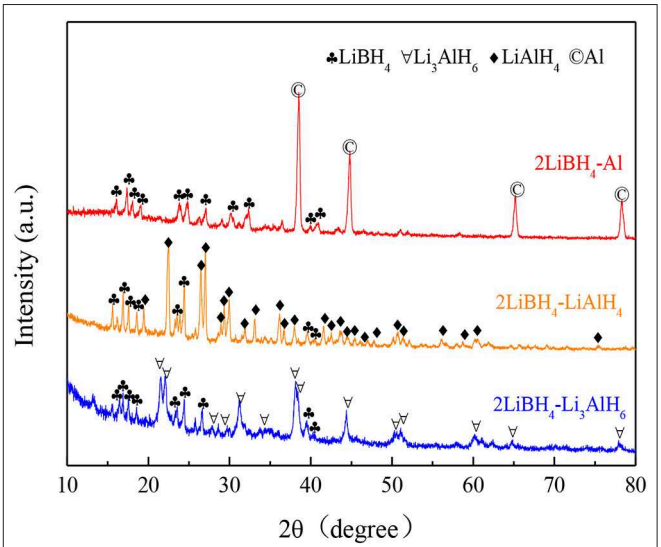

FIGURE 4 | XRD patterns of $2LiBH_4$-Al, $2LiBH_4$-$LiAlH_4$, and $2LiBH_4$-Li_3AlH_6 mixtures after ball milling for 1 h.

LiH peaks can still be found at 27°, 43°, and 46°. As the ball milling time increased, the LiH and $LiAlH_4$ content decreased, which shows that the synthesis reaction proceeds as the milling time increases. Nevertheless, the diffraction intensity of Li_3AlH_6 decreased, which shows that the longer milling time, the more likely the production of an amorphous phase becomes.

FTIR analysis was used to investigate the synthesized powder. In pure $LiAlH_4$ (**Figure 3A**), the bending modes around 1,780 and 1,610 cm^{-1} correspond to the A-H stretching band, as was previously shown by Chen et al. (2001). After 50 h ball milling, this A-H stretching band disappeared in the 2LilH-$LiAlH_4$ mixtures (**Figure 3B**). A new A-H stretching band was generated around 1,380 cm^{-1}, which belongs to Li_3AlH_6. This indicates the completion of the synthesis reaction.

Characterization of the Composite Samples

The $2LiBH_4$ + M (M = Al, $LiAlH_4$, Li_3AlH_6) composite systems were prepared by ball milling, respectively. The ball-milling time was 1 h, with a mole ratio of 2:1. The as-milled mixtures are presented in **Figure 4**. In the $2LiBH_4$-Al composite, the narrow and sharp diffraction peaks are of Al, while the other diffraction peaks are of $LiBH_4$. The intensity of the $LiAlH_4$ peaks in the $2LiBH_4$-$LiAlH_4$ composite are also strong, but both $LiBH_4$ and Li_3AlH_6 have attenuated diffraction peaks in $2LiBH_4$-Li_3AlH_6. The absence of other peaks indicated that there were no side reactions that could generate impurities or by-products during ball milling.

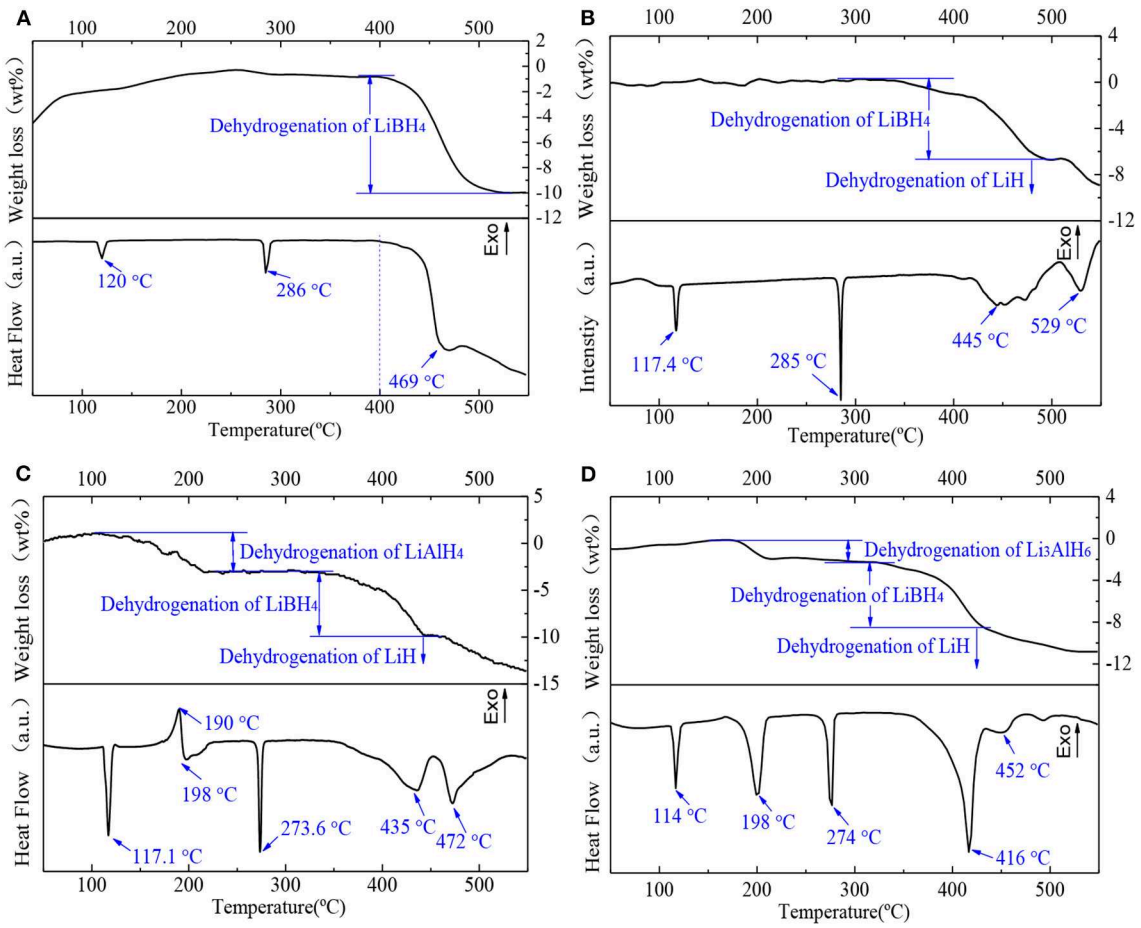

FIGURE 5 | DSC/TG curves of **(A)** pure $LiBH_4$, **(B)** $2LiBH_4$-Al, **(C)** $2LiBH_4$-$LiAlH_4$, and **(D)** $2LiBH_4$-Li_3AlH_6 samples after ball milling for 1 h.

Dehydrogenation Performances

The dehydrogenation performances of the samples were investigated. The four samples were heated to 550°C at a heating rate of 5°C/min in an argon atmosphere. The DSC/TG results are shown in **Figure 5**. In the pure $LiBH_4$ sample (**Figure 5A**), the endothermic peak at 120°C denotes that $LiBH_4$ transformed from an orthorhombic to a hexagonal crystal system. The endothermic peak at 286°C is attributed to the melting of $LiBH_4$. According to the TG curve, $LiBH_4$ began to release hydrogen and lose weight at 400°C. There is a dehydrogenation peak at around 469°C, and the rate of dehydrogenation slowed down after that. Both the transformation and the melting peak of $LiBH_4$ for each composite sample are shown in **Figures 5B–D**. All samples have lower transformation and melting temperatures than pure $LiBH_4$ (transformation temperature: $T_d < T_c < T_b < T_a$; melting temperature: $T_c < T_d < T_b < T_a$). In the as-milled $2LiBH_4$-Al sample (**Figure 5B**), the wide endothermic range around 445°C represents the decomposition of $LiBH_4$. The last peak at 529°C is the decomposition of LiH. As shown in **Figure 5C**, peaks at 190 and 198°C indicated the dehydrogenation of $LiAlH_4$, which were verified in our previous study (Li et al., 2012). $LiAlH_4$ decomposed into Li_3AlH_6 at 190°C, and Li_3AlH_6 started to generate LiH, Al, and release H_2 at 198°C. $LiBH_4$ and LiH started to decompose at 435 and 472°C, respectively. **Figure 5D** shows that the decomposition peak of Li_3AlH_6 is at 198°C, which is consistent with the $2LiBH_4$-$LiAlH_4$ sample. The decomposition peak of $LiBH_4$ (416°C) is lower than that of the $2LiBH_4$-$LiAlH_4$ (435°C) or $2LiBH_4$-Al samples (445°C). In addition, the decomposition peak of LiH, which is around 452°C, is also lower than that of the other composite systems. These results showed that the $LiBH_4$ became more unstable due to the addition of Li_3AlH_6 and that hydrogen was released at a lower temperature. The main reason for this is that the Al present in Li_3AlH_6 was active enough to stimulate the dehydrogenation reaction.

The temperature-programmed desorption (TPD) method was implemented to study the dehydrogenation performance of pure $LiBH_4$, $2LiBH_4$-Al, $2LiBH_4$-$LiAlH_4$, and $2LiBH_4$-Li_3AlH_6; the results are shown in **Figure 6**. The samples were heated to 400°C and held for 5 h. The pure $LiBH_4$ began to release H_2 at around 400°C. Its desorption rate slowed down when 5 wt.% of H_2 had been released. The $2LiBH_4$-Li_3AlH_6 sample released 9.1 wt.% H_2 within 150 min, which is the fastest reaction kinetics in this work. Its decomposition process includes two main steps, with the release of 3 and 6.1 wt.% H_2 as the first and second steps, respectively. In the $2LiBH_4$-$LiAlH_4$ sample, $LiAlH_4$ began to decompose at ∼130°C and released 3.9 wt.% H_2. Subsequently,

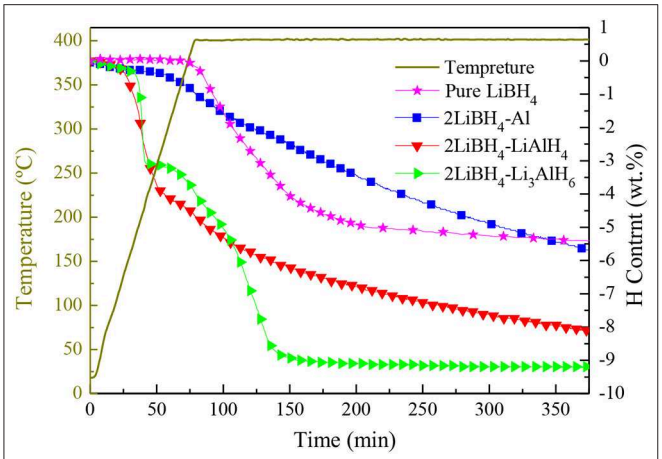

FIGURE 6 | TPD curves of pure $LiBH_4$, $2LiBH_4$-Al, $2LiBH_4$-$LiAlH_4$, and $2LiBH_4$-Li_3AlH_6 samples.

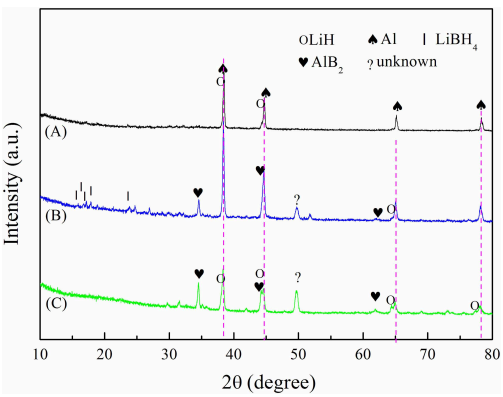

FIGURE 7 | XRD results of dehydrogenated samples at 400°C: **(A)** $2LiBH_4$-Al, **(B)** $2LiBH_4$-$LiAlH_4$, and **(C)** $2LiBH_4$-Li_3AlH_6.

its desorption rate was retarded. This composite released a total of 8 wt.% H_2. The $2LiBH_4$-Al composite had a slower desorption rate. Only 5.7 wt.% H_2 was released after 6 h, which is much lower than the 8.6 wt.% predicted by theoretical capacity. Previous research (Friedrichs et al., 2009) has reported that Al is an effective catalyst to activate $LiBH_4$, and this phenomenon can also be observed in this study. However, the Al element generated from $2LiBH_4$-Li_3AlH_6 is much more effective than for the other samples. Since aluminum can be easily oxidized, an oxide film can easily form on the surface of the Al powder, which can slow down the dehydrogenation kinetics. In contrast, the Al in $2LiBH_4$-Li_3AlH_6, decomposed from Li_3AlH_6 exhibits high purity and is non-oxidized, resulting in the superior reaction kinetics of $LiBH_4$.

Characterization of the Dehydrogenation Materials

The XRD patterns of the dehydrogenated samples are shown in **Figure 7**. In **Figure 7A**, prominent diffraction peaks of LiH and Al are present. However, the $LiBH_4$ phase was not observed, as its diffraction intensity is relatively weaker. In **Figure 7B**, residual peaks of $LiBH_4$ are observed, which demonstrates incomplete dehydrogenation. In **Figure 7C**, besides LiH and Al, the dehydrogenation products contain AlB_2, which was reported as the reversible phase (Friedrichs et al., 2009). AlB_2 can accelerate the formation of $LiBH_4$ in the reverse reaction. The AlB_2 content was higher in $2LiBH_4$-Li_3AlH_6 than in the other samples, which signifies higher reversibility of $2LiBH_4$-Li_3AlH_6. There is an unexpected peak near 50° both in the $2LiBH_4$-$LiAlH_4$ and $2LiBH_4$-Li_3AlH_6 samples, which was not identified but was also detected in previous reports (Yang et al., 2007).

CONCLUSIONS

In this work, the dehydrogenation performance of three different Al source composite systems, $2LiBH_4$-Al, $2LiBH_4$-$LiAlH_4$, and $2LiBH_4$-Li_3AlH_6, was analyzed. Elemental Al was the raw material and was used without further purification in the $2LiBH_4$-Al composite, in contrast to the other two samples, where it was decomposed from $LiAlH_4$ or Li_3AlH_6. Li_3AlH_6 powder was prepared from LiH and $LiAlH_4$. It can be concluded that the optimum synthetic conditions for ball milling are 50 h with a 25:1 ball to powder ratio at 300 rpm. The results demonstrate that Al, $LiAlH_4$, and Li_3AlH_6 had a stimulative effect on $LiBH_4$, allowing dehydrogenation at a relatively lower temperature. Additionally, $2LiBH_4$-Li_3AlH_6 was shown to have the best performance, with the endothermic peak of $LiBH_4$ at 416°C, 53°C lower than that of the pure $LiBH_4$ sample (469°C). The TPD results also verified the superior results of $2LiBH_4$-Li_3AlH_6, which showed the best kinetics performance among the composite samples. $2LiBH_4$-Li_3AlH_6 released 9.1 wt.% H_2 in only 150 min, which is over 95% of its theoretical hydrogen storage capacity. Its dehydrogenation product, AlB_2, was reported as a reversible phase by researchers (Friedrichs et al., 2009), which could promote the reverse reaction of producing $LiBH_4$. Further studies are needed to research the reversibility of the $2LiBH_4$-Li_3AlH_6 composite.

DATA AVAILABILITY STATEMENT

All datasets generated for this study are included in the article/supplementary material.

AUTHOR CONTRIBUTIONS

LC and YL: conception and design of study. YL and JH: acquisition of data. YL and XX: analysis and/or interpretation of data. YL: drafting the manuscript. DZ and SW: revising the manuscript critically for important intellectual content. YL, SW, DZ, JH, XX, and LC: approval of the version of the manuscript to be published.

FUNDING

This work was supported by the National Natural Science Foundation of China (51671173) and the Curriculum Reform Project (KCSZ 201809 and JGXM201912).

REFERENCES

Carrillo-Bucio, J., Tena-García, J., and Suárez-Alcántara, K. (2017). Dehydrogenation of surface-oxidized mixtures of $2LiBH_4$ + Al/additives (TiF_3 or CeO_2). *Inorganics* 5:82. doi: 10.3390/inorganics5040082

Chen, J., Kuriyama, N., Xu, Q., Takeshita, H. T., and Sakai, T. (2001). Reversible hydrogen storage via titanium-catalyzed $LiAlH_4$ and Li_3AlH_6. *J. Phys. Chem. B* 105, 11214–11220. doi: 10.1021/jp012127w

Fang, F., Li, Y., Song, Y., Sun, D., Zhang, Q., Ouyang, L., et al. (2011). Superior destabilization effects of MnF_2 over $MnCl_2$ in the decomposition of $LiBH_4$. *J. Phys. Chem. C* 115, 13528–13533. doi: 10.1021/jp203527c

Friedrichs, O., Kim, J. W., Remhof, A., Buchter, F., Borgschulte, A., Wallacher, D., et al. (2009). The effect of Al on the hydrogen sorption mechanism of $LiBH_4$. *Phys. Chem. Chem. Phys.* 11, 1515–1520. doi: 10.1039/b814282c

He, Q., Zhu, D., Wu, X., Dong, D., Xu, M., and Tong, Z. (2019). Hydrogen desorption properties of $LiBH_4$/x$LiAlH_4$ (x = 0.5, 1, 2) composites. *Molecules* 24:1861. doi: 10.3390/molecules24101861

Huang, X., Xiao, X. Z., Shao, J., Zhai, B., Fan, X. L., Cheng, C. J., et al. (2016). Building robust architectures of carbon-wrapped transition metal nanoparticles for high catalytic enhancement of the $2LiBH_4$-MgH_2 system for hydrogen storage cycling performance. *Nanoscale* 8, 14898–14908. doi: 10.1039/C6NR04100K

Kou, H. Q., Xiao, X. Z., Li, J. X., Li, S. Q., Ge, H. W., Wang, Q. D., et al. (2012). Effects of fluoride additives on dehydrogenation behaviors of $2LiBH_4$ + MgH_2 system. *Int. J. Hydrogen Energy* 37, 1021–1026. doi: 10.1016/j.ijhydene.2011.03.027

Ley, M. B., Jepsen, L. H., Lee, Y. S., Cho, Y. W., von Colbe, J. M. B., Dornheim, M., et al. (2014). Complex hydrides for hydrogen storage - new perspectives. *Mater. Today* 17, 122–128. doi: 10.1016/j.mattod.2014.02.013

Li, Y., Xiao, X., Chen, L., Han, L., Shao, J., Fan, X., et al. (2012). Effects of fluoride additives on the hydrogen storage performance of $2LiBH_4$-Li_3AlH_6 destabilized system. *J. Phys. Chem. C* 116, 22226–22230. doi: 10.1021/jp307572x

Liu, C., Li, F., Ma, L. P., and Cheng, H. M. (2010). Advanced materials for energy storage. *Adv. Mater.* 22, E28–E62. doi: 10.1002/adma.200903328

Lodziana, Z., and Vegge, T. (2004). Structural stability of complex hydrides: $LiBH_4$ revisited. *Phys. Rev. Lett.* 93:145501. doi: 10.1103/PhysRevLett.93.145501

Lombardo, L., Yang, H., and Züttel, A. (2019). Study of borohydride ionic liquids as hydrogen storage materials. *J. Energy Chem.* 33, 17–21. doi: 10.1016/j.jechem.2018.08.011

Mao, J. F., Guo, Z. P., Liu, H. K., and Yu, X. B. (2009). Reversible hydrogen storage in titanium-catalyzed $LiAlH_4$-$LiBH_4$ system. *J. Alloys Comp.* 487, 434–438. doi: 10.1016/j.jallcom.2009.07.158

Orimo, S. I., Nakamori, Y., Ohba, N., Miwa, K., Aoki, M., Towata, S–I., et al. (2006). Experimental studies on intermediate compound of $LiBH_4$. *Appl. Phys. Lett.* 89:021920. doi: 10.1063/1.2221880

Schlapbach, L., and Zuttel, A. (2001). Hydrogen-storage materials for mobile applications. *Nature* 414, 353–358. doi: 10.1038/35104634

Siegel, D. J., Wolverton, C., and Ozolins, V. (2007). Thermodynamic guidelines for the prediction of hydrogen storage reactions and their application to destabilized hydride mixtures. *Phys. Rev. B* 76:134102. doi: 10.1103/PhysRevB.76.134102

Soru, S., Taras, A., Pistidda, C., Milanese, C., Bonatto Minella, C., Masolo, E., et al. (2014). Structural evolution upon decomposition of the $LiAlH_4$ + $LiBH_4$ system. *J. Alloys Comp.* 615, S693–S697. doi: 10.1016/j.jallcom.2013.12.027

Vajo, J. J. (2011). Influence of nano-confinement on the thermodynamics and dehydrogenation kinetics of metal hydrides. *Curr. Opin. Solid State Mater. Sci.* 15, 52–61. doi: 10.1016/j.cossms.2010.11.001

Vajo, J. J., Li, W., and Liu, P. (2010). Thermodynamic and kinetic destabilization in $LiBH_4$/Mg_2NiH_4: promise for borohydride-based hydrogen storage. *Chem. Commun.* 46, 6687–6689. doi: 10.1039/c0cc01026j

Vajo, J. J., and Olson, G. L. (2007). Hydrogen storage in destabilized chemical systems. *Scripta Mater.* 56, 829–834. doi: 10.1016/j.scriptamat.2007.01.002

Yang, J., Sudik, A., and Wolverton, C. (2007). Destabilizing $LiBH_4$ with a metal (M) Mg, Al, Ti, V, Cr, or Sc) or metal hydride (MH_2 = MgH_2, TiH_2, or CaH_2). *J. Phys. Chem. C* 111, 19134–19140. doi: 10.1021/jp076434z

Zhai, B., Xiao, X., Lin, W., Huang, X., Fan, X., Li, S., et al. (2016). Enhanced hydrogen desorption properties of LiBH4–Ca(BH4)2 by a synergetic effect of nanoconfinement and catalysis. *Int. J. Hydrogen Energy* 41, 17462–17470. doi: 10.1016/j.ijhydene.2016.06.170

Zhang, L. T., Zheng, J. G., Xiao, X. Z., Wang, X. C., Huang, X., Liu, M. J., et al. (2017). A new strategy to remarkably improve the low-temperature reversible hydrogen desorption performances of $LiBH_4$ by compositing with fluorographene. *Int. J. Hydrogen Energy* 42, 20046–20055. doi: 10.1016/j.ijhydene.2017.05.060

Zhang, Y., Xiao, X., Luo, B., Huang, X., Liu, M., and Chen, L. (2018). Synergistic effect of $LiBH_4$ and $LiAlH_4$ additives on improved hydrogen storage properties of unexpected high capacity magnesium hydride. *J. Phys. Chem. C* 122, 2528–2538. doi: 10.1021/acs.jpcc.7b11222

Conflict of Interest: The authors declare that the research was conducted in the absence of any commercial or financial relationships that could be construed as a potential conflict of interest.

frontiers in Chemistry

REVIEW
published: 15 May 2020
doi: 10.3389/fchem.2020.00390

Two-Dimensional Transition Metal Oxide and Hydroxide-Based Hierarchical Architectures for Advanced Supercapacitor Materials

Meili Guan[1], Qiuwan Wang[1], Xuan Zhang[1], Jian Bao[1], Xuezhong Gong[2] and Youwen Liu[3]**

[1] Institute for Energy Research, School of Chemistry and Chemical Engineering, Jiangsu University, Zhenjiang, China, [2] National Center of International Joint Research for Hybrid Materials Technology, National Base of International Science and Technology Cooperation on Hybrid Materials, College of Materials Science and Engineering, Institute of Hybrid Materials, Qingdao University, Qingdao, China, [3] State Key Laboratory of Material Processing and Die & Mould Technology, School of Materials Science and Engineering, Huazhong University of Science and Technology, Wuhan, China

The supercapacitor has been widely seen as one of the most promising emerging energy storage devices, by which electricity is converted from chemical energy and stored. Two-dimensional (2D) metal oxides/hydroxides (TMOs/TMHs) are revolutionizing the design of high-performance supercapacitors because of their high theoretical specific capacitance, abundance of electrochemically active sites, and feasibility for assembly in hierarchical structures by integrating with graphitic carbon, conductive polymers, and so on. The hierarchical structures achieved can not only overcome the limitations of using a single material but also bring new breakthroughs in performance. In this article, the research progress on 2D TMOs/TMHs and their use in hierarchical structures as supercapacitor materials are reviewed, including the evolution of supercapacitor materials, the configurations of hierarchical structures, the electrical properties regulated, and the existence of advantages and drawbacks. Finally, a perspective covering directions and challenges related to the development of supercapacitor materials is provided.

Keywords: two-dimensional nanosheets, transition metal oxide and hydroxide, hierarchical structure, integration, supercapacitor

OPEN ACCESS

Edited by:
Tengfei Zhou,
University of Wollongong, Australia

Reviewed by:
Ye Liu,
South-Central University for Nationalities, China
Li Shuang,
China Three Gorges University, China

****Correspondence:***
Xuezhong Gong
xzgong@qdu.edu.cn
Youwen Liu
ywliu@hust.edu.cn

Specialty section:
This article was submitted to Nanoscience, a section of the journal Frontiers in Chemistry

Received: *04 March 2020*
Accepted: *14 April 2020*
Published: *15 May 2020*

Citation:
Guan M, Wang Q, Zhang X, Bao J, Gong X and Liu Y (2020) Two-Dimensional Transition Metal Oxide and Hydroxide-Based Hierarchical Architectures for Advanced Supercapacitor Materials. Front. Chem. 8:390. doi: 10.3389/fchem.2020.00390

INTRODUCTION

Global warming and the rapid depletion of fossil fuels are driving the development of sustainable and renewable energy. At present, the renewable energy sources of wind, tidal, geothermal, and solar energy have been researched and utilized (Yuksel and Ozturk, 2017; Cranmer et al., 2018; Mo et al., 2018; Song et al., 2018). However, these energy sources are highly dependent on nature, which is variable and unpredictable. Hence, an energy storage system is essential for efficiently collecting this natural energy, and, meanwhile, allows the energy to be rapidly exported in the form of stable electric energy. In recent years, the supercapacitor is becoming popular as a kind of energy storage device that is not only efficient and practical but also convenient and environmental friendly (Lukatskaya et al., 2016; Salanne et al., 2016; Wang et al., 2017).

The supercapacitor is also known as a Faraday quasi capacitor or electrochemical capacitor. It stores charges through a reversible redox reaction at the interface between electrode materials

and electrolyte, unlike a traditional capacitor, it offers higher specific capacity and energy density (Simon and Gogotsi, 2010; Kate et al., 2018). Compared with a secondary battery, the supercapacitor possesses overwhelming advantages in terms of a shorter charging time and a long cycle life and, higher power density (Staaf et al., 2014; Zhao and Sun, 2018). Therefore, the supercapacitor is a kind of energy storage device that is intermediate between a traditional capacitor and a secondary battery that can be regarded as a complementary device between a battery and a traditional capacitor and can meet the needs of human beings for new energy.

The structural configuration of a supercapacitor mainly consists of electrode material, a diaphragm, electrolyte, and collecting fluid (Muzaffar et al., 2019). The energy storage is mainly from the charge transfer process at the interface of electrode and electrolyte, so the electrode material is the key factor in the performance of the supercapacitor. At present, there are three prevailing types of electrode materials under research, namely carbon materials [e.g., graphene (Liu et al., 2010), carbon nanotubes (Shang et al., 2015), activated carbon (Gamby et al., 2001; Jin et al., 2016), and porous carbon (Bu et al., 2017)], conducting polymer materials [e.g., polyaniline (PANI) (Lim et al., 2015; Lyu et al., 2019), polypyrrole (PPy) (Huang et al., 2015), polythiophene (PTh) (Ambade et al., 2017), and poly (3, 4-ethylenedioxythiophene) (PEDOT) (Liu et al., 2008)], and TMOs/TMHs [RuO_2 (Sugimoto et al., 2003), MnO_2 (Song et al., 2010; Zhao et al., 2012; Huang et al., 2018), MoO_3 (Brezesinski et al., 2010; Hanlon et al., 2014), Nb_2O_5 (Augustyn et al., 2013), V_2O_5 (Qi et al., 2018), $Ni(OH)_2$ (Ida et al., 2008; Fu et al., 2014), and $Co(OH)_2$ (Ji et al., 2012; Gao et al., 2014)]. In particular, carbon material is the most widely used electrode material due to its diversity and abundance as a resource. The capacitance over a carbon-based supercapacitor electrode is achieved through pure electrosorption of the electrical double-layer; thus, the structure of the electrode material will not collapse with the insertion and withdrawn of electrolyte ions during the charging and discharging processes. This leads to superior cycle stability, extending to tens of thousands or even hundreds of thousands of cycles (Frackowiak and Beguin, 2001; Liu et al., 2014). However, the energy density of carbon-based supercapacitors is low due to the storage mechanism, which rarely meets the needs of practical application. In contrast, conducting polymer electrode materials achieve high charge density by a reversible redox reaction of elements doping/dedoping, thus realizing large electric energy storage (Snook et al., 2011). However, the conducting polymer skeleton is prone to expanding and shrinking in the charging–discharging process, leading to low cycle stability (González et al., 2016). In addition, most of the conducting polymer materials are dense structures with limited interfaces, which restricts the amount of electrode material that is able to fully contact with the electrolyte and results in relatively low power density.

It is noteworthy that TMOs/TMHs exhibit potential for the fabrication of supercapacitor electrodes due to their high theoretic capacity and ultrahigh power density (Yuan et al., 2014; Wang et al., 2015; Zhang H. et al., 2015; Nguyen and Montemor, 2019). The energy storage can be achieved by either electrosorption or reversible redox reactions (Lee et al., 2010). Normally the valance state would change accompany with the charging–discharging process. Hence, for comparison, TMOs/TMHs have exhibited higher powder density and stability than traditional carbon and conducting polymer materials. Although problems arise from their narrow working voltage window, low conductivity, and small reaction area, these can be solved by structural engineering and composition, such as by controlling dimensionality and morphology (Zhu et al., 2014; Najafpour et al., 2015; Xu et al., 2015; Yue and Liang, 2015; Yu et al., 2015).

In this review, we summarize the recent progress in 2D TMOs/TMHs as supercapacitor electrode material. Further, 2D transition metal oxide/hydroxide-based hierarchical structures are covered. The different technical strategies in design and synthesis for optimizing the conductivity, structural stability, surface physical, and chemical properties, and structural morphology of the hierarchical composites are also detailed. A supercapacitor electrode with high specific capacitance, good rate capability, and excellent cycle stability can be obtained by tuning the electrochemical properties of the electrode materials. Finally, a perspective covering directions and challenges related to the development of supercapacitor materials is provided.

TWO-DIMENSIONAL TRANSITION METAL OXIDES/HYDROXIDES

Transition metal oxides/hydroxides (TMOs/TMHs) are the most representative active electrochemical pseudocapacitor materials and are widely known for their high theoretical capacitance, abundance in nature, and high energy density (Jiang et al., 2012). However, poor intrinsic conductivity and other shortcomings have limited their performance as supercapacitor materials. Hence, 2D ultrathin TMOs/TMHs have been widely studied and applied in supercapacitors due to their advantages of high specific surface area and improved planar electronic conductivity (Gao et al., 2014; Liu W. et al., 2017; Zhu et al., 2018). Most importantly, the atomic thickness shortens the ion diffusion path and reduces ion diffusion resistance.

So far, there are two main strategies, that is, "top-down" and "bottom-up" methods, for obtaining 2D TMOs/TMHs (Sun et al., 2017; Mei et al., 2018), as shown in **Table 1**. "Top-down" mainly refers to the chemical or mechanical exfoliation of layered bulk materials, such as by mechanical exfoliation and liquid-phase exfoliation (Coleman et al., 2011; Rui et al., 2013; Zhang Y. Z. et al., 2015; Peng et al., 2017; Zavabeti et al., 2017; Tao et al., 2019). It is reported that MoO_3, MnO_2, and RuO_2 nanosheets, etc., can be made at a large scale by ultrasonic exfoliation in ethanol/water and can be applied to solid-state symmetrical supercapacitors (Dutta et al., 2019). A liquid-phase exfoliation method with the aid of lithium (Li) intercalation and de-intercalation was developed for the preparation of quasi-layered VO_2 ultrathin nanosheet (Liu et al., 2012). The underlying mechanism is the insertion of Li ions to break the chemical bonds of the layers. Subsequent replacement of Li ions by larger molecules and ultrasonic treatment can result in a dispersed VO_2 ultrathin nanosheet. The "bottom-up" synthetic protocol

TABLE 1 | Summary and comparison between top-down and bottom-up strategies for the fabrication of 2D TMOs/TMHs and their pros and cons.

Strategy	Method	2D TMOs/TMHs	References	Pros and cons
Top-down	Mechanical cleavage	MnO_2	Peng et al., 2017; Dutta et al., 2019	Easy operation; Only applicable for layered structure materials
		MoO_3	Dutta et al., 2019	
		RuO_2	Dutta et al., 2019	
		Ti_5NbO_{14}	Zhang et al., 2010	
	Liquid-phase exfoliation	V_2O_5	Rui et al., 2013	
		VO_2	Liu et al., 2012	
		MoO_3	Zhang Y. Z. et al., 2015	
Bottom-up	Self-assembly	TiO_2	Sun J. et al., 2014	Applicable for both layered and non-layered structure materials; Can be produced at large scale; Harsh synthetic conditions; Difficult to obtain high-quality 2D crystals.
		ZnO	Sun et al., 2017	
		Co_3O_4	Hu et al., 2017	
		WO_3	Sun J. et al., 2014	
	Chemical vapor deposition	TiO_2	Lee and Sung, 2012	
		WO_3	Liu et al., 2015	
	Directional connection	SnO_2	Wang C. et al., 2012	
		CeO_2	Yu et al., 2010	
		$Co(OH)_2$	Gao et al., 2014	
	Topological chemical transformation	WO_3	Liu et al., 2016	
		Nb_2O_5	Wen et al., 2017	
		$ZnCo_2O_4$	Bao et al., 2018	
		Cobalt nickel oxide	Yang et al., 2019	

starts from appropriate design at the atomic or molecular level by the aid of technologies, such as self-assembly (Sun J. et al., 2014; Hu et al., 2017; Sun et al., 2017), chemical vapor deposition (Lee and Sung, 2012; Liu et al., 2015), directional connection, and topological chemical transformation of layered intermediates (Liu et al., 2016; Wen et al., 2017; Bao et al., 2018), to synthesize a 2D nanostructure. For instance, five atomic layer thickness $Co(OH)_2$ ultrathin nanosheet was synthesized by the orientation connection method and was assembled into an asymmetric vertical all-solid-state flexible supercapacitor with excellent specific capacitance and cycle stability (Gao et al., 2014). For non-layered 2D materials, Qiu and Zheng, for the first time, successfully observed the *in-situ* transformation of metal oxides from 3D nanoparticles as intermediate products to 2D oxide nanoflakes by LBNL's *in-situ* liquid-phase transmission electron microscopy technology, revealing the new evolution strategy of 3D to 2D materials at the atomic level, and also paving the way to obtaining ultrathin nanostructures from non-layered materials (Yang et al., 2019).

2D TMOs/TMHs-BASED HIERARCHICAL ENGINEERING FOR SUPERCAPACITOR MATERIALS

Although great efforts have been put into the development of 2D TMOs/TMHs for supercapacitor electrodes, challenges still exist when using a single electrode material. The drawback lies in low actual capacitance, limited improvement of energy density, and the poor rate capability caused by low conductivity, which have restricted the performance of such supercapacitors in practical applications (Jiang et al., 2012; Mahmood et al., 2019). In order to overcome the limitations of single electrode materials, it is necessary to combine 2D TMOs/TMHs with other low-dimensional nanomaterials to construct hierarchical nanostructures, which can not only optimize the configuration to overcome the agglomeration of 2D nanosheets but also complement and enhance the performance of different electrode materials so as to realize effective improvement of the performance for the supercapacitor device (**Figure 1**).

TMOs/TMHs HIERARCHICAL STRUCTURES

The engineering of hierarchical structures by hybridizing different TMOs/TMHs is regarded as an efficient strategy to combine the advantages of different materials (Wu et al., 2013; Dinh et al., 2014; Zheng et al., 2016, 2018; Ouyang et al., 2019). The function of this kind of hierarchical structure can be generally summarized as overcoming the drawbacks of the individual components and preventing agglomeration of nanosheets. Thus, capacitance performance is predominantly enhanced because of the expected synergistic effect. Hierarchical structures with different morphologies can be formed through self-assembly (Huang et al., 2014; Feng et al., 2018), layer stacking (Zhu et al., 2012), and heterostructure core-shell engineering (Li et al., 2014; Sun Z. et al., 2014; Ho and Lin, 2019), which also have significant effects on the energy density and stability of the supercapacitors.

A 3D V_2O_5 architecture was constructed by using ultrathin V_2O_5 nanosheets as building blocks with a thickness of 4 nm via a freeze-drying process (Zhu et al., 2013). Due to the benefits of

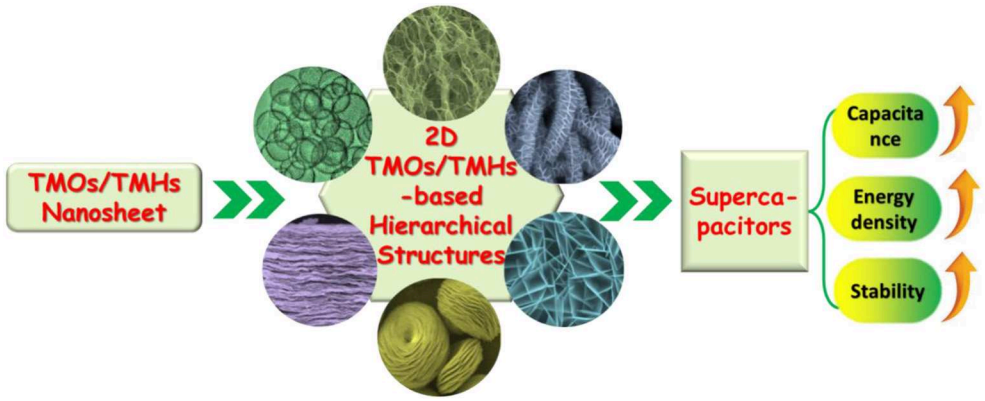

FIGURE 1 | Schematic illustration of the use of TMOs/TMHs nanosheets to form 2D TMOs/TMHs-based hierarchical structures for a supercapacitor with expected performance promotion.

its porous and ultrathin nature, as well as the 3D interpenetrating structure, a high surface area and shortened diffusion length were expected, thus enabling such a supercapacitor electrode to exhibit high capacitance, high energy density, and excellent stability (**Figures 2A–C**). A flexible film-like supercapacitor was fabricated via a vacuum filtration method by integrating MnO_2 and Ti_3C_2 nanoflakes as the electrode, as shown in **Figure 2D** (Liu Y. et al., 2017). With the aid of good solubility, similar two-dimensional geometry, the high theoretical capacity of MnO_2, and the good conductivity of Ti_3C_2, the composite electrode exhibited good capacitance performance with a high mass-specific capacitance of 305 F/g at a current density of 1 A/g. The fabricated symmetrical flexible supercapacitor device exhibited a maximum energy density of 8.3 Wh/kg, and the power density could reach 2,376 W/kg (**Figures 2E,F**). Characterizations and deeper understanding of the interaction between the stacked hierarchical structure and electrochemical performance revealed that the layered stacking structure is more conducive to improve the electrochemical performance of the electrode compared with traditional capacitors.

Forming a heterostructure or core-shell structures has been adopted as an efficient strategy for offering a large surface area for more Faradaic reaction sites and high conductivity to accelerate the charge transfer and therefore to improve the electrochemical performances of nanocomposites. For instance, a $ZnCo_2O_4$-MnO_2 heterostructure on Ni foam was shown to be an active electrode material with a porous nanostructure, providing a considerably large electroactive area, and exhibited ideal capacitive behavior, with a maximum Cs of 2,057 F/g at a current density of 1 A/g and cycling stability of 96.5% after 5,000 cycles (Kumbhar and Kim, 2018) (**Figures 2G–I**). Unique core-shell arrays of $CoFe_2O_4$@MnO_2 on nickel foam were also studied as an electrode material for a supercapacitor. Compared to the individual $CoFe_2O_4$ and MnO_2 nanosheets, the composite electrode exhibited much higher specific area capacitance of 3.59 F/cm^2 (≈1,995 F/g) at a current density of 2 mA/cm^2 and a smaller semicircle in EIS, indicating faster ion insertion/extraction during electrochemical reactions, which can all be attributed to the hierarchical core-shell nanostructure. The asymmetric supercapacitor assembled using a $CoFe_2O_4$@MnO_2 electrode had maximum energy density and maximum power density of 37 Wh/kg and 4,800 W/kg, respectively, with long-term cycling stability (91.4% retention after 2,250 cycles) (Gao et al., 2017).

Besides, mixed dimensional hierarchical structures have also been reported. For instance, a hybrid of $NiCo_2O_4$-MoS_2 consisting of 2D $NiCo_2O_4$ nanosheets and 1D MoS_2 nanowires were grown on a 3D Ni foam network, forming mixed-dimensional hierarchical structures, as shown in **Figures 3A–C**. During the growth process, $NiCo_2O_4$ nanosheets intertwined on the Ni surface, providing sites for MoS_2 nanowires, while a higher concentration of S^{2-} lead to thinner nanowires. These features enable a high specific surface area and a shortened diffusion path for ions and electrons, which lead to the enhancement of the electron/ion transfer rate in the electrodes (Wen et al., 2018). The assembled supercapacitor device delivered a maximum energy density of 18.4 Wh/kg and a power density of 1200.2 W/kg with excellent stability (specific capacitance retention of 98.2% after 8,000 cycles) (**Figures 3D,E**).

TMOs/TMHs/CARBON-BASED HIERARCHICAL STRUCTURES

Graphene, described as the "famous star" among carbon materials (Gong et al., 2016), it is an excellent two-dimensional scaffold upon which to construct composite materials with 2D TMOs/TMHs because its large surface area and the huge amount of cross-linking of the conjugated π-bond structure endow it with superior conductivity (in-plane carrier mobility up to 200,000 $cm^2v^{-1}s^{-1}$) and physical structure stability (high mechanical strength and flexibility) (Novoselov et al., 2012). The electronic conduction and mechanical stability of the hierarchical structure formed are improved by the synergistic effect of the two components (Stankovich et al., 2006). Hence, a supercapacitor with excellent performance is expected due to the improved electrochemical reaction rate and cycle stability.

At present, a large amount of progress has been made in the preparation of high-performance energy storage materials by combining TMOs/TMHs with graphene. The application

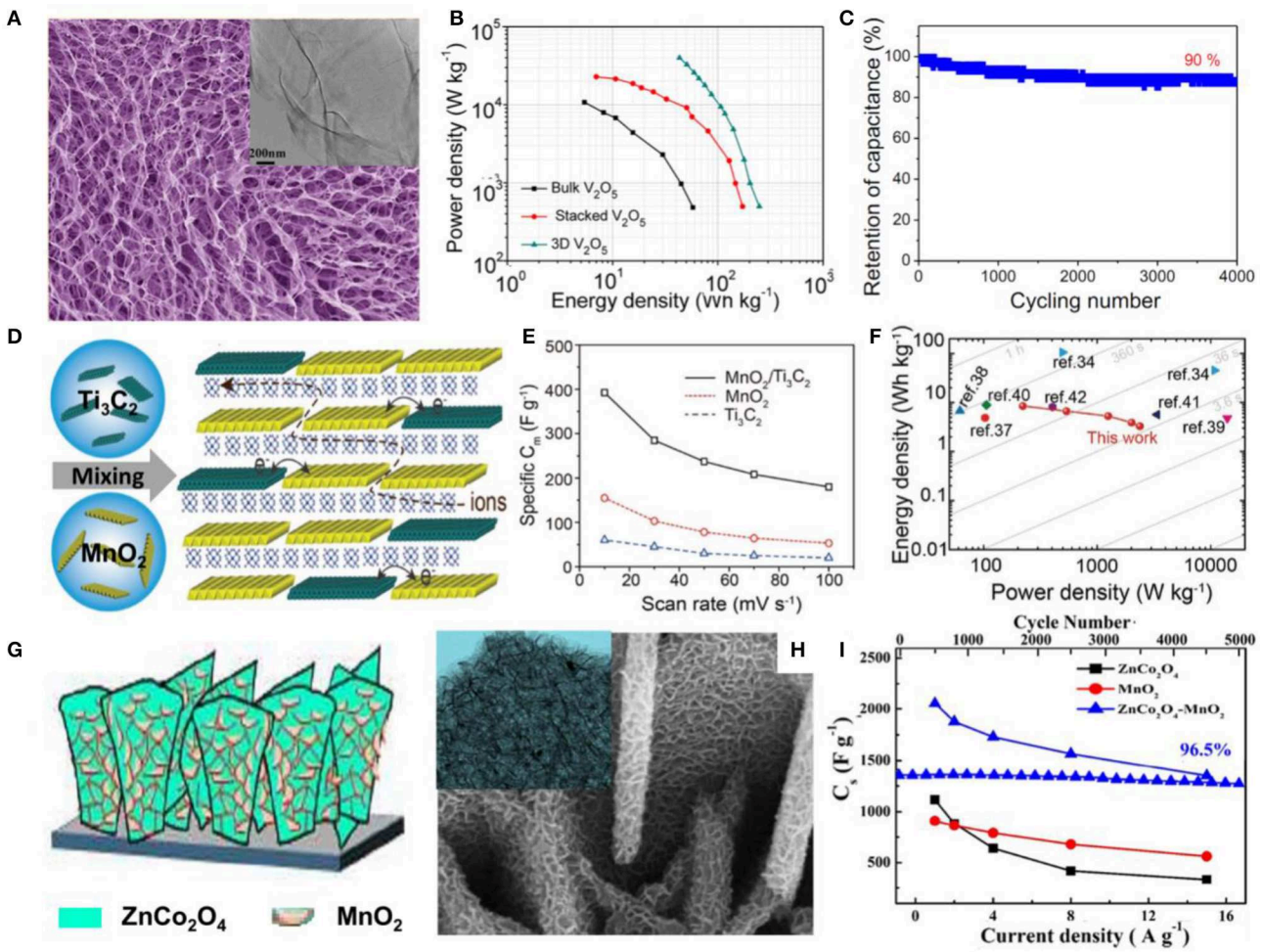

FIGURE 2 | (A) FESEM images of the 3D V_2O_5 architecture constructed from nanosheets (inset: TEM image of a nanosheet). **(B)** Power density and energy density of three electrodes. **(C)** Cycling performance of the 3D V_2O_5 architecture (Zhu et al., 2013). **(D)** Schematic drawing of the fabrication of the MnO_2/Ti_3C_2 hybrid film, with molecular sheets stacked in a randomly interstratified manner. **(E)** Rate capability of the hybrid MnO_2/Ti_3C_2 electrode compared with neat MnO_2 and Ti_3C_2 electrodes. **(F)** Performance comparison of the MnO_2/Ti_3C_2 hybrid with other reported materials on a Ragone plot (Liu W. et al., 2017). **(G)** Schematic of the coating of $ZnCo_2O_4$ nanoflakes with MnO_2 nanosheets. **(H)** FESEM images and (inset) TEM images of $ZnCo_2O_4$ nanoflakes coated with MnO_2 nanosheets. **(I)** Variation in C_s with respect to current density and cycling performance at 15 A/g for electrodes (Gao et al., 2017).

of pseudocapacitive V_2O_5 nanosheets and graphene in all-solid-state flexible thin-film supercapacitors (ASSTFSs) has been reported (Bao et al., 2014). By rationally integrating the two components, electron transfer was accelerated, and diffusion paths were shortened, leading to strong electrochemical performance, with a capacitance of 11,718 $\mu F/cm^2$ at 0.2 A/m^2, an energy density of 1.13 $\mu W\ h/cm^2$ at a power density of 10.0 $\mu W/cm^2$, and excellent long-term cycling stability for 2,000 charge–discharge cycles (**Figure 4**). The superior electrochemical performance thoroughly demonstrated the merit of a hierarchical architecture combining pseudocapacitive V_2O_5 nanosheets and graphene.

The Xie, group for the first time, fabricated a flexible all-solid-state thin-film pseudocapacitor using β-$Ni(OH)_2$/graphene hybrid nanosheets as electrode materials via a layer-by-layer method (Xie et al., 2013). The assembly process of the β-$Ni(OH)_2$/graphene hybrid includes electrostatic interaction between GO and Ni^{2+}, interlayer Ni^{2+} diffusion, and confined $(NiOH)_2$ crystallization, as well as simultaneous reduction of graphene (**Figures 5A–E**). The combination of highly conductive graphene and pseudocapacitive β-$Ni(OH)_2$ guarantees high specific capacitance and excellent stability for this novel energy storage material. The fabricated all-solid-state thin-film pseudocapacitor exhibits a high volumetric specific capacitance of 660.8 F/cm and good cycling ability, as well as excellent flexibility with negligible degradation after 200 bending cycles (**Figures 5F,G**). Meanwhile, the ultrathin configuration of the hybrid nanosheets endows superior mechanical properties for the as-fabricated device, which can be regarded as a feasible energy supply for the exploitation of flexible electronics.

Following the all-solid-state planar configuration, the Xie group developed a quasi-2D ultrathin MnO_2/graphene hybrid for

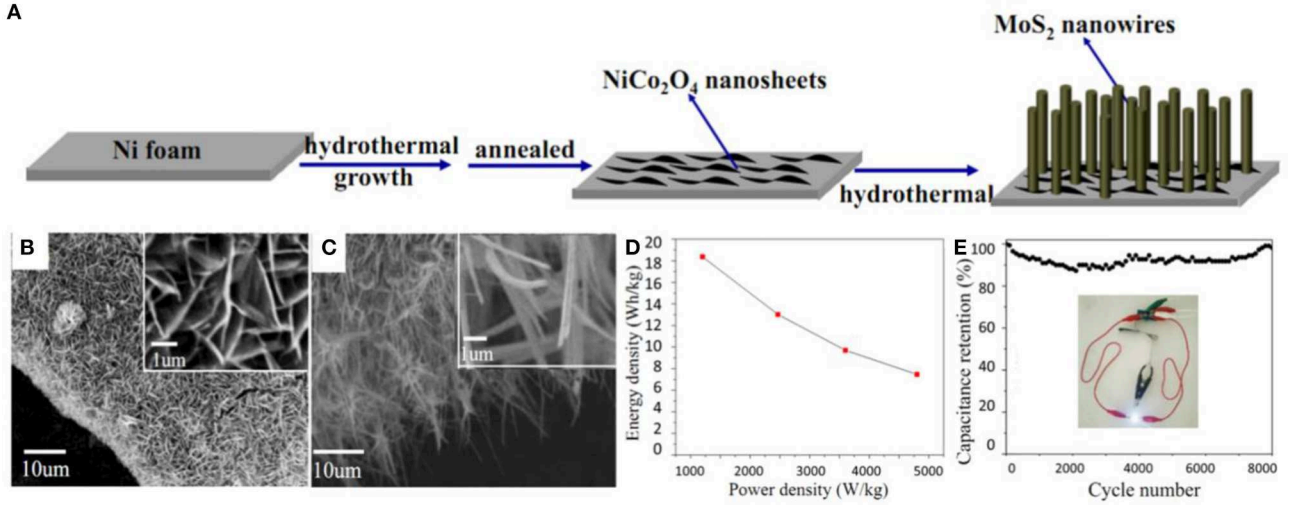

FIGURE 3 | (A) Schematic illustration of the synthesis procedure of a MoS_2 nanowires/$NiCo_2O_4$ nanosheets composite. **(B)** SEM images of the $NiCo_2O_4$ nanosheets supported on Ni foam. **(C)** SEM images of the composite supported on Ni foam. **(D)** Ragone plot and **(E)** cycling performance of the composite (Wen et al., 2018).

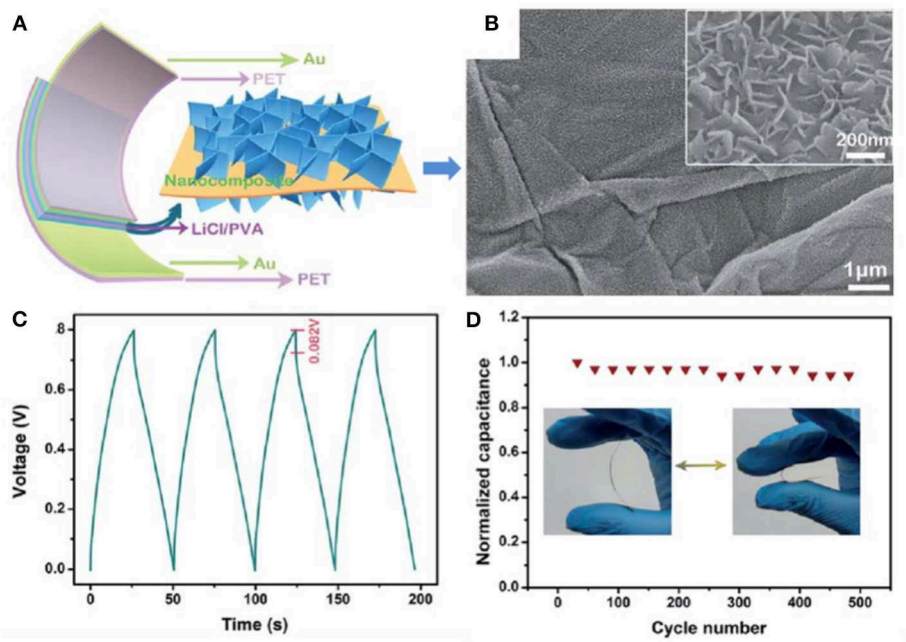

FIGURE 4 | (A) Schematic illustration of the flexible ASSTFS. **(B)** SEM images of the as-obtained V_2O_5 nanosheet/graphene nanocomposite. **(C)** The first four cycles of a galvanostatic charge–discharge curve of the as-fabricated ASSTFS at a current density of 2.5 A/m^2. **(D)** Long-term cycling stability investigation of the ASSTFS after repeated bending/extension for 500 cycles (Bao et al., 2014).

fabricating a novel and high-performance planar supercapacitor (Peng et al., 2013). To make the best of the designed planar structure, a vacuum filtration method is adopted to produce films with controllable thickness and transferability. These hybrid 2D δ-MnO_2/graphene thin films can be transferred onto a range of substrates such as PET, quartz, glass, and silicon wafer. By filling with a gel electrolyte of PVA/H_3PO_4, an all-solid-state planar supercapacitor is fabricated (**Figures 6A,B**). Owing to the planar peculiarity of both graphene and δ-MnO_2 nanosheets, more electrochemically active surfaces for absorption/desorption of electrolyte ions were introduced, and charge transport was accelerated at the hybridized interlayer during the charging and discharging processes (**Figures 6C–E**). The device exhibited high specific capacitances of 267 F/g at a current density of 0.2 A/g and 208 F/g at 10 A/g and excellent rate capability and cycling stability (capacitance retention of 92% after 7,000 cycles) (**Figures 6F,G**).

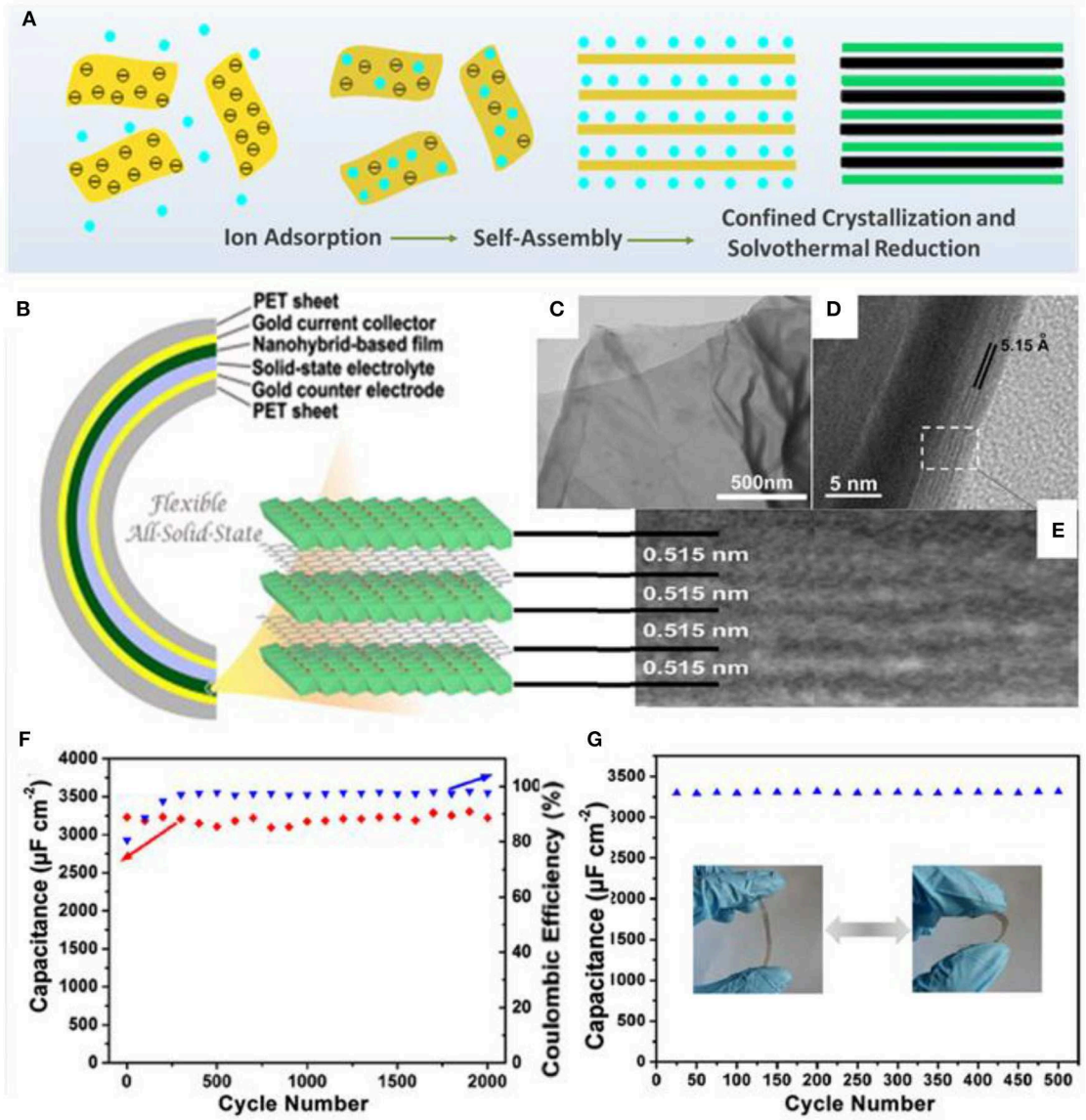

FIGURE 5 | (A) Schematic illustration of the layer-by-layer formation mechanism of β-$Ni(OH)_2$/graphene nanohybrids. **(B)** Schematic illustration of the flexible all-solid-state thin-film supercapacitor with pseudocapacitive β-$Ni(OH)_2$/graphene nanohybrids as active materials. **(C)** TEM image of the as-prepared nanohybrids, confirming the nanosheet morphology. **(D)** Cross-sectional HR-TEM images and **(E)** enlarged view of the HR-TEM image of the curled fringe of the nanohybrid sheet. **(F)** Long-term cycling stability of the flexible ASSTFS based on the nanohybrids (98.2% for the 2,000th cycle). **(G)** Cycling stability of the flexible ASSTFS measured after repeated bending/extension deformation (Xie et al., 2013).

In addition to these pioneering and representative research studies, numerous reports on the integration of TMOs/TMHs with graphene to prepare high-performance electrode materials for supercapacitors have revealed the general functions of the hierarchical structures (Wang G. et al., 2012; Mahmood et al., 2019; Nguyen and Montemor, 2019). The incorporation of graphene improves the conductivity of the pseudocapacitor electrode material and the constraints of the low specific capacitance of the graphene as a double-layer capacitor electrode material, and the advantages of the two are superimposed to achieve a substantial improvement in the capacitance performance, which is a feasible strategy for improving the electrochemical performance of the TMO/TMH electrode material.

TMOs/TMHs/CONDUCTING POLYMER HIERARCHICAL STRUCTURES

Conducting polymer has become an important electrode material for pseudocapacitors due to the advantages of large capacity, good conductivity, facile synthesis, and low cost

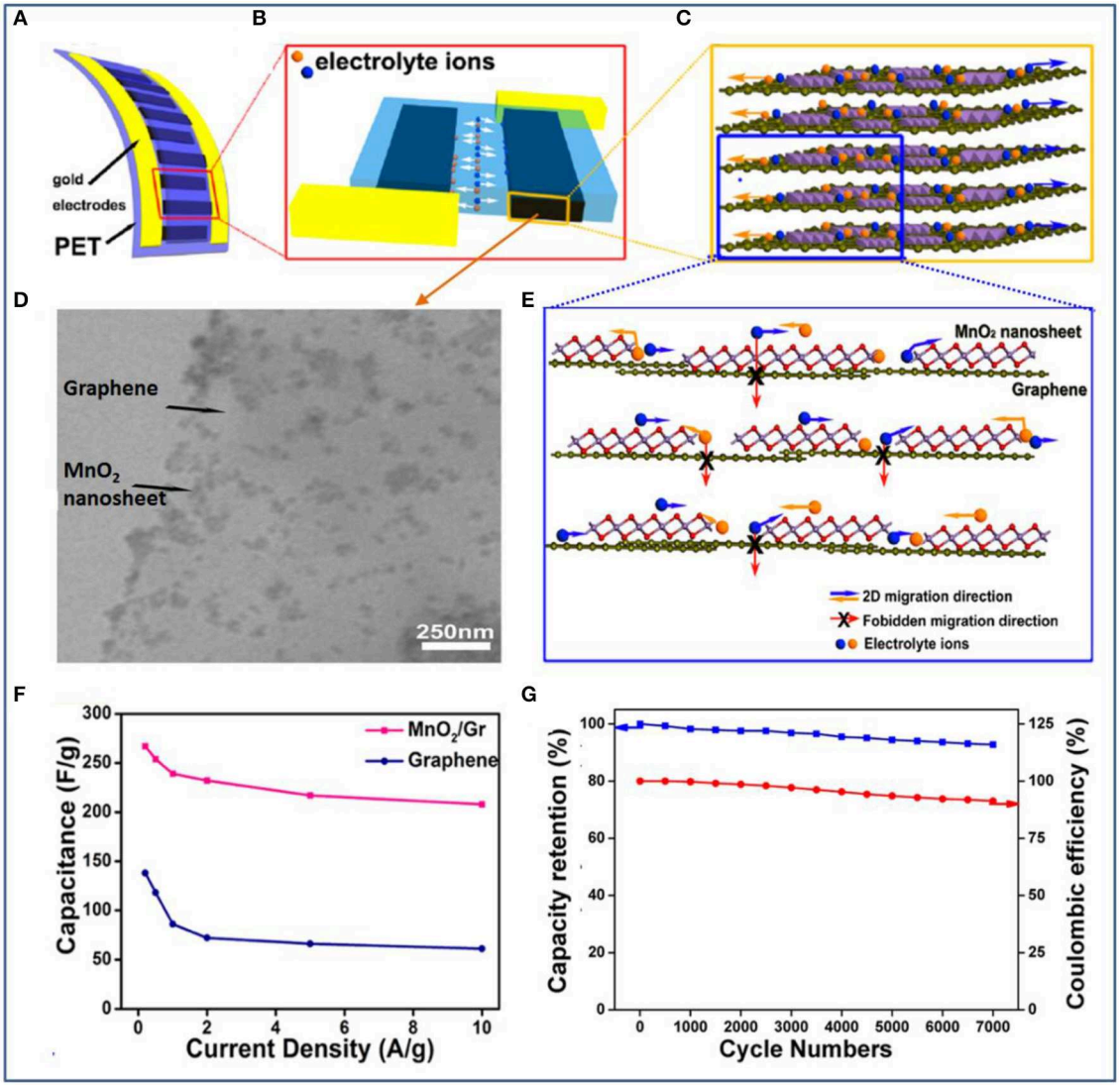

FIGURE 6 | (A) Schematic illustration of an ultraflexible planar supercapacitor constructed with a hybrid film as the working electrode, a current collector, and a gel electrolyte on a plastic polyethylene terephthalate (PET) substrate. **(B)** The planar supercapacitor unit, showing that the 2D hybrid thin film functions as two symmetric working electrodes. **(C)** The hybrid thin film was formed by stacking layers of chemically integrated quasi-2D δ-MnO_2 nanosheets and graphene sheets. **(D)** TEM image of the 2D hybrid structure with δ-MnO_2 nanosheets integrated on graphene surfaces. **(E)** Schematic description of the 2D planar ion transport favored within the 2D δ-MnO_2/graphene hybrid structures. **(F)** Comparison of specific capacitance values for the supercapacitors based on hybrids and based on graphene. **(G)** Capacitance retention (blue) and Coulombic efficiency (red) of the planar supercapacitor device based on hybrids over 7,000 charge/discharge cycles (Peng et al., 2013).

(Kalaji et al., 1999). In the past few years, conducting polymers have attracted increasing attention due to their great potential in supercapacitors. However, the conductive polymer-based electrode still suffers the drawbacks of low stability and poor mechanical properties, which restrict its application in fabricating supercapacitor devices (Liu et al., 2019). In terms of countermeasures, an inorganic-organic composite combination can improve the mechanical properties, electrochemical properties, and stability. Organic-inorganic composite electrode materials with excellent performance can be prepared to improve the specific capacitance and cycle stability of the electrode materials of supercapacitors.

As a representative conducting polymer, polyaniline (PANI) has frequently been used to combine with TMOs/TMHs to fabricate hierarchical structural hybrids for supercapacitor materials. As reported earlier, MoO_3/PANI nanocomposites have been synthesized by a simple *in-situ* synthesis method using molybdenum oxide precursor precipitation and aniline monomer as raw materials, as shown in **Figures 7A–C** (Zheng et al., 2011). The PANI polymer chains are assembled between oxide layers, which cause the nanocomposite to exhibit a flexible layered hierarchical structure. The electrical properties of metal oxides as active supercapacitor materials are greatly improved, which gives them excellent conductivity (**Figure 7D**).

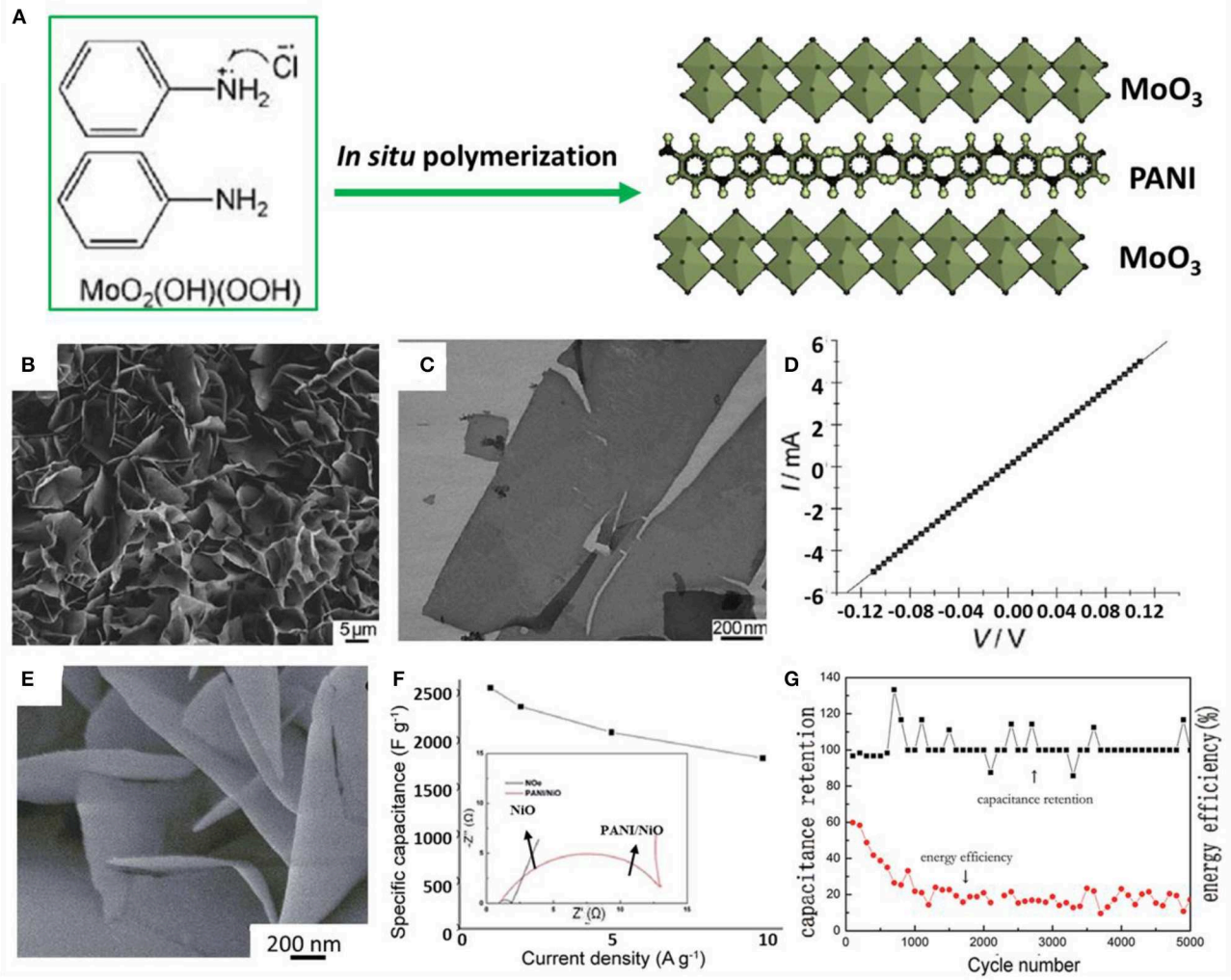

FIGURE 7 | (A) Representation of the simultaneous reaction mechanism of hybrid PANI/MoO_3 nanocomposites. **(B)** SEM images and **(C)** TEM images of the prepared hybrid PANI/MoO_3 nanosheets. **(D)** I–V characteristics of the hybrid nanosheet (Zheng et al., 2011). **(E)** SEM images of the PANI/NiO electrode. **(F)** Specific capacity of the PANI/NiO electrode in different current densities and (inset) EIS curves. **(G)** Capacitance retention and energy efficiency curves of the PANI/NiO electrode produced in the best condition (Sun et al., 2016).

The outstanding performance was inferred to derive from the robust bonding through *in-situ* polymerization. Hence, nanocomposites prepared by *in-situ* reaction at the molecular level have significantly improved specific capacity and cycle stability, making them very suitable for the electrochemical energy storage application.

A PANI-NiO composite on nickel foam that was used as a supercapacitor electrode and was fabricated via a binder-free *in-situ* approach showed high specific capacitance (2,565 F/g at a current density of 1 A/g) and excellent cycling stability (with a high retention of 100% for almost 5,000 cycles) (Sun et al., 2016). The flower-like hierarchical structures offer a structural benefit enabling high levels of redox (**Figures 7E–G**). Detailed studies revealed that the Ni foam was the current collector and Ni source for *in-situ* deposition of NiO, establishing a steadier bonding between collector and active material. PANI that was deposited directly onto the electrode supported the structure and prevented the functional space structure from being destroyed and collapsing during the charging–discharging process. The resultant impressive cycling stability shows considerable potential for commonly used energy storage devices with long service lives.

Post-functionalization of TMOs/TMHs with PANI through polymerization provides the hybrid core-shell or sandwich hierarchical configurations. For example, adsorption of benzene amine on MoO_3 nanobelts and further polymerization lead to the formation of coaxial heterostructure nanobelts of MoO_3/PANI, which exhibited lower electric resistance than MoO_3 nanobelts and pure PANI (**Figures 8A–F**). The supercapacitors achieved high specific capacitances of 714 F/g at a scan rate of I mV/s and 632 F/g at a current density of 1 A/g (Jiang et al., 2014).

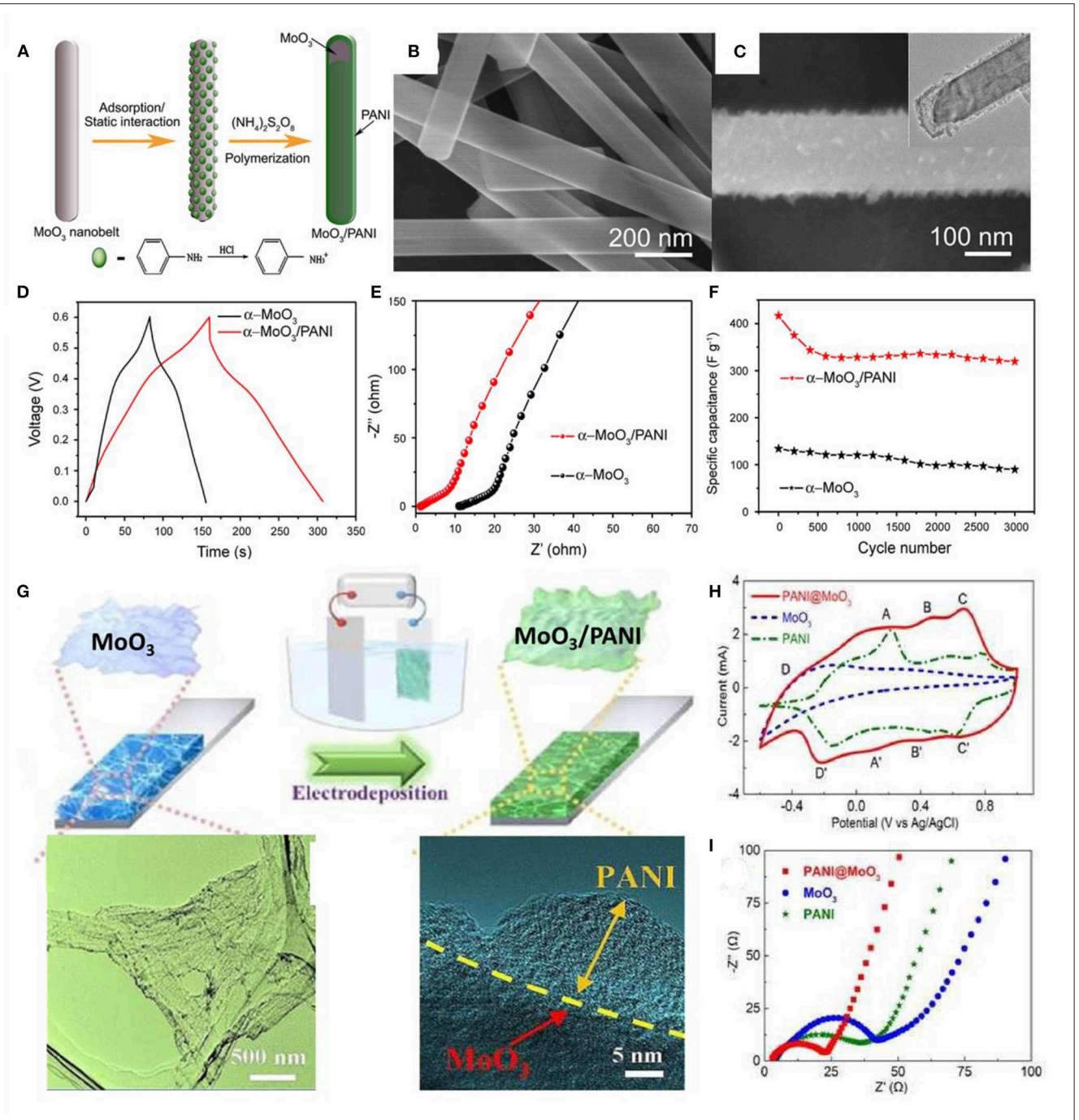

FIGURE 8 | (A) Schematic illustration of the formation of the MoO_3/PANI coaxial heterostructure nanobelts. **(B)** SEM images of the original α-MoO_3 nanobelts. **(C)** SEM images and (inset) TEM images of the as-synthesized MoO_3/PANI coaxial heterostructure nanobelts. **(D)** A comparison of the galvanostatic charge–discharge curves of the two comparative materials at a current density of 2 A/g. **(E)** EIS spectra comparison and **(F)** cycling performance at a scan rate of 50 mV/s of the two comparative materials (Jiang et al., 2014). **(G)** Schematic illustration for the synthesis process of 3D MoO_3/PANI hybrid nanosheet network film. **(H)** CV curves of MoO_3, PANI, and 3D MoO_3/PANI hybrid nanosheet network films in the potential range from −0.6 to 1 V at a scanning rate of 50 mV/s. **(I)** Nyquist plots of the MoO_3, PANI, and 3D MoO_3/PANI hybrid nanosheet network films (Zhang et al., 2017).

In order to overcome the low stability of conducting polymers as electrode material, a porous structure is usually introduced to guard against swelling and shrinking. In the case of a MoO_3/PANI hybrid (Zhang et al., 2017), 3D MoO_3 networks are formed through a freeze-drying process, in which the ice acts as a self-sacrificial template, and the different

nanosheets are connected by van der Waals and hydrogen bonds. The final 3D MoO_3/PANI hybrid networks were achieved by further electropolymerization of PANI onto the MoO_3 surface (**Figure 8G**). Electrochemical impedance characteristics (EIS) measurements demonstrated good electrical conductivity and ion diffusion behavior (**Figures 8H,I**). The intrinsic structural advantages and the synergetic interaction of the 3D networks make such a hierarchical configuration a promising structure for supercapacitor materials.

It can be seen from the above work that preparing inorganic-organic composite electrode materials by combining 2D TMOs/TMHs with conductive polymers can effectively improve the cycling, mechanical properties, and specific capacitance of the electrode, which can be used as an effective and feasible scheme for improving the electrochemical performance of the electrode of a supercapacitor.

SUMMARY AND PERSPECTIVES

A 2D TMOs/TMHs-based hierarchical structure combines the advantages of planar conductivity and a large specific surface area, making it an ideal candidate for the assembly of high-performance supercapacitors. To this end, finding new configurations with a hierarchical structure will guide the fabrication of supercapacitor materials with further-improved electrochemical performances. Besides TMOs/TMHs hierarchical structures, the integration of TMOs/TMHs with graphene or conductive polymer to form hierarchical structures has directed the recent steps forward in supercapacitor materials. In TMOs/TMHs-based hierarchical structures, graphene and conductive polymer are the key components for constructing flexible supercapacitors. By optimizing the TMOs/TMHs nanosheet orientation and stacking, electrons/ion transport channels were created, and performance was enhanced in the hierarchical energy storage devices. In summary, hierarchical structures form the prospective blueprint for fabricating high-performance supercapacitors by regulating morphologies and electronic properties.

Although great efforts have been put into supercapacitor materials in terms of the development of novel materials, synthetic technology, and structure engineering, a few problems remain at present. For instance, in TMOs/TMHs/graphene hierarchical structures, the weak interaction forces between capacitive TMOs/TMHs and graphene at the heterostructure interface have been an impediment to improving electrochemical performance. However, very recently, graphene was demonstrated to eliminate the boundary effect and enable electron behavior of the hybrid comparable with that of a single crystal without grain boundary. It is believed that this discovery may inspire fresh research into hierarchical structures using graphene as a component. Given the advantages of conductive polymer, rational design and synthesis of new types of conductive polymers with higher conductivity and stability are highly desirable, as this would pave the way for next-generation supercapacitors with superior flexibility and performance.

Besides assembling hierarchical structures for improvement of supercapacitor performance, attention could be paid to developing new 2D electroactive materials, such as the newly emerging 2D transition metal carbides/nitrides (MXenes), which possess extremely high intrinsic electronic/ionic conductivity. High intercalation capacitance ($\sim$1,000 F cm^{-3}) in aqueous electrolytes make these promising electrode materials for the future. Meanwhile, supercapacitor performance is also dependent on the voltage window, which is strictly limited by the electrolyte. Thus, a possible way forward is to increase the working voltage by using green electrolytes with a high electronic conductivity and voltage window, such as ionic liquid electrolytes.

AUTHOR CONTRIBUTIONS

All authors listed have made a substantial, direct and intellectual contribution to the work, and approved it for publication.

FUNDING

This work was financially supported by the National Natural Science Foundation of China for Youths (Grant Nos. 21701057, 21601067, 21905147), the Jiangsu Postdoctoral Research Foundation (Grant No. 1701109B), the China Postdoctoral Science Foundation (Grant No. 2017M611708), and the Scientific Research Startup Foundation of Jiangsu University (Grant No. 16JDG063).

REFERENCES

Ambade, R. B., Ambade, S. B., Shrestha, N. K., Salunkhe, R. R., Lee, W., Bagde, S. S., et al. (2017). Controlled growth of polythiophene nanofibers in TiO_2 nanotube arrays for supercapacitor applications. *J. Mater. Chem. A* 5, 172–180. doi: 10.1039/C6TA08038C

Augustyn, V., Come, J., Lowe, M. A., Kim, J. W., Taberna, P. L., Tolbert, S. H., et al. (2013). High-rate electrochemical energy storage through Li^+ intercalation pseudocapacitance. *Nat. Mater.* 12, 518–522. doi: 10.1038/nmat3601

Bao, J., Wang, Z., Liu, W., Xu, L., Lei, F., Xie, J., et al. (2018). $ZnCo_2O_4$ ultrathin nanosheets towards the high performance of flexible supercapacitors and bifunctional electrocatalysis. *J. Alloys Compd.* 764, 565–573. doi: 10.1016/j.jallcom.2018.06.085

Bao, J., Zhang, X., Bai, L., Bai, W., Zhou, M., Xie, J., et al. (2014). All-solid-state flexible thin-film supercapacitors with high electrochemical performance based on a two-dimensional V_2O_5•H_2O/graphene composite. *J. Mater. Chem. A* 2, 10876–10881. doi: 10.1039/c3ta15293f

Brezesinski, T., Wang, J., Tolbert, S. H., and Dunn, B. (2010). Ordered mesoporous α-MoO_3 with iso-oriented nanocrystalline walls for thin-film pseudocapacitors. *Nat. Mater.* 9, 146–151. doi: 10.1038/nmat2612

Bu, Y., Sun, T., Cai, Y., Du, L., Zhuo, O., Yang, L., et al. (2017). Compressing carbon nanocages by capillarity for optimizing porous structures toward ultrahigh-volumetric-performance supercapacitors. *Adv. Mater.* 29:1700470. doi: 10.1002/adma.201700470

Coleman, J. N., Lotya, M., O'Neill, A., Bergin, S. D., King, P. J., Khan, U., et al. (2011). Two-dimensional nanosheets produced by liquid exfoliation of layered materials. *Science* 331, 568–571. doi: 10.1126/science.1194975

Cranmer, A., Baker, E., Liesiö, J., and Salo, A. (2018). A portfolio model for siting offshore wind farms with economic and environmental objectives. *Eur. J. Oper. Res.* 267, 304–314. doi: 10.1016/j.ejor.2017.11.026

Dinh, T. M., Achour, A., Vizireanu, S., Dinescu, G., Nistor, L., Armstrong, K., et al. (2014). Hydrous RuO_2/carbon nanowalls hierarchical structures for all-solid-state ultrahigh-energy-density micro-supercapacitors. *Nano Energy* 10, 288–294. doi: 10.1016/j.nanoen.2014.10.003

Dutta, S., Pal, S., and De, S. (2019). Mixed solvent exfoliated transition metal oxides nanosheets based flexible solid state supercapacitor devices endowed with high energy density. *New J. Chem* 43, 12385–12395. doi: 10.1039/C9NJ03233A

Feng, X., Huang, Y., Chen, M., Chen, X., Li, C., Zhou, S., et al. (2018). Self-assembly of 3D hierarchical $MnMoO_4$/$NiWO_4$ microspheres for high-performance supercapacitor. *J. Alloys Compd.* 763, 801–807. doi: 10.1016/j.jallcom.2018.06.025

Frackowiak, E., and Beguin, F. (2001). Carbon materials for the electrochemical storage of energy in capacitors. *Carbon* 39, 937–950. doi: 10.1016/S0008-6223(00)00183-4

Fu, Y., Song, J., Zhu, Y., and Cao, C. (2014). High-performance supercapacitor electrode based on amorphous mesoporous $Ni(OH)_2$ nanoboxes. *J. Power Sources* 262, 344–348. doi: 10.1016/j.jpowsour.2014.04.002

Gamby, J., Taberna, P. L., Simon, P., Fauvarque, J. F., and Chesneau, M. (2001). Studies and characterisations of various activated carbons used for carbon/carbon supercapacitors. *J. Power Sources* 101, 109–116. doi: 10.1016/S0378-7753(01)00707-8

Gao, H., Cao, S., and Cao, Y. (2017). Hierarchical core-shell nanosheet arrays with MnO_2 grown on mesoporous $CoFe_2O_4$ support for high-performance asymmetric supercapacitors. *Electrochim. Acta* 240, 31–42. doi: 10.1016/j.electacta.2017.04.062

Gao, S., Sun, Y., Lei, F., Liang, L., Liu, J., Bi, W., et al. (2014). Ultrahigh energy density realized by a single-layer β-Co $(OH)_2$ all-solid-state asymmetric supercapacitor. *Angew. Chem. Int. Ed.* 53, 12789–12793. doi: 10.1002/anie.201407836

Gong, X., Liu, G., Li, Y., and Teoh, W. Y. (2016). Functionalized-graphene composites: fabrication and applications in sustainable energy and environment. *Chem. Mater.* 28, 8082–8118. doi: 10.1021/acs.chemmater.6b01447

González, A., Goikolea, E., Barrena, J. A., and Mysyk, R. (2016). Review on supercapacitors: technologies and materials. *Renew. Sust. Energ. Rev.* 58, 1189–1206. doi: 10.1016/j.rser.2015.12.249

Hanlon, D., Backes, C., Higgins, T. M., Hughes, M., O'Neill, A., King, P., et al. (2014). Production of molybdenum trioxide nanosheets by liquid exfoliation and their application in high-performance supercapacitors. *Chem. Mater.* 26, 1751–1763. doi: 10.1021/cm500271u

Ho, K. C., and Lin, L. Y. (2019). A review of electrode materials based on core–shell nanostructures for electrochemical supercapacitors. *J. Mater. Chem. A* 7, 3516–3530. doi: 10.1039/C8TA11599K

Hu, Z., Xiao, X., Jin, H., Li, T., Chen, M., Liang, Z., et al. (2017). Rapid mass production of two-dimensional metal oxides and hydroxides via the molten salts method. *Nat. Commun.* 8, 1–9. doi: 10.1038/ncomms15630

Huang, M., Zhang, Y., Li, F., Zhang, L., Ruoff, R. S., Wen, Z., et al. (2014). Self-assembly of mesoporous nanotubes assembled from interwoven ultrathin birnessite-type MnO_2 nanosheets for asymmetric supercapacitors. *Sci. Rep.* 4:3878. doi: 10.1038/srep03878

Huang, Y., Tao, J., Meng, W., Zhu, M., Huang, Y., Fu, Y., et al. (2015). Super-high rate stretchable polypyrrole-based supercapacitors with excellent cycling stability. *Nano Energy* 11, 518–525. doi: 10.1016/j.nanoen.2014.10.031

Huang, Z. H., Song, Y., Feng, D. Y., Sun, Z., Sun, X., and Liu, X. X. (2018). High mass loading MnO_2 with hierarchical nanostructures for supercapacitors. *ACS Nano* 12, 3557–3567. doi: 10.1021/acsnano.8b00621

Ida, S., Shiga, D., Koinuma, M., and Matsumoto, Y. (2008). Synthesis of hexagonal nickel hydroxide nanosheets by exfoliation of layered nickel hydroxide intercalated with dodecyl sulfate ions. *J. Am. Chem. Soc.* 130, 14038–14039. doi: 10.1021/ja804397n

Ji, X., Hallam, P. M., Houssein, S. M., Kadara, R., Lang, L., and Banks, C. E. (2012). Printable thin film supercapacitors utilizing single crystal cobalt hydroxide nanosheets. *RSC Adv.* 2, 1508–1515. doi: 10.1039/C1RA01061A

Jiang, F., Li, W., Zou, R., Liu, Q., Xu, K., An, L., et al. (2014). MoO_3/PANI coaxial heterostructure nanobelts by *in situ* polymerization for high performance supercapacitors. *Nano Energy* 7, 72–79. doi: 10.1016/j.nanoen.2014.04.007

Jiang, J., Li, Y., Liu, J., Huang, X., Yuan, C., and Lou, X. W. (2012). Recent advances in metal oxide-based electrode architecture design for electrochemical energy storage. *Adv. Mater.* 24, 5166–5180. doi: 10.1002/adma.201202146

Jin, Y., Tian, K., Wei, L., Zhang, X., and Guo, X. (2016). Hierarchical porous microspheres of activated carbon with a high surface area from spores for electrochemical double-layer capacitors. *J. Mater. Chem. A* 4, 15968–15979. doi: 10.1039/C6TA05872H

Kalaji, M., Murphy, P. J., and Williams, G. O. (1999). The study of conducting polymers for use as redox supercapacitors. *Synth. Met.* 102, 1360–1361. doi: 10.1016/S0379-6779(98)01334-4

Kate, R. S., Khalate, S. A., and Deokate, R. J. (2018). Overview of nanostructured metal oxides and pure nickel oxide (NiO) electrodes for supercapacitors: a review. *J. Alloys Compd.* 734, 89–111. doi: 10.1016/j.jallcom.2017.10.262

Kumbhar, V. S., and Kim, D. H. (2018). Hierarchical coating of MnO_2 nanosheets on $ZnCo_2O_4$ nanoflakes for enhanced electrochemical performance of asymmetric supercapacitors. *Electrochim. Acta* 271, 284–296. doi: 10.1016/j.electacta.2018.03.147

Lee, H., Cho, M. S., Kim, I. H., Nam, J. D., and Lee, Y. (2010). RuO_x/polypyrrole nanocomposite electrode for electrochemical capacitors. *Synth. Met.* 160, 1055–1059. doi: 10.1016/j.synthmet.2010.02.026

Lee, W. J., and Sung, Y. M. (2012). Synthesis of anatase nanosheets with exposed (001) facets via chemical vapor deposition. *Cryst. Growth Des.* 12, 5792–5795. doi: 10.1021/cg301317j

Li, Z., Hu, Z., Peng, J., Wu, C., Yang, Y., Feng, F., et al. (2014). Ultrahigh infrared photoresponse from core–shell single-domain-VO_2/V_2O_5 heterostructure in nanobeam. *Adv. Funct. Mater.* 24, 1821–1830. doi: 10.1002/adfm.201302967

Lim, Y., Yoon, J., Yun, J., Kim, D., Hong, S. Y., Lee, S. J., et al. (2015). Correction to biaxially stretchable, integrated array of high performance microsupercapacitors. *ACS Nano* 9, 6634–6634. doi: 10.1021/acsnano.5b02991

Liu, C., Yu, Z., Neff, D., Zhamu, A., and Jang, B. Z. (2010). Graphene-based supercapacitor with an ultrahigh energy density. *Nano Lett.* 10, 4863–4868. doi: 10.1021/nl102661q

Liu, J., Zhang, L., Wu, H. B., Lin, J., Shen, Z., and Lou, X. W. D. (2014). High-performance flexible asymmetric supercapacitors based on a new graphene foam/carbon nanotube hybrid film. *Energy Environ. Sci.* 7, 3709–3719. doi: 10.1039/C4EE01475H

Liu, J., Zhong, M., Li, J., Pan, A., and Zhu, X. (2015). Few-layer WO_3 nanosheets for high-performance UV-photodetectors. *Mater. Lett.* 148, 184–187. doi: 10.1016/j.matlet.2015.02.088

Liu, L., Yao, T., Tan, X., Liu, Q., Wang, Z., Shen, D., et al. (2012). Room temperature intercalation-deintercalation strategy towards VO_2 (B) single layers with atomic thickness. *Small* 8, 3752–3756. doi: 10.1002/smll.201201552

Liu, P., Yan, J., Guang, Z., Huang, Y., Li, X., Huang, W., et al. (2019). Recent advancements of polyaniline-based nanocomposites for supercapacitors. *J. Power Sources* 424, 108–130. doi: 10.1016/j.jpowsour.2019.03.094

Liu, R., Cho, S. I., and Lee, S. B. (2008). Poly(3, 4-ethylenedioxythiophene) nanotubes as electrode materials for a high-powered supercapacitor. *Nanotechnology* 19:215710. doi: 10.1088/0957-4484/19/21/215710

Liu, W., Wang, Z., Su, Y., Li, Q., Zhao, Z., and Geng, F. (2017). Molecularly stacking manganese dioxide/titanium carbide sheets to produce highly flexible and conductive film electrodes with improved pseudocapacitive performances. *Adv. Energy Mater.* 7:1602834. doi: 10.1002/aenm.201602834

Liu, Y., Liang, L., Xiao, C., Hua, X., Li, Z., Pan, B., et al. (2016). Promoting photogenerated holes utilization in pore-rich WO_3 ultrathin nanosheets for efficient oxygen-evolving photoanode. *Adv. Energy Mater.* 6:1600437. doi: 10.1002/aenm.201600437

Liu, Y., Zhou, T., Zheng, Y., He, Z., Xiao, C., Pang, W. K., et al. (2017). Local electric field facilitates high-performance Li-ion batteries. *ACS Nano* 11, 8519–8526. doi: 10.1021/acsnano.7b04617

Lukatskaya, M. R., Dunn, B., and Gogotsi, Y. (2016). Multidimensional materials and device architectures for future hybrid energy storage. *Nat. Commun.* 7, 1–13. doi: 10.1038/ncomms12647

Lyu, W., Yu, M., Feng, J., and Yan, W. (2019). Facile synthesis of coral-like hierarchical polyaniline micro/nanostructures with enhanced supercapacitance and adsorption performance. *Polymer* 162, 130–138. doi: 10.1016/j.polymer.2018.12.037

Mahmood, N., De Castro, I. A., Pramoda, K., Khoshmanesh, K., Bhargava, S. K., and Kalantar-Zadeh, K. (2019). Atomically thin two-dimensional metal oxide

nanosheets and their heterostructures for energy storage. *Energy Storage Mater.* 16, 455–480. doi: 10.1016/j.ensm.2018.10.013

Mei, J., Liao, T., and Sun, Z. (2018). Two-dimensional metal oxide nanosheets for rechargeable batteries. *J. Energy Chem.* 27, 117–127. doi: 10.1016/j.jechem.2017.10.012

Mo, Z., Xu, H., Chen, Z., She, X., Song, Y., Wu, J., et al. (2018). Self-assembled synthesis of defect-engineered graphitic carbon nitride nanotubes for efficient conversion of solar energy. *Appl. Catal. B Environ.* 225, 154–161. doi: 10.1016/j.apcatb.2017.11.041

Muzaffar, A., Ahamed, M. B., Deshmukh, K., and Thirumalai, J. (2019). A review on recent advances in hybrid supercapacitors: design, fabrication and applications. *Renew. Sust. Energ. Rev.* 101, 123–145. doi: 10.1016/j.rser.2018.10.026

Najafpour, M. M., Hołynska, M., and Salimi, S. (2015). Applications of the "nano to bulk" Mn oxides: Mn oxide as a Swiss army knife. *Coordin. Chem. Rev.* 285, 65–75. doi: 10.1016/j.ccr.2014.11.001

Nguyen, T., and Montemor, M. D. F. (2019). Metal oxide and hydroxide–based aqueous supercapacitors: from charge storage mechanisms and functional electrode engineering to need-tailored devices. *Adv. Sci.* 6:1801797. doi: 10.1002/advs.201801797

Novoselov, K. S., Fal, V. I., Colombo, L., Gellert, P. R., Schwab, M. G., and Kim, K. (2012). A roadmap for graphene. *Nature* 490, 192–200. doi: 10.1038/nature11458

Ouyang, Y., Huang, R., Xia, X., Ye, H., Jiao, X., Wang, L., et al. (2019). Hierarchical structure electrodes of NiO ultrathin nanosheets anchored to $NiCo_2O_4$ on carbon cloth with excellent cycle stability for asymmetric supercapacitors. *Chem. Eng. J.* 355, 416–427. doi: 10.1016/j.cej.2018.08.142

Peng, L., Peng, X., Liu, B., Wu, C., Xie, Y., and Yu, G. (2013). Ultrathin two-dimensional MnO_2/graphene hybrid nanostructures for high-performance, flexible planar supercapacitors. *Nano Lett.* 13, 2151–2157. doi: 10.1021/nl400600x

Peng, X., Guo, Y., Yin, Q., Wu, J., Zhao, J., Wang, C., et al. (2017). Double-exchange effect in two-dimensional MnO_2 nanomaterials. *J. Am. Chem. Soc.* 139, 5242–5248. doi: 10.1021/jacs.7b01903

Qi, R., Nie, J., Liu, M., Xia, M., and Lu, X. (2018). Stretchable V_2O_5/PEDOT supercapacitors: a modular fabrication process and charging with triboelectric nanogenerators. *Nanoscale* 10, 7719–7725. doi: 10.1039/C8NR00444G

Rui, X., Lu, Z., Yu, H., Yang, D., Hng, H. H., Lim, T. M., et al. (2013). Ultrathin V_2O_5 nanosheet cathodes: realizing ultrafast reversible lithium storage. *Nanoscale* 5, 556–560. doi: 10.1039/C2NR33422D

Salanne, M., Rotenberg, B., Naoi, K., Kaneko, K., Taberna, P. L., Grey, C. P., et al. (2016). Efficient storage mechanisms for building better supercapacitors. *Nat. Energy* 1, 1–10. doi: 10.1038/nenergy.2016.70

Shang, Y., Wang, C., He, X., Li, J., Peng, Q., Shi, E., et al. (2015). Self-stretchable, helical carbon nanotube yarn supercapacitors with stable performance under extreme deformation conditions. *Nano Energy* 12, 401–409. doi: 10.1016/j.nanoen.2014.11.048

Simon, P., and Gogotsi, Y. (2010). "Materials for electrochemical capacitors," in *Nanoscience and Technology*, 320–329. doi: 10.1142/9789814287005_0033

Snook, G. A., Kao, P., and Best, A. S. (2011). Conducting-polymer-based supercapacitor devices and electrodes. *J. Power Sources* 196, 1–12. doi: 10.1016/j.jpowsour.2010.06.084

Song, M. S., Lee, K. M., Lee, Y. R., Kim, I. Y., Kim, T. W., Gunjakar, J. L., et al. (2010). Porously assembled 2D nanosheets of alkali metal manganese oxides with highly reversible pseudocapacitance behaviors. *J. Phy. Chem. C* 114, 22134–22140. doi: 10.1021/jp108969s

Song, X., Shi, Y., Li, G., Shen, Z., Hu, X., Lyu, Z., et al. (2018). Numerical analysis of the heat production performance of a closed loop geothermal system. *Renew Energy* 120, 365–378. doi: 10.1016/j.renene.2017.12.065

Staaf, L. G. H., Lundgren, P., and Enoksson, P. (2014). Present and future supercapacitor carbon electrode materials for improved energy storage used in intelligent wireless sensor systems. *Nano Energy* 9, 128–141. doi: 10.1016/j.nanoen.2014.06.028

Stankovich, S., Dikin, D. A., Dommett, G. H., Kohlhaas, K. M., Zimney, E. J., Stach, E. A., et al. (2006). Graphene-based composite materials. *Nature* 442, 282–286. doi: 10.1038/nature04969

Sugimoto, W., Iwata, H., Yasunaga, Y., Murakami, Y., and Takasu, Y. (2003). Preparation of ruthenic acid nanosheets and utilization of its interlayer surface for electrochemical energy storage. *Angew. Chem. Int. Ed.* 42, 4092–4096. doi: 10.1002/anie.200351691

Sun, B., He, X., Leng, X., Yang, J., Zhao, Y., Suo, H., et al. (2016). Flower-like polyaniline–NiO structures: a high specific capacity supercapacitor electrode material with remarkable cycling stability. *RSC Adv.* 6, 43959–43963. doi: 10.1039/C6RA02534J

Sun, J., Li, W., Zhang, B., Li, G., Jiang, L., Chen, Z., et al. (2014). 3D core/shell hierarchies of MnOOH ultrathin nanosheets grown on NiO nanosheet arrays for high-performance supercapacitors. *Nano Energy* 4, 56–64. doi: 10.1016/j.nanoen.2013.12.006

Sun, Z., Liao, T., Dou, Y., Hwang, S. M., Park, M. S., Jiang, L., et al. (2014). Generalized self-assembly of scalable two-dimensional transition metal oxide nanosheets. *Nat. Commun.* 5, 1–9. doi: 10.1038/ncomms4813

Sun, Z., Liao, T., and Kou, L. (2017). Strategies for designing metal oxide nanostructures. *Sci. China Mater.* 60, 1–24. doi: 10.1007/s40843-016-5117-0

Tao, P., Yao, S., Liu, F., Wang, B., Huang, F., and Wang, M. (2019). Recent advances in exfoliation techniques of layered and non-layered materials for energy conversion and storage. *J. Mater. Chem. A* 7, 23512–23536. doi: 10.1039/C9TA06461C

Wang, C., Du, G., Stahl, K., Huang, H., Zhong, Y., and Jiang, J. Z. (2012). Ultrathin SnO_2 nanosheets: oriented attachment mechanism, nonstoichiometric defects, and enhanced lithium-ion battery performances. *J. Phys. Chem. C.* 116, 4000–4011. doi: 10.1021/jp300136p

Wang, F., Wu, X., Yuan, X., Liu, Z., Zhang, Y., Fu, L., et al. (2017). Latest advances in supercapacitors: from new electrode materials to novel device designs. *Chem. Soc. Rev.* 46, 6816–6854. doi: 10.1039/C7CS00205J

Wang, G., Zhang, L., and Zhang, J. (2012). A review of electrode materials for electrochemical supercapacitors. *Chem. Soc. Rev.* 41, 797–828. doi: 10.1039/C1CS15060J

Wang, Y., Guo, J., Wang, T., Shao, J., Wang, D., and Yang, Y. W. (2015). Mesoporous transition metal oxides for supercapacitors. *Nanomater* 5, 1667–1689. doi: 10.3390/nano5041667

Wen, P., Ai, L., Liu, T., Hu, D., and Yao, F. (2017). Hydrothermal topological synthesis and photocatalyst performance of orthorhombic Nb_2O_5 rectangle nanosheet crystals with dominantly exposed (010) facet. *Mater. Des.* 117, 346–352. doi: 10.1016/j.matdes.2017.01.004

Wen, S., Liu, Y., Zhu, F., Shao, R., and Xu, W. (2018). Hierarchical MoS_2 nanowires/$NiCo_2O_4$ nanosheets supported on Ni foam for high-performance asymmetric supercapacitors. *Appl. Surf. Sci.* 428, 616–622. doi: 10.1016/j.apsusc.2017.09.189

Wu, H. B., Pang, H., and Lou, X. W. D. (2013). Facile synthesis of mesoporous $Ni_{0.3}Co_{2.7}O_4$ hierarchical structures for high-performance supercapacitors. *Energy Environ. Sci.* 6, 3619–3626. doi: 10.1039/c3ee42101e

Xie, J., Sun, X., Zhang, N., Xu, K., Zhou, M., and Xie, Y. (2013). Layer-by-layer β-Ni $(OH)_2$/graphene nanohybrids for ultraflexible all-solid-state thin-film supercapacitors with high electrochemical performance. *Nano Energy* 2, 65–74. doi: 10.1016/j.nanoen.2012.07.016

Xu, Q., Lv, Y., Dong, C., Sreeprased, T. S., Tian, A., Zhang, H., et al. (2015). Three-dimensional micro/nanoscale architectures: fabrication and applications. *Nanoscale* 7, 10883–10895. doi: 10.1039/C5NR02048D

Yang, J., Zeng, Z., Kang, J., Betzler, S., Czarnik, C., Zhang, X., et al. (2019). Formation of two-dimensional transition metal oxide nanosheets with nanoparticles as intermediates. *Nat. Mater.* 18, 970–976. doi: 10.1038/s41563-019-0415-3

Yu, M., Qiu, W., Wang, F., Zhai, T., Fang, P., Lu, X., et al. (2015). Three dimensional architectures: design, assembly and application in electrochemical capacitors. *J. Mater. Chem. A* 3, 15792–15823. doi: 10.1039/C5TA02743H

Yu, T., Lim, B., and Xia, Y. (2010). Aqueous-phase synthesis of single-crystal ceria nanosheets. *Angew. Chem. Int. Ed.* 49, 4484–4487. doi: 10.1002/anie.201001521

Yuan, C., Wu, H. B., Xie, Y., and Lou, X. W. (2014). Mixed transition-metal oxides: design, synthesis, and energy-related applications. *Angew. Chem. Int. Ed.* 53, 1488–1504. doi: 10.1002/anie.201303971

Yue, Y., and Liang, H. (2015). Hierarchical micro-architectures of electrodes for energy storage. *J. Power Sources* 284, 435–445. doi: 10.1016/j.jpowsour.2015.03.069

Yuksel, Y. E., and Ozturk, M. (2017). Thermodynamic and thermoeconomic analyses of a geothermal energy based integrated system for

hydrogen production. *Int. J. Hydrog. Energ.* 42, 2530–2546. doi: 10.1016/j.ijhydene.2016.04.172

Zavabeti, A., Ou, J. Z., Carey, B. J., Syed, N., Orrell-Trigg, R., Mayes, E. L., et al. (2017). A liquid metal reaction environment for the room-temperature synthesis of atomically thin metal oxides. *Science* 358, 332–335. doi: 10.1126/science.aao4249

Zhang, H., Gao, L., and Gong, Y. (2015). Exfoliated MoO_3 nanosheets for high-capacity lithium storage. *Electrochem. Commun.* 52, 67–70. doi: 10.1016/j.elecom.2015.01.014

Zhang, K., Wang, Y., Ma, X., Zhang, H., Hou, S., Zhao, J., et al. (2017). Three dimensional molybdenum oxide/polyaniline hybrid nanosheet networks with outstanding optical and electrochemical properties. *New J. Chem.* 41, 10872–10879. doi: 10.1039/C7NJ02151H

Zhang, N., Chu, J., Li, C., Chen, H., and Li, Q. (2010). A facile route to synthesize the Ti_5NbO_{14} nanosheets by mechanical cleavage process *J. Am. Ceram. Soc.* 93, 536–540. doi: 10.1111/j.1551-2916.2009.03405.x

Zhang, Y. Z., Wang, Y., Cheng, T., Lai, W. Y., Pang, H., and Huang, W. (2015). Flexible supercapacitors based on paper substrates: a new paradigm for low-cost energy storage. *Chem. Soc. Rev.* 44, 5181–5199. doi: 10.1039/C5CS00174A

Zhao, G., Li, J., Jiang, L., Dong, H., Wang, X., and Hu, W. (2012). Synthesizing MnO_2 nanosheets from graphene oxide templates for high performance pseudosupercapacitors. *Chem. Sci.* 3, 433–437. doi: 10.1039/C1SC00722J

Zhao, Y., and Sun, X. (2018). Molecular layer deposition for energy conversion and storage. *ACS Energy Lett.* 3, 899–914. doi: 10.1021/acsenergylett.8b00145

Zheng, L., Xu, Y., Jin, D., and Xie, Y. (2011). Polyaniline-intercalated molybdenum oxide nanocomposites: simultaneous synthesis and their enhanced application for supercapacitor. *Chem. Asian J.* 6, 1505–1514. doi: 10.1002/asia.201000770

Zheng, M., Xiao, X., Li, L., Gu, P., Dai, X., Tang, H., et al. (2018). Hierarchically nanostructured transition metal oxides for supercapacitors. *Sci. China Mater.* 61, 185–209. doi: 10.1007/s40843-017-9095-4

Zheng, X., Ye, Y., Yang, Q., Geng, B., and Zhang, X. (2016). Hierarchical structures composed of $MnCo_2O_4$@MnO_2 core–shell nanowire arrays with enhanced supercapacitor properties. *Dalton Trans.* 45, 572–578. doi: 10.1039/C5DT03780H

Zhu, G., Xi, C., Xu, H., Zheng, D., Liu, Y., Xu, X., et al. (2012). Hierarchical NiO hollow microspheres assembled from nanosheet-stacked nanoparticles and their application in a gas sensor. *RSC Adv.* 2, 4236–4241. doi: 10.1039/c2ra01307j

Zhu, J., Cao, L., Wu, Y., Gong, Y., Liu, Z., Hoster, H. E., et al. (2013). Building 3D structures of vanadium pentoxide nanosheets and application as electrodes in supercapacitors. *Nano Lett.* 13, 5408–5413. doi: 10.1021/nl402969r

Zhu, S., Li, L., Liu, J., Wang, H., Wang, T., Zhang, Y., et al. (2018). Structural directed growth of ultrathin parallel birnessite on β-MnO_2 for high-performance asymmetric supercapacitors. *ACS Nano* 12, 1033–1042. doi: 10.1021/acsnano.7b03431

Zhu, Y., Cao, C., Tao, S., Chu, W., Wu, Z., and Li, Y. (2014). Ultrathin nickel hydroxide and oxide nanosheets: synthesis, characterizations and excellent supercapacitor performances. *Sci. Rep.* 4:5787. doi: 10.1038/srep 05787

Conflict of Interest: The authors declare that the research was conducted in the absence of any commercial or financial relationships that could be construed as a potential conflict of interest.

frontiers in Chemistry

MINI REVIEW
published: 19 May 2020
doi: 10.3389/fchem.2020.00426

Hierarchical Porous Molybdenum Carbide Based Nanomaterials for Electrocatalytic Hydrogen Production

*Yan Liu[1], Juanjuan Huo[1], Jiaojiao Guo[1], Li Lu[1], Ziyan Shen[1], Weihua Chen[2], Chuntai Liu[2] and Hao Liu[1,3]**

[1] Joint International Laboratory on Environmental and Energy Frontier Materials, School of Environmental and Chemical Engineering, Shanghai University, Shanghai, China, [2] Key Laboratory of Materials Processing and Mold (Zhengzhou University), Ministry of Education, Zhengzhou, China, [3] Centre for Clean Energy Technology, School of Mathematical and Physical Sciences, Faculty of Science, University of Technology Sydney, Sydney, NSW, Australia

The electrocatalytic hydrogen evolution reaction (HER) for the preparation of hydrogen fuel is a very promising technology to solve the shortage of hydrogen storage. However, in practical applications, HER catalysts with excellent performance and moderate price are very rare. Molybdenum carbide (Mo_xC) has attracted extensive attention due to its electronic structure and natural abundance. Here, a comprehensive review of the preparation and performance control of hierarchical porous molybdenum carbide (HP-Mo_xC) based catalysts is summarized. The methods for preparing hierarchical porous materials and the regulation of their HER performance are mainly described. Briefly, the HP-Mo_xC based catalysts were prepared by template method, morphology-conserved transformations method, and secondary conversion method of an organic-inorganic hybrid material. The intrinsic HER kinetics are enhanced by the introduction of a carbon-based support, heteroatom doping, and the construction of a heterostructure. Finally, the future development of HP-Mo_xC based catalysts is prospected in this review.

Keywords: hierarchical structure, electrocatalytic reaction, hydrogen production, porous structure, molybdenum carbide

OPEN ACCESS

Edited by:
Tengfei Zhou,
University of Wollongong, Australia

Reviewed by:
Yao Zheng,
University of Adelaide, Australia
Jintao Zhang,
Shandong University, China
Bin Wang,
China Academy of Engineering Physics, China

***Correspondence:**
Hao Liu
hao.liu@uts.edu.au

Specialty section:
This article was submitted to Nanoscience, a section of the journal Frontiers in Chemistry

Received: *21 March 2020*
Accepted: *23 April 2020*
Published: *19 May 2020*

Citation:
Liu Y, Huo J, Guo J, Lu L, Shen Z, Chen W, Liu C and Liu H (2020) Hierarchical Porous Molybdenum Carbide Based Nanomaterials for Electrocatalytic Hydrogen Production. Front. Chem. 8:426. doi: 10.3389/fchem.2020.00426

INTRODUCTION

Hydrogen is a green energy with high energy density and excellent combustion performance (Martinez et al., 2019; Yang et al., 2019). HER is a key reaction for the renewable production of hydrogen. However, the actual reaction process is inefficient. In order to increase the conversion efficiency of the reaction process and reduce the reaction overpotential, a certain amount of catalyst is usually used (Chen et al., 2018; Huo et al., 2019; Ling et al., 2019). The ideal electrocatalyst for the HER is platinum (Pt) or other precious metals, but its application is severely limited by low richness and high cost (Khaselev and Turner, 1998; Nong et al., 2018).

Mo_xC has a wide range of applications in the fields of energy storage and conversion, for example, hydrodesulf'urization, denitrification (Wang et al., 2007; Ma et al., 2018), methanol reforming, electrolyte, etc. (Gao et al., 2010; Lin et al., 2017b; Yang et al., 2020). Density functional theory (DFT) calculations of carbides show that the hybridization of metal d orbitals with carbon s and p orbitals causes wider d-band structure, showing

a d-band structure similar to Pt (Zhao et al., 2019b). This makes Mo_xC a promising alternative to precious metal catalysts. Conventional Mo_xC based catalysts generally have no voids or low porosity, resulting in low active surface area and poor wettability. Designing hierarchical porous micro/nanostructures can solve these problems. The hierarchical porous material has multi-stage pore structure, which is micropores (<2 nm), mesopores (2–50 nm) and macropores (>50 nm) (Li et al., 2019b). The properties and functions of a material depend on the characteristics of its structure, such as pore size, shape, porosity, etc. (Ryoo, 2019). In general, the presence of micropores provides a large surface area, mesoporous, and macroporous structures are effective in improving electrolyte penetration and promoting ion diffusion. The structure of hierarchical porous materials is usually assembled from nanoscale units by van der Waals forces, ionic bonds, covalent bonds and hydrogen bonds. The preparation of HP-Mo_xC based catalysts prevents the agglomeration of the nanoparticles, greatly increasing the specific surface area of the material and exposing more active sites (Kim et al., 2020). Compared with other non-precious metal catalysts, HP-Mo_xC has a hierarchical porous structure on the macro scale and a d-band structure similar to Pt on the micro scale, which makes it exhibiting unique advantages.

This review focuses on the preparation and performance of HP-Mo_xC based catalysts, including soft-hard template method, morphology-conserved transformations, secondary conversion of organic-inorganic hybrid materials to construct catalysts with specific morphology. By introducing other conductive carriers, heterogeneous doping and construct heterostructured hybrids to optimize the HER performance of HP-Mo_xC based catalysts. **Table 1** shows the performance parameters of each catalyst mentioned in this article. Finally, an overview of the future development of HP-Mo_xC based electrocatalysts is outlined.

CONSTRUCTION OF HP-Mo_XC WITH SPECIAL MORPHOLOGY

HP-Mo_xC based catalysts with a special morphology have many excellent properties such as rapid mass transfer, ultra-high surface area, controlled pore size and nano-effects (Niu et al., 2019; Wang et al., 2019b). Therefore, it is becoming more and

TABLE 1 | Summary of HER performance of Pt/C and various catalysts appearing in the article.

	Method	Catalyst	η_{onset} (mv)	η_{10} (mv)	Electrolyte	Tafel slope (mv dec^{-1})	References
Preparation	Template method	uf-Mo_2C/CF	49	184	Acidic	71	Kou et al., 2018
		Mo_2C/MCS	73	134	Alkaline	51	Yuan et al., 2019
	Morphology-conserved transformations	Nano MoC@GS	84	132	Acidic	46	Shi et al., 2016
		Porous MoCx nano-octahedrons	25	142	Acidic	5	Wu et al., 2015
			80	151	Alkaline	59	
		MoC-Mo_2C/PNCDS	121	\	Alkaline	60	Lu et al., 2019
	Secondary conversion of organic-inorganic hybrid materials	np-Mo_2C NW	70	\	Acidic	\	Liao et al., 2014
		P-Mo_2C NWs	42	89	Acidic	42	Shi et al., 2017
Regulation	Introducing other conductive carriers	Mo_2C-RGO	70	130	Acidic	54	Pan et al., 2014
		Mo_2C/G	\	175	Acidic	88	Huang et al., 2019c
			\	200	Alkaline	82	
		Mo_2C@NC nanomesh	\	37.5	Acidic	33.7	Cheng et al., 2018
	Doping	Mo_2C-N-CNFS	105	192	Acidic	70	Wu et al., 2016
		Ni/Mo_2C-NCNFS	29	143	Alkaline	57.8	Li et al., 2019b
		NP-MO_2C	\	210	Acidic	64	Wang et al., 2018a
	Hierarchical porous molybdenum carbide-based heterostructure	Mo-Mo_2C	67	150	Acidic	55	Dong et al., 2018
		Mo_2C/VC@C	\	122	Acidic	43.8	Huang et al., 2019a
		Pt/C	0	28	Acidic	33	
			0	43	Alkaline	113	

η_{10}, overpotentials to drive the current densities of 10 mA cm^{-2}.
η_{onset}, oneset overpotential.

more important to construct various forms of nano-catalytic materials. The use of nanotechnology makes it possible to expose as many active sites as possible during electrocatalysis, thereby improving HER performance (Hou et al., 2019). However, how to control the structural size and shape of materials still poses great challenges in the current research process.

Template Method to Construct HP-Mo_xC Based Catalysts

The template method is one of the effective methods for preparing hierarchical porous materials, and can effectively control the morphology, particle size, and structure during the preparation process (Huang et al., 2019b; Zhao et al., 2019a). It is mainly divided into hard template method and soft template method. The hard template has rigid structure and specific morphology, and its morphology is copied into the target material by nano-replication technology. The obtained product has good dispersibility, controllable pore size and has been widely used (Chen et al., 2019; Feng et al., 2019).

Due to the stability of the hard template structure, the precursors are often used as "microreactor" in the synthesis process (Liu et al., 2019). The colloidal crystal (Thompson et al., 2019) contains a large amount of monodisperse colloidal particles, which are uniformly arranged in three dimensions. Using colloidal crystals as sacrificial hard templates, ordered and monodisperse pores can be introduced into the material. Kou et al. (2018) prepared hierarchical porous molybdenum carbide nanocrystals (uf-Mo_2C/CF) with efficient HER performance by using uniformly-sized SiO_2 microspheres as confined template (**Figure 1A**). Average size of nanocrystals is <2 nm. This

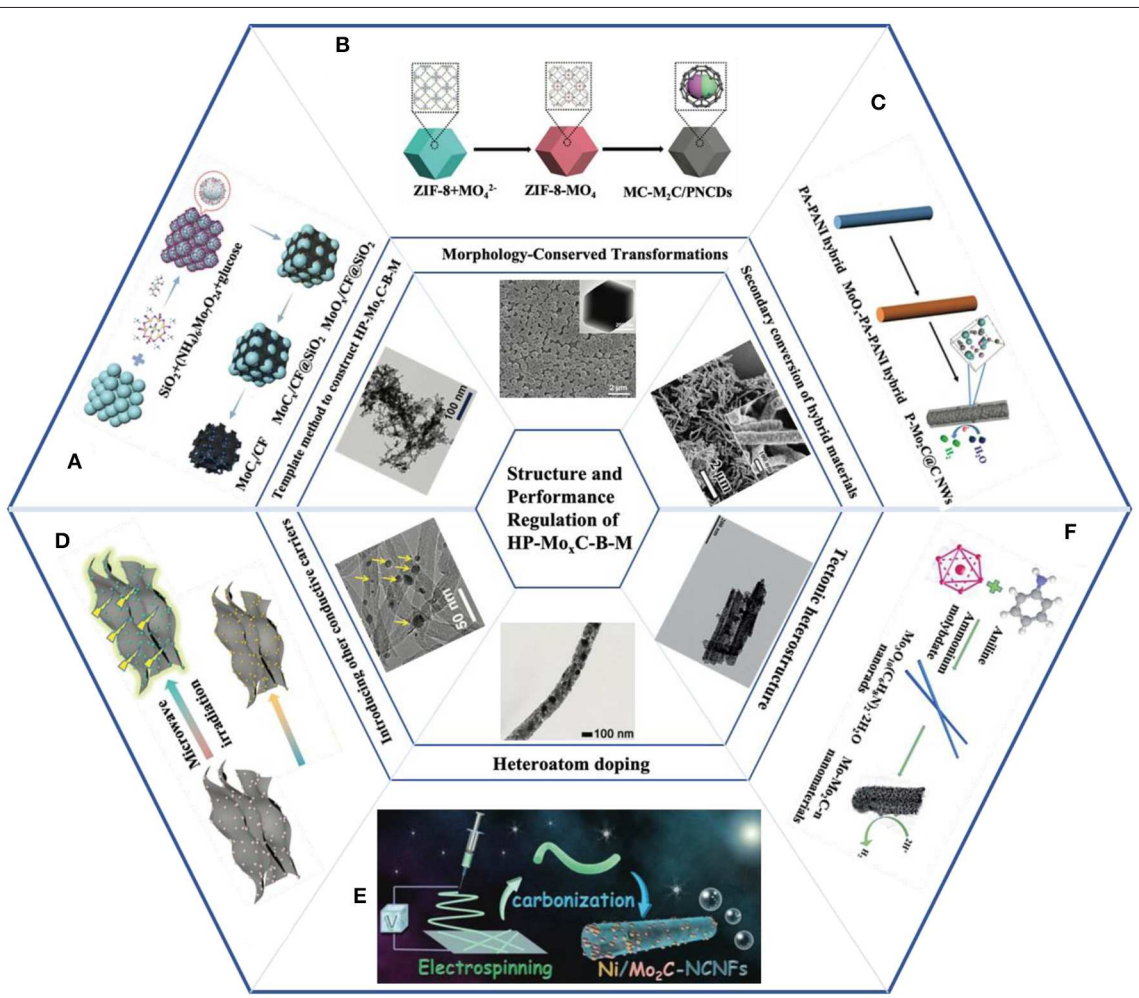

FIGURE 1 | Schematic illustration of synthesis and structures of various HP-Mo_xC based catalysts: **(A)** Schematic synthesis route and TEM image of the uf-Mo_2C/C. Reprinted with permission from Kou et al. (2018) with permission from WILEY-VCH. **(B)** Schematic synthesis route and SEM/TEM images of the MoC-Mo_2C/PNCDs. Reprinted with permission from Lu et al. (2019) with permission from WILEY-VCH. **(C)** Schematic synthesis route and SEM image of the P-Mo_2C@C NWs. Reprinted with permission from Shi et al. (2017) with permission from Royal Society of Chemistry. **(D)** Schematic synthesis route and HR-TEM image of the Mo_2C/G. Reprinted with permission from Huang et al. (2019c) with permission from WILEY-VCH. **(E)** Schematic synthesis route and TEM image of the Ni/Mo_2C-NCNFs. Reprinted with permission from Li et al. (2019b) with permission from WILEY-VCH. **(F)** Schematic synthesis route and TEM image of the Mo-Mo_2C. Reprinted with permission from Dong et al. (2018) with permission from Royal Society of Chemistry.

3D hierarchical porous structure enables a large number of mass transfer channels, high density of active sites, and high electrical conductivity, thereby providing a highly efficient and stable catalytic performance. Soft template method has no fixed structure and morphology. Soft templating agent mainly forms an organic phase with a certain morphology through intermolecular or intramolecular interaction forces (Xue et al., 2019; Zhang et al., 2019). In the process of synthesis, soft templating agent interacts with the inorganic phase to form an organic-inorganic phase with a certain morphology, thereby achieving the purpose of directional synthesis of nanomaterials. Yuan et al. (2019) used the precursor spheres formed by F127 and resoled phenolic resin to limit the growth of molybdenum carbide, and obtained ultra-small Mo_2C particles encapsulated *in situ* in mesoporous carbon spheres (Mo_2C@MCS). The ultra-small particle size exposes more active sites, and the presence of a carbon substrate greatly reduces the resistance of the catalyst, thereby exhibiting excellent electrocatalytic performance in an alkaline medium (Liu et al., 2018; Huang et al., 2019d). This study provides an effective strategy for the synthesis of a Mo_xC@C catalyst.

Morphology-Conserved Transformations

Although the template method can effectively control the morphology and pore size of the catalyst, the synthesis and the removal process of the template cause a lot of waste of resources and increase in cost, which hinders its application. The morphology-conserved transformations method has been developed as a simple and effective synthesis route (Tan et al., 2012). This method usually consists of two steps: first, a hierarchical porous metal intermediate compound is constructed and then converted into a carbon material by specific method. Metal organic frame materials (MOF) have become one of the most promising candidate precursors for the preparation of hierarchical porous materials due to their advantages such as uniform and controllable pore structure and large specific surface area (Dhakshinamoorthy et al., 2019; Garzón-Tovar et al., 2019). Shi et al. (2016) synthesized a highly active and stable MoC encapsulated by graphitized carbon shell (nanoMoC@GS) electrocatalyst by *in-situ* carburization of Mo-based MOF, achieving "atomic-level contact" between Mo and organic species. The rich organic matter in the MOF generates a porous conductive carbon shell layer, which improves the ion transmission to the medium. Wu et al. (2015) adopted the "MOFs-assisted synthesis strategy" synthesized Cu-based MOFs (NENU-5) with MoC_x nano-octahedral hydrogen evolution electrocatalysts with excellent HER activity. Recently, they used an ion exchange method to convert MO_4^{2-} groups by employing an exchange reaction between a zinc-based imidazole MOF (ZIF-8) and a metal salt (Na_2MO_4, M=Mo or W) in an organic solvent (Lu et al., 2019) (**Figure 1B**). The MO_4^{2-} group replaces the Zn (imidazolate)$_4^{2-}$ group in ZIF-8, thereby effectively dispersing and fixing the metal source uniformly in the ZIF-8 framework (Mo_xC/PNCDs). Due to the structural advantages of ZIF-8, the low boiling point of Zn and the controlled exchange of MO_4^{2-}, ultrafine carbide nanocrystals with a porous nitrogen-doped carbon dodecahedron were successfully obtained. And achieve effective control of the carbide phase and composition, which not only provides a more stable active site, but also promotes electron transport during the HER process.

Secondary Conversion of Organic-Inorganic Hybrid Materials (SC-OI-M)

Currently, there are few simple and diverse synthesis methods for new MOF materials, which greatly limits their development and application. In addition, conventional MOFs only have micropores and lack transmission channels such as mesopores and macropores, which will greatly reduce their transmission efficiency in the catalytic process. SC-OI-M refers to the integration of two counterparts into a single structure at the nanoscale (Wang et al., 2018b; Li et al., 2019a). This nano-scale single structure provides a periodic organic-inorganic structure, which has a "barrier effect" between the Mo sources during the high-temperature carbonization process, which can effectively prevent and promote the formation of nanostructures during high-temperature sintering. The hybrid materials generate a large amount of reducing gases such as CH_x, CO, and H_2 under high temperature decomposition to achieve the *in-situ* conversion of molybdenum carbide. The structure, morphology and composition of the synthesized molybdenum carbide have excellent controllability. Liao et al. (2014) synthesized nanoporous Mo_2C Nanowires (np-Mo_2C NWs) by pyrolyzing MoO_x/amine hybrid precursors with sub-nanometer periodic structure. This became the beginning of the "SC-OI-M" for the development of highly active hydrogen evolution catalysts. β-Mo_2C has outstanding HER performance, but it often exhibits excessive hydrogen absorption capacity, which restricts the desorption step of hydrogen atoms in HER (i.e., Heyrovsky/Tafel) (Wan et al., 2014). Shi et al. (2017) used electrostatic assembly to prepare a three-component hybrid precursor of MoO_x-phytic acid-polyaniline. P-doped β-Mo_2C composite nanowire electrocatalyst (P-Mo_2C@C NWs) was obtained after high temperature carbonization (**Figure 1C**). On the nanometer scale, the uniform ultra-small β-Mo_2C particles provide abundant exposed catalytically active sites, and the structure of the one-dimensional nanowire facilitates the radial conduction of electrons. The resulting graphitized carbon greatly improves the overall conductivity and stability of the catalyst. At the atomic scale, the introduction of P atoms effectively increases the electron cloud density of the β-Mo_2C Fermi level, and introduces steric hindrance effects, effectively weakens the Mo-H bond, reduces the ΔGH^* of β-Mo_2C. Experimental and theoretical calculations show that suitable P doping (2.9%) can effectively balance the Volmer and Heyrovsky/Tafel processes in the HER and optimize the intrinsic activity of β-Mo_2C for hydrogen evolution. Based on the controllability of this method, the researcher also proposed a series of electronic and spatial structure control methods. The formation of heterostructures such as by Co atom doping (Lin et al., 2016a), MoC-Mo_2C (Lin et al., 2016b), and Fe_3C-Mo_2C (Lin et al., 2017a), the fine control of the surface and structure of β-Mo_2C was realized, and the electrocatalytic performance was optimized.

REGULATE THE CATALYTIC PERFORMANCE OF HP-Mo_XC BASED CATALYSTS

The key to construct a high-activity catalyst is using the advantages of HP-Mo_xC catalyst with high electronic conductivity and large specific surface area, combined with the regulation of active sites. There are two basic principles in the regulation of catalyst performance namely increasing the active site and enhancing the intrinsic activity of the material. For the former, it can be achieved by porous structure; for the latter, it can be achieved by heteroatom doping and constructing heterostructure.

Introducing Other Conductive Carriers

Enriched active sites of sufficient unsaturated Mo and C atoms promote intimate contact between the electrolyte and the electrode material, thereby enhancing catalytic performance (Wang et al., 2019a; Cui et al., 2020). The introduction of a suitable matrix to form a strong coupling toward the catalyst can improve the intrinsic catalytic activity of Mo_xC, and also increase the conductivity of the catalyst due to the synergistic effect in the hybrid nanostructure, and hance, finally harvest desired electrochemical performance (Amrute1 et al., 2019; Xiong et al., 2019; Zhao et al., 2019c).

Up to now, a series of carbon materials such as reduced graphene oxide and carbon nanotubes have been used for supporting molybdenum carbide particles because of their large surface area and excellent electronic conductivity (Huang et al., 2019c; Li et al., 2019d; Wang et al., 2019e; Yu et al., 2019). Pan et al. (2014) used glucose as GO stabilizer, carbon source and reducing agent to prepare Mo_2C nanoparticles grown on reduced graphene oxide (Mo_2C-RGO), which showed excellent HER electrocatalytic activity. Huang et al. (2019c) developed a new technology for microwave-assisted ultrafast preparation of high performance carbon supported molybdenum carbide catalysts (Mo_2C/G) (**Figure 1D**). They impregnated the carbon support with ammonium molybdate solution and irradiated it with microwave to obtain a carbon-supported molybdenum carbide catalyst. The carbon carrier material acts as an absorbing medium to promote *in-situ* rapid heating of the material, and a carbon source for forming Mo_2C. This method can be applied to a variety of large-scale production of carbon carriers, including graphene, carbon nanotubes, commercial carbon black, and carbon fiber, etc. The *in situ* formation of the carbon support ensures a tight interfacial contact between the active material and the conductive substrate, thereby promoting rapid charge transfer between the substrate and the active material (Zhang et al., 2018; Han et al., 2019; Hou et al., 2019). Finding a way to synthesize molybdenum carbide/carbon support composites in one step is very valuable (Hsieha et al., 2019; Wu et al., 2019). Cheng et al. (2018) synthesized a 1 nm-sized molybdenum carbide nanoparticle in a carbon (Mo_2C@NC) nanomesh through hydrothermal treatment, using dicyandiamide as a carbon and nitrogen source, ammonium molybdate as a molybdenum source. During the hydrothermal process, the intermolecular hydrogen bonding is used to self-assemble into band structure to limit the growth of particles. This mesoporous ribbon nanoweb structure provides a high specific surface area and a rich active site, greatly reduced the energy barrier. This material has excellent HER/ORR performance compared to other materials. This work demonstrates a simple template-free strategy for the synthesis of highly efficient non-precious metal catalysts with large specific surface areas. It also shows the possibility of replacing platinum-based catalysts with molybdenum carbide materials from theoretical to experimental evidence.

Doping

The performance of the catalyst can also be controlled by doping. Heteroatom doping can be combined with addition of conductive support to enhance the intrinsic activity of the materials besides increasing the active site of the catalysts. The doping of heteroatoms into the lattice of the catalyst can adjust the electron and surface structure of the material, thereby affecting the adsorption free energy of the reaction intermediate on the surface, and improving the catalytic efficiency (Jia et al., 2017; Guo et al., 2019; Li et al., 2019a). At present, non-metal atoms (N, S, P, B, etc.), transition metals (Fe, Co, Ni, Zn, etc.) are introduced to replace Mo/C atoms in Mo_xC. It can adjust the intrinsic electron configuration of molybdenum carbide and improve the conductivity (Li et al., 2019c; Wang et al., 2019c,f; Zhong et al., 2019).

Nitrogen-doped nano-carbon support plays an important role in improving electrocatalytic activity (Wu et al., 2018a; Lyu et al., 2019). Wu et al. (2016) synthesized ultrafine Mo_2C nanoparticles embedded within bacterial cellulose-derived 3D N-doped carbon nanofiber networks (Mo_2C@N-CNFs). Theoretical calculations demonstrate that excellent HER activity results from a strong synergistic effect between Mo_2C nanocatalyst and N-CNF. Transition metal dopants (Ni, Co, Fe, etc.) can improve catalytic performance by adjusting the electronic configuration, creating new active sites and activating surrounding sites (Wu et al., 2018b; Cao et al., 2019). Li et al. (2019b) synthesized Ni/Mo_2C nitrogen-doped carbon nanofibers (Ni/Mo_2C-NCNFs) by using the electrospinning method (**Figure 1E**). Synergistic effect between Ni and Mo_2C nanoparticles, high conductivity, large electrochemical active surface area and effective N doping significantly promote HER and OER due to strong hydrogen binding energy on Mo_2C and high conductivity of Ni. This work provides a facile and effective way to produce low cost and high performance dual functional electrocatalysts for efficient overall water splitting. Since a single heteroatom doping has been shown to improve the catalytic performance of carbon materials, researchers developed binary or multi-heteroatom doped carbon materials to adjust the d-orbitals and optimize the electronic structure (Du et al., 2019; Ling et al., 2019; Kou et al., 2020). Ang et al. (2016) reported the formation of layered Mo_2C by carburizing of molybdenum oxide/phenol/thioacetamide hybrids, followed by solvent stripping of layered Mo_2C to further form N/S co-doped molybdenum carbide nanosheets. The synthesized nanosheet has an ultrathin thickness (1 nm) and a large specific surface area (139 $m^2\ g^{-1}$). The incorporated N and S effectively improve the wettability of the material. Wang

et al. (2018a) synthesized NP-Mo_2C by direct carbonization. Theoretical calculations show that the doping of heteroatoms into carbon promotes the transfer of electrons in the catalyst, and the heteroatoms may also act as catalytic active sites (Gao et al., 2019; Singh et al., 2019). Owing to the synergistic coupling, the double doping of the N, P heteroatoms in Mo_2C can remarkably improve the intrinsic activity of each active site.

Hierarchical Porous Molybdenum Carbide-Based Heterostructure

Heterostructured hybrids have shown superior electrochemical performance compared to the corresponding single components (Liang et al., 2019; Yao et al., 2019). Through the interface electron transfer in a heterostructure, a large number of interfaces between multiple components can induce optimization of the electronic configuration (Wang et al., 2019d; He et al., 2020). Therefore, constructing heterojunction is an effective way to optimize the free energy of hydrogen adsorption.

The engineering design of molybdenum carbide-based heterostructures provides a new perspective for electrocatalysis. For example, heterostructures of Mo-Mo_2C (Dong et al., 2018), Mo_2C-Mo_2N (Chen et al., 2013), MoP@Mo_2C (Huang et al., 2018), and $(Mo_2C)_x$-$(WC)_{1-x}$-QDs (Huo et al., 2017). The synergistic effect of the interface portion exhibits superior HER performance over the single component molybdenum carbide. Dong et al. (2018) obtained a new Mo-rich molybdenum carbide-based electrocatalyst (Mo-Mo_2C) by calcining $Mo_3O_{10}(C_6H_8N)_2\bullet 2H_2O$ precursor (**Figure 1F**). The overpotential of the Mo-Mo_2C hydrogen evolution reaction is only 67 mV, and the Tafel slope is as low as 55 mV/dec. Its excellent HER performance can be attributed to the improvement of the internal charge transfer ability of the catalyst.

Recently, Huang et al. (2019a) constructed a Mo_2C/VC heterostructure. The CO_2 decomposed from Mg and $NaHCO_3$ reacts at high temperature to generate a three-dimensional carbon network. At the same time, the micro-scale precursor V_2MoO_8 is broken into two-phase materials Mo_2C and VC that are not completely separated and embedded in the three-dimensional carbon network. The three-dimensional conductive carbon network and the cross-linked structure fully provide electron transportability and structural stability. Mo_2C has strong hydrogen adsorption capacity, while VC has strong hydrogen desorption capacity, so single component Mo_2C@C and VC@C exhibit poor hydrogen evolution reactivity, while Mo_2C/VC@C shows rapid adsorption capacity and rapid desorption kinetics. Based on the combination of experiment and theory, this experiment proposes that the method of preparing a rich interface structure by phase separation is a way to efficiently prepare high performance catalyst. This approach can be extended to other highly efficient heterogeneous catalysts and different energy sources in the future.

DISCUSSION

In summary, molybdenum carbide-based materials are an ideal HER material. In this review, recent developments in the structural design and electronic regulation of molybdenum-based catalysts are illustrated. Template method, morphology-conserved transformations method, and secondary conversion of organic-inorganic hybrid materials method are effective strategies for synthesizing various molybdenum carbide-based materials. By compounding with a conductive carrier, element doping and designing a heterojunction can achieve electronic optimization of HER kinetics, greatly improving catalyst activity and stability. In practical applications, material combinations and properties, flexible selection of synthesis methods and performance control methods can synergistically achieve highly efficient catalysts. However, the large-scale application of electrolyzed water for hydrogen evolution still has a long way to go. In combination with the rapid development of molybdenum carbide in electrocatalytic hydrogen evolution in recent years. Future research on molybdenum carbide catalysts may focus on the development of efficient new synthetic methods, the development of molybdenum carbide hydrogen evolution devices, mechanism research, standardized test and the mining and understanding of structure-activity relationships.

AUTHOR CONTRIBUTIONS

All authors listed have made a substantial, direct and intellectual contribution to the work, and approved it for publication.

REFERENCES

Amrute1, A. P., Łodziana, Z., Schreyer, H., Weidenthaler, C., and Schüth, F. (2019). High-surface-area corundum by mechanochemically induced phase transformation of boehmite. *Science* 366, 485–489. doi: 10.1126/science.aaw9377

Ang, H., Tan, H. T., Luo, Z. M., Zhang, Y., Guo, Y. Y., Guo, G., et al. (2016). Hydrophilic nitrogen and sulfur co-doped molybdenum carbide nanosheets for electrochemical hydrogen evolution. *Small* 11, 6278–6284. doi: 10.1002/smll.201502106

Cao, Q., Zhao, L., Wang, A., Yang, L., Lai, L., Wang, Z., et al. (2019). Tailored synthesis of Zn-N co-doped porous MoC nanosheets towards efficient hydrogen evolution. *Nanoscale* 11, 1700–1709. doi: 10.1039/C8NR07463A

Chen, W., Pei, J., He, C.-T., Wan, J., Ren, H., Wang, Y., et al. (2018). Single tungsten atoms supported on MOF-derived N-doped Carbon for robust electrochemical hydrogen evolution. *Adv. Mater.* 30:1800396. doi: 10.1002/adma.201800396

Chen, W.-F., Wang, C.-H., Sasaki, K., Marinkovic, N., Xu, W., Muckerman, J. T., et al. (2013). Highly active and durable nanostructured molybdenum carbide electrocatalysts for hydrogen production. *Energy Environ. Sci.* 6, 943–951. doi: 10.1039/C2EE23891H

Chen, Y., Li, Z., Zhu, Y., Sun, D., Liu, X., Xu, L., et al. (2019). Atomic Fe dispersed on N-doped carbon hollow nanospheres for high-efficiency electrocatalytic oxygen reduction. *Adv. Mater.* 31:1806312. doi: 10.1002/adma.201806312

Cheng, Z., Fu, Q., Han, Q., Xiao, Y., Liang, Y., Zhao, Y., et al. (2018). A type of 1 nm molybdenum carbide confined within carbon nanomesh as highly efficient bifunctional electrocatalyst. *Adv. Funct. Mater.* 28:1705967. doi: 10.1002/adfm.201705967

Cui, Q., Chen, C., Yu, C., Lu, T., Long, H., Yan, S., et al. (2020). Effect of molybdenum particles on thermal and mechanical properties of graphite flake/copper composites. *Carbon* 161, 169–180. doi: 10.1016/j.carbon.2020.01.059

Dhakshinamoorthy, A., Asiri, A. M., and Garcia, H. (2019). 2D Metal-organic frameworks as multifunctional materials in heterogeneous catalysis and electro/photocatalysis. *Adv. Mater.* 31:1900617. doi: 10.1002/adma.201900617

Dong, J., Wu, Q., Huang, C., Yao, W., and Xu, Q. (2018). Cost effective Mo rich Mo_2C electrocatalysts for hydrogen evolution reaction. *J. Mater. Chem. A* 6, 10028–10035. doi: 10.1039/C8TA02550A

Du, R., Jin, X. Y., Hübner, R., Fan, X. L., Hu, Y., and Eychmüller, A. (2019). Engineering self-supported noble metal foams toward electrocatalysis and beyond. *Adv. Energy Mater.* 10:1901945. doi: 10.1002/aenm.201901945

Feng, Q., Zhao, S., Xu, Q., Chen, W., Tian, S., Wang, Y., et al. (2019). Mesoporous nitrogen-doped carbon-nanosphere-supported isolated single-atom Pd catalyst for highly efficient semihydrogenation of Acetylene. *Adv. Mater.* 31:1901024. doi: 10.1002/adma.201901024

Gao, K., Wang, B., Tao, L., Cunning, B. V., Zhang, Z. P., Wang, S. Y., et al. (2019). Efficient metal-free electrocatalysts from N-doped carbon nanomaterials: mono-doping and Co-doping. *Adv. Mater.* 31:1805121. doi: 10.1002/adma.201805121

Gao, Q., Zhang, C., Wang, S., Shen, W., Zhang, Y., Xu, H., et al. (2010). Preparation of supported Mo_2C-based catalysts from organic-inorganic hybrid precursor for hydrogen production from methanol decomposition. *Chem. Commun.* 46, 6494–6496. doi: 10.1039/c0cc01430c

Garzón-Tovar, L., Pérez-Carvajal, J., Yazdi, A., Hernández-Muñoz, J., Tarazona, P., Imaz, I., et al. (2019). A MOF@COF composite with enhanced uptake through interfacial pore generation. *Angew. Chem.* 131, 9612–9616. doi: 10.1002/ange.201904766

Guo, J., Huo, J., Liu, Y., Wu, W., Wang, Y., Wu, M., et al. (2019). Nitrogen-doped porous carbon supported nonprecious metal single-atom electrocatalysts: from synthesis to application. *Small Methods* 3:1900159. doi: 10.1002/smtd.201900159

Han, X., Zhang, W., Ma, X., Zhong, C., Zhao, N., Hu, W., et al. (2019). Identifying the activation of bimetallic sites in $NiCo_2S_4$@g-C_3N_4-CNT hybrid electrocatalysts for synergistic oxygen reduction and evolution. *Adv. Mater.* 31:1808281. doi: 10.1002/adma.201808281

He, L., Zhang, W., Mo, Q., Huang, W., Yang, L., and Gao, Q. (2020). Molybdenum carbide-oxide heterostructures: *in situ* surface reconfiguration toward efficient electrocatalytic hydrogen evolution. *Angew. Chem. Int. Ed.* 59, 3544–3548. doi: 10.1002/anie.201914752

Hou, J., Wu, Y., Zhang, B., Cao, S., Li, Z., and Sun, L. (2019). Rational design of nanoarray architectures for electrocatalytic water splitting. *Adv. Funct. Mater.* 29:1808367. doi: 10.1002/adfm.201808367

Hsieha, Y.-Y., Fang, Y., Daum, J., Kanakaraj, S. N., Zhang, G., Mishra, S., et al. (2019). Bio-inspired, nitrogen doped CNT-graphene hybrid with amphiphilic properties as a porous current collector for lithium-ion batteries. *Carbon* 145, 677–689. doi: 10.1016/j.carbon.2019.01.055

Huang, C., Miao, X., Pi, C., Gao, B., Zhang, X., Qin, P., et al. (2019a). Mo_2C/VC heterojunction embedded in graphitic carbon network: an advanced electrocatalyst for hydrogen evolution. *Nano Energy* 60, 520–526. doi: 10.1016/j.nanoen.2019.03.088

Huang, C., Peng, J., Wan, S., Du, Y., Dou, S., Wagner, H. D., et al. (2019b). Ultra-tough inverse artificial nacre based on epoxy-graphene by freeze-casting. *Angew. Chem. Int. Ed.* 58, 7636–7640. doi: 10.1002/anie.201902410

Huang, H., Yu, C., Huang, H., Guo, W., Zhang, M., Han, X., et al. (2019c). Microwave-assisted ultrafast synthesis of molybdenum carbide nanoparticles grown on carbon matrix for efficient hydrogen evolution reaction. *Small Methods* 3:1900259. doi: 10.1002/smtd.201900259

Huang, J., Xiao, Y., Peng, Z., Xu, Y., Li, L., Tan, L., et al. (2019d). Co_3O_4 supraparticle-based bubble nanofiber and bubble nanosheet with remarkable electrochemical performance. *Adv. Sci.* 6:1900107. doi: 10.1002/advs.201900107

Huang, Y., Ge, J., Hu, J., Zhang, J., Hao, J., Wei, Y., et al. (2018). Nitrogen-doped porous molybdenum carbide and phosphide hybrids on a carbon matrix as highly effective electrocatalysts for the hydrogen evolution reaction. *Adv. Energy Mater.* 8:1701601. doi: 10.1002/aenm.201701601

Huo, J., Chen, Y., Liu, Y., Guo, J., Lu, L., Li, W., et al. (2019). Bifunctional iron nickel phosphide nanocatalysts supported on porous carbon for highly efficient overall water splitting. *Sust. Mater. Technol.* 22:e00117. doi: 10.1016/j.susmat.2019.e00117

Huo, L., Liu, B., Gao, Z., and Zhang, J. (2017). 0D/2D heterojunctions of molybdenum carbide-tungsten carbide quantum dots/N-doped graphene nanosheets as superior and durable electrocatalysts for hydrogen evolution reaction. *J. Mater. Chem. A* 5, 18494–18501. doi: 10.1039/C7TA02864D

Jia, J., Xiong, T., Zhao, L., Wang, F., Liu, H., Hu, R., et al. (2017). Ultrathin N-doped Mo_2C nanosheets with exposed active sites as efficient electrocatalyst for hydrogen evolution reactions. *ACS Nano* 11, 12509–12518. doi: 10.1021/acsnano.7b06607

Khaselev, O., and Turner, J. A. (1998). A monolithic photovoltaic-photoelectrochemical device for hydrogen production via water splitting. *Science* 280, 425–427. doi: 10.1126/science.280.5362.425

Kim, S., Choi, C., Hwang, J., Park, J., Jeong, J., Jun, H., et al. (2020). Interaction mediator assisted synthesis of mesoporous molybdenum carbide: mo-valence state adjustment for optimizing hydrogen evolution. *ACS Nano* 14, 4988–4999. doi: 10.1021/acsnano.0c01285

Kou, Z., Wang, T., Cai, Y., Guan, C., Pu, Z., Zhu, C., et al. (2018). Ultrafine molybdenum carbide nanocrystals confined in carbon foams via a colloid-confinement route for efficient hydrogen production. *Small Methods* 2:1700396. doi: 10.1002/smtd.201700396

Kou, Z., Yu, Y., Liu, X., Gao, X., Zheng, L., Zou, H., et al. (2020). Potential-dependent phase transition and Mo-enriching surface reconstruction of γ-CoOOH in heterostructured Co-Mo2C precatalyst enable water oxidation. *ACS Catal.* 10, 4411–4419. doi: 10.1021/acscatal.0c00340

Li, B., Ma, J.-G., and Cheng, P. (2019a). Integration of metal nanoparticles into metal-organic frameworks for composite catalysts: design and synthetic strategy. *Small* 15:1804849. doi: 10.1002/smll.201804849

Li, M., Zhu, Y., Wang, H., Wang, C., Pinna, N., Lu, X., et al. (2019b). Ni strongly coupled with Mo_2C encapsulated in nitrogen-doped carbon nanofibers as robust bifunctional catalyst for overall water splitting. *Adv. Energy Mater.* 9:1803185. doi: 10.1002/aenm.201803185

Li, Y., Tan, X., Chen, S., Bo, X., Ren, H., Smith, S. C., et al. (2019c). Processable surface modification of nickel-heteroatom (N, S) bridge sites for promoted alkaline hydrogen evolution. *Angew. Chem.* 131, 471–476. doi: 10.1002/ange.201808629

Li, Z., Zhang, L., Chen, X., Li, B. L., Wang, H., and Li, Q. (2019d). Three-dimensional graphene-like porous carbon nanosheets derived from molecular precursor for high-performance supercapacitor application. *Electrochim. Acta* 296, 8–17. doi: 10.1016/j.electacta.2018.11.002

Liang, Q., Zhong, L., Du, C., Luo, Y., Zhao, J., Zheng, Y., et al. (2019). Interfacing epitaxial dinickel phosphide to 2D nickel thiophosphate nanosheets for boosting electrocatalytic water splitting. *ACS Nano* 13, 7975–7984. doi: 10.1021/acsnano.9b02510

Liao, L., Wang, S., Xiao, J., Bian, X., Zhang, Y., Scanlon, M. D., et al. (2014). A nanoporous molybdenum carbide nanowire as an electrocatalyst for hydrogen evolution reaction. *Energy Environ. Sci.* 7, 387–392. doi: 10.1039/C3EE42441C

Lin, H., Liu, N., Shi, Z., Guo, Y., Tang, Y., and Gao, Q. (2016a). Cobalt-doping in molybdenum-carbide nanowires toward efficient electrocatalytic hydrogen evolution. *Adv. Funct. Mater.* 26, 5590–5598. doi: 10.1002/adfm.201600915

Lin, H., Shi, Z., He, S., Yu, X., Wang, S., Gao, Q., et al. (2016b). Heteronanowires of MoC-Mo_2C as efficient electrocatalysts for hydrogen evolution reaction. *Chem. Sci.* 7, 3399–3405. doi: 10.1039/C6SC00077K

Lin, H., Zhang, W., Shi, Z., Che, M., Yu, X., Tang, Y., et al. (2017a). Cover picture: electrospinning hetero-nanofibers of Fe_3C-Mo_2C/nitrogen-doped-carbon as efficient electrocatalysts for hydrogen evolution. *ChemSusChem* 10, 2597–2640. doi: 10.1002/cssc.201700207

Lin, L., Zhou, W., Gao, R., Yao, S., Zhang, X., Xu, W., et al. (2017b). Low-temperature hydrogen production from water and methanol using Pt/α-MoC catalysts. *Nature* 544, 80–83. doi: 10.1038/nature21672

Ling, T., Zhang, T., Ge, B., Han, L., Zheng, L., Lin, F., et al. (2019). Well-dispersed nickel-and zinc-tailored electronic structure of a transition metal oxide for highly active alkaline hydrogen evolution reaction. *Adv. Mater.* 31:1807771. doi: 10.1002/adma.201807771

Liu, T., Zhang, M., Wang, Y. L., Wang, Q. Y., Lv, C., Liu, K. X., et al. (2018). Engineering the surface/interface of horizontally oriented carbon nanotube

macrofilm for foldable lithium-ion battery withstanding variable weather. *Adv. Energy Mater.* 8:1802349. doi: 10.1002/aenm.201802349

Liu, Y., Li, X., Shen, W., Dai, Y., Kou, W., Zheng, W., et al. (2019). Multishelled transition metal-based microspheres: synthesis and applications for batteries and supercapacitors. *Small* 15:1804737. doi: 10.1002/smll.201804737

Lu, X. F., Yu, L., Zhang, J. T., and Lou, X. W. (2019). Ultrafine dual-phased carbide nanocrystals confined in porous nitrogen-doped carbon dodecahedrons for efficient hydrogen evolution reaction. *Adv. Mater.* 31:1900699. doi: 10.1002/adma.201900699

Lyu, F., Zeng, S., Sun, Z., Qin, N., Cao, L., Wang, Z., et al. (2019). Lamellarly stacking porous N, P co-doped Mo_2C/C nanosheets as high performance anode for lithium-ion batteries. *Small* 15:1805022. doi: 10.1002/smll.201805022

Ma, Y.-Y., Lang, Z.-L., Yan, L.-K., Wang, Y.-H., Tan, H.-Q., Feng, K., et al. (2018). Highly efficient hydrogen evolution triggered by a multi-interfacial Ni/WC hybrid electrocatalyst. *Energy Environ. Sci.* 11, 2114–2123. doi: 10.1039/C8EE01129J

Martinez, U., Babu, S. K., Holby, E. F., Chung, H. T., Yin, X., and Zelenay, P. (2019). Progress in the development of Fe-based PGM-free electrocatalysts for the oxygen reduction reaction. *Adv. Mater.* 31:1806545. doi: 10.1002/adma.201806545

Niu, S., Jiang, W.-J., Tang, T., Yuan, L.-P., Luo, H., and Hu, J.-S. (2019). Autogenous growth of hierarchical $NiFe(OH)_x$/FeS nanosheet-on-microsheet arrays for synergistically enhanced high-output water oxidation. *Adv. Funct. Mater.* 29:1902180. doi: 10.1002/adfm.201902180

Nong, S., Dong, W., Yin, J., Dong, B., Lu, Y., Yuan, X., et al. (2018). Well-dispersed ruthenium in mesoporous crystal TiO_2 as an advanced electrocatalyst for hydrogen evolution reaction. *J. Am. Chem. Soc.* 140, 5719–5727. doi: 10.1021/jacs.7b13736

Pan, L. F., Li, Y. H., Yang, S., Liu, P. F., Yu, M. Q., and Yang, H. G., et al. (2014). Molybdenum carbide stabilized on graphene with high electrocatalytic activity for hydrogen evolution reaction. *Chem. Commun.* 50, 13135–13137. doi: 10.1039/C4CC05698A

Ryoo, R. (2019). Birth of a class of nanomaterial. *Nature* 575, 40–41. doi: 10.1038/d41586-019-02835-7

Shi, Z., Nie, K., Shao, Z., Gao, B., Lin, H., Zhang, H., et al. (2017). Phosphorus-Mo_2C@carbon nanowires toward efficient electrochemical hydrogen evolution: composition, structural and electronic regulation. *Energy Environ. Sci.* 10, 1262–1271.doi: 10.1039/C7EE00388A

Shi, Z., Wang, Y., Lin, H., Zhang, H., Shen, M., Xie, S., et al. (2016). Porous nanoMoC@graphite shell derived from a MOFs-directed strategy: an efficient electrocatalyst for the hydrogen evolution reaction. *J. Mater. Chem. A* 2016 4, 6006–6013. doi: 10.1039/C6TA01900E

Singh, S. K., Takeyasu, K., and Nakamura, J. (2019). Active sites and mechanism of oxygen reduction reaction electrocatalysis on nitrogen-doped carbon materials. *Adv. Mater.* 31:1804297. doi: 10.1002/adma.201804297

Tan, Y., Xu, C., Chen, G., Fang, X., Zheng, N., and Xie, Q. (2012). Facile synthesis of manganese-oxide-containing mesoporous nitrogen-doped carbon for efficient oxygen reduction. *Adv. Funct. Mater.* 22, 4584–4591. doi: 10.1002/adfm.201201244

Thompson, B. R., Horozov, T. S., Stoyanov, S. D., and Paunov, V. N. (2019). Hierarchically structured composites and porous materials from soft templates: fabrication and applications. *J. Mater. Chem. A* 7, 8030–8049. doi: 10.1039/C8TA09750

Wan, C., Regmi, Y. N., and Leonard, B. M. (2014). Multiple phases of molybdenum carbide as electrocatalysts for the hydrogen evolution reaction. *Angew. Chem. Int. Ed.* 53, 6407–6410. doi: 10.1002/anie.201402998

Wang, D., Liu, T., Wang, J., and Wu, Z. (2018a). N, P (S) co-doped Mo_2C/C hybrid electrocatalysts for improved hydrogen generation. *Carbon* 139, 845–852. doi: 10.1016/j.carbon.2018.07.043

Wang, F., Jiang, J., Wang, K., Zhai, Q., Long, F., Liu, P., et al. (2019a). Hydrotreatment of lipid model for diesel-like alkane using nitrogen-doped mesoporous carbon-supported molybdenum carbide. *Appl. Catal. B Environ.* 242, 150–160. doi: 10.1016/j.apcatb.2018.09.077

Wang, H., Xiao, X., Liu, S., Chiang, C.-L., Kuai, X., Peng, C.-K., et al. (2019b). Structural and electronic optimization of MoS_2 edges for hydrogen evolution. *J. Am. Chem. Soc.* 141. 18578–18584. doi: 10.1021/jacs.9b09932

Wang, H.-M., Wang, X.-H., Zhang, M.-H., Du, X.-Y., Li, W., and Tao, K.-Y. (2007). Synthesis of bulk and supported molybdenum carbide by a single-step thermal carburization method. *Chem. Mater.* 19, 1801–1807. doi: 10.1021/cm0615471

Wang, M., Wang, W., Qian, T., Liu, S., Li, Y., Hou, Z., et al. (2019c). Oxidizing vacancies in nitrogen-doped carbon enhance air-cathode activity. *Adv. Mater.* 31:1803339. doi: 10.1002/adma.201803339

Wang, X.-D., Huang, Y.-H., Liao, J.-F., Jiang, Y., Zhou, L., Zhang, X.-Y., et al. (2019d). *In situ* construction of a Cs_2SnI_6 perovskite nanocrystal/SnS_2 nanosheet heterojunction with boosted interfacial charge transfer. *J. Am. Chem. Soc.* 141, 13434–13441. doi: 10.1021/jacs.9b04482

Wang, X.-L., Dong, L.-Z., Qiao, M., Tang, Y.-J., Liu, J., Li, Y., et al. (2018b). Exploring the performance improvement of the oxygen evolution reaction in a stable bimetal-organic framework system. *Angew. Chem. Int. Ed.* 57, 9660–9664. doi: 10.1002/anie.201803587

Wang, Y., Adekoya, D., Sun, J., Tang, T., Qiu, H., Xu, L., et al. (2019e). Manipulation of edge-site Fe-N_2 moiety on holey Fe, N codoped graphene to promote the cycle stability and rate capacity of Li-S batteries. *Adv. Funct. Mater.* 29:1807485. doi: 10.1002/adfm.201807485

Wang, Y., Wang, Y., Kang, W., Cao, D., Li, C., Cao, D., et al. (2019f). TiO_2-coated interlayer-expanded $MoSe_2$/phosphorus-doped carbon nanospheres for ultrafast and ultralong cycling sodium storage. *Adv. Sci.* 6:1801222. doi: 10.1002/advs.201801222

Wu, C., Liu, D., Li, H., Li, J., et al. (2018a). Molybdenum carbide-decorated metallic cobalt@ nitrogen-doped carbon polyhedrons for enhanced electrocatalytic hydrogen evolution. *Small* 14:1704227. doi: 10.1002/smll.201704227

Wu, H., Li, Y., Ren, J., Rao, D., Zheng, Q., Zhou, L., et al. (2019). CNT-assembled dodecahedra core@ nickel hydroxide nanosheet shell enabled sulfur cathode for high-performance lithium-sulfur batteries. *Nano Energy* 55, 82–92. doi: 10.1016/j.nanoen.2018.10.061

Wu, H. B., Xia, B. Y., Yu, L., Yu, X.-Y., and Lou, X. W. (2015). Porous molybdenum carbide nano-octahedrons synthesized via confined carburization in metal-organic frameworks for efficient hydrogen production. *Nat. Commun.* 6:6512. doi: 10.1038/ncomms7512

Wu, Z., Zou, Z., Huang, J., Gao, F., et al. (2018b). Fe-doped NiO mesoporous nanosheets array for highly efficient overall water splitting. *J. Catal.* 358, 243–252. doi: 10.1016/j.jcat.2017.12.020

Wu, Z.-Y., Hu, B.-C., Wu, P., Liang, H.-W., Yu, Z.-L., Lin, Y., et al. (2016). Mo_2C nanoparticles embedded within bacterial cellulose-derived 3D N-doped carbon nanofiber networks for efficient hydrogen evolution. *Npg Asia Mater.* 8:e288. doi: 10.1038/am.2016.87

Xiong, H., Wu, L., Liu, Y., Gao, T., Li, K., Long, Y., et al. (2019). Controllable synthesis of mesoporous TiO_2 polymorphs with tunable crystal structure for enhanced photocatalytic H_2 production. *Adv. Energy Mater.* 9:1901634. doi: 10.1002/aenm.201901634

Xue, Z., Wang, P., Peng, A., and Wang, T. (2019). Architectural design of self-assembled hollow superstructures. *Adv. Mater.* 31:1801441. doi: 10.1002/adma.201801441

Yang, C., Guo, K., Yuan, D., Cheng, J., and Wang, B. (2020). Unraveling reaction mechanisms of Mo2C as cathod catalyst in Li-Co2 battery. *J. Am. Chem. Soc.* 142, 6983–6990. doi: 10.1021/jacs.9b12868

Yang, L., Shui, J., Du, L., Shao, Y., Liu, J., Dai, L., et al. (2019). Carbon-based metal-free ORR electrocatalysts for fuel cells: past, present, and future. *Adv. Mater.* 31:1804799. doi: 10.1002/adma.201804799

Yao, N., Li, P., Zhou, Z., Zhao, Y., Cheng, G., Chen, S., et al. (2019). Synergistically tuning water and hydrogen binding abilities over Co_4N by Cr doping for exceptional alkaline hydrogen evolution electrocatalysis. *Adv. Energy Mater.* 9:1902449. doi: 10.1002/aenm.201902449

Yu, B., Yang, D., Hu, Y., He, J., Chen, Y., and He, W. (2019). Mo_2C nanodots anchored on N-doped porous CNT microspheres as electrode for efficient Li-ion storage. *Small Methods* 3:1800287. doi: 10.1002/smtd.201800287

Yuan, S., Xu, S., Liu, Z., Huang, G., Zhang, C., Ai, J., et al. (2019). Ultra-small molybdenum carbide nanoparticles *in situ* entrapped in mesoporous carbon spheres as efficient catalysts for hydrogen evolution. *ChemCatChem* 11, 2643–2648. doi: 10.1002/cctc.201900324

Zhang, J., Liu, J., Xi, L., Yu, Y., Chen, N., Sun, S., et al. (2018). Single-atom Au/NiFe layered double hydroxide electrocatalyst: probing the origin of activity for oxygen evolution reaction. *J. Am. Chem. Soc.* 140, 3876–3879. doi: 10.1021/jacs.8b00752

Zhang, L., Doyle-Davis, K., and Sun, X. (2019). Pt-based electrocatalysts with high atom utilization efficiency: from nanostructures to single atoms. *Energy Environ. Sci.* 12, 492–517. doi: 10.1039/C8EE02939C

Zhao, Q., Zhu, Q., Miao, J., Zhang, P., Wan, P., He, L., et al. (2019a). Flexible 3D porous MXene foam for high-performance lithium-lon batteries. *Small* 15:1904293. doi: 10.1002/smll.201904293

Zhao, X., Sun, W., Geng, D., Fu, W., Dan, J., Xie, Y., et al. (2019b). Edge segregated polymorphism in 2D molybdenum carbide. *Adv. Mater.* 31:1808343. doi: 10.1002/adma.201808343

Zhao, Z., Chen, C., Liu, Z., Huang, J., Wu, M., Liu, H., et al. (2019c). Pt-based nanocrystal for electrocatalytic oxygen reduction. *Adv. Mater.* 31:1808115. doi: 10.1002/adma.201808115

Zhong, H., Yang, C., Fan, L., Fu, Z., Yang, X., Wang, X., et al. (2019). Dyadic promotion of photocatalytic aerobic oxidation via the Mott-Schottky effect enabled by nitrogen-doped carbon from imidazolium-based ionic polymers. *Energy Environ. Sci.* 12, 418–426. doi: 10.1039/C8EE02727G

Conflict of Interest: The authors declare that the research was conducted in the absence of any commercial or financial relationships that could be construed as a potential conflict of interest.

frontiers in Chemistry

ORIGINAL RESEARCH
published: 19 May 2020
doi: 10.3389/fchem.2020.00382

Hierarchical 0D–2D Co/Mo Selenides as Superior Bifunctional Electrocatalysts for Overall Water Splitting

Lu Xia[1,2], Hao Song[1], Xingxing Li[1], Xuming Zhang[1], Biao Gao[1,3], Yang Zheng[1]*, Kaifu Huo[1] and Paul K. Chu[3]*

[1] The State Key Laboratory of Refractories and Metallurgy and Institute of Advanced Materials and Nanotechnology, Wuhan University of Science and Technology, Wuhan, China, [2] The College of Resources and Environment Engineering, Wuhan University of Science and Technology, Wuhan, China, [3] Departments of Physics, Materials Science and Engineering, and Biomedical Engineering, City University of Hong Kong, Hong Kong, China

Development of efficient electrocatalysts combining the features of low cost and high performance for both the hydrogen evolution reaction (HER) and oxygen evolution reaction (OER) still remains a critical challenge. Here, we proposed a facile strategy to construct *in situ* a novel hierarchical heterostructure composed of 0D–2D $CoSe_2$/$MoSe_2$ by the selenization of $CoMoO_4$ nanosheets grafted on a carbon cloth (CC). In such integrated structure, $CoSe_2$ nanoparticles dispersed well and tightly bonded with $MoSe_2$ nanosheets, which can not only enhance kinetics due to the synergetic effects, thus promoting the electrocatalytic activity, but also effectively improve the structural stability. Benefiting from its unique architecture, the designed $CoSe_2$/$MoSe_2$ catalyst exhibits superior OER and HER performance. Specifically, a small overpotential of 280 mV is acquired at a current density of 10 mA·cm^{-2} for OER with a small Tafel slope of 86.8 mV·dec^{-1}, and the overpotential is 90 mV at a current density of 10 mA·cm^{-2} for HER with a Tafel slope of 84.8 mV·dec^{-1} in 1 M KOH. Furthermore, the symmetrical electrolyzer assembled with the $CoSe_2$/$MoSe_2$ catalysts depicts a small cell voltage of 1.63 V at 10 mA·cm^{-2} toward overall water splitting.

Keywords: cobalt selenide, molybdenum selenide, hierarchical heterostructure, bifunctional electrocatalysts, overall water splitting

OPEN ACCESS

Edited by:
Guanglin Xia,
Fudan University, China

Reviewed by:
Shichun Mu,
Wuhan University of Technology, China
Fei Ma,
Xi'an Jiaotong University, China

***Correspondence:**
Xuming Zhang
xumzhang@wust.edu.cn
Yang Zheng
yzheng@wust.edu.cn

Specialty section:
This article was submitted to Nanoscience, a section of the journal Frontiers in Chemistry

Received: *02 March 2020*
Accepted: *14 April 2020*
Published: *19 May 2020*

Citation:
Xia L, Song H, Li X, Zhang X, Gao B, Zheng Y, Huo K and Chu PK (2020) Hierarchical 0D–2D Co/Mo Selenides as Superior Bifunctional Electrocatalysts for Overall Water Splitting. Front. Chem. 8:382. doi: 10.3389/fchem.2020.00382

INTRODUCTION

Hydrogen is a promising energy source that boasts a high power density and environmental friendliness; therefore, electrolysis of water is hotly pursued as a renewable, efficient, and pollution-free technique (Amiinu et al., 2017; Luo et al., 2018; Zhu et al., 2018). Electrocatalytic water splitting consists of the hydrogen evolution reaction (HER) and oxygen evolution reaction (OER), and electrocatalysts as the chemical reaction centers play a critical role in the water splitting electrolyzer. Although some noble metal oxide catalysts (RuO_2 and IrO_2) have high electrocatalytic performance for the OER and some noble metal catalysts (Pt and Ir) deliver good electrochemical property in the HER, the high cost and scarcity restrict their wide industrial application (Trasatti, 1972, 1984). Therefore, noble-metal-free catalysts with high stability and efficiency are crucial to large-scale hydrogen production from water splitting. Currently, the OER activity in alkaline solution is the

bottleneck in overall water splitting due to the sluggish kinetics arising from the multiproton-coupled electron transfer steps (Jamesh and Sun, 2018). In practice, the HER catalyst in the electrolyzer should be compatible with the OER catalyst and functions in the same medium. Hence, development of suitable bifunctional noble-metal-free electrocatalyts with both high HER and OER performance in alkaline media is of great significance.

In recent years, transition metal dichalcogenides (TMDs) have attracted significant research interests owing to their earth-abundant reserves and acceptable activity for electrocatalytic HER (Xie et al., 2013; Zhang et al., 2017a; Xue et al., 2018; Wang et al., 2019). Particularly, layered $MoSe_2$ has been considered as a promising HER electrocatalyst because of its unique structure features and high electrochemical activity (Shi et al., 2015; Chen et al., 2018a; Zhang et al., 2018). Theoretical research has demonstrated that the Gibbs free energy for H atom absorption on the edge of $MoSe_2$ is lower than that of MoS_2 due to the more metallic nature of $MoSe_2$, revealing the higher HER performance (Tang et al., 2014; Lai et al., 2017; Yang et al., 2018). In addition, it also has been experimentally confirmed that the unsaturated Se edges in $MoSe_2$ nanosheets are extremely active as the S edges in MoS_2, which is responsible for the high HER activity (Jaramillo et al., 2007; Tang and Jiang, 2016). However, similar to MoS_2, the HER activity of layered $MoSe_2$ is largely limited by its poor conductivity and serious aggregation or restacking during the synthesis procedure (Mao et al., 2015; Qu et al., 2015), inhibiting the practical application of $MoSe_2$ catalyst. Therefore, it is significant to improve the electrochemical activity of $MoSe_2$-based catalyst. Recent works have shown that coupling $MoSe_2$ with other transition metal selenides and constructing heterostrucurted materials could be an effective approach to further enhance the electrochemical performance of $MoSe_2$. For instance, Wang et al. found that the $MoSe_2$@$Ni_{0.85}Se$ nanowire delivered enhanced kinetics and performance for HER in alkaline conditions due to the high density of active edges of $MoSe_2$ and the good conductivity of $Ni_{0.85}Se$ (Wang et al., 2017a). Zhang et al. synthesized 3D $MoSe_2$/$NiSe_2$ nanowires, which significantly enhanced HER activity with a low Tafel slope and overpotential in 0.5 M H_2SO_4, because the 3D structure affords more active sites (Zhang et al., 2017a). Liu et al. fabricated $MoSe_2$-NiSe@carbon heteronanostructures and achieved glorious HER catalytic properties and excellent durability in both acidic and base conditions (Liu et al., 2018). In addition, the hierarchical mesoporous $MoSe_2$@CoSe/N–C composite also exhibits outstanding HER activity (Chen et al., 2019b). Despite significant success, most of previous reports mainly focused on the improvement of HER performance, while the OER activity of $MoSe_2$ catalyst in alkaline media has been ignored. Hence, the rational design and fabrication of $MoSe_2$-based bifunctional electrocatalysts with satisfactory activity and stability toward overall water splitting in alkaline solution still remain a big challenge.

In this work, we developed a facile *in situ* phase separation strategy to construct a novel hierarchical heterostructure consisting of 0D−2D $CoSe_2$/$MoSe_2$ via the selenization of $CoMoO_4$ nanosheets supported on a carbon cloth (CC) (**Figure 1**). Due to the *in situ* phase transformation, $CoSe_2$ nanoparticles are uniformly anchored on $MoSe_2$ nanosheets in the integrated structure, which can not only enhance reaction kinetics because of the synergetic effects, thus boosting the electrocatalytic activity, but also effectively suppress the aggregation/restacking of $MoSe_2$ nanosheets, thereby improving the structural stability. Moreover, the hierarchical structure assembled by 0D−2D $CoSe_2$/$MoSe_2$ could provide abundant active sites for the electrochemical reactions. As a result, the designed $CoSe_2$/$MoSe_2$ architecture exhibits outstanding OER and HER performance in alkaline media. More specifically, a small overpotential of 280 mV is achieved at a current density of 10 $mA{\cdot}cm^{-2}$ for OER with a small Tafel slope of 86.8 $mV{\cdot}dec^{-1}$, and the overpotential is 90 mV at a current density of 10 $mA{\cdot}cm^{-2}$ for HER with a Tafel slope of 84.8 $mV{\cdot}dec^{-1}$ in 1 M KOH. Moreover, the symmetrical electrolyzer assembled with the $CoSe_2$/$MoSe_2$ catalysts delivers a small cell voltage of 1.63 V at 10 $mA{\cdot}cm^{-2}$ toward overall water splitting.

EXPERIMENTAL SECTION

Synthesis of $CoMoO_4$ Nanosheet

Firstly, a pristine carbon cloth (CC) was treated with nitric acid solution overnight, subsequently ultrasonicated in deionized (DI) water and dried in an oven at 80°C for 2 h. After that, 1 mmol cobalt acetate, 1 mmol ammonium molybdate, 2 mmol urea, and 5 mmol ammonium fluoride were dissolved in 30 mL DI water, followed by ultrasonication for 30 min. Then, the homogeneous solution was poured into a 50-mL Teflon-lined stainless autoclave with the CC kept at 150°C for 6 h. After cooling to room temperature, the CC was washed with DI water for several times and dried in a vacuum freeze-dryer overnight. Finally, the obtained sample was treated at 400°C for 2 h with a ramp rate of 5°C min^{-1} in an argon atmosphere.

Synthesis of $CoSe_2$/$MoSe_2$

The as-prepared $CoMoO_4$ precursor was reacted with 0.5 g selenium powder at 450°C for 1 h under an Ar/H_2 (90%/10%) atmosphere to form the $CoSe_2$/$MoSe_2$.

Synthesis of $CoSe_2$

The $CoSe_2$ was prepared through two steps. Firstly, the treated CC was immersed in a 0.1 M $Co(NO_3)_2$ solution for the electrodeposition of Co (Yang et al., 2015). Then, the collected sample was reacted with 0.5 g selenium powder under an Ar/H_2 (90%/10%) atmosphere at 450°C for 1 h.

Synthesis of $MoSe_2$

Firstly, MoS_2 was prepared via hydrothermal reaction with the CC at 200°C for 12 h, followed by heating at 400°C for 2 h to form MoO_3 (Wu et al., 2018). Then, the obtained MoO_3 was reacted with 0.5 g selenium powder at 450°C for 1 h under an Ar/H_2 (90%/10%) atmosphere.

Preparation of Pt/C

Four milligrams of 20% Pt/C and 20 μL 5% Nafion solution were added into 1 mL solution of isopropanol and DI water (9:1) and then sonicated to form a uniform solution. Finally, the 1*1 cm^2

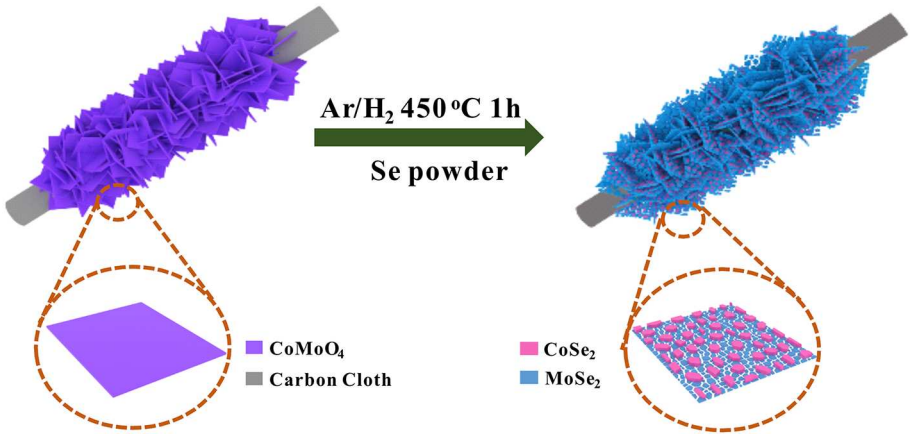

FIGURE 1 | Schematic illustration of the fabrication of $CoSe_2/MoSe_2$.

CC was soaked in the homogeneous solution and dried in air at atmospheric temperature.

Preparation of RuO_2

Four milligrams of RuO_2 and 20 μL 5% Nafion solution were added into 1 mL solution of isopropanol and DI water (9:1), and then the sample was sonicated to form a uniform solution. Finally, the 1*1 cm^2 CC was soaked in the homogeneous solution and dried in air at atmospheric temperature.

CHARACTERIZATION

The phase composition of the samples were characterized by X-ray diffraction (XRD, Bruker D8A A25), and the chemical states were determined through X-ray photoelectron spectroscopy (XPS, ESCALB 250Xi). The morphology and microstructure were recorded via field emission scanning electron microscopy (FE-SEM, FEI Nova NANOSEM 400) and high-resolution transmission electron microscopy (HR-TEM, JEM-2100 UHR STEM).

ELECTROCHEMICAL MEASUREMENTS

All samples made use of a three-electrode system performed by a biologic VSP300 type electrochemical workstation (Biologic Science Instruments, France). The sample of $CoSe_2/MoSe_2$ was put on the electrode holder as the working electrode with a mass loading of 4 mg/cm^2, the saturated calomel electrode (SCE) was the reference electrode, and a carbon rod served as the counter electrode. The electrolyte was 1 M KOH solution with saturated N_2. Linear sweep voltammetry (LSV) was characterized by polarization curves of OER with a scanning rate of 5 mV s^{-1} from 0 to 0.8 V vs. SCE. Similarly, the polarization curves of HER were determined under the same condition from 0 to −0.8 V vs. SCE. The potentials were standardized by a reversible hydrogen electrode (RHE) as shown in the following: E (RHE) = E (SCE) + 0.059 × pH with instrument automatic 85% iR compensation. The electrochemically active surface area (ECSA) was calculated by cyclic voltammetry (CV) performed from −0.3 to −0.2 V vs. SCE with different scanning rates of 40, 60, 80, 100, and 120 mV s^{-1}. Electrochemical impedance spectroscopy (EIS) measurements were conducted by biologic VMP3 (Biologic Science Instruments, France) from 100 KHz to 0.1 Hz. The overall water-splitting electrolyzer was performed with $CoSe_2/MoSe_2$ as electrodes and 1 M KOH as the electrolyte.

RESULTS AND DISCUSSION

Figure 2A presents the FE-SEM image of the as-prepared $CoMoO_4$ precursor, which presents uniform nanosheets (with a lateral size of 2 μm) perpendicularly grown on the CC substrate with high coverage. After a selenization process, the obtained $CoSe_2/MoSe_2$ sample well maintains the pristine morphology of the $CoMoO_4$ precursor (**Figure 2B**). Moreover, the high-magnification SEM image further reveals that lots of nanoparticles are well dispersed on the surface of the nanosheet (**Figure 2C**), implying the structure and phase evolution during the selenization treatment. The elemental maps in (**Figure 2D**) show that Mo, Co, and Se are uniformly distributed throughout the nanosheets. In addition, the low-resolution TEM images in (**Figures 2E,F**) display that nanoparticles are uniformly distributed on the nanosheet during the thermal reduction procedure, forming the 0D/2D structure. Furthermore, the high-resolution TEM (**Figure 2G**) shows the lattice fringes of 0.26 nm and 0.65 nm corresponding to the (111) and (002) planes of $CoSe_2$ and $MoSe_2$, respectively (Qu et al., 2016; Liu et al., 2017), demonstrating the successful formation of the $CoSe_2/MoSe_2$ after the selenization reaction.

To investigate phase evolution during the selenization process, the crystal structure and phase composition of the obtained samples were characterized by X-ray diffraction (XRD) analysis (**Figure 3A**). The diffraction peaks of $CoMoO_4$ precursor (in the black line) can be well indexed to the $CoMoO_4$ phase (JCPDS No: 21-0868) (Wang et al., 2016). After the thermal reduction, some

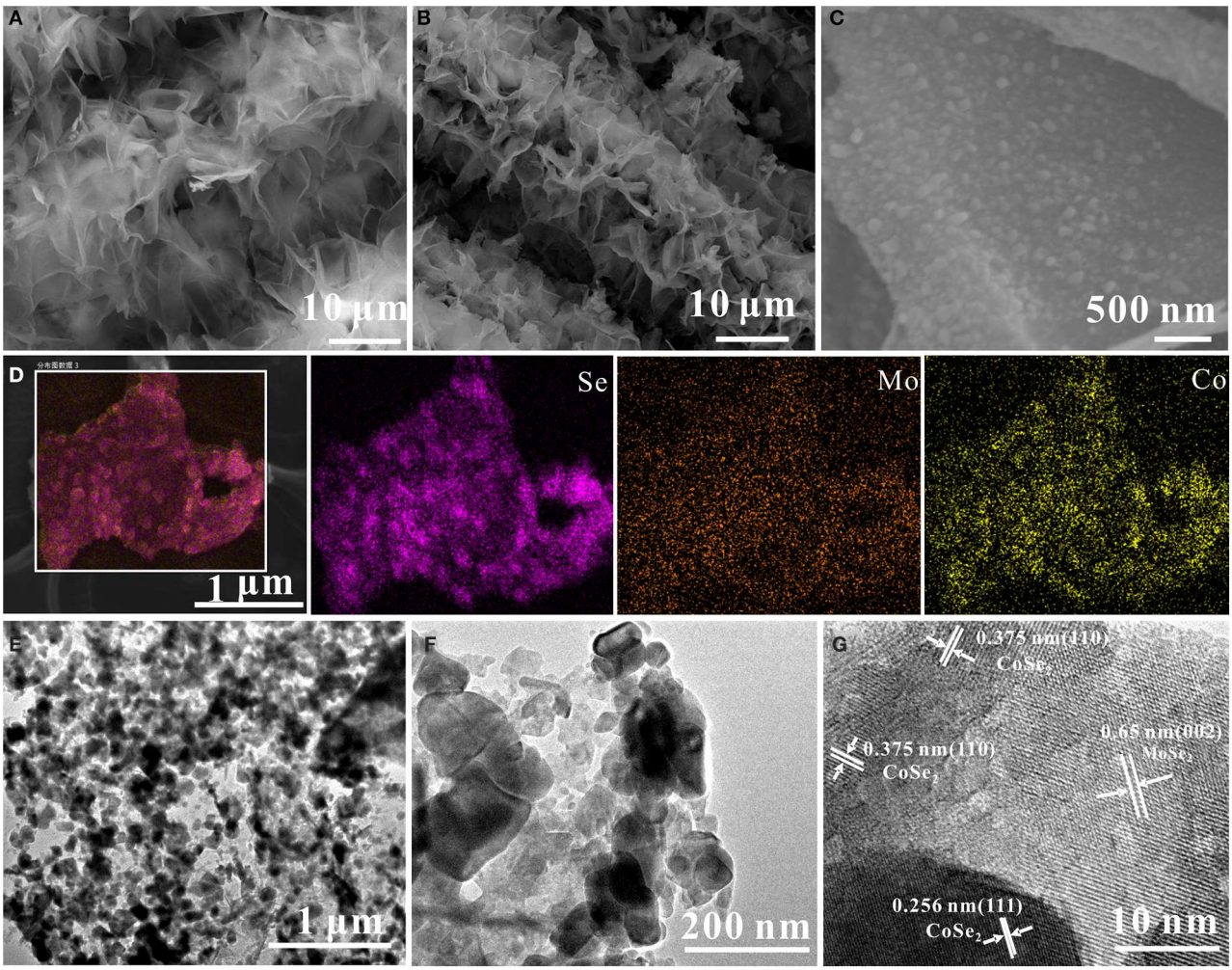

FIGURE 2 | FE-SEM images of **(A)** $CoMoO_4$ and **(B,C)** $CoSe_2/MoSe_2$; **(D)** elemental maps of $CoSe_2/MoSe_2$; **(E,F)** TEM of $CoSe_2/MoSe_2$; **(G)** HR-TEM images of $CoSe_2/MoSe_2$.

new diffraction peaks can be observed. The diffraction peaks at around 13.7 °, 27.6 °, 31.4 °, and 37.8 ° can be assigned to the $MoSe_2$ phase (JCPDS No: 77-1715) (Qu et al., 2016), while the other peaks could be attributed to the phase of $CoSe_2$ (JCPDS No:53-0449) (Liu et al., 2017). The XRD result clearly manifests the successful phase separation of the $CoSe_2$ and $MoSe_2$ from the $CoMoO_4$ precursor via the selenization process.

X-ray photoelectron spectroscopy (XPS) measurement was carried out to analyze the composition and chemical state of as-prepared samples. (**Figure 3B**) illustrates the high-resolution Co 2p peaks at 778.8 eV (Co $2p_{3/2}$), 793.7 eV (Co $2p_{1/2}$), 780 eV (Co $2p_{3/2}$), and 796 eV (Co $2p_{1/2}$), corresponding to $CoSe_2$ and cobalt–oxide bond, while those peaks at 784.1 eV and 801.5 eV are the satellite peaks (Mu et al., 2016; Wang et al., 2017b; Gao et al., 2018). Furthermore, the fine Mo 3d XPS spectrum (**Figure 3C**) shows the main peaks at 228.8 eV and 231.9 eV, which represent the Mo $3d_{5/2}$ and Mo $3d_{3/2}$ of $MoSe_2$ (Wang et al., 2018a,b). Additionally, the peak located at 230 eV can be ascribed to the Se 3s of $MoSe_2$ (Zhao et al., 2018). The Se 3d XPS spectrum (**Figure 3D**) displays the characteristic of $CoSe_2$ and $MoSe_2$ at 54.5 eV and 55.4 eV in agreement with the Se $3d_{5/2}$ and Se $3d_{3/2}$, respectively (Gao et al., 2018). Moreover, the peak at around 59.8 eV is confirmed to correspond to the selenium–oxygen bond (Kong et al., 2014). According to these results, the selenization process induced the phase separation from $CoMoO_4$ into the nanoscale $CoSe_2$ and $MoSe_2$.

It is generally recognized that highly efficient electrocatalysts worked in alkaline solution is the bottleneck for large-scale application of overall water splitting. Linear sweep voltammetry (LSV) at a scanning rate of 5 mV s^{-1} was characterized by the electrocatalytic HER and OER capacities of the samples by a three-electrode system in 1 M KOH solution with saturated N_2. By contrast, $CoSe_2$, $MoSe_2$ (**Figure S1**), RuO_2, and Pt/C catalysts were performed in the same condition. The HER polarization curves and corresponding Tafel slops

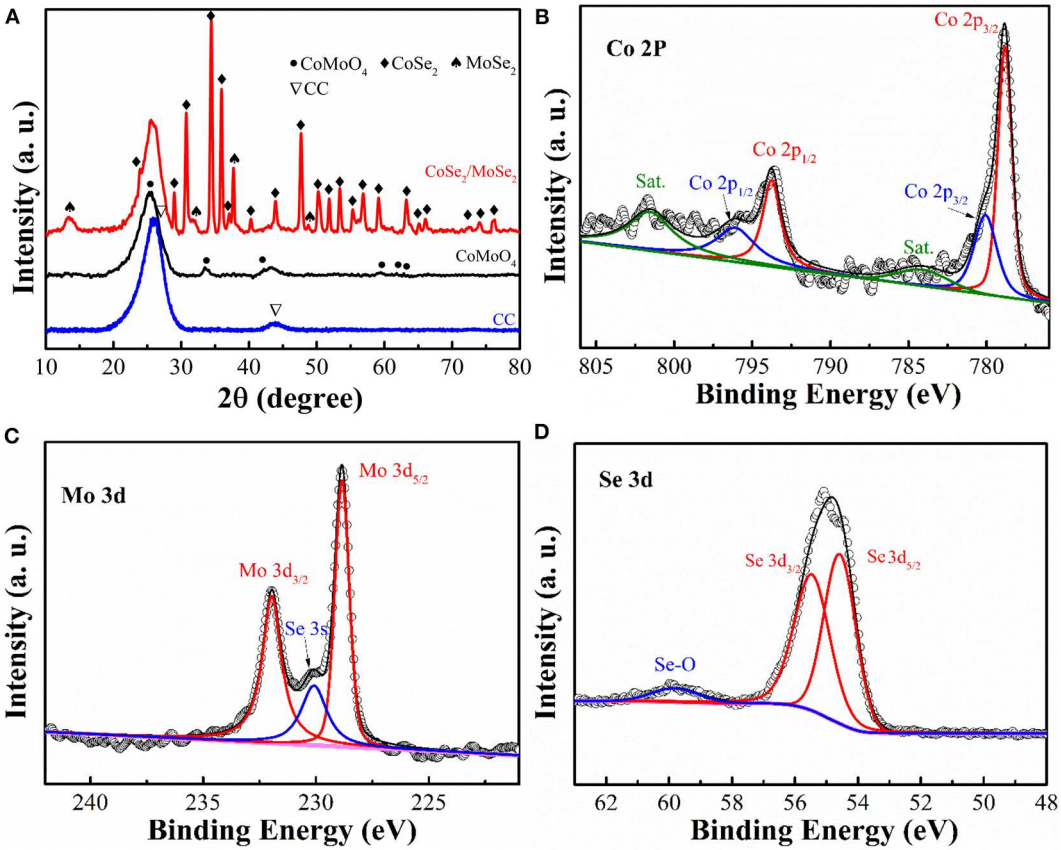

FIGURE 3 | (A) XRD patterns of CC, $CoMoO_4$, and $CoSe_2/MoSe_2$; high-resolution XPS spectra of **(B)** Mo 3d, **(C)** Co 2p, and **(D)** Se 3d of $CoSe_2/MoSe_2$.

are depicted in (**Figures 4A,B**). The overpotential (η_{10}) and Tafel slope of $CoSe_2/MoSe_2$ are 90 mV and 84.8 mV·dec^{-1}, which are better than those of $CoMoO_4$ (277 mV, 123.6 mV·dec^{-1}), $CoSe_2$ (205 mV, 195.2 mV·dec^{-1}), and $MoSe_2$ (199 mV, 152.4 mV·dec^{-1}). $CoSe_2$ has a metallic character, which can promote the dissociation of water and provide protons under alkaline conditions, thus improving the HER performance of $MoSe_2$ (Kwak et al., 2016). In addition, the hierarchical nanosheet array assembled by the $CoSe_2/MoSe_2$ provides abundant active sites for the electrochemical reaction at the phase interface, which can further enhance the HER performance (Zhang et al., 2017a). Therefore, the $CoSe_2/MoSe_2$ catalyst exhibits improved HER performance benefiting from the synergistic effect. The catalyst of Pt/C illustrates an overpotential (η_{10}) (59 mV) and Tafel slope (36.9 mV·dec^{-1}) in 1 M KOH that are similar to those in other literatures (Chen et al., 2018b; Wan et al., 2018). Moreover, the overpotential of $CoSe_2/MoSe_2$ is superior to those of recently reported selenide catalysts such as NiSe NWs/Ni Foam (96 mV) (Tang et al., 2015), EG/cobalt selenide/NiFe–LDH (260 mV) (Hou et al., 2016), o-$CoSe_2$/P (104 mV) (Zheng et al., 2018), $CoSe_2$ NCs (520 mV) (Kwak et al., 2016), $Co_{0.75}Ni_{0.25}Se$/NF (106 mV) (Liu et al., 2019), 1T $MoSe_2$/NiSe (120 mV) (Zhang et al., 2019), and SWCNTs/$MoSe_2$ (219 mV) (Najafi et al., 2019) (**Table S1**).

The electrocatalytic OER properties are determined by LSV and polarization measurements as shown in (**Figures 4D,E**). The $CoSe_2/MoSe_2$ catalyst shows a lower overpotential (η_{10} of 280 mV) than those of the $CoMoO_4$ (352 mV), $CoSe_2$ (322 mV), $MoSe_2$ (404 mV), and RuO_2 (318 mV), respectively. More importantly, the OER performance of the designed $CoSe_2/MoSe_2$ sample exceeds those of recently reported selenide catalysts in OER, for instance, the Ag–$CoSe_2$ (320 mV) (Zhao et al., 2017), $CoSe_2$ NCs (430 mV) (Kwak et al., 2016), $CoSe_2$/DETA (392 mV) (Guo et al., 2017), $NiCo_2Se_4$ holey nanosheets (295 mV) (Fang et al., 2017), NiSe–$Ni_{0.85}Se$/CP (300 mV) (Chen et al., 2018a), SWCNTs/$MoSe_2$ (295 mV) (Najafi et al., 2019), 1T/2H $MoSe_2$ (397 mV) (Li et al., 2019), and $CoSe_2$@$MoSe_2$ (309 mV) (Chen et al., 2019c) (**Table S2**). Furthermore, the corresponding Tafel slope of $CoSe_2/MoSe_2$ is 86.8 mV·dec^{-1}, which is smaller than those of the $CoMoO_4$ (101.8 mV·dec^{-1}), $CoSe_2$ (124 mV·dec^{-1}), $MoSe_2$ (130 mV·dec^{-1}), and RuO_2 (93.4 mV·dec^{-1}). The $CoSe_2/MoSe_2$ has lower overpotential and smaller Tafel, which can be attributed to its unique hierarchical heterostructure, facilitating electron transfer and accelerating OER kinetics. In this heterostructure, the transfer of electrons from $CoSe_2$ phase to

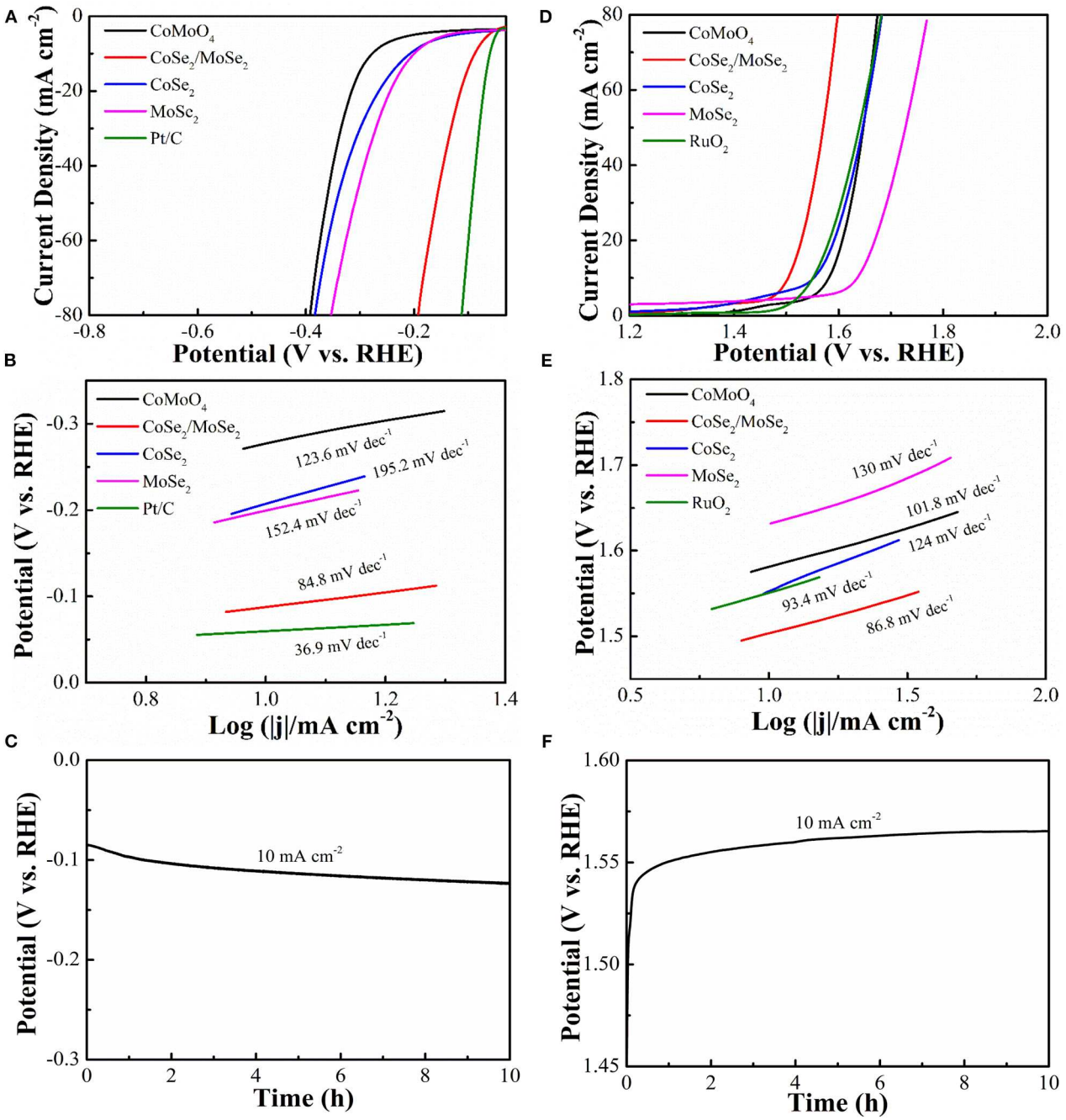

FIGURE 4 | (A) HER polarization curves of $CoMoO_4$, $CoSe_2/MoSe_2$, $CoSe_2$, $MoSe_2$, and Pt/C; **(B)** Tafel slopes; **(C)** galvanostatic of $CoSe_2/MoSe_2$ for HER; **(D)** OER polarization curves of $CoMoO_4$, $CoSe_2/MoSe_2$, $CoSe_2$, $MoSe_2$, and RuO_2; **(E)** Tafel slopes in OER; **(F)** galvanostatic of $CoSe_2/MoSe_2$ for OER.

$MoSe_2$ phase in the $CoSe_2/MoSe_2$ interface can result in electron-poor Co species and electron-rich Mo species (Liu et al., 2018). It is believed that the Se anion can affect the electron transfer between Co and Mo species, which is important for boosting catalytic ability (Yan et al., 2019). Besides, the formation of CoOOH is the primary cause to promote OER activity (Liu et al., 2015), and the increased 3d−4p repulsion between the center of the metal d band and the center of the p band of the Se site further promotes the rapid transfer of dioxygen molecules, thus improving OER performance (Li et al., 2017).

To understand the effects of the structure and composition of prepared catalyst on the electrochemical performance, several $CoSe_2/MoSe_2$ catalysts were collected at different selenization temperatures and the HER and OER performance were evaluated

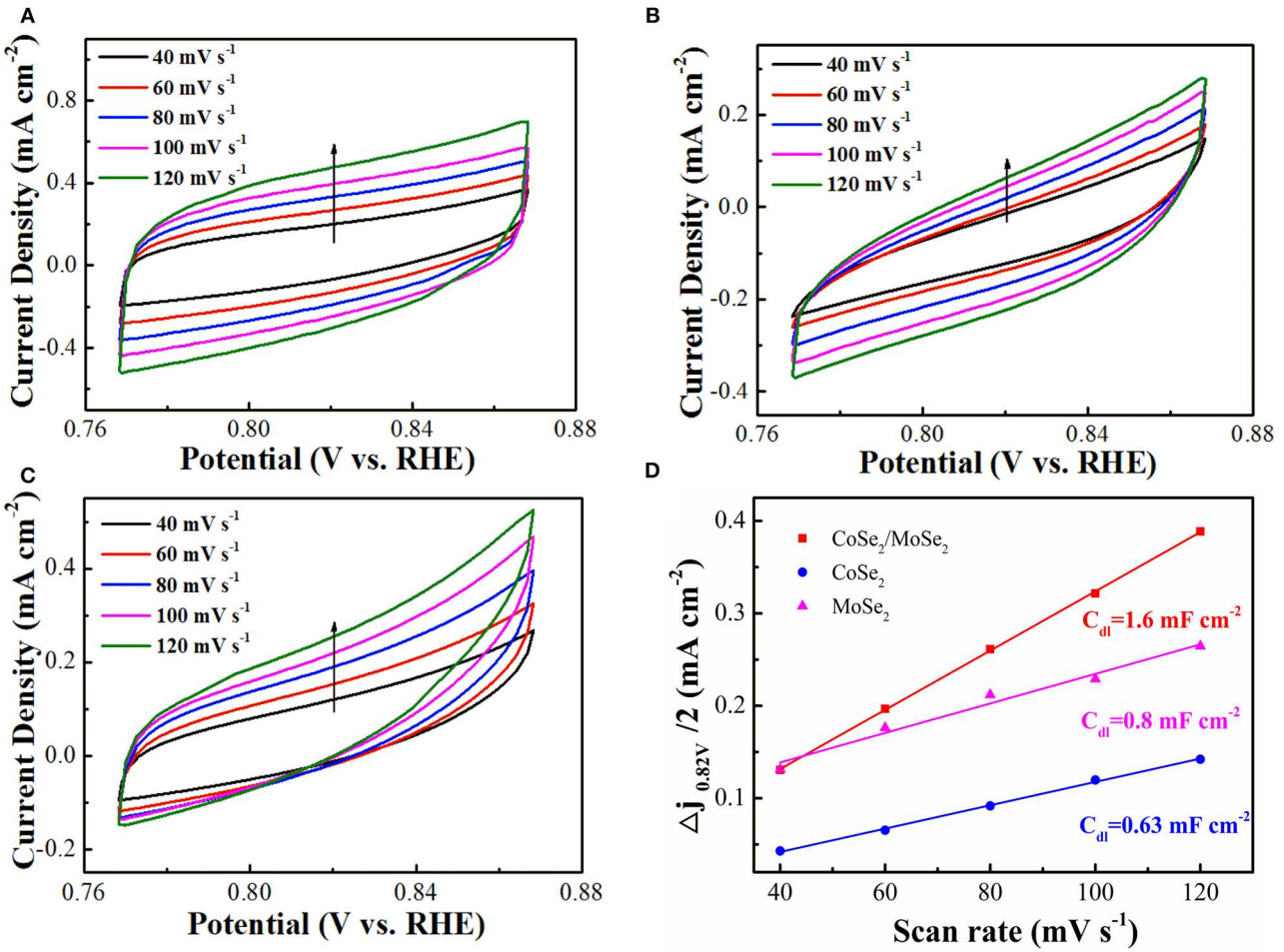

FIGURE 5 | Electrochemical double-layer capacitance with the CV curves acquired at different scanning rates from 40, 60, 80, 100, and 120 mV s^{-1}: **(A)** $CoSe_2/MoSe_2$, **(B)** $CoSe_2$, and **(C)** $MoSe_2$; **(D)** current densities (Δj = janode – jcathode, at 0.82 V) as a function of scanning rates of $CoSe_2/MoSe_2$, $CoSe_2$, and $MoSe_2$ with the corresponding slope being twice that of the C_{dl} values.

by LSV analysis (**Figure S2**). It can be seen that the $CoSe_2/MoSe_2$ sample obtained at 450°C ($CoSe_2/MoSe_2$-450) possesses better electrocatalytic properties than other counterparts, which can be ascribed to its superior structure. As shown in (**Figure S3**), with the selenization temperature increasing, the size of nanoparticles on the surface of nanosheets increased as well, indicating higher crystallinity. Generally, larger particle size will reduce the active surface of catalyst (Zhang et al., 2017b; Chen et al., 2019a). Therefore, when the selenization temperature elevated to 500°C ($CoSe_2/MoSe_2$-500), the catalytic performance slightly declined owing to its larger particle size and lower active surface. In addition, (**Figure S4**) displays the composition of the $CoSe_2/MoSe_2$ catalysts achieved at a different selenization temperature. As can be seen, when the selenization process proceeded at low temperature, the obtained $CoSe_2/MoSe_2$ catalyst has poor $MoSe_2$ phase and low crystallinity, which are responsible for the poor electrochemical catalytic performance of the catalysts ($CoSe_2/MoSe_2$-350 and $CoSe_2/MoSe_2$-400). Therefore, the catalyst synthesized at 450°C shows the best performance, benefiting from the appropriate crystal structure and phase composition.

The electrochemically active surface area (ECSA) of as-prepared catalyst was evaluated by the double-layer capacitance (C_{dl}), which was measured by CV in a non-Faradaic reaction potential range (Deng et al., 2015). The C_{dl} values of the $CoSe_2/MoSe_2$ (1.6 mF cm^{-2}) is higher than those of $CoSe_2$ (0.63 mF cm^{-2}) and $MoSe_2$ (0.8 mF cm^{-2}), as shown in (**Figure 5**), suggesting more active sites of the $CoSe_2/MoSe_2$ catalyst. Furthermore, the smaller R_{ct} value for the $CoSe_2/MoSe_2$ catalyst in the EIS measurement (**Figure S5**) implies the promoted charge transfer and boosted kinetics, which can be ascribed to the abundant interfaces and synergetic effect between the $CoSe_2$ and $MoSe_2$.

The structural stability is another significant parameter for catalysts in HER and OER. (**Figures 4C,F**) show a galvanostatic for $CoSe_2/MoSe_2$ catalyst in both the HER and OER processes. The morphology and composition of the catalyst after galvanostatic cycling are characterized by SEM and XPS. The

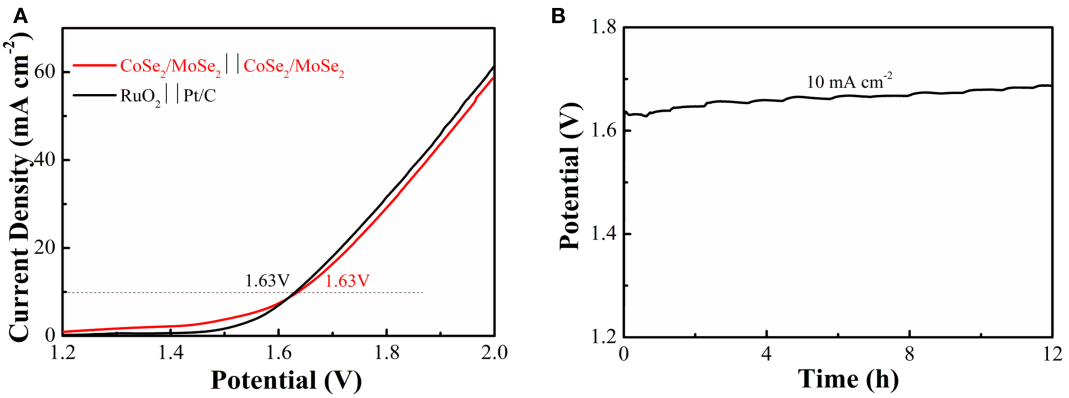

FIGURE 6 | (A) LSV curves of water splitting with $CoSe_2/MoSe_2$ as the anode and cathode; **(B)** galvanostatic testing of the $CoSe_2/MoSe_2$-based water splitting electrolyzer for 12 h at 10 mA cm^{-2}.

$CoSe_2/MoSe_2$ could well inherit the pristine sheet-like structure, demonstrating good structural stability. In addition, the fine XPS spectra of the Co 2p, Mo 3d, Se 3d acquired from the sample of $CoSe_2/MoSe_2$ after galvanostatic measurement confirm the reservation of $CoSe_2$ and $MoSe_2$ (**Figure S6**), indicating phase stability during the electrochemical reactions.

To investigate its practical application of the obtained catalyst, an overall water splitting electrolyzer is assembled with $CoSe_2/MoSe_2$ as electrodes in 1 M KOH. It can decompose water at a low cell voltage of 1.63 V (current density at 10 mA·cm^{-2}) (**Figure 6A**), and the efficiency is similar to those constituting of the noble-metal-based cathode and anode (RuO_2 vs. Pt/C). Moreover, the overall water splitting performance of the $CoSe_2/MoSe_2$ is better than those of other recently reported non-noble metals at the same current density, such as $(Ni,Co)_{0.85}Se$ NSAs (1.65 V) (Xiao et al., 2018), a-CoSe/Ti mesh (1.65 V) (Liu et al., 2015), CoO_x-CoSe (1.64 V) (Xu et al., 2016), $Co_{0.85}Se$@NC (1.76 V) (Meng et al., 2017), $CoB_2/CoSe_2$ (1.73 V) (Guo et al., 2017), $NiSe_2$/Ni (1.64 V) (Zhang et al., 2018), 1T/2H $MoSe_2$/MXene (1.64 V) (Li et al., 2019), and Ni_3Se_2/CF (1.65 V) (Shi et al., 2015) (**Table S3**). Additionally, $CoSe_2/MoSe_2$ electrolyzer exhibits a slight increase in the potential after being cycled for 12 h in alkaline solution (**Figure 6B**).

CONCLUSION

In summary, a novel hierarchical 0D−2D Co/Mo selenide was developed by a facile *in situ* phase separation strategy. Benefiting from its unique structure and composition, the constructed $CoSe_2/MoSe_2$ catalyst exhibits small η_{10} of 280 mV and 90 mV and Tafel slopes of 86.8 mV·dec^{-1} and 84.8 mV·dec^{-1} for OER and HER, respectively. Furthermore, the electrolyzer comprising $CoSe_2/MoSe_2$ as the bifunctional catalyst shows a small water splitting cell voltage of 1.63 V at a current density of 10 mA·cm^{-2}. This work provides insights into rational design and development of economical and valid bifunctional catalysts for overall water splitting.

DATA AVAILABILITY STATEMENT

All datasets generated for this study are included in the article/**Supplementary Material**.

AUTHOR CONTRIBUTIONS

LX implemented the experiment, analyzed the data and wrote the article. HS, XL, XZ, and BG participated in the formulation of the experimental scheme. YZ, KH, and PC revised the article.

FUNDING

This work was financially supported by the National Natural Science Foundation of China (Nos. 51572100, 61434001, and 31500783).

SUPPLEMENTARY MATERIAL

The Supplementary Material for this article can be found online at: https://www.frontiersin.org/articles/10.3389/fchem.2020.00382/full#supplementary-material

REFERENCES

Amiinu, I. S., Pu, Z., Liu, X., Owusu, K. A., Monestel, H. G. R., Boakye, F. O., et al. (2017). Multifunctional Mo–N/C@MoS_2 electrocatalysts for her, oer, orr, and Zn–air batteries. *Adv. Funct. Mater.* 27:1702300. doi: 10.1002/adfm.201702300

Chen, J., Ge, Y., Feng, Q., Zhuang, P., Chu, H., Cao, Y., et al. (2019a). Nesting Co_3Mo binary alloy nanoparticles onto molybdenum oxide nanosheet arrays for superior hydrogen evolution reaction. *ACS Appl. Mater. Interfaces* 11, 9002–9010. doi: 10.1021/acsami.8b19148

Chen, J., Pan, A., Wang, Y., Cao, X., Zhang, W., Kong, X., et al. (2019b). Hierarchical mesoporous $MoSe_2$@CoSe/N-doped carbon nanocomposite for

sodium ion batteries and hydrogen evolution reaction applications. *Energy Storage Mater.* 21, 97–106. doi: 10.1016/j.ensm.2018.10.019

Chen, Y., Ren, Z., Fu, H., Zhang, X., Tian, G., and Fu, H. (2018a). NiSe-$Ni_{0.85}Se$ heterostructure nanoflake arrays on carbon paper as efficient electrocatalysts for overall water splitting. *Small* 14:1800763. doi: 10.1002/smll.201800763

Chen, Z., Wang, W., Huang, S., Ning, P., Wu, Y., Gao, C., et al. (2019c). Well-defined $CoSe_2$@$MoSe_2$ hollow heterostructured nanocubes with enhanced dissociation kinetics for overall water splitting. *Nanoscale* 12, 326–335. doi: 10.1039/C9NR08751F

Chen, Z., Wu, R., Liu, Y., Ha, Y., Guo, Y., Sun, D., et al. (2018b). Ultrafine Co nanoparticles encapsulated in carbon-nanotubes-grafted graphene sheets as advanced electrocatalysts for the hydrogen evolution reaction. *Adv. Mater.* 30:1802011. doi: 10.1002/adma.201802011

Deng, Z. H., Li, L., Ding, W., Xiong, K., and Wei, Z. D. (2015). Synthesized ultrathin MoS_2 nanosheets perpendicular to graphene for catalysis of hydrogen evolution reaction. *Chem. Commun.* 51, 1893–1896. doi: 10.1039/C4CC08491H

Fang, Z., Peng, L., Lv, H., Zhu, Y., Yan, C., Wang, S., et al. (2017). Metallic transition metal selenide holey nanosheets for efficient oxygen evolution electrocatalysis. *ACS Nano* 11, 9550–9557. doi: 10.1021/acsnano.7b05481

Gao, J., Li, Y., Shi, L., Li, J., and Zhang, G. (2018). Rational design of hierarchical nanotubes through encapsulating $CoSe_2$ nanoparticles into $MoSe_2$/C composite shells with enhanced lithium and sodium storage performance. *ACS Appl. Mater. Interfaces* 10, 20635–20642. doi: 10.1021/acsami.8b06442

Guo, Y., Yao, Z., Shang, C., and Wang, E. (2017). Amorphous Co_2B grown on $CoSe_2$ nanosheets as a hybrid catalyst for efficient overall water splitting in alkaline medium. *ACS Appl. Mater. Interfaces* 9, 39312–39317. doi: 10.1021/acsami.7b10605

Hou, Y., Lohe, M. R., Zhang, J., Liu, S., Zhuang, X., and Feng, X. (2016). Vertically oriented cobalt selenide/NiFe layered-double-hydroxide nanosheets supported on exfoliated graphene foil: an efficient 3D electrode for overall water splitting. *Energy Environ. Sci.* 9, 478–483. doi: 10.1039/C5EE03440J

Jamesh, M. I., and Sun, X. (2018). Recent progress on earth abundant electrocatalysts for oxygen evolution reaction (OER) in alkaline medium to achieve efficient water splitting-a review. *J. Power Sources* 400, 31–68. doi: 10.1016/j.jpowsour.2018.07.125

Jaramillo, T. F., Jørgensen, K. P., Bonde, J., Nielsen, J. H., Horch, S., and Chorkendorff, I. (2007). Identification of active edge sites for electrochemical H_2 evolution from MoS_2 nanocatalysts. *Science* 317:100. doi: 10.1126/science.1141483

Kong, D., Wang, H., Lu, Z., and Cui, Y. (2014). $CoSe_2$ nanoparticles grown on carbon fiber paper: an efficient and stable electrocatalyst for hydrogen evolution reaction. *J. Am. Chem. Soc.* 136, 4897–4900. doi: 10.1021/ja501497n

Kwak, I. H., Im, H. S., Jang, D. M., Kim, Y. W., Park, K., Lim, Y. R., et al. (2016). $CoSe_2$ and $NiSe_2$ nanocrystals as superior bifunctional catalysts for electrochemical and photoelectrochemical water splitting. *ACS Appl. Mater. Interfaces* 8, 5327–5334. doi: 10.1021/acsami.5b12093

Lai, F., Yong, D., Ning, X., Pan, B., Miao, Y. E., and Liu, T. (2017). Bionanofiber assisted decoration of few-layered $MoSe_2$ nanosheets on 3D conductive networks for efficient hydrogen evolution. *Small* 13:1602866. doi: 10.1002/smll.201602866

Li, N., Zhang, Y., Jia, M., Lv, X., Li, X., Li, R., et al. (2019). 1T/2H $MoSe_2$-on-MXene heterostructure as bifunctional electrocatalyst for efficient overall water splitting. *Electrochim. Acta* 326:134976. doi: 10.1016/j.electacta.2019.134976

Li, W., Gao, X., Xiong, D., Wei, F., Song, W. G., Xu, J., et al. (2017). Hydrothermal synthesis of monolithic Co_3Se_4 nanowire electrodes for oxygen evolution and overall water splitting with high efficiency and extraordinary catalytic stability. *Adv. Energy Mater.* 7:1602579. doi: 10.1002/aenm.201602579

Liu, C., Wang, K., Zheng, X., Liu, X., Liang, Q., and Chen, Z. (2018). Rational design of $MoSe_2$-NiSe@carbon heteronanostructures for efficient electrocatalytic hydrogen evolution in both acidic and alkaline media. *Carbon* 139, 1–9. doi: 10.1016/j.carbon.2018.06.034

Liu, S., Jiang, Y., Yang, M., Zhang, M., Guo, Q., Shen, W., et al. (2019). Highly conductive and metallic cobalt-nickel selenide nanorods supported on Ni foam as an efficient electrocatalyst for alkaline water splitting. *Nanoscale* 11, 7959–7966. doi: 10.1039/C8NR10545F

Liu, T., Liu, Q., Asiri, A. M., Luo, Y., and Sun, X. (2015). An amorphous CoSe film behaves as an active and stable full water-splitting electrocatalyst under strongly alkaline conditions. *Chem. Commun.* 51, 16683–16686. doi: 10.1039/C5CC06892

Liu, X., Liu, Y., and Fan, L. Z. (2017). MOF-derived $CoSe_2$ microspheres with hollow interiors as high-performance electrocatalysts for the enhanced oxygen evolution reaction. *J. Mater. Chem. A* 5, 15310–15314. doi: 10.1039/C7TA04662F

Luo, Y., Li, X., Cai, X., Zou, X., Kang, F., Cheng, H. M., et al. (2018). Two-dimensional MoS_2 confined $Co(OH)_2$ electrocatalysts for hydrogen evolution in alkaline electrolytes. *ACS Nano* 12, 4565–4573. doi: 10.1021/acsnano.8b00942

Mao, S., Wen, Z., Ci, S., Guo, X., Ostrikov, K., and Chen, J. (2015). Perpendicularly oriented $MoSe_2$/graphene nanosheets as advanced electrocatalysts for hydrogen evolution. *Small* 11, 414–419. doi: 10.1002/smll.201401598

Meng, T., Qin, J., Wang, S., Zhao, D., Mao, B., and Cao, M. (2017). In situ coupling of $Co_{0.85}Se$ and N-doped carbon via one-step selenization of metal-organic frameworks as a trifunctional catalyst for overall water splitting and Zn-air batteries. *J. Mater. Chem. A* 5, 7001–7014. doi: 10.1039/C7TA01453H

Mu, C. H., Qi, H. X., Song, Y. Q., Liu, Z. P., Ji, L. X., Deng, J. G., et al. (2016). One-pot synthesis of nanosheet-assembled hierarchical $MoSe_2$/$CoSe_2$ microcages for the enhanced performance of electrocatalytic hydrogen evolution. *RSC Adv.* 6, 23–30. doi: 10.1039/C5RA21638A

Najafi, L., Bellani, S., Oropesa-Nuñez, R., Prato, M., Martín-García, B., Brescia, R., et al. (2019). Carbon nanotube-supported $MoSe_2$ holey flake:Mo_2C ball hybrids for bifunctional pH-universal water splitting. *ACS Nano* 13, 3162–3176. doi: 10.1021/acsnano.8b08670

Qu, B., Li, C., Zhu, C., Wang, S., Zhang, X., and Chen, Y. (2016). Growth of $MoSe_2$ nanosheets with small size and expanded spaces of (002) plane on the surfaces of porous N-doped carbon nanotubes for hydrogen production. *Nanoscale* 8, 16886–16893. doi: 10.1039/C6NR04619C

Qu, B., Yu, X., Chen, Y., Zhu, C., Li, C., Yin, Z., et al. (2015). Ultrathin $MoSe_2$ nanosheets decorated on carbon fiber cloth as binder-free and high-performance electrocatalyst for hydrogen evolution. *ACS Appl. Mater. Interfaces* 7, 14170–14175. doi: 10.1021/acsami.5b02753

Shi, J., Hu, J., Luo, Y., Sun, X., and Asiri, A. M. (2015). Ni_3Se_2 film as a non-precious metal bifunctional electrocatalyst for efficient water splitting. *Catal. Sci. Technol.* 5, 4954–4958. doi: 10.1039/C5CY01121C

Tang, C., Cheng, N., Pu, Z., Xing, W., and Sun, X. (2015). NiSe nanowire film supported on nickel foam: an efficient and stable 3D bifunctional electrode for full water splitting. *Angew. Chem. Int. Ed.* 54, 9351–9355. doi: 10.1002/anie.201503407

Tang, H., Dou, K., Kaun, C. C., Kuang, Q., and Yang, S. (2014). $MoSe_2$ nanosheets and their graphene hybrids: synthesis, characterization and hydrogen evolution reaction studies. *J. Mater. Chem. A* 2, 360–364. doi: 10.1039/C3TA13584E

Tang, Q., and Jiang, D. E. (2016). Mechanism of hydrogen evolution reaction on 1T-MoS_2 from first principles. *ACS Catal.* 6, 4953–4961. doi: 10.1021/acscatal.6b01211

Trasatti, S. (1972). Work function, electronegativity, and electrochemical behaviour of metals: iii. electrolytic hydrogen evolution in acid solutions. *J. Electroanal. Chem.* 39, 163–184. doi: 10.1016/S0022-0728(72)80485-6

Trasatti, S. (1984). Electrocatalysis in the anodic evolution of oxygen and chlorine. *Electrochim. Acta* 29, 1503–1512. doi: 10.1016/0013-4686(84)85004-5

Wan, S., Jin, W., Guo, X., Mao, J., Zheng, L., Zhao, J., et al. (2018). Self-templating construction of porous $CoSe_2$ nanosheet arrays as efficient bifunctional electrocatalysts for overall water splitting. *ACS Sustain. Chem. Eng.* 6, 15374–15382. doi: 10.1021/acssuschemeng.8b03804

Wang, B., Li, S., Wu, X., Liu, J., Tian, W., and Chen, J. (2016). Self-assembly of ultrathin mesoporous $CoMoO_4$ nanosheet networks on flexible carbon fabric as a binder-free anode for lithium-ion batteries. *New J. Chem.* 40, 2259–2267. doi: 10.1039/c5nj02910d

Wang, B., Wang, Z., Wang, X., Zheng, B., Zhang, W., and Chen, Y. (2018a). Scalable synthesis of porous hollow $CoSe_2$-$MoSe_2$/carbon microspheres for highly efficient hydrogen evolution reaction in acidic and alkaline media. *J. Mater. Chem. A* 6, 12701–12707. doi: 10.1039/C8TA03523G

Wang, C., Zhang, P., Lei, J., Dong, W., and Wang, J. (2017a). Integrated 3D $MoSe_2$@$Ni_{0.85}Se$ nanowire network with synergistic cooperation as highly efficient electrocatalysts for hydrogen evolution reaction in alkaline medium. *Electrochim. Acta* 246, 712–719. doi: 10.1016/j.electacta.2017.06.028

Wang, P., Pu, Z., Li, W., Zhu, J., Zhang, C., Zhao, Y., et al. (2019). Coupling $NiSe_2$-Ni_2P heterostructure nanowrinkles for highly efficient overall water splitting. *J. Catal.* 377, 600–608. doi: 10.1016/j.jcat.2019.08.005

Wang, X., Li, F., Li, W., Gao, W., Tang, Y., and Li, R. (2017b). Hollow bimetallic cobalt-based selenide polyhedrons derived from metal-organic framework: an efficient bifunctional electrocatalyst for overall water splitting. *J. Mater. Chem. A* 5, 17982–17989. doi: 10.1039/C7TA03167J

Wang, X., Zheng, B., Yu, B., Wang, B., Hou, W., Zhang, W., et al. (2018b). In situ synthesis of hierarchical $MoSe_2$-$CoSe_2$ nanotubes as an efficient electrocatalyst for the hydrogen evolution reaction in both acidic and alkaline media. *J. Mater. Chem. A* 6, 7842–7850. doi: 10.1039/C8TA01552J

Wu, K., Zhan, J., Xu, G., Zhang, C., Pan, D., and Wu, M. (2018). MoO_3 nanosheet arrays as superior anode materials for Li- and Na-ion batteries. *Nanoscale* 10, 16040–16049. doi: 10.1039/C8NR03372B

Xiao, K., Zhou, L., Shao, M., and Wei, M. (2018). Fabrication of $(Ni,Co)_{0.85}Se$ nanosheet arrays derived from layered double hydroxides toward largely enhanced overall water splitting. *J. Mater. Chem. A* 6, 7585–7591. doi: 10.1039/C8TA01067F

Xie, J., Zhang, H., Li, S., Wang, R., Sun, X., Zhou, M., et al. (2013). Defect-rich MoS_2 ultrathin nanosheets with additional active edge sites for enhanced electrocatalytic hydrogen evolution. *Adv. Mater.* 25, 5807–5813. doi: 10.1002/adma.201302685

Xu, X., Du, P., Chen, Z., and Huang, M. (2016). An electrodeposited cobalt-selenide-based film as an efficient bifunctional electrocatalyst for full water splitting. *J. Mater. Chem. A* 4, 10933–10939. doi: 10.1039/C6TA03788G

Xue, X., Zhang, J., Saana, I. A., Sun, J., Xu, Q., and Mu, S. (2018). Rational inert-basal-plane activating design of ultrathin $1T'$ phase MoS_2 with a MoO_3 heterostructure for enhancing hydrogen evolution performances. *Nanoscale* 10, 16531–16538. doi: 10.1039/C8NR05270K

Yan, H., Xie, Y., Wu, A., Cai, Z., Wang, L., Tian, C., et al. (2019). Anion-modulated HER and OER activities of 3D Ni-V-based interstitial compound heterojunctions for high-efficiency and stable overall water splitting. *Adv. Mater.* 31:1901174. doi: 10.1002/adma.201901174

Yang, L. J., Deng, Y. Q., Zhang, X. F., Liu, H., and Zhou, W. J. (2018). $MoSe_2$ nanosheet/MoO_2 nanobelt/carbon nanotube membrane as flexible and multifunctional electrodes for full water splitting in acidic electrolyte. *Nanoscale* 10, 9268–9275. doi: 10.1039/C8NR01572D

Yang, X., Lu, A. Y., Zhu, Y., Hedhili, M. N., Min, S., Huang, K. W., et al. (2015). CoP nanosheet assembly grown on carbon cloth: a highly efficient electrocatalyst for hydrogen generation. *Nano Energy* 15, 634–641. doi: 10.1016/j.nanoen.2015.05.026

Zhang, J., Wang, Y., Zhang, C., Gao, H., Lv, L., Han, L., et al. (2018). Self-supported porous $NiSe_2$ nanowrinkles as efficient bifunctional electrocatalysts for overall water splitting. *ACS Sustainable Chem. Eng.* 6, 2231–2239. doi: 10.1021/acssuschemeng.7b03657

Zhang, L., Wang, T., Sun, L., Sun, Y., Hu, T., Xu, K., et al. (2017a). Hydrothermal synthesis of 3D hierarchical $MoSe_2$/$NiSe_2$ composite nanowires on carbon fiber paper and their enhanced electrocatalytic activity for the hydrogen evolution reaction. *J. Mater. Chem. A* 5, 19752–19759. doi: 10.1039/C7TA05352E

Zhang, Q., Li, P., Zhou, D., Chang, Z., Kuang, Y., and Sun, X. (2017b). Superaerophobic ultrathin Ni-Mo alloy nanosheet array from in situ topotactic reduction for hydrogen evolution reaction. *Small* 13:1701648. doi: 10.1002/smll.201701648

Zhang, X., Zhang, Y. Y., Zhang, Y., Jiang, W. J., Zhang, Q. H., Yang, Y. G., et al. (2019). Phase-controlled synthesis of 1T-$MoSe_2$/NiSe heterostructure nanowire arrays via electronic injection for synergistically enhanced hydrogen evolution. *Small Methods* 3:1800317. doi: 10.1002/smtd.201800317

Zhao, G., Li, P., Rui, K., Chen, Y., Dou, S. X., and Sun, W. (2018). $CoSe_2$/$MoSe_2$ heterostructures with enriched water adsorption/dissociation sites towards enhanced alkaline hydrogen evolution reaction. *Chem. Eur. J.* 24, 11158–11165. doi: 10.1002/chem.201801693

Zhao, X., Zhang, H., Yan, Y., Cao, J., Li, X., Zhou, S., et al. (2017). Engineering the electrical conductivity of lamellar silver-doped cobalt(II) selenide nanobelts for enhanced oxygen evolution. *Angew. Chem. Int. Ed.* 56, 328–332. doi: 10.1002/anie.201609080

Zheng, Y. R., Wu, P., Gao, M. R., Zhang, X. L., Gao, F. Y., Ju, H. X., et al. (2018). Doping-induced structural phase transition in cobalt diselenide enables enhanced hydrogen evolution catalysis. *Nat. Commun.* 9:2533. doi: 10.1038/s41467-018-04954-7

Zhu, C., Wang, A. L., Xiao, W., Chao, D., Zhang, X., Tiep, N. H., et al. (2018). In situ grown epitaxial heterojunction exhibits high-performance electrocatalytic water splitting. *Adv. Mater.* 30:1705516. doi: 10.1002/adma.201705516

Conflict of Interest: The authors declare that the research was conducted in the absence of any commercial or financial relationships that could be construed as a potential conflict of interest.

frontiers in Chemistry

ORIGINAL RESEARCH
published: 12 June 2020
doi: 10.3389/fchem.2020.00457

Influence of K_2NbF_7 Catalyst on the Desorption Behavior of $LiAlH_4$

*Nurul Amirah Ali, Noratiqah Sazelee, Muhammad Syarifuddin Yahya and Mohammad Ismail**

Energy Storage Research Group, Faculty of Ocean Engineering Technology and Informatics, Universiti Malaysia Terengganu, Terengganu, Malaysia

In this study, the modification of the desorption behavior of $LiAlH_4$ by the addition of K_2NbF_7 was explored for the first time. The addition of K_2NbF_7 causes a notable improvement in the desorption behavior of $LiAlH_4$. Upon the addition of 10 wt.% of K_2NbF_7, the desorption temperature of $LiAlH_4$ was significantly lowered. The desorption temperature of the $LiAlH_4$ + 10 wt.% K_2NbF_7 sample was lowered to 90°C (first-stage reaction) and 149°C (second-stage reaction). Enhancement of the desorption kinetics performance with the $LiAlH_4$ + 10 wt.% K_2NbF_7 sample was substantiated, with the composite sample being able to desorb hydrogen 30 times faster than did pure $LiAlH_4$. Furthermore, with the presence of 10 wt.% K_2NbF_7, the calculated activation energy values for the first two desorption stages were significantly reduced to 80 and 86 kJ/mol; 24 and 26 kJ/mol lower than the as-milled $LiAlH_4$. After analysis of the X-ray diffraction result, it is believed that the *in situ* formation of NbF_4, LiF, and K or K-containing phases that appeared during the heating process promoted the amelioration of the desorption behavior of $LiAlH_4$ with the addition of K_2NbF_7.

Keywords: hydrogen storage, lithium aluminum hydride, desorption, catalyst, metal halide

OPEN ACCESS

Edited by:
Guanglin Xia,
Fudan University, China

Reviewed by:
Xuezhang Xiao,
Zhejiang University, China
Chu Liang,
Zhejiang University of Technology, China

****Correspondence:***
Mohammad Ismail
mohammadismail@umt.edu.my

Specialty section:
This article was submitted to Inorganic Chemistry, a section of the journal Frontiers in Chemistry

Received: *16 February 2020*
Accepted: *01 May 2020*
Published: *12 June 2020*

Citation:
Ali NA, Sazelee N, Yahya MS and Ismail M (2020) Influence of K_2NbF_7 Catalyst on the Desorption Behavior of $LiAlH_4$. Front. Chem. 8:457. doi: 10.3389/fchem.2020.00457

INTRODUCTION

The excessive consumption of fossil fuels and the emission of carbon dioxide are the roots of environmental pollution. As a resolution to this global issue, the utilization of clean, and sustainable energy resources such as hydrogen, wind, and solar has become an inescapable need. Recently, hydrogen has received a large amount of attention as a future energy carrier. Hydrogen promises to be a clean and renewable energy carrier. Moreover, the production of hydrogen can be achieved from various resources, both renewable (e.g., solar, wind, and hydro) and non-renewable (e.g., natural gas and coal; Winter, 2009; Parra et al., 2019). Furthermore, energy production via hydrogen-oxygen reaction will only produce water as a by-product (Crabtree et al., 2004).

In pursuit of the success of hydrogen as a future energy carrier, the need for an efficient and reliable storage method has become the top priority. In general, there are three forms of hydrogen storage which are: (i) compressed hydrogen gas, which requires high pressure, (ii) liquefaction, and (iii) solid-state hydrogen storage via hydrides (Dalebrook et al., 2013; Zhang et al., 2016; Barthelemy et al., 2017). Solid-state hydrogen storage has been perceived to be an efficient and favorable method because of its safety, storage requirements, and storage capacity.

Lithium aluminum hydride ($LiAlH_4$) has major benefits and is the preferable solid-state material. $LiAlH_4$ is attractive due to its low temperature of hydrogen release and high storage capacity (10.6 wt.%; Andrei et al., 2005; Ares et al., 2008). The desorption process of $LiAlH_4$ occurs in three stages, as follows:

$$3LiAlH_4 \rightarrow Li_3AlH_6 + 2Al + 3H_2 \quad (1)$$

$$Li_3AlH_6 + 2Al \rightarrow 3LiH + 3Al + 3/2H_2 \quad (2)$$

$$3LiH + 3Al \rightarrow 3LiAl + 3/2\,H_2 \quad (3)$$

The first reaction (1) occurs in a temperature range of 150–175°C and desorbs 5.2 wt.% of the hydrogen. The second reaction (2) takes places at 180–220°C and desorbs 2.6 wt.% of the hydrogen, while the third reaction (3) happens at temperatures > 400°C, with 2.6 wt.% of the hydrogen desorbed.

In spite of its advantages, $LiAlH_4$ has some shortcomings, such as irreversible and slow desorption kinetics (Pukazhselvan et al., 2012). Moreover, the thermal decomposition in reaction 3 is considered incompatible with applied applications due to its high requirement for temperature (>400°C) to release hydrogen. Tremendous efforts have been devoted to overcoming the shortcomings of $LiAlH_4$, such as the implementation of the ball milling method (Balema et al., 2000, 2001; Liu et al., 2009) and impurity-doping with various catalysts such as metals (Resan et al., 2005; Xueping et al., 2009; Langmi et al., 2010; Varin and Parviz, 2012), metal oxides (Zhai et al., 2012; Li Z. et al., 2013; Li et al., 2014; Liu et al., 2014; Sulaiman and Ismail, 2017; Ali et al., 2019; Sazelee et al., 2019), Ti-based additives (Ismail et al., 2011; Amama et al., 2012; Wohlwend et al., 2012; Li L. et al., 2013), and metal halides (Fernandez et al., 2007; Suttisawat et al., 2007; Xueping et al., 2007; Sun et al., 2008; Li et al., 2012).

Among these catalysts, previous studies have revealed that metal halides provide essential catalytic effects on the performance of $LiAlH_4$. Cao et al. (2018) reported that the addition of $ScCl_3$ had a superior effect on the performance of lithium alanates. The desorption process of the $LiAlH_4$-10 mol% $ScCl_3$ sample began at a lower temperature (∼120°C), while the undoped $LiAlH_4$ released hydrogen from around 150°C. Besides, the time needed to complete the dehydrogenation process was shortened with the addition of 1–10 mol% $ScCl_3$. Meanwhile, Sun et al. (2008) found that $NiCl_2$ significantly boosted the desorption behavior of $LiAlH_4$. A composite sample of $LiAlH_4$-$NiCl_2$ demonstrated three times the desorption rate of pure $LiAlH_4$, which was not able to desorb any hydrogen at 100°C. It was believed that the $LiAlH_4$-$NiCl_2$ sample presented this notable improvement due to the formation of Ni, which plays a vital role in accelerating the $LiAlH_4$-$NiCl_2$ system. Another investigation of the catalytic effect of metal halides was carried out by Liu et al. (2012). They proved that a $LiAlH_4$-$TiCl_3$ sample could release hydrogen at a lower temperature (80°C) than the pure $LiAlH_4$. Furthermore, the dehydrogenated sample had good cyclability, with the composite sample able to retain a high capacity for hydrogen (6.4 wt.%) even after completing the 3rd cycle. Moreover, Ismail et al. (2010) observed that the composite sample of $LiAlH_4$-1 mol NbF_5 showed a 5–6 times faster dehydrogenation rate than the milled $LiAlH_4$. Additionally, the $LiAlH_4$-NbF_5 composite sample had lower activation energy; 67 kJ/mol (first-stage reaction) and 77 kJ/mol (second-stage reaction), respectively. However, the improvement of $LiAlH_4$ through the addition of a catalyst is still lacking, and further enhancements still need to be carried out. Moreover, different catalysts will enable different effects and performances. Therefore, it is interesting to enhance the desorption performance of $LiAlH_4$ by the addition of other metal halides.

Metal halides, especially fluorides, are known to be highly effective catalysts for solid-state materials (Sulaiman et al., 2016; Yap et al., 2017; Youn et al., 2017). A number of researchers have reported that niobium fluoride exhibits a notable effect on the hydrogenation behavior of metal hydrides and the complex hydrides. A study conducted by Luo et al. (2008) revealed that the addition of 2 mol of NbF_5 led to faster desorption kinetics for the MgH_2-NbF_5 sample as compared to pure MgH_2. At 573 K, the MgH_2-NbF_5 sample could desorb 4.7 wt.% of hydrogen, while the pristine MgH_2 desorbed almost no hydrogen. Other than that, Kou et al. (2014) added NbF_5 to $LiBH_4$ and demonstrated notable improvement on the desorption performance of $LiBH_4$. In comparison to the milled $LiBH_4$, which started to desorbed hydrogen at >400°C, the composite sample of $LiBH_4$-NbF_5 had a lower desorption temperature, 60°C. Moreover, Wang and colleagues (Wang et al., 2020) showed that a composite of $Mg(BH_4)_2$-doped NbF_5 possessed the best dehydrogenation performance, with the ability to release hydrogen at low temperature (120°C), as compared to amorphous $Mg(BH_4)_2$ (126.9°C), and pristine $Mg(BH_4)_2$ (282.7°C). Meanwhile, Cheng et al. (2018) demonstrated that upon the addition of NbF_5, the composite of $4LiBH_4$-MgH_2-Al exhibited excellent kinetics and reversibility performance. It took <4 h to achieve 90% of the total amount of hydrogen desorption. Other than that, Xiao et al. (2012) proved that the performance of $LiBH_4/MgH_2$ was significantly improved with the addition of NbF_5. Here, the addition of NbF_5 not only had reduced the onset decomposition temperature but also improved the dehydrogenation and absorption rates.

On the other hand, potassium (*K*) is another well-known additive for hydrogen storage systems. Wang et al. (2009) demonstrated that the addition of *K* significantly boosted the desorption process of $Mg(NH_2)_2$/LiH by reducing the overall reaction temperature. Furthermore, Dong et al. (2014) revealed that superior results for the hydrogenation performance of the LiH-NH_3 system were obtained by the addition of various potassium compounds.

In respect to this matter, it is interesting to mix niobium fluoride with potassium as a ternary compound in the form of K_2NbF_7 and to study its potential catalytic effect. To date, no studies have been conducted using doped K_2NbF_7 as a catalyst for $LiAlH_4$. Moreover, previous studies reported that K_2NbF_7 enables a remarkable improvement in the hydrogen storage performance of MgH_2 (Yahya et al., 2018; Yahya M. S. and Ismail M., 2018). Thus, it is of great interest to explore the influence of K_2NbF_7 on the desorption performances of $LiAlH_4$. It is anticipated that the addition of K_2NbF_7 will have notable effects on the desorption and kinetic performances of $LiAlH_4$.

EXPERIMENTAL DETAILS

Commercial powders of $LiAlH_4$ (purity 95%) and K_2NbF_7 (purity 98%) were obtained from Sigma Aldrich and were used without any modification. To minimize exposure to oxygen and water moisture, the samples were prepared and handled in the Ar-filled Mbraun Unilab glove box. In this study, 10 wt.% of K_2NbF_7 was mechanically milled together with $LiAlH_4$ to explore its effect on the desorption behavior of $LiAlH_4$. The milling process was done in a planetary ball mill (NQM-0.4) for 1 h, starting with 0.5 h of milling, followed by 6 min of rest time, and then another 0.5 h of milling in a different rotation direction at a speed of 400 rpm. The samples were placed in a hardened stainless-steel jar with four stainless balls, each 1 cm in size. The ratio of the balls to the weight of the powder was 40:1. For comparison purposes, the as-received $LiAlH_4$ was treated under the same conditions.

The hydrogenation performances of $LiAlH_4$ + 10 wt.% K_2NbF_7 were studied with temperature-programmed desorption (TPD) using Sievert-type pressure-composition-temperature (PCT) equipment (Advanced Materials Corporation). In order to determine the initial decomposition temperature, the sample was heated from room temperature to 250°C (heating rate: 5°C/min). Other than that, the desorption kinetics performances were evaluated at 90°C under 1.0 atm of pressure. The apparent activation energy, E_A, was determined using differential scanning calorimetry (DSC, Mettler Toledo, DSC/TGA 1), loading 5–7 mg of the samples into a crucible and heating from 25 to 300°C at heating ramps of 15, 20, 25, and 30°C/min under an argon flow (50 ml/min). In terms of the morphology and phase structure characterizations, the samples were analyzed using scanning electron microscopy (SEM: JEOL JSM 6350LA), X-ray diffractometry (XRD, Rigaku Miniflex), and Fourier transform infrared (IR Shimadzu Tracer-100).

RESULTS AND DISCUSSION

Figure 1 demonstrates the TPD results of the $LiAlH_4$ and modified $LiAlH_4$ system. The results show that the as-received and as-milled $LiAlH_4$ have similar desorption processes that occur in two stages of desorption, as in Equations (1, 2), with 7.4 wt.% hydrogen capacity. Before the ball milling process, the first stage of desorption occurred at 147°C, with 5 wt.% of hydrogen released. Meanwhile, the desorption process for the second stage was recorded to happen at around 175°C, with a capacity of 2.4 wt.% of the hydrogen. After the milling process, the initial desorption temperature of the sample was similar to that of pure $LiAlH_4$ but with slight temperature reductions to 144°C (first stage) and 174°C (second stage). This phenomenon showed that the 1-h milling process had an insignificant effect on the desorption behavior of $LiAlH_4$. In contrast, the addition of 10 wt.% of K_2NbF_7 significantly decreased the decomposition temperature for both stages, to 90 and 149°C. However, the amount of hydrogen released from the $LiAlH_4$ + 10 wt.% K_2NbF_7 sample was decreased to 6.3 wt.%. This is expected due to the dead weight of K_2NbF_7, which does not hold any hydrogen.

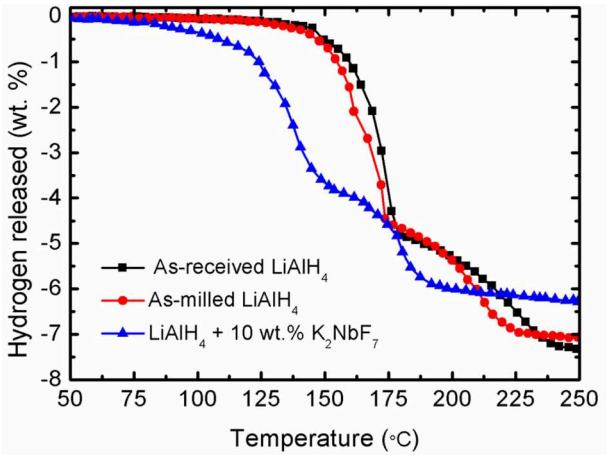

FIGURE 1 | TPD profile for the as-received $LiAlH_4$, as-milled $LiAlH_4$, and $LiAlH_4$ + 10 wt.% K_2NbF_7.

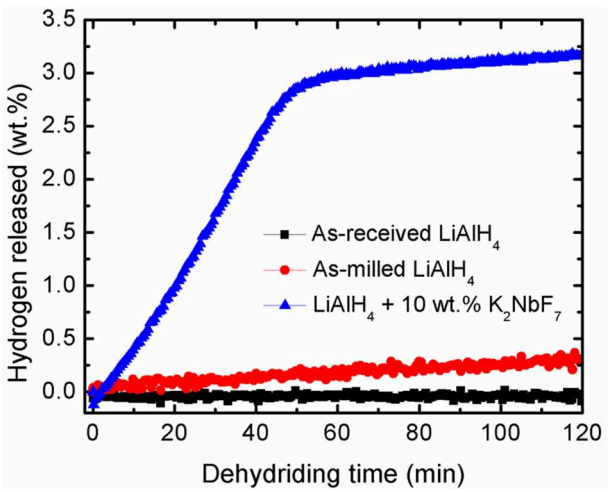

FIGURE 2 | Dehydriding kinetics curves of as-received $LiAlH_4$, as-milled $LiAlH_4$, and $LiAlH_4$ + 10 wt.% K_2NbF_7 at 90°C.

Further study on the catalytic activity of K_2NbF_7 was performed based on the desorption kinetics experiment. **Figure 2** depicts a comparison of the hydrogen desorption at 90°C for $LiAlH_4$ and $LiAlH_4$ modified by the addition of 10 wt.% K_2NbF_7. It is noticeable that within 120 min, the undoped $LiAlH_4$ was only able to desorb a small amount of hydrogen; 0.1 wt.% for the as-received $LiAlH_4$ and 0.4 wt.% for the as-milled $LiAlH_4$. Surprisingly, with the addition of 10 wt.% K_2NbF_7, the doped sample desorbed ~3.2 wt.% H_2 within the same duration. This desorption rate was 30 times faster than that of the as-received $LiAlH_4$. This enhancement may be correlated to the formation of surface defects and active materials through the reaction of the $LiAlH_4$ + 10 wt.% K_2NbF_7 composite (Cai et al., 2016).

In terms of thermal behavior, DSC experiments were conducted for the doped and un-doped $LiAlH_4$ samples. **Figure 3**

displays the DSC curves of the samples at a heating ramp of 15°C/min. Both the doped and un-doped $LiAlH_4$ have two endothermic and exothermic peaks. The first exothermic peak corresponds to the reaction of $LiAlH_4$ with surface hydroxyl groups, while the first endothermic peak is ascribed as its melting process. The second exothermic peak is attributed to the decomposition of $LiAlH_4$, as described in Equation (1), and the second endothermic peak correlates with the decomposition of Li_3AlH_6, as described by Equation (2). Both samples exhibit similar thermal behavior, but the peaks of the $LiAlH_4$ + 10 wt.% K_2NbF_7 sample occur at a lower temperature as compared to as-milled $LiAlH_4$.

Fundamentally, the enhancement of the initial temperature to release hydrogen and the faster desorption kinetics rates are correlated with the energy barrier of $LiAlH_4$. In this study, the decomposition activation energy (E_A) is the least possible amount of energy needed by $LiAlH_4$ to begin the hydrogen desorption process. **Figure 4** shows DSC traces for several heating ramps (15, 20, 25, and 25°C/min). By referring to the plots, the activation energies for both decomposition stages of the as-milled $LiAlH_4$ and $LiAlH_4$ + 10 wt.% K_2NbF_7 samples were determined using the Kissinger analysis, as in equation (4):

$$\ln [\beta/T_p^2] = -E_A/RT_p + A \quad (4)$$

where β, T_p, R, and A are the heating rate, peak temperature in the DSC curve, gas constant, and linear constant, respectively. The apparent activation energy was determined from the slope of $\ln [\beta / T_p^2]$ versus $1000/T_p$, as shown in **Figure 5**.

The activation energy was calculated based on the second exothermic (decomposition of $LiAlH_4$) and second endothermic (decomposition of Li_3AlH_6) reactions. For the as-milled $LiAlH_4$, the activation energy values were 104 and 112 kJ/mol for the first two stages of reaction, respectively. After the addition of 10 wt.% K_2NbF_7, the activation energy values dropped to 80 kJ/mol (first stage) and 86 kJ/mol (second stage), 23% lower than those of the un-doped $LiAlH_4$. These results are in good agreement with other studies that prove the addition of a catalyst is able to reduce the activation energy of $LiAlH_4$. **Table 1** lists the activation energy from previous studies for comparison purposes. The reduction in these activation energies verifies that K_2NbF_7 plays a major role in enhancing the desorption kinetics performance of $LiAlH_4$.

The morphological structures of the doped and un-doped $LiAlH_4$ were examined using SEM equipment. **Figure 6** shows SEM images of the un-doped and doped-$LiAlH_4$ samples. As shown in **Figure 6**, the pure $LiAlH_4$ exhibits larger particle sizes than the milled sample. The as-received $LiAlH_4$ (**Figure 6A**) has larger (15–40 μm), non-uniform rod-shaped particles. Furthermore, the as-received $LiAlH_4$ shows a uniform size distribution and consists of "blocky" particles, consistent with the report by Varin and Zbroniec (2010). Meanwhile, after 1 hour of milling, the milled $LiAlH_4$ (**Figure 6B**) displays a reduction in particle sizes but with some agglomeration and inconsistency in particle size. Then, with the addition of 10 wt.% of K_2NbF_7 (**Figure 6C**), the morphological structure of the sample was notably enhanced. The doped sample has smaller

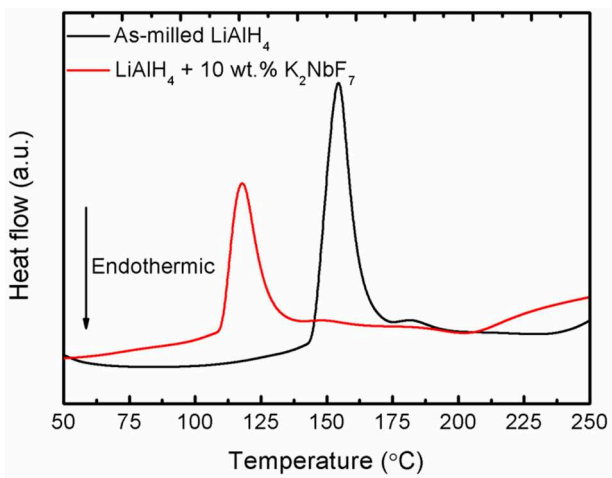

FIGURE 3 | DSC traces of the as-milled $LiAlH_4$ and $LiAlH_4$ + 10 wt.% K_2NbF_7 (heating ramp: 15°C/min).

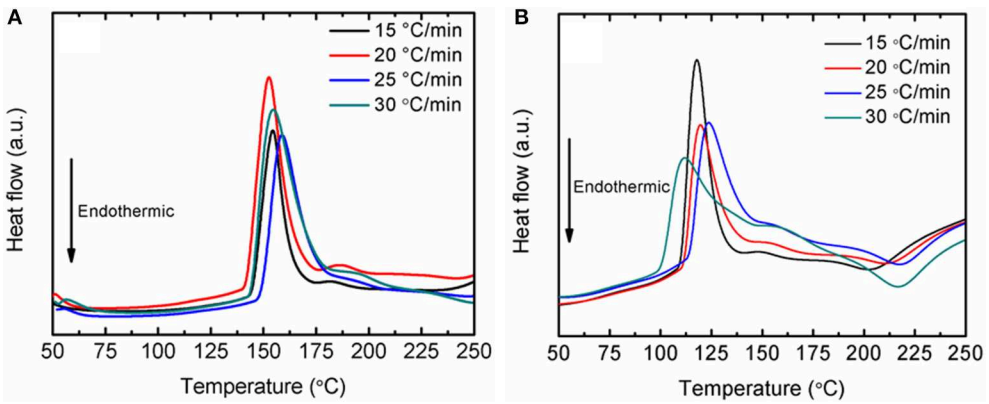

FIGURE 4 | DSC traces at various heating ramps of the $LiAlH_4$ when **(A)** as-milled and **(B)** with 10 wt.% of K_2NbF_7.

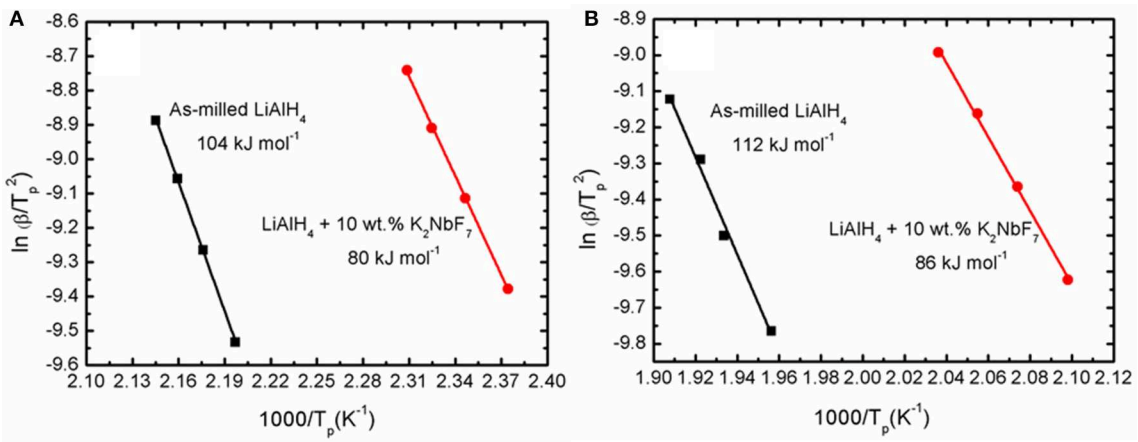

FIGURE 5 | Corresponding Kissinger plots of the as-milled $LiAlH_4$ and $LiAlH_4$ + 10 wt.% K_2NbF_7 for the **(A)** first stage and **(B)** second stage of reaction.

TABLE 1 | Activation energy of catalyst-doped $LiAlH_4$ from previous studies.

System	Activation energy (kJ/mol)		References
	First stage	Second stage	
$LiAlH_4$+K_2TiF_6	78.20	90.80	Li et al., 2012
$LiAlH_4$+Ti_3C_2	79.81	99.68	Xia et al., 2019
$LiAlH_4$+$FeCl_2$	81.48	105.01	Cai et al., 2016
LiAlH4+$ScCl_3$	82.30	93.20	Cao et al., 2018
$LiAlH_4$+Co@C	95.36	115.60	Li et al., 2015

particle sizes and is less agglomerated. This observation is in line with numerous research results that have shown a reduction of particle sizes with the addition of a catalyst (Aguey-Zinsou et al., 2007; Ali et al., 2018; Yahya M. and and Ismail M., 2018). In this study, K_2NbF_7 functioned as a dispersing agent that impeded the sample from agglomerating. The particle size is important because smaller particles provide more area for surface defects and additional grain boundaries (Schulz et al., 1999; Sakintuna et al., 2007; Ranjbar et al., 2009). As a consequence, the desorption kinetics of $LiAlH_4$ will be improved.

Figure 7 presents the XRD profiles of the as-received $LiAlH_4$, as-milled $LiAlH_4$, and $LiAlH_4$-K_2NbF_7 sample. The XRD characterization was performed to explore the reaction process and the mechanism that operated during the milling process. **Figure 7A** displays the XRD pattern of the as-received $LiAlH_4$ and shows that only the $LiAlH_4$ phase was detected, which confirms the purity of the $LiAlH_4$. The XRD pattern of the milled $LiAlH_4$ **Figure 7B** shows similar peaks to the as-received $LiAlH_4$. This result shows that $LiAlH_4$ has high stability during the milling process and agrees well with a previous study (Ismail et al., 2010). Meanwhile, with the addition of 10 wt.% of K_2NbF_7 (**Figure 7C**), only $LiAlH_4$ and Al peaks are visible and no peak of K_2NbF_7 was detected, suggesting that the amount of catalyst was too small to be picked up by the XRD. The appearance of Al peaks indicates that a part of the $LiAlH_4$ had decomposed to Li_3AlH_6 and Al (reaction 1) during the milling process in the presence of 10 wt.% K_2NbF_7. Surprisingly, the XRD result for the 10 wt.% K_2NbF_7-doped $LiAlH_4$ sample does not show any peaks of Li_3AlH_6. Additional characterization was carried out for a doped sample with 30 wt.% K_2NbF_7 (**Figure 7D**). A K_2NbF_7 peak was against not detected by the XRD for this sample. This may be because the K_2NbF_7 is in an amorphous state. Similar phenomena were reported by previous studies, where several catalysts like TiO_2 and TiF_3 were not detected by the XRD after the milling process (Ismail et al., 2011; Zang et al., 2015). However, for the $LiAlH_4$ + 30 wt.% K_2NbF_7 sample, diffraction peaks corresponding to the decomposition product, Al and Li_3AlH_6, were detected. Meanwhile, unlike for the $LiAlH_4$ + 10 wt.% K_2NbF_7 sample, for which only peaks of Al were detected while peaks of Li_3AlH_6 could not be discovered by XRD.

Figure 8 shows the IR spectra of the as-received $LiAlH_4$, as-milled $LiAlH_4$, and $LiAlH_4$ + 10 wt.% K_2NbF_7 in the range of 800 to 2,000 cm^{-1}. The FTIR characterizations were conducted to identify the presence of Li_3AlH_6 in the 10 wt.% K_2NbF_7-doped $LiAlH_4$ sample. For all samples, two distinct regions of Al-H modes were detected at around 800–900 cm^{-1} ($[AlH_4]^-$ stretching modes) and 1,600–1,800 cm^{-1} ($[AlH_4]^-$ bending modes), respectively. Furthermore, with the addition of 10 wt.% K_2NbF_7, a weak IR absorption peak at 1,398 cm^{-1} was detected, which indicates the presence of Li_3AlH_6. This result suggests that with the addition of 10 wt.% K_2NbF_7, $LiAlH_4$ was partially decomposed to Li_3AlH_6 and Al (reaction 1) during the milling process, consistent with the XRD results (**Figure 7C**).

To investigate the specific mechanism that is related to the enhanced desorption performance of $LiAlH_4$, the dehydrogenated sample was examined using XRD. The XRD pattern for the dehydrogenated sample is depicted in **Figure 9**. After the dehydrogenation process at 250°C, the main peaks observed are the $LiAlH_4$ dehydrogenation products, LiH and Al, which indicates complete dehydrogenation of $LiAlH_4$. In addition, peaks for LiF and NbF_4 were detected after the dehydrogenation process. However, the peak of the K-containing

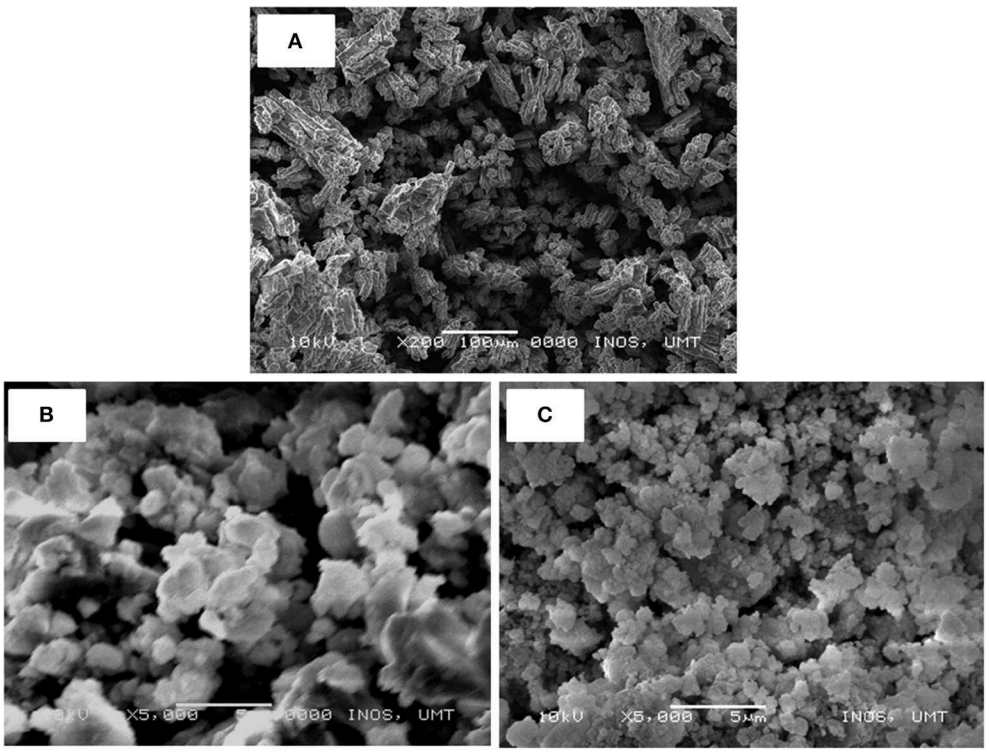

FIGURE 6 | SEM images of $LiAlH_4$ when **(A)** as-received, **(B)** as-milled, and **(C)** with 10 wt.% of K_2NbF_7.

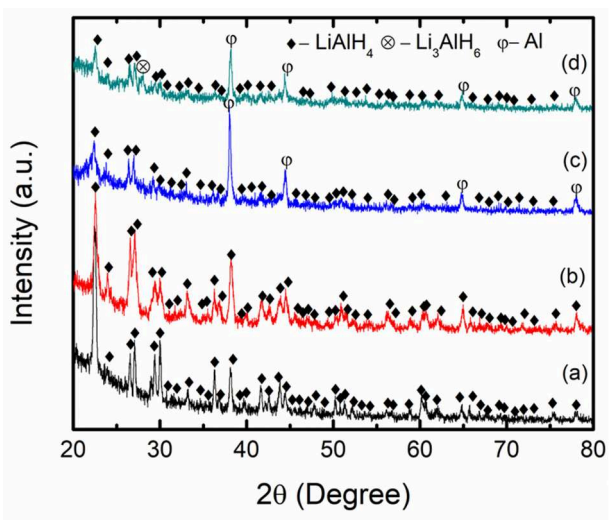

FIGURE 7 | XRD patterns of **(a)** as-received $LiAlH_4$, **(b)** as-milled $LiAlH_4$, **(c)** $LiAlH_4$ + 10 wt.% K_2NbF_7, and **(d)** $LiAlH_4$ + 30 wt.% K_2NbF_7.

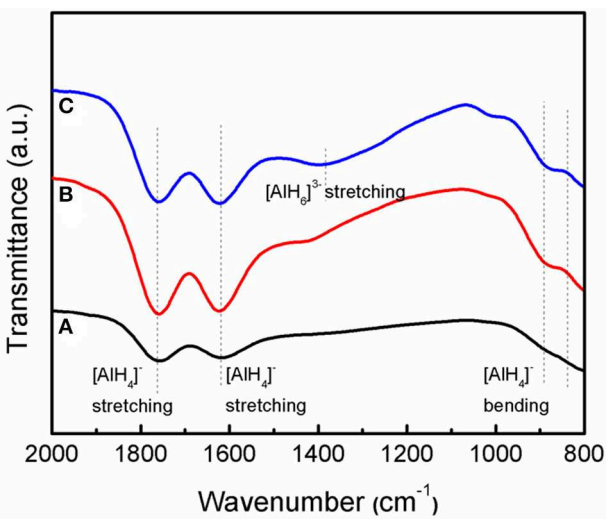

FIGURE 8 | IR spectra of the $LiAlH_4$ when **(A)** as-received, **(B)** as-milled, and **(C)** with 10 wt.% of K_2NbF_7.

phase was not detected after the dehydrogenation process, potentially due to the low amount of catalyst.

Niobium fluoride is well established as a promising catalyst that plays a vital role in enhancing the hydrogenation performance of solid-state material (Luo et al., 2007; Malka et al., 2011; Mao et al., 2013). It is reasonable to state that the NbF_4 that formed *in situ* after the desorption process contributes to a remarkable amelioration of the desorption behavior of $LiAlH_4$. This result well-agreed with previous research that demonstrates the outstanding dehydrogenation performance of $LiAlH_4$-NbF_5

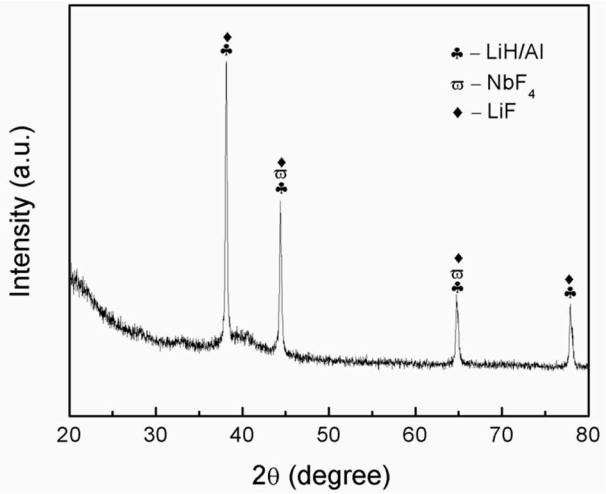

FIGURE 9 | XRD pattern of dehydrogenated $LiAlH_4$ + 10 wt.% K_2NbF_7 sample at 250°C.

(Ismail et al., 2010). On the other hand, the LiF formed was believed to significantly affect the hydrogenation behavior of the doped sample based on work carried out as by Gosalawit-Utke et al. (2010). Additionally, it is believed that the formation of LiF plays a similar role in the growth of LiH and Al, since LiF has a similar cubic structure (space group: Fm-3m; Y. Liu et al., 2010). Also, LiF crystallites act as nucleation sites and facilitate the growth of LiH and Al crystallites, which promotes to the change of the nucleation morphology. These two factors significantly contribute to the kinetics enhancement achieved in the doped sample. Additionally, it is believed that *K* or K-containing phases also play a vital role in enhancing the desorption behavior of $LiAlH_4$. This was deduced based on successful previous work on the application of K as a catalyst for solid-state materials (Wang et al., 2009; Dong et al., 2014). Therefore, it can be concluded that the *in situ* formation of LiF, NbF_4, and K or K-containing phases synergistically contributed to the amelioration of the dehydrogenation kinetics of $LiAlH_4$.

CONCLUSION

K_2NbF_7 demonstrated an excellent catalytic effect on the desorption behavior of $LiAlH_4$. The initial temperatures at which $LiAlH_4$ + 10 wt.% K_2NbF_7 released hydrogen, 90 and 149°C for the first two stages, were lower than those of the as-milled $LiAlH_4$ (147 and 175°C). In terms of desorption kinetics behavior, the $LiAlH_4$ + 10 wt.% K_2NbF_7 released 3.2 wt.% of hydrogen within 120 min, which is 30 faster than the pure $LiAlH_4$. The addition of K_2NbF_7 significantly reduced the decomposition activation energy from 104 to 80 kJ/mol for the first stage and 112 to 86 kJ/mol for the second stage. The XRD spectra suggested that the *in situ* formation of LiF, NbF_4, and K or K-containing phases acted as boosters and ameliorated the dehydrogenation behavior of $LiAlH_4$. This work demonstrates that K_2NbF_7 was has a superior catalytic effect and confers better desorption behavior to $LiAlH_4$.

DATA AVAILABILITY STATEMENT

The datasets generated for this study are available on request to the corresponding author.

AUTHOR CONTRIBUTIONS

All authors listed have made a substantial, direct and intellectual contribution to the work, and approved it for publication.

FUNDING

This work was financially supported by Golden Goose Research Grant (GGRG) VOT 55190, Universiti Malaysia Terengganu.

ACKNOWLEDGMENTS

The authors would like to acknowledge Universiti Malaysia Terengganu for providing complete facilities at which to perform this research.

REFERENCES

Aguey-Zinsou, K. F., Fernandez, J. A., Klassen, T., and Bormann, R. (2007). Effect of Nb_2O_5 on MgH_2 properties during mechanical milling. *Int. J. Hydrogen Energy* 32, 2400–2407. doi: 10.1016/j.ijhydene.2006.10.068

Ali, N. A., Idris, N. H., Din, M. F. M., Mustafa, N. S., Sazelee, N. A., Halim Yap, F. A., et al. (2018). Nanolayer-like-shaped $MgFe_2O_4$ synthesised via a simple hydrothermal method and its catalytic effect on the hydrogen storage properties of MgH_2. *RSC Adv.* 8, 15667–15674. doi: 10.1039/C8RA02168F

Ali, N. A., Idris, N. H., Sazelee, N. A., Yahya, M. S., Yap, F. A. H., and Ismail, M. (2019). Catalytic effects of $MgFe_2O_4$ addition on the dehydrogenation properties of $LiAlH_4$. *Int. J. Hydrogen Energy* 44, 28227–28234. doi: 10.1016/j.ijhydene.2019.09.083

Amama, P. B., Grant, J. T., Shamberger, P. J., Voevodin, A. A., and Fisher, T. S. (2012). Improved dehydrogenation properties of Ti-doped $LiAlH_4$: role of Ti precursors. *J. Phys. Chem. C* 116, 21886–21894. doi: 10.1021/jp307225w

Andrei, C., Walmsley, J., Blanchard, D., Brinks, H., Holmestad, R., and Hauback, B. (2005). Electron microscopy studies of lithium aluminum hydrides. *J. Alloy. Compd.* 395, 307–312. doi: 10.1016/j.jallcom.2004.11.058

Ares, J., Aguey-Zinsou, K. F., Porcu, M., Sykes, J., Dornheim, M., Klassen, T., et al. (2008). Thermal and mechanically activated decomposition of $LiAlH_4$. *Mater. Res. Bull.* 43, 1263–1275. doi: 10.1016/j.materresbull.2007.05.018

Balema, V., Pecharsky, V., and Dennis, K. (2000). Solid state phase transformations in $LiAlH_4$ during high-energy ball-milling. *J. Alloy. Compd.* 313, 69–74. doi: 10.1016/S0925-8388(00)01201-9

Balema, V., Wiench, J., Dennis, K., Pruski, M., and Pecharsky, V. (2001). Titanium catalyzed solid-state transformations in $LiAlH_4$ during high-energy ball-milling. *J. Alloy. Compd.* 329, 108–114. doi: 10.1016/S0925-8388(01)01570-5

Barthelemy, H., Weber, M., and Barbier, F. (2017). Hydrogen storage: recent improvements and industrial perspectives. *Int. J. Hydrogen Energy* 42, 7254–7262. doi: 10.1016/j.ijhydene.2016.03.178

Cai, J., Zang, L., Zhao, L., Liu, J., and Wang, Y. (2016). Dehydrogenation characteristics of $LiAlH_4$ improved by *in-situ* formed catalysts. *J. Energy Chem.* 25, 868–873. doi: 10.1016/j.jechem.2016.06.004

Cao, Z., Ma, X., Wang, H., and Ouyang, L. (2018). Catalytic effect of $ScCl_3$ on the dehydrogenation properties of $LiAlH_4$. *J. Alloys Compd.* 762, 73–79. doi: 10.1016/j.jallcom.2018.05.213

Cheng, C., Chen, M., Xiao, X., Huang, X., Zheng, J., and Chen, L. (2018). Superior reversible hydrogen storage properties and mechanism of $LiBH_4$-MgH_2-Al doped with NbF_5 additive. *J. Phys. Chem. C* 122, 7613–7620. doi: 10.1021/acs.jpcc.8b00959

Crabtree, G. W., Dresselhaus, M. S., and Buchanan, M. V. (2004). The hydrogen economy. *Phys. Today* 57, 39–44. doi: 10.1063/1.1878333

Dalebrook, A. F., Gan, W., Grasemann, M., Moret, S., and Laurenczy, G. (2013). Hydrogen storage: beyond conventional methods. *Chem. Commun.* 49, 8735–8751. doi: 10.1039/c3cc43836h

Dong, B. X., Song, L., Teng, Y. L., Ge, J., and Zhang, S. Y. (2014). Enhanced hydrogen desorption reaction kinetics by optimizing the reaction conditions and doping potassium compounds in the LiH–NH_3 system. *Int. J. Hydrogen Energy* 39, 13838–13843. doi: 10.1016/j.ijhydene.2014.03.005

Fernandez, J. A., Aguey-Zinsou, F., Elsaesser, M., Ma, X., Dornheim, M., Klassen, T., et al. (2007). Mechanical and thermal decomposition of $LiAlH_4$ with metal halides. *Int. J. Hydrogen Energy* 32, 1033–1040. doi: 10.1016/j.ijhydene.2006.07.011

Gosalawit-Utke, R., Bellosta von Colbe, J. M., Dornheim, M., Jensen, T. R., Cerenius, Y., Bonatto Minella, C., et al. (2010). LiF–MgB_2 system for reversible hydrogen storage. *J. Phys. Chem. C* 114, 10291–10296. doi: 10.1021/jp910266m

Ismail, M., Zhao, Y., Yu, X. B., and Dou, S. X. (2010). Effects of NbF_5 addition on the hydrogen storage properties of $LiAlH_4$. *Int. J. Hydrogen Energy* 35, 2361–2367. doi: 10.1016/j.ijhydene.2009.12.178

Ismail, M., Zhao, Y., Yu, X. B., Nevirkovets, I. P., and Dou, S. X. (2011). Significantly improved dehydrogenation of $LiAlH_4$ catalysed with TiO_2 nanopowder. *Int. J. Hydrogen Energy* 36, 8327–8334. doi: 10.1016/j.ijhydene.2011.04.074

Kou, H., Sang, G., Zhou, Y., Wang, X., Huang, Z., Luo, W., et al. (2014). Enhanced hydrogen storage properties of $LiBH_4$ modified by NbF_5. *Int. J. Hydrogen Energy* 39, 11675–11682. doi: 10.1016/j.ijhydene.2014.05.179

Langmi, H. W., McGrady, G. S., Liu, X., and Jensen, C. M. (2010). Modification of the H_2 desorption properties of $LiAlH_4$ through doping with Ti. *J. Phys. Chem. C* 114, 10666–10669. doi: 10.1021/jp102641p

Li, L., An, C., Wang, Y., Xu, Y., Qiu, F., Wang, Y., et al. (2014). Enhancement of the H_2 desorption properties of $LiAlH_4$ doping with $NiCo_2O_4$ nanorods. *Int. J. Hydrogen Energy* 39, 4414–4420. doi: 10.1016/j.ijhydene.2013.12.210

Li, L., Qiu, F., Wang, Y., Xu, Y., An, C., Liu, G., et al. (2013). Enhanced hydrogen storage properties of TiN–$LiAlH_4$ composite. *Int. J. Hydrogen Energy* 38, 3695–3701. doi: 10.1016/j.ijhydene.2013.01.088

Li, L., Wang, Y., Jiao, L., and Yuan, H. (2015). Enhanced catalytic effects of Co@C additive on dehydrogenation properties of $LiAlH_4$. *J. Alloys Compd.* 645(Suppl.1), S468–S471. doi: 10.1016/j.jallcom.2014.12.080

Li, Z., Li, P., Wan, Q., Zhai, F., Liu, Z., Zhao, K., et al. (2013). Dehydrogenation improvement of $LiAlH_4$ catalyzed by Fe_2O_3 and Co_2O_3 nanoparticles. *J. Phys. Chem. C* 117, 18343–18352. doi: 10.1021/jp405844z

Li, Z., Liu, S., Si, X., Zhang, J., Jiao, C., Wang, S., et al. (2012). Significantly improved dehydrogenation of $LiAlH_4$ destabilized by K_2TiF_6. *Int. J. Hydrogen Energy* 37, 3261–3267. doi: 10.1016/j.ijhydene.2011.10.038

Liu, S., Ma, Q., Lü, H., Zheng, X., Feng, X., Xiao, G., et al. (2014). Study on hydrogen release capacity of $LiAlH_4$ doped with CeO_2. *Rare Metal. Mat. Eng.* 43, 544–547. doi: 10.1016/S1875-5372(14)60073-4

Liu, S. S., Sun, L. X., Zhang, Y., Xu, F., Zhang, J., Chu, H. L., et al. (2009). Effect of ball milling time on the hydrogen storage properties of TiF_3-doped $LiAlH_4$. *Int. J. Hydrogen Energy* 34, 8079–8085. doi: 10.1016/j.ijhydene.2009.07.090

Liu, X., Beattie, S. D., Langmi, H. W., McGrady, G. S., and Jensen, C. M. (2012). Ti-doped $LiAlH_4$ for hydrogen storage: rehydrogenation process, reaction conditions and microstructure evolution during cycling. *Int. J. Hydrogen Energy* 37, 10215–10221. doi: 10.1016/j.ijhydene.2012.04.018

Liu, Y., Wang, F., Cao, Y., Gao, M., Pan, H., and Wang, Q. (2010). Mechanisms for the enhanced hydrogen desorption performance of the TiF_4-catalyzed Na_2LiAlH_6 used for hydrogen storage. *Energy Environ. Sci.* 3, 645–653. doi: 10.1039/b920270f

Luo, Y., Wang, P., Ma, L. P., and Cheng, H. M. (2007). Enhanced hydrogen storage properties of MgH_2 co-catalyzed with NbF_5 and single-walled carbon nanotubes. *Scripta Mater.* 56, 765–768. doi: 10.1016/j.scriptamat.2007.01.016

Luo, Y., Wang, P., Ma, L. P., and Cheng, H. M. (2008). Hydrogen sorption kinetics of MgH_2 catalyzed with NbF_5. *J. Alloys Compd.* 453, 138–142. doi: 10.1016/j.jallcom.2006.11.113

Malka, I., Pisarek, M., Czujko, T., and Bystrzycki, J. (2011). A study of the ZrF_4, NbF_5, TaF_5, and $TiCl_3$ influences on the MgH_2 sorption properties. *Int. J. Hydrogen Energy* 36, 12909–12917. doi: 10.1016/j.ijhydene.2011.07.020

Mao, J., Guo, Z., Yu, X., and Liu, H. (2013). Combined effects of hydrogen back-pressure and NbF_5 addition on the dehydrogenation and rehydrogenation kinetics of the $LiBH_4$-MgH_2 composite system. *Int. J. Hydrogen Energy* 38, 3650–3660. doi: 10.1016/j.ijhydene.2012.12.106

Parra, D., Valverde, L., Pino, F. J., and Patel, M. K. (2019). A review on the role, cost and value of hydrogen energy systems for deep decarbonisation. *Renew. Sust. Energ Rev.* 101, 279–294. doi: 10.1016/j.rser.2018.11.010

Pukazhselvan, D., Kumar, V., and Singh, S. (2012). High capacity hydrogen storage: basic aspects, new developments and milestones. *Nano Energy* 1, 566–589. doi: 10.1016/j.nanoen.2012.05.004

Ranjbar, A., Guo, Z., Yu, X., Wexler, D., Calka, A., Kim, C., et al. (2009). Hydrogen storage properties of MgH_2-SiC composites. *Mater. Chem. Phys.* 114, 168–172. doi: 10.1016/j.matchemphys.2008.09.001

Resan, M., Hampton, M. D., Lomness, J. K., and Slattery, D. K. (2005). Effects of various catalysts on hydrogen release and uptake characteristics of $LiAlH_4$. *Int. J. Hydrogen Energy* 30, 1413–1416. doi: 10.1016/j.ijhydene.2004.12.009

Sakintuna, B., Lamari-Darkrim, F., and Hirscher, M. (2007). Metal hydride materials for solid hydrogen storage: a review. *Int J Hydrogen Energy* 32, 1121–1140. doi: 10.1016/j.ijhydene.2006.11.022

Sazelee, N., Yahya, M., Idris, N., Din, M. M., and Ismail, M. (2019). Desorption properties of $LiAlH_4$ doped with $LaFeO_3$ catalyst. *Int. J. Hydrogen Energy* 44, 11953–11960. doi: 10.1016/j.ijhydene.2019.03.102

Schulz, R., Huot, J., Liang, G., Boily, S., Lalande, G., Denis, M., et al. (1999). Recent developments in the applications of nanocrystalline materials to hydrogen technologies. *Mater. Sci. Eng. A* 267, 240–245. doi: 10.1016/S0921-5093(99)00098-2

Sulaiman, N., and Ismail, M. (2017). Catalytic effect of $SrFe_{12}O_{19}$ on the hydrogen storage properties of $LiAlH_4$. *Int. J. Hydrogen Energy* 42, 19126–19134. doi: 10.1016/j.ijhydene.2017.06.005

Sulaiman, N., Mustafa, N., and Ismail, M. (2016). Effect of Na_3FeF_6 catalyst on the hydrogen storage properties of MgH_2. *Dalton Trans.* 45, 7085–7093. doi: 10.1039/C6DT00068A

Sun, T., Huang, C., Wang, H., Sun, L., and Zhu, M. (2008). The effect of doping $NiCl_2$ on the dehydrogenation properties of $LiAlH_4$. *Int. J. Hydrogen Energy* 33, 6216–6221. doi: 10.1016/j.ijhydene.2008.08.027

Suttisawat, Y., Rangsunvigit, P., Kitiyanan, B., Muangsin, N., and Kulprathipanja, S. (2007). Catalytic effect of Zr and Hf on hydrogen desorption/absorption of $NaAlH_4$ and $LiAlH_4$. *Int J Hydrogen Energy* 32, 1277–1285. doi: 10.1016/j.ijhydene.2006.07.020

Varin, R., and Zbroniec, L. (2010). Decomposition behavior of unmilled and ball milled lithium alanate ($LiAlH_4$) including long-term storage and moisture effects. *J. Alloy. Compd.* 504, 89–101. doi: 10.1016/j.jallcom.2010.05.059

Varin, R. A., and Parviz, R. (2012). The effects of the micrometric and nanometric iron (Fe) additives on the mechanical and thermal dehydrogenation of lithium alanate ($LiAlH_4$), its self-discharge at low temperatures and rehydrogenation. *Int. J. Hydrogen Energy* 37, 9088–9102. doi: 10.1016/j.ijhydene.2012.02.182

Wang, J., Liu, T., Wu, G., Li, W., Liu, Y., Araújo, C. M., et al. (2009). Potassium-modified $Mg(NH_2)_2$/2 LiH system for hydrogen storage. *Angew Chem. Int. Ed.* 48, 5828–5832. doi: 10.1002/anie.200805264

Wang, X., Xiao, X., Zheng, J., Huang, X., Chen, M., and Chen, L. (2020). *In-situ* synthesis of amorphous $Mg(BH4)_2$ and chloride composite modified by NbF_5 for superior reversible hydrogen storage properties. *Int. J. Hydrogen Energy* 45, 2044–2053. doi: 10.1016/j.ijhydene.2019.11.023

Winter, C. J. (2009). Hydrogen energy—abundant, efficient, clean: a debate over the energy-system-of-change. *Int. J. Hydrogen Energy* 34, S1–52. doi: 10.1016/j.ijhydene.2009.05.063

Wohlwend, J. L., Amama, P. B., Shamberger, P. J., Varshney, V., Roy, A. K., and Fisher, T. S. (2012). Effects of Titanium-containing additives on the

dehydrogenation properties of $LiAlH_4$: a computational and experimental study. *J. Phys. Chem. C* 116, 22327–22335. doi: 10.1021/jp3050109

Xia, Y., Zhang, H., Sun, Y., Sun, L., Xu, F., Sun, S., et al. (2019). Dehybridization effect in improved dehydrogenation of $LiAlH_4$ by doping with two-dimensional Ti_3C_2. *Mater. Today Nano.* 8:100054. doi: 10.1016/j.mtnano.2019.100054

Xiao, X., Shao, J., Chen, L., Kou, H., Fan, X., Deng, S., et al. (2012). Effects of NbF_5 addition on the de/rehydrogenation properties of $2LiBH_4/MgH_2$ hydrogen storage system. *Int. J. Hydrogen Energy* 37, 13147–13154. doi: 10.1016/j.ijhydene.2012.03.140

Xueping, Z., Ping, L., Humail, I., Fuqiang, A., Guoqing, W., and Xuanhui, Q. (2007). Effect of catalyst $LaCl_3$ on hydrogen storage properties of lithium alanate ($LiAlH_4$). *Int. J. Hydrogen Energy* 32, 4957–4960. doi: 10.1016/j.ijhydene.2007.06.031

Xueping, Z., Ping, L., and Xuanhui, Q. (2009). Effect of additives on the reversibility of lithium alanate ($LiAlH_4$). *Rare. Metal Mat. Eng.* 38, 766–769. doi: 10.1016/S1875-5372(10)60034-3

Yahya, M., and Ismail, M. (2018). Synergistic catalytic effect of $SrTiO_3$ and Ni on the hydrogen storage properties of MgH_2. *Int. J. Hydrogen Energy* 43, 6244–6255. doi: 10.1016/j.ijhydene.2018.02.028

Yahya, M. S., and Ismail, M. (2018). Improvement of hydrogen storage properties of MgH_2 catalyzed by K_2NbF_7 and multiwall carbon nanotube. *J. Phys. Chem. C* 122, 11222–11233. doi: 10.1021/acs.jpcc.8b02162

Yahya, M. S., Sulaiman, N. N., Mustafa, N. S., Halim Yap, F. A., and Ismail, M. (2018). Improvement of hydrogen storage properties in MgH_2 catalysed by K_2NbF_7. *Int. J. Hydrogen Energy* 43, 14532–14540. doi: 10.1016/j.ijhydene.2018.05.157

Yap, F. H., Yahya, M., and Ismail, M. (2017). Enhancement of hydrogen storage properties in $4MgH_2$ -Na_3AlH_6 composite catalyzed by TiF_3. *Int. J. Hydrogen Energy* 42, 21096–21104. doi: 10.1016/j.ijhydene.2017.07.012

Youn, J. S., Phan, D. T., Park, C. M., and Jeon, K. J. (2017). Enhancement of hydrogen sorption properties of MgH_2 with a MgF_2 catalyst. *Int. J. Hydrogen Energy* 42, 20120–20124. doi: 10.1016/j.ijhydene.2017.06.130

Zang, L., Cai, J., Zhao, L., Gao, W., Liu, J., and Wang, Y. (2015). Improved hydrogen storage properties of $LiAlH_4$ by mechanical milling with TiF_3. *J. Alloys Compd.* 647, 756–762. doi: 10.1016/j.jallcom.2015.06.036

Zhai, F., Li, P., Sun, A., Wu, S., Wan, Q., Zhang, W., et al. (2012). Significantly improved dehydrogenation of $LiAlH_4$ destabilized by $MnFe_2O_4$ nanoparticles. *J. Phys. Chem. C* 116, 11939–11945. doi: 10.1021/jp302721w

Zhang, F., Zhao, P., Niu, M., and Maddy, J. (2016). The survey of key technologies in hydrogen energy storage. *Int. J. Hydrogen Energy* 41, 14535–14552. doi: 10.1016/j.ijhydene.2016.05.293

Conflict of Interest: The authors declare that the research was conducted in the absence of any commercial or financial relationships that could be construed as a potential conflict of interest.

frontiers in Chemistry

REVIEW
published: 02 July 2020
doi: 10.3389/fchem.2020.00552

Enhancing Hydrogen Storage Properties of MgH_2 by Transition Metals and Carbon Materials: A Brief Review

*Ze Sun, Xiong Lu, Farai Michael Nyahuma, Nianhua Yan, Jiankun Xiao, Shichuan Su and Liuting Zhang**

College of Energy and Power, Jiangsu University of Science and Technology, Zhenjiang, China

Magnesium hydride (MgH_2) has attracted intense attention worldwide as solid state hydrogen storage materials due to its advantages of high hydrogen capacity, good reversibility, and low cost. However, high thermodynamic stability and slow kinetics of MgH_2 has limited its practical application. We reviewed the recent development in improving the sorption kinetics of MgH_2 and discovered that transition metals and their alloys have been extensively researched to enhance the de/hydrogenation performance of MgH_2. In addition, to maintain the cycling property during the de/hydrogenation process, carbon materials (graphene, carbon nanotubes, and other materials) have been proved to possess excellent effect. In this work, we introduce various categories of transition metals and their alloys to MgH_2, focusing on their catalytic effect on improving the hydrogen de/absorption performance of MgH_2. Besides, carbon materials together with transition metals and their alloys are also summarized in this study, which show better hydrogen storage performance. Finally, the existing problems and challenges of MgH_2 as practical hydrogen storage materials are analyzed and possible solutions are also proposed.

Keywords: hydrogen storage, MgH_2, transition metals, carbon materials, cycling performance

OPEN ACCESS

Edited by:
Guanglin Xia,
Fudan University, China

Reviewed by:
Yunfeng Zhu,
Nanjing Tech University, China
Xiaowei Chen,
Jimei University, China

****Correspondence:***
Liuting Zhang
zhanglt89@just.edu.cn

Specialty section:
This article was submitted to Inorganic Chemistry, a section of the journal Frontiers in Chemistry

Received: *14 April 2020*
Accepted: *28 May 2020*
Published: *02 July 2020*

Citation:
Sun Z, Lu X, Nyahuma FM, Yan N, Xiao J, Su S and Zhang L (2020) Enhancing Hydrogen Storage Properties of MgH_2 by Transition Metals and Carbon Materials: A Brief Review. Front. Chem. 8:552. doi: 10.3389/fchem.2020.00552

INTRODUCTION

Since the industrial revolution, human society is developing rapidly with continuous improvement in technology and rising demand for energy consumption (Pudukudy et al., 2014; He et al., 2016). Unfortunately, fossil fuels, which play dominate role in promoting the development of world, are not renewable and going to be running out in near future. Besides, the severe environmental problems caused by the excessive exploitation and use of fossil fuels, such as the greenhouse effect, ozone layer depletion, acid rains, and pollution, are damaging and threating the ecological balance of the earth. To mitigate the degradation of the earth, various measures have been taken by scientists to explore renewable and clean alternatives to fossil fuels.

Hydrogen, with its safe, high energy density (142 KJ/kg), environment friendliness, convenient and renewability, is proved to be the most promising sustainable and clean energy to replace fossil energy (Cao et al., 2016; Wan et al., 2020). As an energy carrier, hydrogen is abundant on earth and can be produced from any primary energy fuel: coal, oil, nuclear, natural gas, all sorts of renewable energies, and from grid electricity. Hydrogen also has a huge calorific value of energy, which is

three times higher than that of petrol (43 MJ/kg) after combustion. Moreover, the dominating combustion product of hydrogen is clean and non-toxic water. Due to above advantages, hydrogen has received extensive attention from researchers worldwide and has made a rapid progress in recent decades (Winter, 2009; Sadhasivam et al., 2017; Peter, 2018). In order to realize the practical application of hydrogen energy, three challenges need to be conquered presciently, which are hydrogen preparation, storage and application. Among which, hydrogen storage has become the bottleneck technology in the wide spread of hydrogen energy (Felderhoff et al., 2007; Yang J. et al., 2010; Pukazhselvan et al., 2012; Kim et al., 2018).

Hydrogen can be stored as cryogenic liquid, high compression gas or solid-state materials (Yu et al., 2017; Abe et al., 2019). Compared with high cost cryogenic liquid storage and dangerous high compression gas tanks, hydrogen stored in solid-state materials shows easy manipulability temperature, low working pressure (Khafidz et al., 2016; Rusman and Dahari, 2016; Razavi et al., 2019). In the past decades, oceans of materials for hydrogen storage have been investigated, including physical adsorbents (carbon and MOF), complex hydrides ($LiBH_4$, $LiNH_4$, $NaAlH_4$), alloys hydrides (Mg_2NiH_4, $TiFeH_2$, $NaMgH_3$), and metal hydrides (MgH_2) (Shao et al., 2015; Zhai et al., 2016; Xiao et al., 2017; Chen et al., 2019; Goto et al., 2019; He et al., 2019, 2020; Liu H. et al., 2019, 2020; Song et al., 2019; Jansa et al., 2020; Yao et al., 2020).

Among different solid-state hydrogen storage materials, magnesium hydride (MgH_2) has been much discussed and holds tremendous hope for storing hydrogen (Bogdanović and Spliethoff, 1990; Norberg et al., 2011; Zhang X. L. et al., 2020). As the sixth abundant metal element in the earth's crust, magnesium is widely distributed in nature. More importantly, MgH_2 has a high gravimetric capacity of 7.6 wt% (volumetric capacity of 110 g/L) and excellent reversibility. However, the practical application of MgH_2 has been hindered by the high desorption temperature and poor hydrogen absorption/desorption kinetics caused by high thermal stability ($\Delta H = 76$ kJ/mol) and kinetic barrier (Ea =160 kJ/mol) (Webb, 2015; Peng et al., 2017; Zhou et al., 2019a; Jain et al., 2020).

To overcome above challenges, alloying (Bououdina and Guo, 2002; Liao et al., 2004; Kumar et al., 2013; Xu et al., 2018; Ali et al., 2019), nanostructuring (Chen et al., 2012, 2018; Yu et al., 2014; Sterl et al., 2018), nanoconfinement (Nielsen et al., 2009; Gosalawit-Utke et al., 2011; Jeon et al., 2011; Konarova et al., 2013; He et al., 2015), and doping with catalysts (Su et al., 2016; Sun et al., 2016; Zhang et al., 2018; Pluengphon et al., 2019; Wang et al., 2019) have been adopted to enhance the hydrogen storage properties of MgH_2. According to recent studies, the transition metals (Ti, Fe, Co, Ni, Mn, Nb, V, Zr, etc.) and their alloys (Shang, 2004; Yavari et al., 2005; Xie et al., 2009; Pighin et al., 2012; Zahiri et al., 2012; Wang et al., 2016) doped in MgH_2 showed superior modification impacts on the hydrogen storage properties while carbon materials (graphene, carbon nanotubes, and other materials) were proved to enhance the cycling property of MgH_2. In this work, we systematically review transition metals, their alloys and carbon materials as catalysts to improve the hydrogen storage properties of MgH_2. In addition, the remaining problems and possible solutions are proposed and discussed.

TRANSITION METALS AND THEIR ALLOYS

On the whole, doping transition metals and their alloys into magnesium hydride has been considered as one of the most feasible methods to accelerate the sorption kinetics of MgH_2. During recent years, numerous transition metals and their alloys have been developed and researched. In this paper, these catalysts are reviewed and classified, presented as monometallic catalysts, binary alloys, ternary and multicomponent alloys and the composites of alloys and carbon materials. Their catalytic effects on hydrogen storage properties of MgH_2 were summarized in **Table 1**.

MONOMETALLIC CATALYSTS

Nickel (Ni)

Monometallic catalysts, especially transition metals (Ershova et al., 2008; Gasan et al., 2012; El-Eskandarany et al., 2016; Tanniru et al., 2020), have shown great catalytic impact on improving the hydrogen storage properties of MgH_2. Among all the transition metals studied in recent years, nickel has been the mostly adopted catalysts for MgH_2. As early as 2005, Hanada et al. (2005) mixed purchased MgH_2 powder with metal Ni by ball milling to get the MgH_2+nano-Ni composite. Through the thermal desorption mass spectra (TDMS), they found that the hydrogen desorption peak of the Ni doped composite decreased to 260°C, which was much lower than that of pure MgH_2 (370°C). Although the superior catalytic effect of Ni nanoparticles was confirmed, other factors such as particle size and catalyst amount were also widely researched lately. Xie et al. (2009) studied the hydrogen storage kinetics of the MgH_2 nanoparticles doped with different concentration of Ni nanoparticles. The DSC curves depicted that the MgH_2+10 wt% nano-Ni composite could desorb 6.1 wt% hydrogen within 10 min at 250°C. The desorption rate of MgH_2+nano-Ni composite increased obviously with the increasing amount of catalyst. However, the activation energy of desorption could not be further lowered when the amount of Ni exceeded a certain value by using Kissinger equation. It was concluded that the catalytic effect of Ni could further be increased by reducing the particle size of catalyst and maintaining the hydrogen storage capacity at the same time. Yang W. N. et al. (2010) investigated the size effect of Ni particles on the hydrogen desorption of MgH_2. The results showed that the MgH_2 mixed with only 2 at% of fine Ni particles rapidly desorbed hydrogen from 200°C and almost 6.5 wt% hydrogen could be released when the temperature rose to 340°C. Nevertheless, DSC curves showed that the peak temperature of the $MgH_2 + 2Ni_{90}$ mixture is around 280°C, which was only about10°C lower than those of the $MgH_2 + 2Ni_{200}$ and the $MgH_2 + 2Ni_{100}$ composites. They finally concluded that the site density of the catalyst over the MgH_2 particles but not the particle size was the key factor to improve the hydrogen adsorption kinetics of MgH_2 after comparing with other references.

TABLE 1 | Dehydrogenation properties of MgH_2 catalyzed with various materials.

Samples	Non-isothermal dehydrogenation			Isothermal dehydrogenation			Ea (kJ/mol^{-1})	References
	T_{onset} (°C)	T_{peak} (°C)	Capacity (wt%)	T (°C)	t (min)	Capacity (wt%)		
MgH_2-10wt%Ni		278.7		250	10	6.1	118	Xie et al., 2009
MgH_2-10wt%Ti	257	372	6.18				103.9	Wang et al., 2015
MgH_2-5wt%nano-Fe	177.6	222.6	6.6	300	10	5.44	40.7	Montone et al., 2012
MgH_2-10wt%nano-$ZrMn_2$	182	251	6.7	300	5	6.7	82.2	Zhang et al., 2019a
MgH_2-10wt%$TiMn_2$		377		225	6.7	5.1	82.9	El-Eskandarany et al., 2019a
MgH_2- TiVMn				270	3	5.5	85.2	Zhou et al., 2013
MgH_2- $Ti_{0.4}Cr_{0.15}Mn_{0.15}V_{0.3}$				290	30	5.7		Yu et al., 2010
MgH_2-5wt%FeCoNi@GS	255			290	8.5	6.14	85.1	Singh et al., 2017
MgH_2-10wt%$Zr_{0.4}Ti_{0.6}Co$/5wt%CNTs	200			300	10	6.1	70.5	Zhang L. et al., 2020

Titanium (Ti)

In comparison with nickel, titanium has also been demonstrated as a good catalyst for MgH_2. In 1999, Liang et al. (1999a) studied the catalytic mechanism of titanium mainly through XRD results. During the synthesis process of the MgH_2+5at%Ti composite via mechanical milling, a very stable TiH_2 phase was formed by reaction of MgH_2 with Ti. Interestingly, TiH_2 could be obtained after desorption, which suggests that no decomposition of TiH_2 phase occurred under the mild desorption condition of 300°C. The desorption curves showed that MgH_2−5at%Ti composites could desorb hydrogen completely within 1,000 s at 250°C while the ball-milled MgH_2 released no hydrogen under the same conditions. A lot of work has been done by researchers to further study the de/hydrogenation kinetics and microstructure of MgH_2-Ti composites. Wang et al. (2015) also prepared the MgH_2-Ti composite by ball milling, and found that the initial dehydrogenation temperature of the composite to be 257°C, which was 51°C lower than that of pure MgH_2. The hydrogen capacity could reach 6.18 wt% at the same time. Compared to the sluggish desorption kinetics of pure MgH_2, the *Ea* for the MgH_2-Ti sample was 103.9 kJ mol^{-1}, about 35.8% lower than that of pure MgH_2 (161.3 kJ mol^{-1}). By analyzing the mechanism it was depicted that elemental Ti reacted with MgH_2 and formed active $TiH_{1.971}$ during ball-milling, which acted as active species throughout the desorption process. Shao et al. (2011) mainly researched nanostructured Ti-catalyzed MgH_2 for hydrogen storage. Through EDX measurements, it was discovered that Ti covered the MgH_2 surface. The DTA curve showed that decomposition of Ti-catalyzed MgH_2 sample started from below 300°C, which was about 130°C lower than that of the commercial MgH_2 sample. Hydrogen absorption kinetics of MgH_2-Ti sample were also investigated and the dehydrogenated sample could absorb 6 mass% hydrogen in <1 h at 257°C, while the commercial MgH_2 needed an absorption time of about 3 h to reach a capacity of 6 mass% even at 350°C.

Iron (Fe)

As the most common metal element in life, Fe has been widely concerned and studied in recent years. Bassetti et al. (2005) mixed different concentration values of Fe with MgH_2 by ball milling to explore its catalytic effect. The Mg_2FeH_6 phase could be detected when the ball to powder ratio rose to 20:1. They also concluded that the optimum catalyst concentration was around 10 wt% and lower values seemed to be insufficient to avoid the presence of poorly catalyzed regions. DSC curves revealed that about 5 wt% of hydrogen could be released in 600 s at 300°C. Besides the desorption property, the cycling performance and the nano-sized Fe were further studied. Montone et al. (2012) explored the cycling properties of MgH_2-Fe nanocomposite in 47 cycles at 300°C. Cycling results demonstrated that the maximum storage capacity and the rate of sorption remained stable after the first 10 cycles. They also discovered that the major effect of cycling on particle morphology was the progressive extraction of Mg from the MgO shell surrounding the powder particles. In our previous study (Zhang et al., 2019b), Fe nanosheets obtained by wet-chemical ball milling were introduced in MgH_2 for the first time. The MgH_2+5 wt% nano-Fe composite began to release and absorb hydrogen at 182.1 and 75°C, respectively. Moreover, the dehydrogenated composite could absorb 6 wt% H_2 within just 10 min at 200°C. Cycling experiment depicted that the hydrogen capacity of MgH_2+5 wt% nano-Fe composite could still maintain at about 5 wt% after 50 cycles. During the first cycle, it could been seen from microstructure pictures that the Fe nanosheets on the surface of MgH_2 turned to be numerous ultrafine nanoparticles, which could provide more active sites in the following cycling. Further calculation results revealed that the addition of Fe could greatly weaken the Mg-H interaction strength, facilitating the dehydrogenation of MgH_2 (**Figure 1**).

Other Monometallic Catalysts

Besides Ni, Ti, and Fe, other monometallic catalysts have also been developed to improve the hydrogen storage

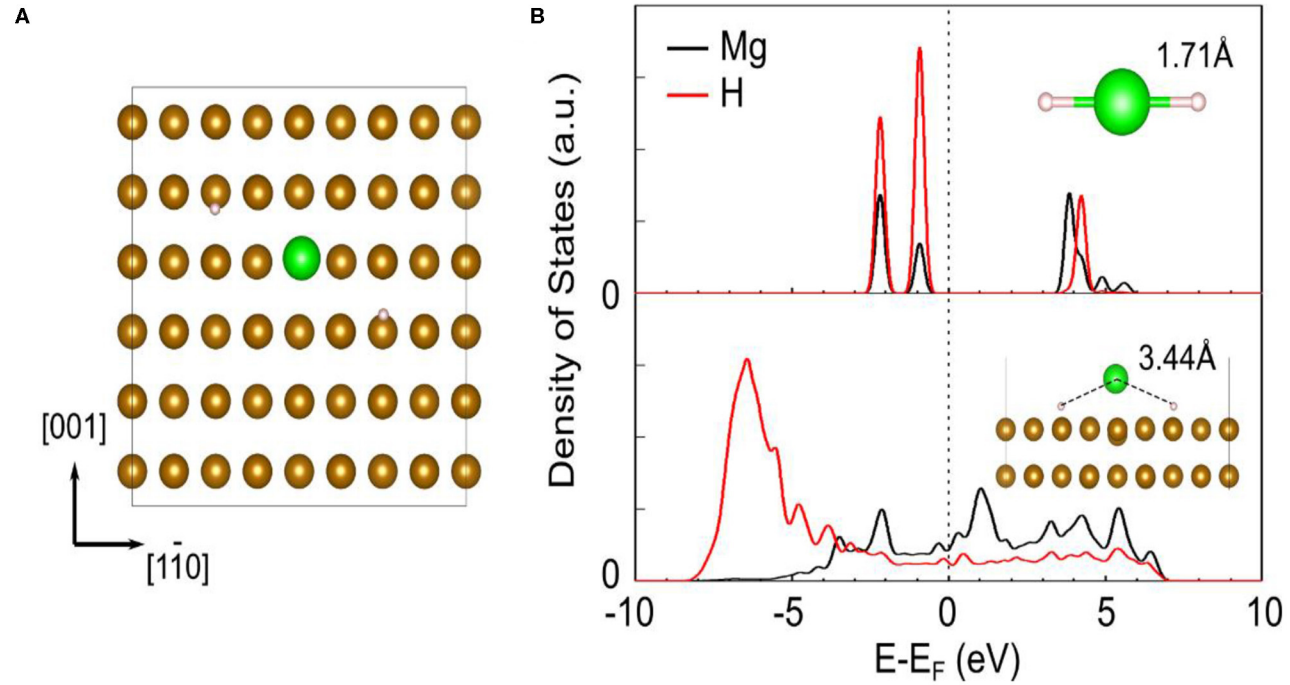

FIGURE 1 | The adsorption geometry of MgH_2 on Fe (110) surface in top view **(A)**. The brown, green, and white ball represent Fe, Mg, and H, respectively. The projected density of states (PDOS) of Mg and H of MgH_2 before (upper) and after (lower) adsorption on Fe (110) **(B)**. The Mg-H distances are shown as inset. The vertical dash line represents the Fermi energy. Reproduced from Zhang et al. (2019b) with permission from Elsevier.

properties of MgH_2. Cui et al. (2014) researched a series of core-shell structured Mg-TM (TM: Ti, Nb, V, Co, Mo, or Ni) nanocomposites by a wet-chemical method. The dehydrogenation performance was ranked as Mg-Ti > Mg-Nb > Mg-Ni > Mg-V > Mg-Co > Mg-Mo (**Figure 2**). All these composites could release hydrogen at a low temperature of 225°C, which was much lower than that of prepared MgH_2. Gasan et al. (2012) studied the impacts of 5 wt% of additives (V and Nb) on the hydrogen desorption temperature of MgH_2. XRD results demonstrated that the addition of V powders had a significant impact on the transformation of Mg into the MgO for the amount of MgO in MgH_2-V system was higher than other systems, relevant samples were studied by others and this phenomenon needs to be further researched. Also, SEM images verified that the mean particle size of composites was decreased by mechanical milling to micro scale. DSC tests showed that the addition of 5 wt% additives reduced hydrogen desorption temperatures of MgH_2 by about 40–50°C. Liang et al. (1999b) presented the hydrogen storage properties of MgH_2+V composite prepared by ball milling. The MgH_2+5 at% V composite could desorb hydrogen at 200°C and reabsorb hydrogen rapidly even at room temperature, the activation energy of hydrogen desorption was decreased to 62 kJ mol^{-1}.

BINARY ALLOYS

Zr-Based Binary Alloys

Recently, many papers reported an interesting strategy for improving hydrogen storage performance of MgH_2 by using intermetallic compounds of transition metals as catalyst. The corresponding results showed that the absorption/desorption properties of modified MgH_2 systems should be evidently enhanced by the synergetic effects of both phases. Following above idea, we successfully synthesized $ZrMn_2$ nanoparticles ranging from 100 to 300 nm by a facile wet chemical method to explore their catalytic effect on enhancing the hydrogen storage properties of MgH_2 (Zhang et al., 2019a). The MgH_2+10 wt% nano-$ZrMn_2$ composite began to release hydrogen from 181.9°C and 6.7 wt% hydrogen could be discharged in 5 min at 300°C. Isothermal absorption measurements represented that the dehydrogenated sample could absorb 5.3 wt% hydrogen within 10 min at 100°C under 3 MPa hydrogen pressure. Based on the XRD, TEM and calculation results, the $ZrMn_2$ nanoparticles were distributed well on the surface of MgH_2 and helped weaken Mg-H bond strength, which resulted in the enhanced hydrogen storage performance of MgH_2 (**Figure 3**). With the above research experience, we also studied the catalytic effect of ZrCo nanosheets (Zhang et al., 2019c). The modified MgH_2 composite could desorb almost 6.3 wt% H_2 within 5 min at 300°C and took up 4.4 wt% H_2 under 3 Mpa hydrogen pressure in 10 min even at 120°C for doping 10 wt% ZrCo nanosheets. The homogenously distributed ZrCo served as "hydrogen pump" to promote the de/composition of H_2 molecules, which was the key to decrease the de/hydrogenation temperature of MgH_2. Cycling performance (10 cycles) revealed that there was an apparent reduction in hydrogen storage capacity. In comparison to our studies, the MgH_2-$ZrNi_5$ nanocomposite system possessed more excellent hydrogen absorption/desorption performance

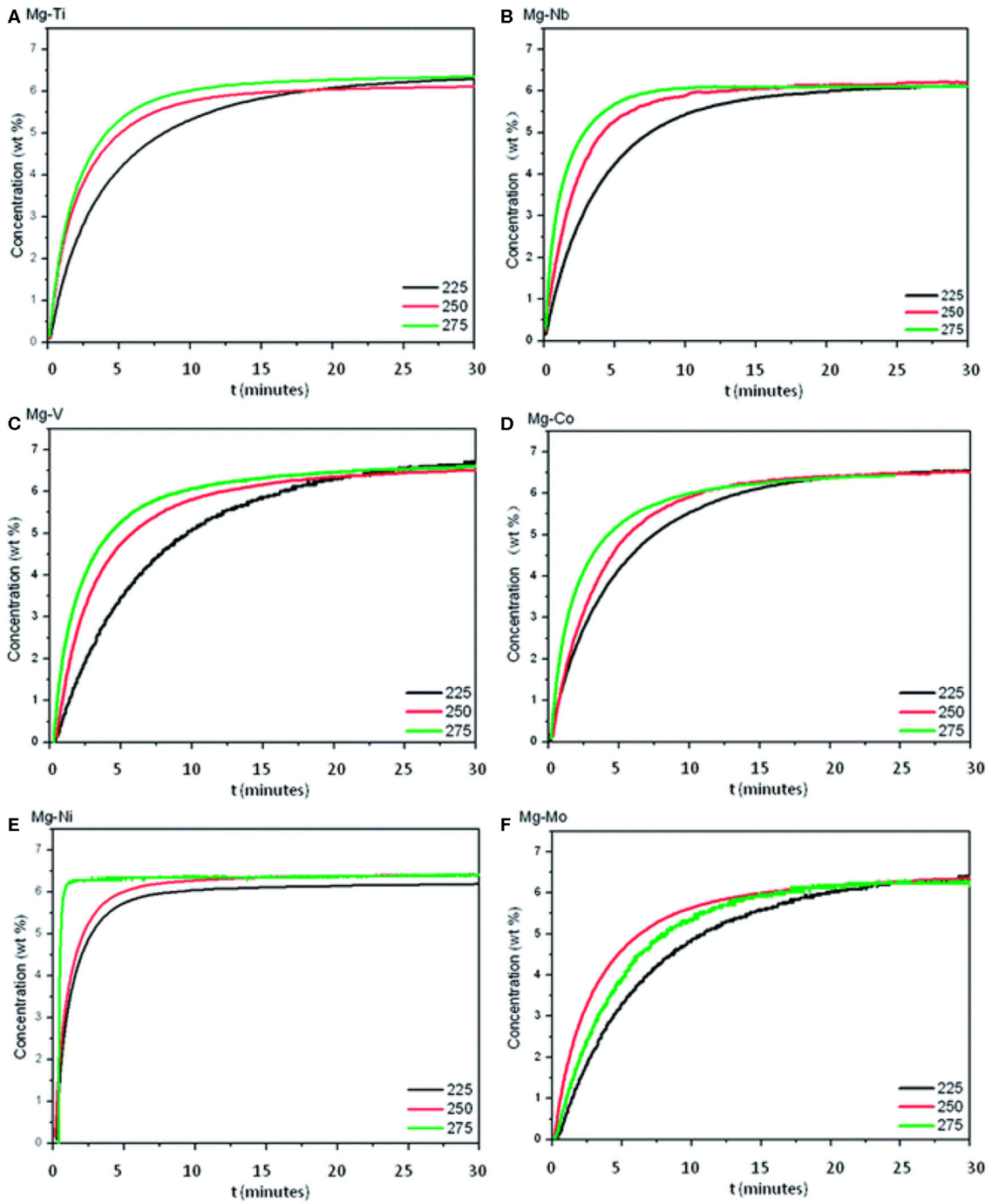

FIGURE 2 | Isothermal dehydrogenation curves of Mg–TM samples at 225, 250, and 275°C. **(A)** Mg-Ti; **(B)** Mg-Nb; **(C)** Mg-V; **(D)** Mg-Co; **(E)** Mg-Ni; **(F)** Mg-Mo. Reproduced from Cui et al. (2014) with permission from Royal Society of Chemistry.

without serious degradation after 600 complete cycles (El-Eskandarany et al., 2017). The prepared MgH_2-10 wt% $ZrNi_5$ sample required 1 and 10 min to absorb and discharge 5.3 wt% H_2 at 275°C, respectively. Based on the FE-SEM and XRD results, nano-scaled $ZrNi_5$ grains were uniformly distributed into the MgH_2 matrix and $ZrNi_5$ particles could create a network of micro channel that extending into the body of metal hydride to provide hydrogen diffusers during the de/hydrogenation processes.

Ti-Based Binary Alloys

El-Eskandarany et al. (2019a) employed $TiMn_2$ compound for improving the de/hydrogenation kinetics of MgH_2 powders. The 200 h ball milled MgH_2-$TiMn_2$ nanocomposites had a

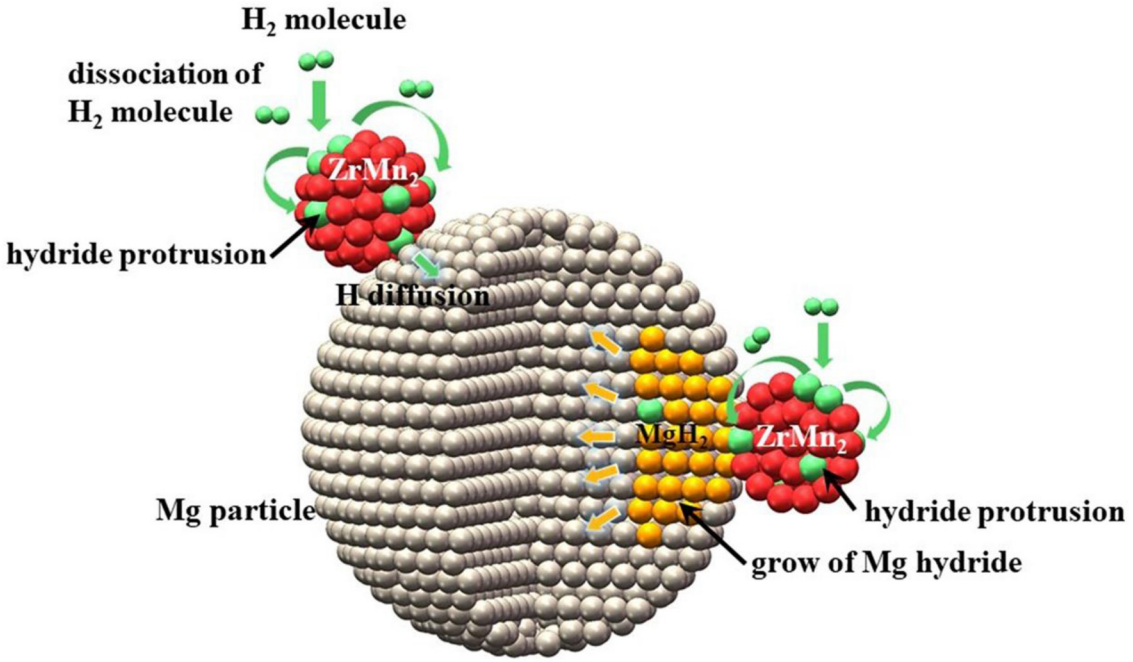

FIGURE 3 | Schematic summary of hydrogenation mechanism of Mg particle catalyzed by $ZrMn_2$ nanoportals. Reproduced from Zhang et al. (2019a) with permission from Royal Society of Chemistry.

nearly spherical shape with particle size ranging between 100 and 320 nm. DSC analysis presented that this composite could absorb/desorb 5.1 wt% hydrogen within 100 and 400 s at 225°C, respectively. For cycling performance, no obvious degradation in storage capacity was found during the long cyclic-life-time (600 h). FE-SEM micrographs highlighted that $TiMn_2$ particles could prevent a serious growth of Mg/MgH_2 grains, which led to reduced hydrogen uptake/release kinetics. Neto et al. (2017) doped TiFe compound into MgH_2 and concluded that a fine dispersion could be achieved by increasing milling time or using higher energy ball mill. To attain the best hydrogen kinetics, the sample prepared in the planetary mill for 36 h was the optimum selection and the MgH_2+ 40 wt%TiFe sample milled for 36 h could release about 3 wt% hydrogen within the first hour. Other Ti-based binary alloys such as TiAl and TiNb have also shown excellent enhancement for catalyzing MgH_2 (Zhou et al., 2013). Thermo gravimetric analysis and pressure composition temperature (PCT) isothermal tests showed that the MgH_2-TiAl and MgH_2-TiNb samples began to desorb hydrogen below 250°C, and the addition of TiAl or TiNb could make the dehydrogenated sample take up hydrogen even at room temperature. In terms of the dehydrogenation reaction, the Mg-H bond would be destabilized by doping with TM elements, which could be confirmed in the theoretical model. The TiAl catalyst illustrated the most effective impact on reducing the activation energy to 65 kJ/mol^{-1} among the Ti-based catalysts. Nevertheless, the Ti intermetallic catalyst did not change the thermodynamic equilibrium pressure of MgH_2.

La-Based Binary Alloys

Rare earth elements, especially lanthanides, are considered as one of the most promising catalysts because of their high activity. Many researchers have used La-based binary alloys as catalyst dopants in MgH_2 to explore the resulting catalytic effects. In 2000, Liang et al. (2000) studied MgH_2-$LaNi_5$ composite and found that Mg, LaH_3, Mg_2NiH_4 were formed during the milling process. The first desorption of mechanically milled MgH_2-30 wt% $LaNi_5$ could release about 4 wt% hydrogen within 150 s at 300°C and the dehydrogenated sample could absorb 3.7 wt% hydrogen in 2,000 s at room temperature. In order to understand the cycling properties of the composite, SEM images manifested that no apparent change in particle size was observed after 20 absorption and desorption cycles. To systematically study the MgH_2-$LaNi_5$ composite, MgH_2 with different amount of $LaNi_5$ were synthesized by Fu et al. (2008). XRD patterns illustrated that the extended milling time of 40 h caused an additional decrease of peak intensity for the materials containing 5 and 15 wt% $LaNi_5$, which could be ascribed to the brittleness of $LaNi_5$. Further kinetics results showed that the influence of $LaNi_5$ on absorption kinetics was more pronounced at lower temperatures. Additionally, other La-based binary alloys could also improve the hydrogen storage properties of MgH_2. El-Eskandarany et al. (2019b) researched the ball-milled MgH_2+ nano-$LaNi_3$ composite and found a single amorphous phase after 100 h ball-milling. The milled MgH_2-7 wt% $LaNi_3$ sample could discharge 5.6 wt% H_2 within 37 min at 225°C. For absorption, the dehydrogenated sample could absorb 3.8 wt% H_2 within 40 min at 125°C. In addition, the MgH_2-$LaNi_3$ sample possessed

an extraordinary long cycle-life-time (2,000 h) at 225°C without obvious degradation on its hydrogen storage capacity.

Other Binary Alloys

Santos et al. (2014) doped a vacuum grade commercial alloy FeNb into MgH_2 to study its catalytic effect. The MgH_2-FeNb nanocomposites depicted broaden XRD peaks, which indicated small crystallite size and presence of micro strain. Compared with Fe and Nb, the FeNb exhibited lower activity due to the diverse chemical interfacial energies associated to the nano-interfaces of Mg (MgH_2)/Fe (or Nb) and Mg (MgH_2)/FeNb alloy. Recently, we synthesized FeCo nanosheets and confirmed superior catalytic effect on MgH_2 (Yang et al., 2019). For hydrogen storage performance, DSC curves indicated that the MgH_2-FeCo composite started to desorb hydrogen from 200°C, which was 150°C lower than that of pure MgH_2. The dehydrogenated sample could rapidly uptake H_2 from room temperature and almost 6.7 wt% H_2 could be absorbed within 1 min at 300°C. Moreover, the MgH_2-FeCo composite showed excellent cycling performance over 10 cycles. Further TEM and XRD results demonstrated that the FeCo nanoparticles were evenly distributed on the surface of MgH_2 and functioned as "hydrogen spillover," which referred that the hydrogen molecules dissociated on the surfaces of FeCo nanosheets and in turn facilitated easy transfer of hydrogen atoms to the surface of Mg particles to generate MgH_2 during the hydrogenation process. On the other hand, FeCo also effortlessly took up hydrogen atoms from MgH_2 to form hydrogen molecule, thus remarkably improved the hydrogen storage properties of MgH_2.

TERNARY AND MULTICOMPONENT ALLOYS

Ti-Based Ternary Alloys

Based on the great improvement of the binary alloy, ternary alloys which replace part of the binary alloy with another transition metal have also been concerned in recent years (Hu et al., 2004; Shahi et al., 2013; El-Eskandarany, 2016; Lu et al., 2018). For instance, Zhou et al. (2013) doped TiVMn alloy into MgH_2 to study its hydrogen storage performance. On the contrast with other Ti-based binary alloys catalysts, the dehydrogenation kinetics of the MgH_2-TiVMn composite was much better (**Figure 4**). Moreover, PCT curves also depicted that the addition of TiVMn exhibited the best catalytic effect, which could release more hydrogen under the same condition. The dehydrogenation activation energy was calculated to be 85.2 kJ/mol·H_2 by OFW model, which was much lower than that of pure MgH_2. Khodaparast and Rajabi (2015) prepared the MgH_2+5 at% Ti-Mn-Cr sample by milling the Ti-Mn-Cr alloy produced by melt spinning method with pure MgH_2. When Ti-Mn-Cr was doped into MgH_2, the dehydrogenation temperature of the composite reduced from 399 to 345°C, much lower than that of prepared MgH_2 under the same conditions. Mahmoudi et al. (2011) prepared MgH_2-5 at% $TiCr_{1.2}Fe_{0.6}$ composites at the nanoscale. In comparison to pure MgH_2, the initial desorption temperature of the MgH_2-5 at% $TiCr_{1.2}Fe_{0.6}$ sample decreased to 241°C and almost 5 wt% hydrogen could be obtained at 300°C. Further, XRD and TEM studies stated that the interface of the $TiCr_{1.2}Fe_{0.6}$ alloy with magnesium also acted as active sites for nucleation of the hydride phase, thereby decreasing the nucleation barrier and enhancing the dehydrogenation property.

Non-Ti-Based Ternary Alloys

Besides Ti-based alloys, other alloys formed by various single transition metals also illustrated their remarkable effect on improving hydrogen storage performance of MgH_2. Agarwal et al. (2009) studied the catalytic effect of ZrCrNi alloy on hydrogenation properties of MgH_2. The ZrCrNi alloy was prepared by melting the three pure metals in an arc furnace and then milling with MgH_2 for 5 h in a SPEX 8,000 mixer-miller to receive the MgH_2-10 wt% ZrCrNi sample. They also performed 20 cycles of de/hydrogenation to explore the stabilization of kinetics and the achievement of hydrogen capacity. In aspect of de/hydrogenation performance, the composite could quickly desorb and absorb about 90% of its maximum hydrogen capacity within 7 min at 300°C after the 20th cycle. XRD and SEM patterns demonstrated that there was no other phases formed during milling and cycling. Also, the alloy was homogeneously dispersed in the MgH_2/Mg matrix. To improve hydrogen desorption properties of MgH_2, Motavalli and Rajabi (2014) prepared the MgH_2-5 at% Ni_3FeMn sample by mechanical milling, where the Ni_3FeMn catalyst was in two states: as-cast and melt-spun ribbon. DTA curves clarified that 30 h mechanically alloyed catalysts in both states could significantly decrease the desorption temperature. MgH_2-Ni_3FeMn melt-spun composite could discharge H_2 in lower temperature due to the ability to improve particle size refinement of MgH_2 and a more pronounced homogeneous distribution of the alloyed elements. The MgH_2-5 at% Ni_3FeMn melt-spun ribbon composite could release 3.39 wt% hydrogen within 1,000 s at 340°C. Zhou et al. (2019b) doped purchased VTiCr into MgH_2 and demonstrated a reversible capacity of 4 wt% H_2 between 150 and 350°C for the MgH_2-VTiCr composite. Besides, the dehydrogenated sample could absorb hydrogen in a low hydrogen pressure of 0.04–0.4 bar. The VTiCr catalyst was uniformly dispersed on the surface of MgH_2 matrix. VTiCr was deemed as a strong catalyst that provided not only excellent catalytic effect but also offer effective cyclic stability in the sense that the reaction kinetics still remained stable after the 10 cycles.

Multicomponent Alloys

As mentioned above, single transition metals and their binary and ternary alloys have shown great catalytic effects on MgH_2-based systems (Haghparast and Rajabi, 2015; El-Eskandarany et al., 2018). Further, studies about multicomponent alloys were also stated, Yu et al. (2010) found that the addition of $Ti_{0.4}Cr_{0.15}Mn_{0.15}V_{0.3}$ alloy could apparently improve the de/absorption properties of MgH_2. The MgH_2-$Ti_{0.4}Cr_{0.15}Mn_{0.15}V_{0.3}$ composite began to release hydrogen at 255°C and reached its peak at 294°C, which was much lower than that of unanalyzed MgH_2. Besides, the dehydrogenated sample could absorb 3.1 wt% H_2 in 500 min even at 29°C. The cycling results manifested that the dehydrogenation rate increased slowly in the first 20 cycles and then remained

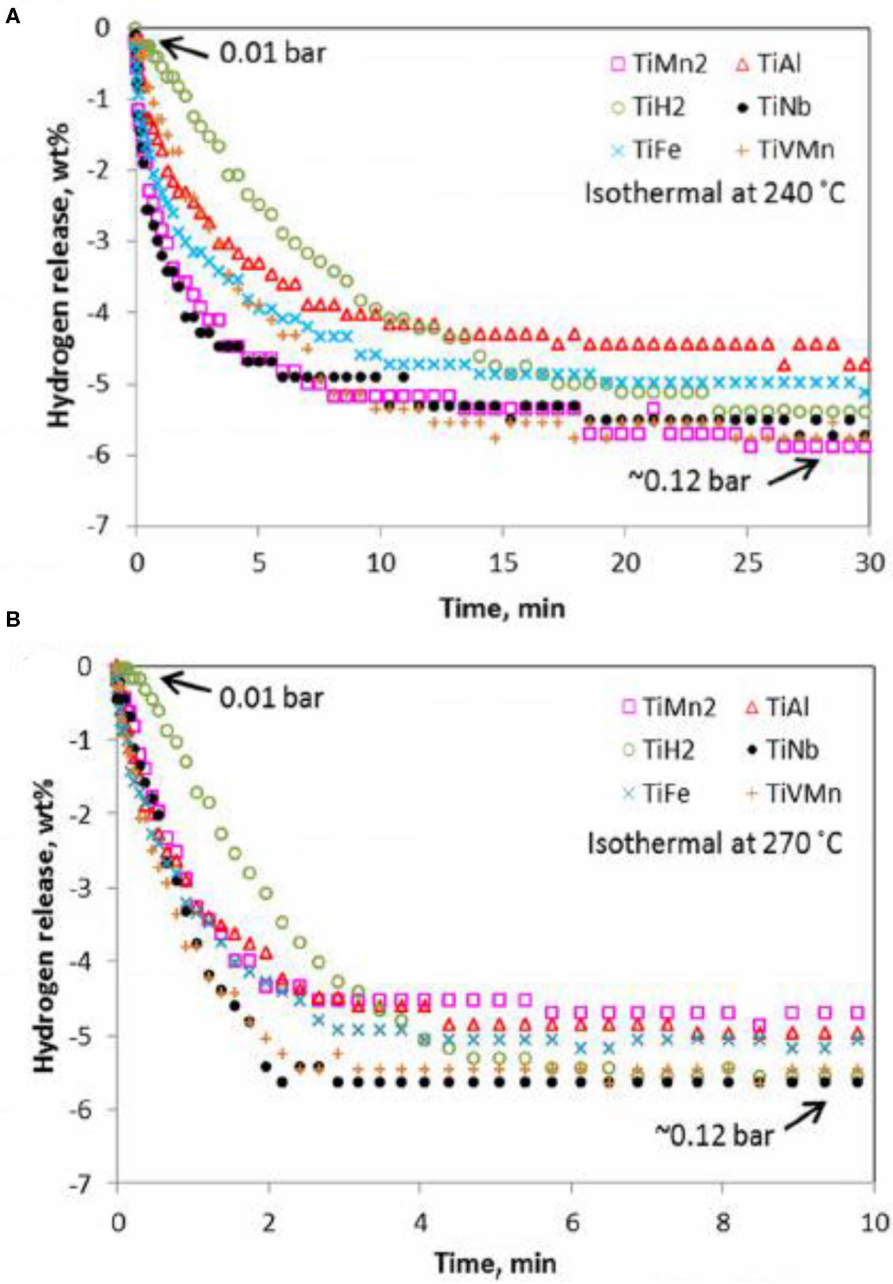

FIGURE 4 | PCT dehydrogenation kinetics for different Ti-based alloy catalyzed magnesium hydrides at 240 °C **(A)** and 270 °C **(B)**. Reproduced from Zhou et al. (2013) with permission from ACS Publications.

stable after 20 cycles. SEM and TEM techniques showed that the $Ti_{0.4}Cr_{0.15}Mn_{0.15}V_{0.3}$ alloy hydride nanoparticles were well-distributed on the surface of MgH_2. Meena et al. (2018) found that MgH_2 could desorb H_2 even at 180°C with the addition of 50 wt% $NiMn_{9.3}Al_{4.0}Co_{14.1}Fe_{3.6}$ alloy. Compared to as-milled MgH_2 sample, the *Ea* of this composite was lower by about 46.56 kJ/mol. Haghparast and Rajabi (2015) studied the de/hydrogenation kinetics of MgH_2-$TiCrMn_{0.4}Fe_{0.4}V_{0.2}$ composite and found that the dehydrogenation temperature of modified MgH_2 decreased to 378°C, which was lower than that of as-received MgH_2 (421°C). $V_{45}Zr_{20}Ni_{20}Cu_{10}Al_3Pd_2$ powders were doped into MgH_2 by El-Eskandarany et al. (2018) and found that the desorption temperature of MgH_2-10 wt% $V_{45}Zr_{20}Ni_{20}Cu_{10}Al_3Pd_2$ powders was 308.9°C, which was 116°C lower than that of pure MgH_2.This prepared nanocomposite possessed superior de/hydrogenation kinetics at relatively low temperature (180°C), absorbing and desorbing 5.5 wt% H_2 within 200 s.

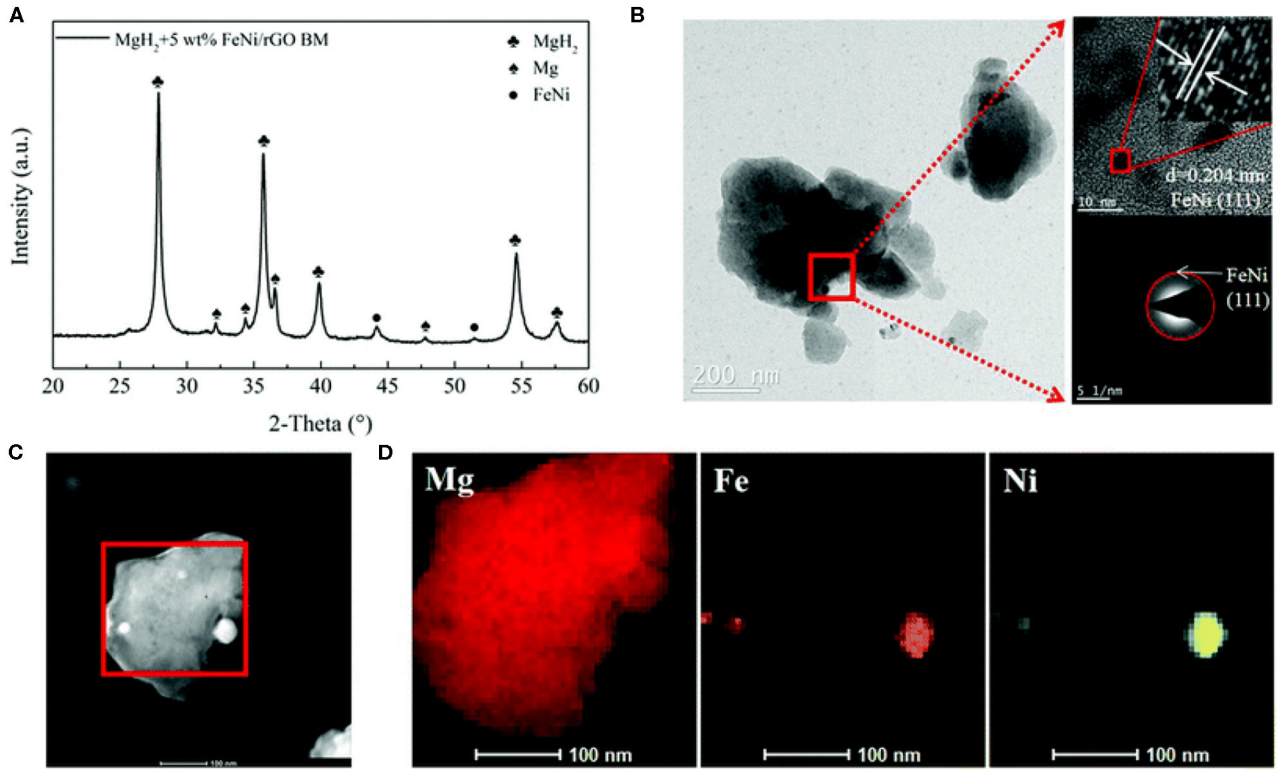

FIGURE 5 | Structural characterization of ball-milled MgH_2 + 5 wt% FeNi/rGO: **(A)** XRD pattern, **(B)** TEM photograph with the HRTEM image and SAED pattern, and **(C,D)** corresponding EDS spectra with elemental mapping of Mg, Fe, and Ni. Reproduced from Ji et al. (2020) with permission from Royal Society of Chemistry.

ALLOYS AND CARBON MATERIALS

Alloys and Graphene

All above catalytic materials have shown remarkable improvement on the hydrogen storage performance of MgH_2, however, stable cycling performance is still the bottleneck for realizing the practical application of MgH_2. Carbon materials such as graphene and carbon nanotubes, were widely researched and lots of studies have proven that carbon materials are helpful in preserving stable cycling properties (Xia et al., 2015). Hudson et al. (2016) reported that graphene together with Fe nanoclusters could enhance the hydrogen sorption kinetics of MgH_2. From the TPD and DSC curves, the peak temperature of desorption for MgH_2+5wt% Fe@G was 281.7°C, lower than that of exhibited peak ball-milled MgH_2. In addition, the activation energy of MgH_2+5wt% Fe@G composite was reduced to 119.1 kJ/mol (24% lower than that of ball-milled MgH_2). Furthermore, TEM confirmed that the grain size of MgH_2 increased only 15 nm after 6 cycles, displaying a low grain growth rate during cycling due to the addition of graphene. Density functional theory calculations demonstrated that the defect in graphene and the presence of iron clusters at the defect site of graphene played important role in desorbing hydrogen. Ji et al. (2020) prepared FeNi nanoparticles dispersed on reduced graphene oxide nanosheets (FeNi/rGO) and then found that this catalyst played a vital role in improving the hydrogen storage performance of MgH_2. The MgH_2-FeNi/rGO sample started to release hydrogen at 230°C and the dehydrogenated sample could absorb 5.4 wt% within 20 min at 125°C. Further investigations proved that FeNi nanoparticles were well distributed on the MgH_2 surface in the nanoscale range (**Figure 5**). More importantly, cycling tests exhibited that 6.9 wt% hydrogen capacity was maintained even after 50 cycles. Singh et al. (2017) investigated the catalytic effect of FeCoNi@GS on hydrogen sorption of MgH_2. The onset desorption temperature of this sample was around 255, 25°C lower than that of FeCoNi catalyzed MgH_2. The FeCoNi@GS remained stable even after 24 cycles with FeCoNi particles uniformly distributed on the surface of GS.

Alloys and Carbon Nanotubes

Carbon nanotubes (CNTs), were widely researched in every field for its small particle size and great microstructure (Luo et al., 2007; Gao et al., 2019; Liu M. et al., 2019). Lillo-Ródenas et al. (2008) demonstrated that the de/hydrogenation performance of MgH_2 could be strengthened by the addition of different carbon materials. Comparing with other materials, the mixtures involving CNTs and MWCNTs showed the best results to achieve low temperature operation and high hydrogen storage capacity. Ismail et al. (2014) evidenced an apparent catalytic effect of co-doping MgH_2 with $FeCl_3$ and carbon nanotubes on hydrogen storage performance. The CNT-added MgH_2-$FeCl_3$

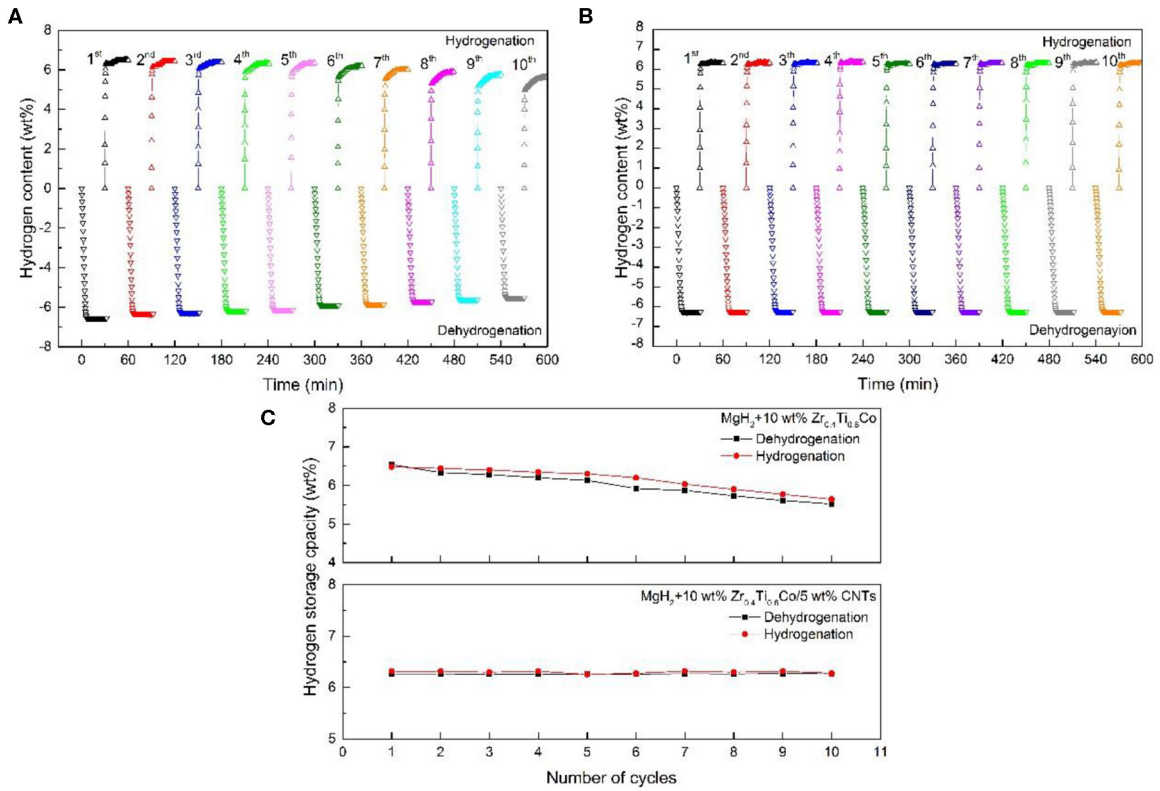

FIGURE 6 | Non-isothermal dehydrogenation/hydrogenation curves of the MgH_2+10 wt% $Zr_{0.4}Ti_{0.6}Co$ **(A)**, MgH_2+10 wt% $Zr_{0.4}Ti_{0.6}Co$/5 wt% CNTs **(B)** composites and as a function of cycling and the resulting line chart **(C)**. Reproduced from Zhang L. et al. (2020) with permission from Elsevier.

composite started to release hydrogen at 230, 45°C lower than that of MgH_2-$FeCl_3$. Moreover, the MgH_2-$FeCl_3$/CNT sample could desorb more hydrogen than that of MgH_2-$FeCl_3$ under the same isothermal condition. SEM images confirmed that the CNT was not destroyed after the short milling process and indicated that the sample with CNT appeared to have less agglomeration. It was believed that the presence of the unique structure of the CNTs played a critical role in the improvement of hydrogen storage properties in the MgH_2-$FeCl_3$/CNTs composite. In our recent investigation (Zhang L. et al., 2020), CNTs combined with $Zr_{0.4}Ti_{0.6}Co$ nanosheets was adopt to strengthen the hydrogen storage properties of MgH_2. With the addition of $Zr_{0.4}Ti_{0.6}Co$ sheets, the sorption kinetics were evidently improved while hydrogen capacity was slowly decreasing. Meanwhile, the MgH_2-$Zr_{0.4}Ti_{0.6}Co$/CNTs exhibited no reduction in cycling performance even after 10 cycles after doping CNTs (**Figure 6**). Deeper structure investigation revealed that particle size of MgH_2-$Zr_{0.4}Ti_{0.6}Co$/CNTs was almost unchanged, contributing to the stable cycling performance.

Alloys and Other Carbon Materials

Apart from carbon materials mentioned above, other carbon materials also have distinguished effect on ameliorating the de/hydrogenation kinetics of MgH_2 (Xia et al., 2018). An et al. (2014) reported that the one-dimensional porous Ni@C nanorods modified MgH_2 performed an excellent hydrogen storage properties. The addition of Ni@C decreased the onset temperature of MgH_2 to 175°C. Cycling results illustrated no significant loss of hydrogen storage capacity and the MgH_2-5 wt% Ni@C composite had favorable cycle stability. Chen et al. (2018) reported the mesoporous carbon CMK-3 performed well in enhancing the hydrogen storage properties of MgH_2. The onset desorption temperature of MgH_2-10 wt% Ni/CMK-3 was 170°C lower than that of pure MgH_2 (above 350°C) and the sample could discharge 6 wt% H_2 even at 295°C. The more fascinating fact was that 3.9 wt% hydrogen was absorbed at 55°C for MgH_2-Ni/CMK-3 composite. The sample maintained nearly 90.8% of the original de/hydrogenation capacity when cycled for 10 times, indicating that MgH_2-Ni/CMK-3 had a good cycle stability. Wang et al. (2018) combined graphene oxide-based porous carbon (GC) and $TiCl_3$ to improve the reversible kinetics of MgH_2. The MgH_2/GC-$TiCl_3$ composite could reversibly deliver about 7.6 wt% hydrogen at 300°C within 9 min and the average dehydrogenation rate was several times faster than that of the single catalytic MgH_2 system. Concerning cycling property, the capacity of the MgH_2/GC-$TiCl_3$ sample was also stable with slower kinetics, owing to the nanoconfinement effect of the ball-milled GC. In a word, graphite and carbon with their derivatives could mainly improve the cycling performance, which results in remarkably enhanced the hydrogen storage properties of MgH_2.

CONCLUSIONS AND PERSPECTIVES

To realize the practical application of hydrogen energy, numerous effects still need to be carried out in the coming future. For hydrogen storage materials, magnesium hydride is generally believed as a promising material due to its natural abundance, excellent reversibility, light weight and efficient cost. Among the methods investigated, the transition metals have demonstrated excellent catalytic effect on improving the hydrogen storage properties of MgH_2. Further studies about alloys based on transition metals are demonstrated to be more effective than the single metal counterparts. In our recent studies, Zr-based alloys and Fe-based alloys were successfully prepared and confirmed to striking improve the de/hydrogenation performance of MgH_2. Although the transition metals and their alloys have shown superior enhancement on the de/absorption performance of MgH_2, maintaining good cyclic performance is still a challenge for MgH_2-based systems. A large number of experiments indicated that carbon materials show excellent effect on maintaining good hydrogen absorption and desorption performance. Our group also demonstrated that carbon nanotubes and reduced graphene oxide together with transition metal alloys can improve the de/hydrogenation kinetics of MgH_2 while maintain stable cycling properties at the same time. From above review on literature and our own work, we propose the following strategy to further enhance the hydrogen storage properties of MgH_2: (1) regulate the components of transition metal alloys to its best catalytic effect, (2) make the particle size of the alloys as small as possible, (3) combine alloys and carbon materials to synthetically improve the hydrogen storage properties of MgH_2. In summary, nanoscale transition metal alloys together with carbon materials would be a promising catalyst for realizing the practical application of MgH_2.

AUTHOR CONTRIBUTIONS

LZ, SS, and JX contributed conception and design of the study. ZS wrote the first draft of the manuscript. XL, FN, and NY wrote sections of the manuscript. All authors contributed to manuscript revision, read and approved the submitted version.

ACKNOWLEDGMENTS

The authors would like to acknowledge financial support from the National Natural Science Foundation of China (Grant No. 51801078), the National Science Foundation of Jiangsu Province (Grant No. BK20180986) and the Postgraduate Research and Practice Innovation Program of Jiangsu Province (SJCX19_0614).

REFERENCES

Abe, J. O., Popoola, A. P. I., Ajenifuja, E., and Popoola, O. M. (2019). Hydrogen energy, economy and storage: review and recommendation. *Int. J. Hydrogen Energy* 44, 15072–15086. doi: 10.1016/j.ijhydene.2019.04.068

Agarwal, S., Aurora, A., Jain, A., Jain, I. P., and Montone, A. (2009). Catalytic effect of ZrCrNi alloy on hydriding properties of MgH_2. *Int. J. Hydrogen Energy* 34, 9157–9162. doi: 10.1016/j.ijhydene.2009.09.034

Ali, N. A., Idris, N. H., Din, M. F. M., Yahya, M. S., and Ismail, M. (2019). Nanoflakes $MgNiO_2$ synthesised via a simple hydrothermal method and its catalytic roles on the hydrogen sorption performance of MgH_2. *J. Alloy. Compd.* 796, 279–286. doi: 10.1016/j.jallcom.2019.05.048

An, C., Liu, G., Li, L., Wang, Y., Chen, C., Wang, Y., et al. (2014). *In situ* synthesized one-dimensional porous Ni@C nanorods as catalysts for hydrogen storage properties of MgH_2. *Nanoscale* 6, 3223–3230. doi: 10.1039/c3nr05607d

Bassetti, A., Bonetti, E., Pasquini, L., Montone, A., Grbovic, J., and Vittori Antisari, M. (2005). Hydrogen desorption from ball milled MgH_2 catalyzed with Fe. *Eur. Phys. J. B.* 43, 19–27. doi: 10.1140/epjb/e2005-00023-9

Bogdanović, B. R. A., and Spliethoff, B. (1990). Active MgH_2ð*Mg systems for reversible chemical energy storage. *Angew. Chem. Int. Edit.* 29, 223–234. doi: 10.1002/anie.199002233

Bououdina, M., and Guo, Z. X. (2002). Comparative study of mechanical alloying of (Mg+Al) and (Mg+Al+Ni) mixtures for hydrogen storage. *J. Alloy. Compd.* 336, 222–231. doi: 10.1016/S0925-8388(01)01856-4

Cao, Z., Ouyang, L., Wang, H., Liu, J., Sun, L., Felderhoff, M., et al. (2016). Development of ZrFeV alloys for hybrid hydrogen storage system. *Int. J. Hydrogen Energy.* 41, 11242–11253. doi: 10.1016/j.ijhydene.2016.04.083

Chen, G., Zhang, Y., Chen, J., Guo, X., Zhu, Y., and Li, L. (2018). Enhancing hydrogen storage performances of MgH_2 by Ni nanoparticles over mesoporous carbon CMK-3. *Nanotechnology* 29:265705. doi: 10.1088/1361-6528/aabcf3

Chen, G., Zhang, Y., Cheng, H., Zhu, Y., Li, L., and Lin, H. (2019). Effects of two-dimension MXene Ti_3C_2 on hydrogen storage performances of MgH_2-$LiAlH_4$ composite. *Chem. Phys.* 522, 178–187. doi: 10.1016/j.chemphys.2019.03.001

Chen, M., Yang, X. B., Cui, J., Tang, J. J., Gan, L. Y., Zhu, M., et al. (2012). Stability of transition metals on Mg(0001) surfaces and their effects on hydrogen adsorption. *Int. J. Hydrogen Energy* 37, 309–317. doi: 10.1016/j.ijhydene.2011.09.065

Cui, J., Liu, J., Wang, H., Ouyang, L., Sun, D., Zhu, M., et al. (2014). Mg–TM (TM: Ti, Nb, V, Co, Mo or Ni) core–shell like nanostructures: synthesis, hydrogen storage performance and catalytic mechanism. *J. Mater. Chem. A* 2, 9645–9655. doi: 10.1039/C4TA00221K

El-Eskandarany, M. S. (2016). Metallic glassy $Zr_{70}Ni_{20}Pd_{10}$ powders for improving the hydrogenation/dehydrogenation behavior of MgH_2. *Sci. Rep.* 6:26936. doi: 10.1038/srep26936

El-Eskandarany, M. S., Ahmed, S. A., and Shaban, E. (2018). Metallic glassy $V_{45}Zr_{20}Ni_{20}Cu_{10}Al_3Pd_2$ alloy powders for superior hydrogenation/dehydrogenation kinetics of MgH_2. *Mater. Today* 5, 13718–13725. doi: 10.1016/j.matpr.2018.02.010

El-Eskandarany, M. S., Al-Ajmi, F., Banyan, M., and Al-Duweesh, A. (2019a). Synergetic effect of reactive ball milling and cold pressing on enhancing the hydrogen storage behavior of nanocomposite MgH_2/10 wt% $TiMn_2$ binary system. *Int. J. Hydrogen Energy* 44, 26428–26443. doi: 10.1016/j.ijhydene.2019.08.093

El-Eskandarany, M. S., Saeed, M., Al-Nasrallah, E., Al-Ajmi, F., and Banyan, M. (2019b). Effect of $LaNi_3$ amorphous alloy nanopowders on the performance and hydrogen storage properties of MgH_2. *Energies* 12:1005. doi: 10.3390/en12061005

El-Eskandarany, M. S., Shaban, E., Ali, N., Aldakheel, F., and Alkandary, A. (2016). *In-situ* catalyzation approach for enhancing the hydrogenation/dehydrogenation kinetics of MgH_2 powders with Ni particles. *Sci. Rep.* 6:37335. doi: 10.1038/srep37335

El-Eskandarany, M. S., Shaban, E., Al-Matrouk, H., Behbehani, M., Alkandary, A., Aldakheel, F., et al. (2017). Structure, morphology and hydrogen storage kinetics of nanocomposite MgH_2/10 wt% $ZrNi_5$ powders. *Mater. Today Energy* 3, 60–71. doi: 10.1016/j.mtener.2016.12.002

Ershova, O. G., Dobrovolsky, V. D., Solonin, Y. M., Khyzhun, O. Y., and Koval, A. Y. (2008). Influence of Ti, Mn, Fe, and Ni addition upon thermal stability and decomposition temperature of the MgH_2 phase of alloys

synthesized by reactive mechanical alloying. *J. Alloy. Compd.* 464, 212–218. doi: 10.1016/j.jallcom.2007.10.064

Felderhoff, M., Weidenthaler, C., Helmolt, V. R., and Eberle, U. (2007). Hydrogen storage: the remaining scientific and technological challenges. *Phys. Chem.* 9, 2643–2653. doi: 10.1039/b701563c

Fu, Y., Groll, M., Mertz, R., and Kulenovic, R. (2008). Effect of $LaNi_5$ and additional catalysts on hydrogen storage properties of Mg. *J. Alloy. Compd.* 460, 607–613. doi: 10.1016/j.jallcom.2007.06.008

Gao, S., Wang, X., Liu, H., He, T., Wang, Y., Li, S., et al. (2019). Effects of nano-composites (FeB, FeB/CNTs) on hydrogen storage properties of MgH_2. *J. Power Sources* 438:227006. doi: 10.1016/j.jpowsour.2019.227006

Gasan, H., Celik, O. N., Aydinbeyli, N., and Yaman, Y. M. (2012). Effect of V, Nb, Ti and graphite additions on the hydrogen desorption temperature of magnesium hydride. *Int. J. Hydrogen Energy* 37, 1912–1918. doi: 10.1016/j.ijhydene.2011.05.086

Gosalawit-Utke, R., Nielsen, T. K., Saldan, I., Laipple, D., Cerenius, Y., Jensen, T. R., et al. (2011). Nanoconfined $2LiBH_4$-MgH_2 prepared by direct melt infiltration into nanoporous materials. *J. Phys. Chem. C* 115, 10903–10910. doi: 10.1021/jp2021903

Goto, K., Hirata, T., Yamamoto, I., and Nakao, W. (2019). Suitability evaluation of $LaNi_5$ as hydrogen-storage-alloy actuator by in-situ displacement measurement during hydrogen pressure change. *Molecules* 24:2420. doi: 10.3390/molecules24132420

Haghparast, M. R., and Rajabi, M. (2015). Hydrogen desorption properties of MgH_2-5 at% Ti-Cr-Mn-Fe-V composite via combined vacuum arc remelting and mechanical alloying. *Proc. Mater. Sci.* 11, 605–610. doi: 10.1016/j.mspro.2015.11.091

Hanada, N., Ichikawa, T., and Fujii, H. (2005). Catalytic effect of Ni nano-particle and Nb oxide on H-desorption properties in MgH_2 prepared by ball milling. *J. Alloy. Compd.* 404–406, 716–719. doi: 10.1016/j.jallcom.2004.12.166

He, D., Wang, Y., Wu, C., Li, Q., Ding, W., and Sun, C. (2015). Enhanced hydrogen desorption properties of magnesium hydride by coupling non-metal doping and nano-confinement. *Appl. Phys. Lett.* 107:243907. doi: 10.1063/1.4938245

He, Q., Zhu, D., Wu, X., Dong, D., Xu, M., and Tong, Z. (2019). Hydrogen desorption properties of $LiBH_4$/$xLiAlH_4$ (x = 0.5, 1, 2) composites. *Molecules* 24:1861. doi: 10.3390/molecules24101861

He, T., Pachfule, P., Wu, H., Xu, Q., and Chen, P. (2016). Hydrogen carriers. *Nat. Rev. Mater.* 1:12. doi: 10.1038/natrevmats.2016.59

He, T., Wang, X., Liu, H., Gao, S., Wang, Y., Li, S., et al. (2020). Enhanced hydrogen desorption/absorption properties of magnesium hydride with CeF3@Gn. *Int. J. Hydrogen Energy* 45, 4754–4764. doi: 10.1016/j.ijhydene.2019.12.111

Hu, Y. Q., Yan, C., Zhang, H. F., Ye, L., and Hu, Z. Q. (2004). Preparation and hydrogenation characteristics of Mg−30 wt.% $Ti_{37.5}V_{25}Cr_{37.5}$ composite. *J. Alloy. Compd.* 375, 265–269. doi: 10.1016/j.jallcom.2003.11.046

Hudson, M. S. L., Takahashi, K., Ramesh, A., Awasthi, S., Ghosh, A. K., Ravindran, P., et al. (2016). Graphene decorated with Fe nanoclusters for improving the hydrogen sorption kinetics of MgH_2-experimental and theoretical evidence. *Catal. Sci. Technol.* 6, 261–268. doi: 10.1039/C5CY01016K

Ismail, M., Juahir, N., and Mustafa, N. S. (2014). Improved hydrogen storage properties of MgH_2 co-doped with $FeCl_3$ and carbon nanotubes. *J. Phys. Chem. C* 118, 18878–18883. doi: 10.1021/jp5046436

Jain, I. P., Lal, C., and Jain, A. (2020). Hydrogen storage in Mg: a most promising material. *Int. J. Hydrogen Energy* 35, 5133–5144. doi: 10.1016/j.ijhydene.2009.08.088

Jansa, L. I., Kalantzopoulos, G. N., Nordholm, K., and Hauback, B. C. (2020). Destabilization of $NaBH_4$ by transition metal fluorides. *Molecules* 25:780. doi: 10.3390/molecules25040780

Jeon, K. J., Moon, H. R., Ruminski, A. M., Jiang, B., Kisielowski, C., Bardhan, R., et al. (2011). Air-stable magnesium nanocomposites provide rapid and high-capacity hydrogen storage without using heavy-metal catalysts. *Nat. Mater.* 10, 286–290. doi: 10.1038/nmat2978

Ji, L., Zhang, L., Yang, X., Zhu, X., and Chen, L. (2020). The remarkably improved hydrogen storage performance of MgH2 by the synergetic effect of an FeNi/rGO nanocomposite. *Dalton Trans.* 49:4146. doi: 10.1039/D0DT00230E

Khafidz, N. Z. A. K., Yaakob, Z., Lim, K. L., and Timmiati, S. N. (2016). The kinetics of lightweight solid-state hydrogen storage materials: a review. *Int. J. Hydrogen Energy* 41, 13131–13151. doi: 10.1016/j.ijhydene.2016.05.169

Khodaparast, V., and Rajabi, M. (2015). Hydrogen desorption properties of MgH_2-5 wt% Ti-Mn-Cr composite via combined melt spinning and mechanical alloying. *Proc. Mater. Sci.* 11, 611–615. doi: 10.1016/j.mspro.2015.11.092

Kim, J., Jun, A., Gwon, O., Yoo, S., Liu, M., Shin, J., et al. (2018). Hybrid-solid oxide electrolysis cell: a new strategy for efficient hydrogen production. *Nano Energy* 44, 121–126. doi: 10.1016/j.nanoen.2017.11.074

Konarova, M., Tanksale, A., Beltramini, J. N., and Lu, G., Qing. (2013). Effects of nano-confinement on the hydrogen desorption properties of MgH_2. *Nano Energy* 2, 98–104. doi: 10.1016/j.nanoen.2012.07.024

Kumar, V., Pukazhselvan, D., Tyagi, A. K., and Singh, S. K. (2013). Effect of Ni concentration on the structural and hydrogen storage characteristics of Zr–Mn based laves phase system. *Mater. Renew. Sust. Energy* 2:12. doi: 10.1007/s40243-013-0012-3

Liang, G., Hout, J., Boil, S., Neste, V. A., and Schul, R. (1999b). Hydrogen storage properties of the mechanically milled MgH_2-V nanocomposite. *J. Alloy. Compd.* 291, 295–299. doi: 10.1016/S0925-8388(99)00268-6

Liang, G., Hout, J., Boily, S., Neste, V. A., and Schulz, R. (1999a). Catalytic effect of transition metals on hydrogen sorption in nanocrystalline ball milled MgH_2 -Tm (Tm=Ti, V, Mn, Fe and Ni) systems. *J. Alloy. Compd.* 292, 247–252. doi: 10.1016/S0925-8388(99)00442-9

Liang, G., Hout, J., Boily, S., Neste, V. A., and Schulz, R. (2000). Hydrogen storage in mechanically milled Mg-$LaNi_5$ and MgH_2-$LaNi_5$ composites. *J. Alloy. Compd.* 297, 261–265. doi: 10.1016/S0925-8388(99)00592-7

Liao, B., Lei, Y. Q., Chen, L. X., Lu, G. L., Pan, H. G., and Wang, Q. D. (2004). Effect of the La/Mg ratio on the structure and electrochemical properties of $LaxMg_3$-xNi_9 (x=1.6–2.2) hydrogen storage electrode alloys for nickel–metal hydride batteries. *J. Power Sources* 129, 358–367. doi: 10.1016/j.jpowsour.2003.11.044

Lillo-Ródenas, M. A., Guo, Z. X., Aguey-Zinsou, K. F., Cazorla-Amorós, D., and Linares-Solano, A. (2008). Effects of different carbon materials on MgH_2 decomposition. *Carbon* 46, 126–137. doi: 10.1016/j.carbon.2007.10.033

Liu, H., Ma, H., Zhang, L., Gao, S., Wang, X., Xu, L., et al. (2019a). Wet chemical synthesis of non-solvated rod-Like alpha'-AlH_3 as a hydrogen storage material. *Front. Chem.* 7:892. doi: 10.3389/fchem.2019.00892

Liu, H., Zhang, L., Ma, H., Lu, C., Luo, H., Wang, X., et al. (2020). Aluminum hydride for solid-state hydrogen storage: structure, synthesis, thermodynamics, kinetics, and regeneration. *J. Energy Chem.* 52, 428–440.doi: 10.1016/j.jechem.2020.02.008

Liu, M., Xiao, X., Zhao, S., Saremi-Yarahmadi, S., Chen, M., Zheng, J., et al. (2019b). ZIF-67 derived Co@CNTs nanoparticles: remarkably improved hydrogen storage properties of MgH_2 and synergetic catalysis mechanism. *Int. J. Hydrogen Energy* 44, 1059–1069. doi: 10.1016/j.ijhydene.2018.11.078

Lu, Y., Wang, H., Liu, J., Ouyang, L., and Zhu, M. (2018). Destabilizing the dehydriding thermodynamics of MgH_2 by reversible intermetallics formation in Mg–Ag–Zn ternary alloys. *J. Power Sources* 396, 796–802. doi: 10.1016/j.jpowsour.2018.06.060

Luo, Y., Wang, P., Ma, L. P., and Cheng, H. M. (2007). Enhanced hydrogen storage properties of MgH_2 co-catalyzed with NbF5 and single-walled carbon nanotubes. *Scripta Mater.* 56, 765–768. doi: 10.1016/j.scriptamat.2007.01.016

Mahmoudi, N., Kaflou, A., and Simchi, A. (2011). Hydrogen desorption properties of MgH_2-$TiCr_{1.2}Fe_{0.6}$ nanocomposite prepared by high-energy mechanical alloying. *J. Power Sources* 196, 4604–4608. doi: 10.1016/j.jpowsour.2011.01.001

Meena, P., Singh, R., Sharma, V. K., and Jain, I. P. (2018). Role of $NiMn_{9.3}Al_{4.0}Co_{14.1}Fe_{3.6}$ alloy on dehydrogenation kinetics of MgH_2. *J. Magnes. Alloy.* 6, 318–325. doi: 10.1016/j.jma.2018.05.007

Montone, A., Aurora, A., Gattia, D. M., and Antisari, M. V. (2012). Microstructural and kinetic evolution of Fe doped MgH_2 during H_2 cycling. *Catalysts* 2, 400–411. doi: 10.3390/catal2030400

Motavalli, A., and Rajabi, M. (2014). Catalytic effect of melt-spun Ni_3FeMn alloy on hydrogen desorption properties of nanocrystalline MgH_2 synthesized by mechanical alloying. *Int. J. Hydrogen Energy* 39, 17047–17053. doi: 10.1016/j.ijhydene.2014.08.061

Neto, R. M. L., Rafael, A. S., Floriano, R., Coutinho, G. C. S., Falcão, R. B., and Leiva, D. R. (2017). Synthesis by high-energy ball milling of MgH_2-TiFe composites for hydrogen storage. *Mater. Sci. Forum.* 899, 13–18. doi: 10.4028/www.scientific.net/MSF.899.13

Nielsen, T. K., Manickam, K., and Hirscher, M. (2009). Confinement of MgH\r, 2\r nanoclusters within nanoporous aerogel scaffold materials. *ACS Nano.* 3, 3521–3528. doi: 10.1021/nn901072w

Norberg, N. S., Arthur, T. S., Fredrick, S. J., and Prieto, A. L. (2011). Size-dependent hydrogen storage properties of Mg nanocrystals prepared from solution. *J. Am. Chem. Soc.* 133, 10679–10681. doi: 10.1021/ja201791y

Peng, X., Wang, H., Hu, R., Ouyang, L., Liu, J., and Zhu, M. (2017). Electrochemical performances of MgH_2 and MgH_2-C films for lithium ion battery anode. *J. Alloy. Compd.* 711, 473–479. doi: 10.1016/j.jallcom.2017.03.180

Peter, S. C. (2018). Reduction of CO_2 to chemicals and fuels: a solution to global warming and energy crisis. *ACS Energy Lett.* 3, 1557–1561. doi: 10.1021/acsenergylett.8b00878

Pighin, S. A., Capurso, G., Russo, S. L., and Peretti, H. A. (2012). Hydrogen sorption kinetics of magnesium hydride enhanced by the addition of Zr_8Ni_{21} alloy. *J. Alloy. Compd.* 530, 111–115. doi: 10.1016/j.jallcom.2012.03.100

Pluengphon, P., Bovornratanaraks, T., Tsuppayakorn-aek, P., Pinsook, U., and Inceesungvorn, B. (2019). High-pressure phases induce H-vacancy diffusion kinetics in TM-doped MgH_2: Ab initio study for hydrogen storage improvement. *Int. J. Hydrogen Energy*. 44, 21948–21954. doi: 10.1016/j.ijhydene.2019.06.066

Pudukudy, M., Yaakob, Z., Mohammad, M., Narayanan, B., and Sopian, K. (2014). Renewable hydrogen economy in Asia–Opportunities and challenges: an overview. *Renew. Sust. Energ. Rev*. 30, 743–757. doi: 10.1016/j.rser.2013.11.015

Pukazhselvan, D., Kumar, V., and Singh, S. K. (2012). High capacity hydrogen storage: basic aspects, new developments and milestones. *Nano Energy*.1, 566–589. doi: 10.1016/j.nanoen.2012.05.004

Razavi, F. S., Morassaei, M. S., Salehabadi, A., Salavati-Niasari, M., and Moayedi, H. (2019). Auto-combustion synthesis, structural analysis, and electrochemical solid-state hydrogen storage performance of strontium cobalt oxide nanostructures. *Int. J. Hydrogen Energy* 44, 31183–31191. doi: 10.1016/j.ijhydene.2019.10.012

Rusman, N. A. A., and Dahari, M. (2016). A review on the current progress of metal hydrides material for solid-state hydrogen storage applications. *Int. J. Hydrogen Energy* 41, 12108–12126. doi: 10.1016/j.ijhydene.2016.05.244

Sadhasivam, T., Kim, H., Jung, S., Roh, S., Park, J., and Jung, H. (2017). Dimensional effects of nanostructured Mg/MgH_2 for hydrogen storage applications: a review. *Renew. Sust. Energ. Rev.* 72, 523–534. doi: 10.1016/j.rser.2017.01.107

Santos, S. F., Ishikawa, T. T., Botta, W. J., and Huot, J. (2014). MgH_2+FeNb nanocomposites for hydrogen storage. *Mater. Chem. Phys.* 147, 557–562. doi: 10.1016/j.matchemphys.2014.05.031

Shahi, R. R., Tiwari, A. P., Shaz, M. A., and Srivastava, O. N. (2013). Studies on de/rehydrogenation characteristics of nanocrystalline MgH_2 co-catalyzed with Ti, Fe and Ni. *Int. J. Hydrogen Energy* 38, 2778–2784. doi: 10.1016/j.ijhydene.2012.11.073

Shang, C. (2004). Mechanical alloying and electronic simulations of (MgH_2+M) systems (M=Al, Ti, Fe, Ni, Cu and Nb) for hydrogen storage. *Int. J. Hydrogen Energy* 29, 73–80. doi: 10.1016/S0360-3199(03)00045-4

Shao, H., Felderhoff, M., Schuth, F., and Weidenthaler, C. (2011). Nanostructured Ti-catalyzed MgH_2 for hydrogen storage. *Nanotechnology* 22:235401. doi: 10.1088/0957-4484/22/23/235401

Shao, J., Xiao, X., Fan, X., Huang, X., Zhai, B., Li, S., et al. (2015). Enhanced hydrogen storage capacity and reversibility of $LiBH_4$ nanoconfined in the densified zeolite-templated carbon with high mechanical stability. *Nano Energy* 15, 244–255. doi: 10.1016/j.nanoen.2015.04.023

Singh, M. K., Bhatnagar, A., Pandey, S. K., Mishra, P. C., and Srivastava, O. N. (2017). Experimental and first principle studies on hydrogen desorption behavior of graphene nanofibre catalyzed MgH_2. *Int. J. Hydrogen Energy* 42, 960–968. doi: 10.1016/j.ijhydene.2016.09.210

Song, J., Wang, J., Hu, X., Meng, D., and Wang, S. (2019). Activation and disproportionation of Zr_2Fe alloy as hydrogen storage material. *Molecules* 24:1542. doi: 10.3390/molecules24081542

Sterl, F., Linnenbank, H., Steinle, T., Morz, F., Strohfeldt, N., and Giessen, H. (2018). Nanoscale hydrogenography on single magnesium nanoparticles. *Nano Lett*. 18, 4293–4302. doi: 10.1021/acs.nanolett.8b01277

Su, W., Zhu, Y., Zhang, J., Liu, Y., Yang, Y., Mao, Q., et al. (2016). Effect of multi-wall carbon nanotubes supported nano-nickel and TiF_3 addition on hydrogen storage properties of magnesium hydride. *J.Alloy. Compd.* 669, 8–18. doi: 10.1016/j.jallcom.2016.01.253

Sun, G., Li, Y., Zhao, X., Wu, J., Wang, L., and Mi, Y. (2016). First-principles investigation of the effects of Ni and Y co-doped on destabilized MgH_2. *RSC Adv.* 6, 23110–23116. doi: 10.1039/C5RA23996F

Tanniru, M., Slattery, D. K., and Ebrahimi, F. (2020). A study of stability of MgH_2 in Mg−8at%Al alloy powder. *Int. J. Hydrogen Energy*. 35, 3555–3564. doi: 10.1016/j.ijhydene.2010.01.109

Wan, C., Zhou, L., Sun, L., Xu, L. X., Cheng, D. G., Chen, F. Q., et al. (2020). Boosting visible-light-driven hydrogen evolution from formic acid over AgPd/2D g-C3N4 nanosheets Mott-Schottky photocatalyst. *Chem. Eng. J.* 396:125229. doi: 10.1016/j.cej.2020.125229

Wang, H., Lin, H. J., Cai, W. T., Ouyang, L. Z., and Zhu, M. (2016). Tuning kinetics and thermodynamics of hydrogen storage in light metal element based systems – A review of recent progress. *J. Alloy. Compd.* 658, 280–300. doi: 10.1016/j.jallcom.2015.10.090

Wang, K., Wu, G., Cao, H., Li, H., and Zhao, X. (2018). Improved reversible dehydrogenation properties of MgH_2 by the synergetic effects of graphene oxide-based porous carbon and $TiCl_3$. *Int. J. Hydrogen Energy* 43, 7440–7446. doi: 10.1016/j.ijhydene.2018.02.195

Wang, Y., Zhang, Q., Wang, Y., Jiao, L., and Yuan, H. (2015). Catalytic effects of different Ti-based materials on dehydrogenation performances of MgH_2. *J. Alloy. Compd.* 645, S509–S512. doi: 10.1016/j.jallcom.2014.12.071

Wang, Z., Zhang, X., Ren, Z., Liu, Y., Hu, J., Li, H., et al. (2019). In situ formed ultrafine NbTi nanocrystals from a NbTiC solid-solution MXene for hydrogen storage in MgH_2. *J. Mater. Chem. A* 7, 14244–14252. doi: 10.1039/C9TA03665B

Webb, C. J. (2015). A review of catalyst-enhanced magnesium hydride as a hydrogen storage material. *J. Phys. Chem. Solids* 84, 96–106. doi: 10.1016/j.jpcs.2014.06.014

Winter, C. J. (2009). Hydrogen energy — Abundant, efficient, clean: a debate over the energy-system-of-change. *Int. J. Hydrogen Energy* 34, S1–S52. doi: 10.1016/j.ijhydene.2009.05.063

Xia, G. L., Tan, Y. B., Chen, X. W., Sun, D. L., Guo, Z. P., Liu, H. K., Ouyang, L. Z., et al. (2015). Monodisperse magnesium hydride nanoparticles uniformly self-assembled on graphene. *Adv. Mater.* 27, 5981–5988. doi: 10.1002/adma.201502005

Xia, G. L., Zhang, L. J., Chen, X. W., Huang, Y. Q., Sun, D. L., Fang, F., et al. (2018). Carbon hollow nanobubbles on porous carbon nanofibers: an ideal host for high-performance sodium-sulfur batteries and hydrogen storage. *Energy Storage Mat.* 14, 314–323. doi: 10.1016/j.ensm.2018.05.008

Xiao, X., Qin, T., Jiang, Y., Jiang, F., Li, M., Fan, X., et al. (2017). Significantly enhanced hydrogen desorption properties of $Mg(AlH_4)_2$ nanoparticles synthesized using solvent free strategy. *Prog. Natl.Acad. Sci. U.S.A.* 27, 112–120. doi: 10.1016/j.pnsc.2017.01.006

Xie, L., Liu, Y., Zhang, X., Qu, J., Wang, Y., and Li, X. (2009). Catalytic effect of Ni nanoparticles on the desorption kinetics of MgH_2 nanoparticles. *J. Alloy. Compd.* 482, 388–392. doi: 10.1016/j.jallcom.2009.04.028

Xu, S., Wang, F., Tang, W., Wang, Y., and Yu, R. (2018). Microstructure and hydrogen storage properties of $Zr_{0.8}Ti_{0.2}Co_{1-x}Fe$ (x=0, 0.1, 0.2, 0.3) alloys. *Int. J. Hydrogen Energy* 43, 839–847. doi: 10.1016/j.ijhydene.2017.11.151

Yang, J., Sudik, A., Wolverton, C., and Siegel, D. J. (2010). High capacity hydrogen storage materials: attributes for automotive applications and techniques for materials discovery. *Chem. Soc. Rev.* 39, 656–675. doi: 10.1039/B802882F

Yang, W. N., Shang, C. X., and Guo, Z. X. (2010). Site density effect of Ni particles on hydrogen desorption of MgH_2. *Int. J. Hydrogen Energy* 35, 4534–4542. doi: 10.1016/j.ijhydene.2010.02.047

Yang, X., Ji, L., Yan, N., Sun, Z., Lu, X., Zhang, L., et al. (2019). Superior catalytic effects of FeCo nanosheets on MgH_2 for hydrogen storage. *Dalton Trans.* 48, 12699–12706. doi: 10.1039/C9DT02084E

Yao, L., Lyu, X., Zhang, J., Liu, Y., Zhu, Y., Lin, H., et al. (2020). Remarkable synergistic effects of Mg2NiH4 and transition metal carbides (TiC, ZrC, WC) on enhancing the hydrogen storage properties of MgH2. *Int. J. Hydrogen Energy* 45, 6765–6779. doi: 10.1016/j.ijhydene.2019.12.139

Yavari, A., Lemoulec, A., Decastro, F., Deledda, S., Friedrichs, O., Botta, W., et al. (2005). Improvement in H-sorption kinetics of MgH powders by using Fe nanoparticles generated by reactive FeF addition. *Scripta Mater.* 52, 719–724. doi: 10.1016/j.scriptamat.2004.12.020

Yu, H., Bennici, S., and Auroux, A. (2014). Hydrogen storage and release: kinetic and thermodynamic studies of MgH_2 activated by

transition metal nanoparticles. *Int. J. Hydrogen Energy*. 39, 11633–11641. doi: 10.1016/j.ijhydene.2014.05.069

Yu, X., Tang, Z., Sun, D., Ouyang, L., and Zhu, M. (2017). Recent advances and remaining challenges of nanostructured materials for hydrogen storage applications. *Prog. Mater. Sci.* 88, 1–48. doi: 10.1016/j.pmatsci.2017.03.001

Yu, X. B., Yang, Z. X., Liu, H. K., Grant, D. M., and Walker, G. S. (2010). The effect of a Ti-V-based BCC alloy as a catalyst on the hydrogen storage properties of MgH_2. *Intern. J. Hydrogen Energy* 35, 6338–6344. doi: 10.1016/j.ijhydene.2010.03.089

Zahiri, B., Danaie, M., Tan, X., Amirkhiz, B. S., Botton, G. A., and Mitlin, D. (2012). Stable hydrogen storage cycling in magnesium hydride, in the range of room temperature to 300 °C, achieved using a new bimetallic Cr-V nanoscale catalyst. *J. Phys. Chem. C* 116, 3188–3199. doi: 10.1021/jp211254k

Zhai, B., Xiao, X., Lin, W., Huang, X., Fan, X., Li, S., et al. (2016). Enhanced hydrogen desorption properties of $LiBH_4$-$Ca(BH_4)_2$ by a synergetic effect of nanoconfinement and catalysis. *Int. J. Hydrogen Energy* 41, 17462–17470. doi: 10.1016/j.ijhydene.2016.06.170

Zhang, J., Shi, R., Zhu, Y., Liu, Y., Zhang, Y., Li, S., et al. (2018). Remarkable synergistic catalysis of Ni-doped ultrafine TiO_2 on hydrogen sorption kinetics of MgH_2. *ACS Appl. Mater. Inter.* 10, 24975–24980. doi: 10.1021/acsami.8b06865

Zhang, L., Cai, Z., Yao, Z., Ji, L., Sun, Z., Yan, N., et al. (2019a). A striking catalytic effect of facile synthesized $ZrMn_2$ nanoparticles on the de/rehydrogenation properties of MgH_2. *J. Mater. Chem. A* 7, 5626–5634. doi: 10.1039/C9TA00120D

Zhang, L., Cai, Z., Zhu, X., Yao, Z., Sun, Z., Ji, L., et al. (2019b). Two-dimensional ZrCo nanosheets as highly effective catalyst for hydrogen storage in MgH_2. *J. Alloy. Compd.* 805, 295–302. doi: 10.1016/j.jallcom.2019.07.085

Zhang, L., Ji, L., Yao, Z., Yan, N., Sun, Z., Yang, X., et al. (2019c). Facile synthesized Fe nanosheets as superior active catalyst for hydrogen storage in MgH_2. *Int. J. Hydrogen Energy* 44, 21955–21964. doi: 10.1016/j.ijhydene.2019.06.065

Zhang, L., Sun, Z., Cai, Z., Yan, N., Lu, X., Zhu, X., et al. (2020a). Enhanced hydrogen storage properties of MgH2 by the synergetic catalysis of Zr0.4Ti0.6Co nanosheets and carbon nanotubes. *Appl. Surf. Sci*. 504:144465. doi: 10.1016/j.apsusc.2019.144465

Zhang, X. L., Liu, Y. F., Zhang, X., Hu, J. J., Gao, M. X., and Pan, H. G. (2020b). Empowering hydrogen storage performance of MgH_2 by nanoengineering and nanocatalysis. *Mater.Today Nano* 9:100064. doi: 10.1016/j.mtnano.2019.100064

Zhou, C., Bowman, R. C., Fang, Z. Z., Lu, J., Xu, L., Sun, P., et al. (2019a). Amorphous TiCu-based additives for improving hydrogen storage properties of magnesium hydride. *ACS Appl. Mater. Interfaces* 11, 38868–38879. doi: 10.1021/acsami.9b16076

Zhou, C., Fang, Z. Z., Ren, C., Li, J., and Lu, J. (2013). Effect of Ti intermetallic catalysts on hydrogen storage properties of magnesium hydride. *J. Phys. Chem. C* 117, 12973–12980. doi: 10.1021/jp402770p

Zhou, C., Fang, Z. Z., Sun, P., Xu, L., and Liu, Y. (2019b). Capturing low-pressure hydrogen using VTiCr catalyzed magnesium hydride. *J. Power Sources* 413, 139–147. doi: 10.1016/j.jpowsour.2018.12.048

Conflict of Interest: The authors declare that the research was conducted in the absence of any commercial or financial relationships that could be construed as a potential conflict of interest.

Advantages of publishing in Frontiers

OPEN ACCESS
Articles are free to read for greatest visibility and readership

FAST PUBLICATION
Around 90 days from submission to decision

HIGH QUALITY PEER-REVIEW
Rigorous, collaborative, and constructive peer-review

TRANSPARENT PEER-REVIEW
Editors and reviewers acknowledged by name on published articles

Frontiers
Avenue du Tribunal-Fédéral 34
1005 Lausanne | Switzerland

Visit us: www.frontiersin.org
Contact us: info@frontiersin.org | +41 21 510 17 00

REPRODUCIBILITY OF RESEARCH
Support open data and methods to enhance research reproducibility

DIGITAL PUBLISHING
Articles designed for optimal readership across devices

FOLLOW US
@frontiersin

IMPACT METRICS
Advanced article metrics track visibility across digital media

EXTENSIVE PROMOTION
Marketing and promotion of impactful research

LOOP RESEARCH NETWORK
Our network increases your article's readership